Title

Dynamic behavior of two advanced materials: ultrafine-grained titanium and high-entropy alloys

Permalink

https://escholarship.org/uc/item/6fs5c1pk

Author

Li, Zezhou

Publication Date

2019

UNIVERSITY OF CALIFORNIA SAN DIEGO

Dynamic behavior of two advanced materials: ultrafine-grained titanium and high-entropy alloys

A dissertation submitted in partial satisfaction of the requirements

for the degree of Doctor of Philosophy

in
Materials Science and Engineering
by

Zezhou Li

Committee in charge:

Professor Marc A. Meyers, Chair
Professor Shengqiang Cai
Professor Vlado A. Lubarda
Professor Xanthippi Markenscoff
Professor Kenneth S. Vecchio

2019

This dissertation of Zezhou Li is approved, and it is acceptable in quality and form for publication on microfilm and electronically:

Chair

University of California San Diego

2019

DEDICATION

To my parents

TABLE OF CONTENTS

SIGNATURE PAGE……………..…………………………………..……………………………iii

DEDICATION……………………………………………………………………..………iv

TABLE OF CONTENTS..v

LIST OF FIGURES x

LIST OF TABLES xviii

ACKNOWLEDGMENTS xix

VITA xxiii

ABSTRACT OF DISSERTATION..xxv

Chapter 1. Introduction 1

Chapter 2. Background 6

2.1 Adiabatic shear localization 6

2.1.1 Basic character and classification of shear bands..6

2.1.2 Material sensitivity to shear localization..8

2.1.3. Formation and growth of the shear bands 13

2.2 Recovery, recrystallization and grain growth 20

2.3 Nanostructured materials..27

2.3.1 Pile-up break down...27

2.3.2 Grain boundary sliding....30

2.3.3 Grain- boundary rotation/ grain coalescence....32

2.3.4 Twinning....33

2.3.5 Grain boundary dislocation and annihilation....34

2.3.6 Strain-rate sensitivity....35

2.3.7 Shear band formation....36

2.3.8 Amorphization....37

2.4 High-entropy alloys....38

2.4.1 Definition....38

2.4.2 Strengthening mechanisms....40

Chapter 3. Materials and Experimental Procedures....45

3.1 Description of materials....45

3.2 Quasi-static and dynamic compression....45

3.3 Forced shear setup with hat-shaped specimen....49

3.4 Optical microscopic observation....50

3.5 Microhardness measurement....51

3.6 Scanning electron microscopy (SEM)....52

3.6.1 Energy dispersive X-ray spectroscopy (EDS)....53

3.6.2 Micro-orientation measurement 54

3.7 Transmission electron microscopy (TEM) 55

3.8 X-ray diffractometer 56

Chapter 4. Dynamic response of CG and UFG titanium 58

4.1 Introduction 58

4.2 Experiments 59

4.3 Results 61

4.3.1 Microstructure 61

4.3.2 Mechanical response of UFG titanium 62

4.3.3 Mechanical response of shear band 67

4.3.4 Microhardness of adiabatic shear band 71

4.3.5 Microstructure evolution of ASB 73

4.3.6. Cooling of the shear bands 81

4.3.7 Fracture of the shear band 83

4.4 Discussion 84

4.4.1 Width of shear band 84

4.4.1.1 Effect of thermal conductivity 84

4.4.1.2 Effect of heat capacity 85

4.4.1.3 Effect of thermal softening……..…………………………………………86

4.4.1.4 Combined effects on shear-band width…………………………………..…..87

4.4.2 Dislocation evolution during deformation for CG and UFG 500 nm titanium 91

4.4.3 Dislocation evolution during deformation for UFG 100 nm titanium 103

4.4.4 Effect of Zener-Hollomon parameter 105

Chapter 5. Dynamic response of the $Al_{0.3}$CoCrFeNi high-entropy alloy 108

5.1 Background 108

5.2 Microstructure of the $Al_{0.3}$CoCrFeNi HEA...110

5.3 Mechanical behavior 111

5.4 Resistance to shear localization...115

Chapter 6. Dynamic response of the CoCrFeMnNi high-entropy alloy 122

6.1 Dynamic behavior of the annealed CoCrFeMnNi high-entroy alloy 122

6.1.1. Microstructure of the CoCrFeMnNi high-entroy alloy 122

6.1.2 Lattice constants for the CoCrFeMnNi high-entropy alloy..................................124

6.1.3 Mechanical behavior of the CoCrFeMnNi high-entroy alloy 125

6.1.4 Strengthening and shear localization mechanisms in the Cantor alloy 126

6.2 Dynamic behavior of the as-processed CoCrFeMnNi high-entroy alloy....................134

6.2.1. Microstructure 134

    6.2.2. Mechanical response 137

    6.2.3 Width of shear bands 138

  6.3 Summary of the chapter 140

Chapter 7. Summary and perspectives 142

  7.1 Dislocation dynamics in ultrafine-grained titanium 142

  7.2 Strengthening mechanism in CoCrNi-based high-entropy alloys…………………….143

  7.3. Width of shear bands 145

  7.4 Perspectives 146

References 149

LIST OF FIGURES

Figure 1.1. The increase in the volume fraction of grain boundaries and triple junctions as a function of grain size in the nanocrystalline (<100 nm) and ultrafine-grained (100 nm–1000 nm) regimes. These plots are based on space-filling tetrakaidekahedral grains with a grain boundary thickness of 1 nm (thick line), where the dotted lines ……..……….……………..……………2

Figure 1.2. The effect of atom size difference on atom positions in (a) a dilute solution, where solute atoms are constrained to occupy lattice sites by surrounding solvent atoms and (b) a complex, concentrated solution, where there is no dominant atom species and atom positions usually deviate from mean lattice positions. The …….……………………………………………….….………..3

Figure 1.3. (a) Change of the mixing entropy with changing the number of equimolar elements in HEAs. (b) The alloy systems separated by the configuration entropy [20]……………………..…5

Figure 2.1.1 Scanning electron micrograph of the formation of the shear band in coarse-grained (CG) pure titanium [10]………………………………………………………………….……..6

Figure 2.1.2.1. Schematic drawing of passive geometric flow control of shear bands. The degree of constraint on the flow is set by the parameter [28]….………………..………………….………12

Figure. 2.1.2.2. Cutting of Mg AZ31B alloy by the free surface and constrained……….………12

Figure 2.1.3.1. Graph showing there is a shear band width with minimum growth time [33]…...17

Figure 2.1.3.2. In-situ experiments of shear band propagation in the C-300 steel [33]…………..18

Figure 2.1.3.3. Temperature profiles at different distances from the notch tip, Ti-6Al-4V, V=64.5 ms^{-1} [33]……….……………………………………………………………..………..19

Figure 2.1.3.4. (a) Shear band speed histories for C-300 at different impact velocities. (b) Maximum and average shear band speeds as functions of impact velocity for C-300 steel……..20

Figure 2.2.1 Schematic illustration of microstructural evolution during high-strain-rate deformation. (a) Randomly distributed dislocations; (b) Elongated dislocation cell formation (i.e. dynamic recovery); (c) Elongated subgrain formation; (d) Initial break-up of elongated subgrains; (e) Recrystallized microstructure [13]…………………………...………………...…………..24

Figure 2.2.2. Schematic diagram of recrystallized grain evolution in an adiabatic shear band from the starting single crystal (A), to formation of elongated subgrains (B), to rotation of equiaxed subgrains (C), to high angle misorientations between some subgrains (D). The final stage is boundary refinement during cooling (E) [40]……….…………………..…………………..……26

Figure 2.3.1.1 plots showing the yield stress changes as a function of grain size with conventional Hall-Petch curve: (a) Cu, (b) Fe, (c) Ni, (d) Ti [2]…………………………………………….28

Figure 2.3.1.2. (a) The model contains bulk and grain boundary material. (b) Ideal nanogrian with spherical diameter *D* and thickness *t* [5]……………………………………………………….29

Figure. 2.3.2 (a) Schematic representation of grain-boundary sliding in polycrystal; (b) grain-boundary sliding path; (c) idealized sinusoidal path with diffusional migration of boundary according to Raj and Ashby [43]; (d) decrease in wave amplitude h with increasing plastic strain…………………………………………………………..…………………………….31

Figure. 2.3.3. Model of (a) rotation of nanograins, (b) annihilation of grain boundary, and (c) coalescence of nanograins [2]...…………………………………………….……….…….……..32

Figure. 2.3.4. Critical shear stress required for the activation of a twin nucleus as a function of size [46]………………………………………………………………………...…………..….33

Figure 2.3.5. Model representing grain boundary source and sink…………………………..……34

Figure 2.3.6. The strain-rate sensitivity in (a) fcc Cu (b) fcc Ni and (c) bcc iron and Ta with different grain sizes [50]…………………………………...……………………..……36

Figure 2.3.7. Change of deformation mode for ultrafine-grained Fe. (a) Uniformed deformation at low strain-rate compression with grain size 980 nm at the strain ~0.14. (b) Non-uniform low-rate deformation with grain size 268 nm. (c) Non-uniform high strain-rate deformation with grain size 268 nm [52]……………………………...……………………………………………..…...37

Figure 2.3.8. The uniaxial compression of nanocrystalline NiTi pillar with grain size 65 nm. The localized shear band obtains amorphous phase [55]…………………….………………..38

Figure 2.4.1 Ashby plot for HEAs compared with other materials describing the relationship of fracture toughness and yield strength [56]…………………………………………………..…39

Figure 2.4.2.1. Yield stress with both predicted lines and experimental points [62]………..……41

Figure 2.4.2.2. Stacking fault energy variation with local chemical ordering. (A) Distribution of intrinsic stacking fault energy, γ_{isf}, for equimolar CrCoNi alloys in four specific states, i.e., CH_0, CH_1, CH_2 and CH_F, which expand from random solid solution to the highest degree of chemical ordering. Totally 108 stacking faults were considered for analysis ………………..….43

Figure 2.4.2.3. Deformation map for the $Cr_{10}Mn_{30}Fe_{50}Co_{10}$ high-entropy alloy under the tension, noting that formation of hcp phases and mechanical twins to provides strength of the materials [60]………………..……………………………………………………………………..….44

Figure 3.2.1. The split Hopkinson pressure bar system [68]…………………………..………47

Figure 3.2.2. (a) Stress vs. time plot of 50-50 NiTi super-elastic alloy at room temperature. (b) Strain rate vs. strain curves of metals show the strain hardening induced inhomogeneous strain rate [68]……………...…………………………………………………………….……….47

Figure 3.2.3. Incident and reflected waves with different thicknesses of pulse shapers [68]…….48

Figure 3.3. The hat-shaped specimen right in the middle of two the bars: (a) before the impact; and (b) after the impact…………………………...……………………………………………..50

Figure 3.5. Schematic of the square-based diamond pyramidal indenter used for the Vickers test and an example of the indentation it produces [71]……………………………………….…51

Figure 3.6.1. (a) Components of the scanning electron microscopy (SEM); (b) schematic drawing showing the components in the SEM chamber……………………………………...………53

Figure 3.6.2. Schematic drawing of the diffracting cones with respect to the reflecting plane, the specimen, and the phosphor screen [77]……………………..…..……………………………54

Figure 3.7. Schematic ray path for a transmission electron microscope (TEM)…………….……56

Figure 3.8. Schematic diagram of diffraction of X-rays by a crystal (Bragg condition)………....57

Figure. 4.1. (a) Bright- field and (b) Dark-field images of microstructure of high-pressure torsion processed commercial pure titanium annealed at 250 °C for 10 min. (c) Mechanical response of high-pressure torsion processed and post-annealed commercial pure titanium [82] …………………………………………………………………………………….…...58

Figure. 4.2. (a) SEM image showing focused ion beam position right in the middle of shear bands; (b) TEM sample attached to a holder grid; (c) The sample was about 8 μm in length and 6 μm in width. (d) The thickness of TEM sample was less than 100 nm ……………………………..….60

Figure 4.3.1. (a1) Transmission electron microscopy image showing Ti with average grain size of 500 nm; (b1) microstructure of ultrafine-grained Ti; (c1) selected area diffraction (SAD) pattern in (a1). (a2) Transmission electron microscopy image showing Ti with average grain size of 100 nm; (b2) microstructure of ultrafine-grained grains; (c2) ……..…………………………..…..……..62

Figure 4.3.2.1. (a) Stress-strain relationships of UFG titanium cylindrical samples at different strain-rates. (b) Strain-hardening rate as a function of strain. (c) Strain-rate sensitivity of CG titanium and UFG titanium. (d) Stress-stress relationship and Zerilli-Armstrong constitutive equation fit to experimental results at strain rates 10^{-5} s^{-1}, 1300 s^{-1} and 1700 s^{-1}…………….…..…..63

Figure 4.3.2.2. (a) Microhardness Hall-Petch relationship of titanium. (b) Stress-strain curves of Ti with different grain sizes under dynamic loading strain-rates ~10^3 s^{-1}……………………..…….67

Figure 4.3.3. (a) Shear stress and shear strain plots in shear region for CG titanium. (b) Shear stress and shear strain in shear region for UFG 500 nm titanium. (c) Shear stress and shear strain in shear region for UFG 100 nm titanium…………………………………………………..……….69

Figure 4.3.4. Microhardness of shear bands for CG titanium at (a) 173 K and UFG titanium at (b) 293 K and (c) 173 K…………………………………………………………………..……..72

Figure 4.3.5.1 TEM images of the shear band formed in CG titanium at (a1) 293 K, (b1) 173 K, (c1) 77 K. TEM images of the shear band formed in UFG 500 nm titanium at (a2) 293 K, (b2) 293 K, (c2) 77 K. TEM images of the shear band formed in UFG 100 nm titanium at (a3) 293 K, (b3) 173 K, (c3) 77 K……………………………………………………………………….……75

Figure 4.3.5.2. Microstructure inside the shear bands for CG Ti at (a1) 293 K and (b1) 77 K. Microstructure inside the shear bands for UFG 500 nm Ti at (a2) 293 K and (b2) 173 K. (a3) Microstructure inside the shear bands for UFG 100 nm Ti at 293 K. The red arrows show the formation of recrystallized subgrains in the elongated nano-bundle. (b3) Dark-field ………..….76

Figure 4.3.5.3. Grain size distribution in shear bands in CG titanium at (a1) 293 K and (b1) 77K. Grain size distribution in shear bands in UFG 500 nm titanium at (a2) 293 K and (b2) 173 K. Grain size distribution in shear bands in UFG 100 nm titanium at (a3) 293 K and (b3) 77 K……………………………………………………………………………………….77

Figure 4.3.5.4. TEM images of the microstructure (a) of the sample B (perpendicular to shear band), (b) near the shear band, (c) inside the shear band. (Shear direction nominally perpendicular to the foil; misorientation is possible)…………………………………………………………..……78

Figure 4.3.5.5. TEM images of (a) the microstructure of the sample C (inside shear band), (b) the dark-field microstructure, (c) the equiaxed grains. (Shear direction indicated in dark-field micrograph (b))……………………………………...…………………………….…….80

Figure 4.3.6. Temperature in the middle of the shear bands as a function of cooling time for CG and UFG titanium ...………………………..………………………………………82

Fig. 4.3.7. SEM images of the sample with max-displacement 1 mm showing (a) dimples along the shear band, (b) alignment between dimples and fracture surface, and of the sample with max-displacement 1.15 mm (c) ductile areas and cleavage plane, (d) dimples areas, (e) cleavage planes. (f) Schematic illustration of ASB failure of UFG 500 nm titanium……………………….…..84

Fig. 4.4.1.1 SEM images showing the width of shear bands in different titanium at different temperatures…………………………………….…………………………………..…86

Figure 4.4.1.2. Relationship of the thermal conductivity of titanium with different grain sizes [11,108]..………………………………..……………………………………………..…87

Figure 4.4.1.3. Specific heat capacity of titanium……………………………………..……89

Figure. 4.4.1.4. Thermal softening effect of CG and UFG titanium [113]……………….…….90

Figure 4.4.1.5. Width of the shear band in pure titanium for different grain sizes and temperatures. The full lines represented Bai-Dodd [104] and Grady equation [105] predictions applied for CG and UFG 100 nm titanium…………………………………………………………….….…91

Figure 4.4.2.1. Schematic illustration of microstructural evolution inside the shear band according to the rotational dynamic recrystallization mechanism: (a) randomly distributed equiaxed grains; (b) formation of elongated grains through plastic deformation (shear direction indicated by arrows); (c) dislocations accumulation forming subgrain boundaries; …………………………………92

Figure 4.4.2.2. Angle of rotation of grain boundary during the deformation process as a function of time for (a) different grain sizes (40, 70, and 100 nm) at T=900 K and (b) different temperatures (700, 800, and 900 K) for grain size L=40 nm. (c) Schematic showing force acting on the grain boundary with radius of curvature R. (d) Grain-boundary velocity as a …………………..…….96

Figure 4.4.2.3. (a1,a2) Change of dislocation density with the variation of dislocation density. (b1,b2) Relationship between critical dislocation density and subgrain size with Zener- Hollomon parameter (ln Z) [119]…………………………………...…..…………………….………100

Figure 4.4.2.4. (a) Width of shear band as function of initial grain size. (b) Recrystallized grain size as a function of shear band width. (c) Recrystallized grain size as a function of estimated local shear strain ………………………………………………………………………………..…….102

Figure 4.4.3.1. Schematic drawing showing the shear-rotational dynamic recrystallization mechanism for UFG 100 nm to form recrystallized equiaxed nanograins. (a) Original ultrafine-grains; (b) formation of low-angle grain boundaries and subsequent grain rotation under the applied shear stress; (c) formation of recrystallized equiaxed nanograins ……………….……….105

Figure 4.4.4. The relationship of Zener-Hollomon parameter [119] with the average recrystallized grain size for titanium……………………………………………..…………………………107

Figure 5.1.1. Arc-melting method to make high-entropy alloys [136]…………………………..108

Figure 5.1.2. Microhardness of $Al_xCoCrCuFeNi$, $Al_xCoCrFeNi$ and $Al_xCoCrFeNi_2$ high-entropy alloys and corresponding phase [137]………….……………………………………………109

Figure 5.2. (a) Electron backscattered diffraction (EBSD)-inverse pole figure (IPF) showing the microstructure of the $Al_{0.3}CoCrFeNi$ high-entropy alloy with annealing twins. (b) Neutron-diffraction pattern of the $Al_{0.3}CoCrFeNi$ high-entropy alloy. (c) APT analysis showing the homogeneous distribution of Al, Co, Cr, Fe, and Ni elements. (d) APT results…………………111

Fig. 5.3. (a) True stress-true strain curves of the $Al_{0.3}CoCrFeNi$ high-entropy alloy at different strain rates (with Jonson-Cook model fitting curves) and true stress-true strain curve of the CG pure aluminum at the quasi-static 10^{-2} s^{-1}. (b) Strain-hardening rate as a function of true strain of the $Al_{0.3}CoCrFeNi$ high-entropy alloy and pure aluminum at the strain rate 10^{-2} s^{-1}..………..…115

Figure 5.4.1. TEM bright-field images of the deformed samples at the strain rates of (a) 10^{-4} s^{-1}; (b) and (c) 1800 s^{-1}. (d) Schematic sketches showing the deformation mechanisms of the $Al_{0.3}CoCrFeNi$ high-entropy alloy under dynamic loading…………………………..………117

Figure 5.4.2. (a) Dimension of the hat-shaped sample. (b) Optical microscopy image of the deformed hat-shaped sample. (c) EBSD image near the deformation tip. (d) EBSD image showing deformation twins near the deformation tip……………………………………………………..118

Figure 5.4.3. Plot comparing the strain-hardening rate (at a compressive true strain of 0.2) as a function of Young's modulus for $Al_{0.3}CoCrFeNi$ HEA and other structural materials [43, 123-137]. (The strain hardening rate of the structural materials was calculated to be zero at the condition when the materials are fractured at a true strain of 0.2)……………………………………….…...121

Figure 6.1.1.1. EBSD (electron backscatter diffraction) image depicting the initial microstructure

of the as-received CoCrFeMnNi HEA ………………………………………………………….……..…..122
.

Figure 6.1.1.2. Images showing gas-atomised CrMnFeCoNi high-entropy alloy powders: (a) morphology of powders; (b) surface of powders ………………………………….……..…..123

Figure 6.1.1.3. Elementary distribution and chemical composition by Energy-dispersive X-ray spectrometry [178]……………………..……………………..……………………..…124

Figure. 6.1.2. (a) X-ray diffraction pattern of the alloy using Cu Kα radiation. (b) Selected area diffraction pattern of the alloy………………..……………………………………...…….125

Figure 6.1.3. Mechanial behavior of the Cantor alloy at different of strain-rates…………..…..126

Figure 6.1.4.1. (a) Schematic drawing of dynamic loading of the hat-shaped specimen with the stopper ring (in mm) by the split-Hopkinson pressure bar; (b) shear stress, strain and temperature evolution of the shear band; (c) scanning electron microscope (SEM) image of the shear band. (d) predicted critical shear strain for shear localization……………………………………………129

Figure 6.1.4.2. (a,b,c) Microstructure of the Cantor alloy deformed at a shear strain of 2.5. (d,e,f) Microstructure of recrystallized grains with annealed twins in the shear bands at s strain ~7 ……………………………………………………………………………….…………..…..129

Figure 6.1.4.3. (a) Bright-field TEM image of the microstructure inside the shear band; (b) corresponding dark-field TEM image of (a); (c) recrystallized grains with dislocations and twins; (d) recrystallized grains with dislocations; (e) recrystallized equiaxed grains; (f) the nanotwin inside one recrystallized grain…………………………………..………………….………..130

Figure 6.1.4.4. The shear-strain curve and corresponding star predicted by the constitutive model……………………………………………………………………………….………..133

Figure 6.1.4.5. (a1,b1,c1) Images describe the evolution of microstructure under dynamic impact. (a2,b2,c2) Schematic drawing shows the corresponding strengthening mechanism and shear localization mechanism of low-stacking energy HEA……….…………………………..…..133

Figure 6.2.1.1. The initial microstructure in the transverse direction. (a) Backscattered electron (BSE) image of the microstructure and X-ray diffraction pattern; (b) Electron backscatter diffraction (EBSD) image………………………………………………………………..…..135

Figure 6.2.1.2. (a) TEM images showing the severely deformed initial microstructure. (b) Selected diffraction pattern showing the fcc structure. (c) Slip bands obtains dislocations. (d) Wavy dislocations ……………………………...…………………………………………………..136

Figure 6.2.2. (a) Mechanical response of the CrMnFeCoNi Cantor HEA in compression, noting that the material can still continuously deform without shear fracture. (b) The strain-hardening rate of the material as a function of true strain……………………………………………………137

Figure 6.2.3.1. Shear stress and shear strain curves in shear bands occurring at 293 K and 77 K. The shear strain-rates are ~$6*10^5$ s^{-1} for both……………….………………………...……..138

Figure 6.2.3.2 (a) Secondary electron microscopy (SEM) image of shear band formed at 293 K; (b,c,d) corresponding TEM images showing the formation of ultra-fine grains. (e) SEM image of shear band formed at 77 K. (f,g,h) Corresponding TEM images showing formation of ultra-fine and nano- grains. Some of grains contains nanotwins pointed by ……………………………..139

Figure. 6.3. (a) Mechanical response of $Al_{0.3}$CoCrFeNi HEA and the Cantor alloy under high strain-rates; (b) the value of $\rho C_p n$ for pure Ti, Ti-6Al-4V alloy, 1006-Steel, Copper, Brass, $Al_{0.3}$CoCrFeNi HEA and the Cantor alloy; (c) thermal-softening effect of different materials; (d) predicted and experimental critical shear strain for shear localization [186]……………….…..141

Figure. 7.4. Summary of critical shear strain for shear localization in our materials and other structural materials [186]…………………………………………………………………….…148

LIST OF TABLES

Table 2.1. Theoretical and experimental shear band widths……………………………….……..16

Table 3.1.1. Grain size and crystal structure of the as-received materials………….……………45

Table 3.4. Etchants for the samples………………………………………………….………..50

Table 4.3.5. The width of shear bands and average recrystallized grain size inside the shear bands...……………………………………………….……………………………………..78

Table 4.4.2. Constants for the Kocks-Mecking model and critical dislocation density for shear localization ……………………………………………………………………..…...……100

Table 4.4.4. Parameters for the relationship of Zener-Hollomon parameter [119] with the average recrystallized grain size for titanium……………………………………......................………...107

Table 6.1. *d*-spacings (in Å) of the different (hkl) planes of the fcc CrMnFeCoNi HEA measured by different testing methods…………………………………………………………….……125

ACKNOWLEDGMENTS

I gratefully thanks for my advisor, Marc A. Meyers, giving me opportunity and support to work in this area (dynamic properties of materials). His profound knowledge enlightens my research significantly. He is also extremely patient on my research and helps significantly on the improvement of our papers. His intelligence on research often motives me to move forward. His curiosity, wisdom and dynamic energy to scientific and fundamental questions inspire me importantly when I met difficulties and are very influential to my academic career. I cannot achieve any goals without his guide and advisory.

I am thankful for the continuous advice of my committee members, Prof. Shengqiang Cai, Prof. Vlado A. Lubarda, Prof. Xanthippi Markenscoff, Prof. Kenneth S. Vecchio. Their suggestions and inspiration advance my research importantly on the deeper understanding and modeling of shear localization evolution.

I also would like to thank Shiteng Zhao, as a young scholar, who teaches me electron microscopy and mechanical testing. He introduces me to the group initially on the Hopkinson bar tests with Prof. Bingfeng Wang. He is very helpful on the guide and discussion on my research. His enthusiasm on academic career also inspires me to pursue my research goal.

Prof. R.Z. Valiev is greatly acknowledged for providing us the samples of ultrafine-grained titanium. He is a pioneer in the research field of severe plastic deformation and nanocrystalline materials.

Haoyan Diao and Prof. Peter K. Liaw are also greatly appreciated for providing us the samples of $Al_{0.3}CoCrFeNi$ high-entropy alloy. It is grateful that Haoyan Diao would like to help us on the materials characterization by electron backscatter diffraction (EBSD) and atom probe tomography (APT).

I would also like to thank Prof. Bingfeng Wang and Prof. Yong Liu to provide us the CoCrFeMnNi high-entropy alloy. With their excellent materials and encouragement, we can continue to pursue and examine the dynamic properties of single phase fcc high-entropy alloys.

Prof. R.O. Ritchie and Dr. Wen Yang is greatly appreciated for the collaboration work in the area of high-entropy alloys. They encourage me a lot on my research. It is a great opportunity to learn from Prof. Ritchie on both our review paper and collaborated research.

At UCSD, all of my lab mates and friends are all very helpful, including Haocheng Quan, Andrei Pissarenko, Rachel Flanagan, Audrey Velasco-Hogan, Joshua Pelz, Gaia Righi, Boya Li, Zida (Kotachi) Liu, Dr. Na Yan, Conger Bai, Tarah Sullivan, Andrew Martin Marquez, Senhat Alotaibi, Camila Rita de Souza, Yang (Daniel) Yu, Eric Nicholas Hahn, Vincent Robert Sherman, Bin Wang, Steve Naleway, Tane Remington, Everett Criss, Chaoyi Zhu, Cheng Zhang, Rui Kou, Qingyang Wang, Zhijian Wang, Qiguang He, Xudong Liang, Yue Zheng, Yang Wang, Shuang Cui.

The research was supported by the U.S. Department of Energy through grant NNSA/SSAP (DE-NA0002080), a UC Research Laboratories Grant (09- LR-06-118456-MEYM), the UCSD Center for High Energy Density Science (UCOP LAB FEES GRANT ID: LFR-17-449059) and the NNSA/DOE Center for Matter under Extreme Pressure (CMEC). China Scholarship Council (grant no. 201508020004) for Zezhou Li is also greatly acknowledged.

Chapter 4, in part, is a reprint of the materials as it appears in “Dynamic deformation and failure of ultrafine-grained titanium, Acta Materialia 2017 125: 210-218”. This work was coauthored by Zezhou Li, Bingfeng Wang, Shiteng Zhao, Ruslan Z Valiev, Kenneth S Vecchio, Marc A Meyers. The dissertation author was the primary author of this paper.

Chapter 4, in part, is currently being submitted as it appears in “The Effects of Ultra-Fine-Grained Structure and Cryogenic Temperature on Adiabatic Shear Localization in Titanium, Acta Materialia”. This work was coauthored by Zezhou Li, Shiteng Zhao, Bingfeng Wang, Shuang Cui, Renkun Chen, Ruslan Z. Valiev, Marc A. Meyers. The dissertation author was the primary investigator and primary author of this paper.

Chapter 5, in full, is a reprint of the materials as it appears in “High-velocity deformation of $Al_{0.3}CoCrFeNi$ high-entropy alloy: Remarkable resistance to shear failure, Scientific Reports, 2017 7:42742”. This work was coauthored by Zezhou Li, Shiteng Zhao, Haoyan Diao, Peter K. Liaw, Marc A. Meyers. The dissertation author was the primary author of this paper.

Chapter 6, in part, is a reprint of the materials as it appears in “Adiabatic shear localization in the CrMnFeCoNi high-entropy alloy, Acta Materialia 2018 151: 424-431.” And “Mechanical properties of high-entropy alloys with emphasis on face-centered cubic alloys, Progress in materials science 2019 102:296-345”. This work was coauthored by “Zezhou Li, Shiteng Zhao, Senhat M Alotaibi, Yong Liu, Bingfeng Wang, Marc A Meyers” and “Zezhou Li, Shiteng Zhao,

Robert O Ritchie, Marc A Meyers", respectively. The dissertation author was the primary author of these two papers.

Chapters 6, in part, is currently being prepared for submission for publication of the material. Shiteng Zhao*, Zezhou Li*, Wen Yang, Robert O. Ritchie, and Marc A. Meyers will be the coauthors. The dissertation author was the primary investigator and primary author of this paper.

VITA

2013 ***Bachelor of Science in Materials Science and Engineering***, University of Science and Technology, Beijing

2014 ***Master of Science in Materials Science and Engineering***, University of California San Diego

2019 ***Doctor of Philosophy in Materials Science and Engineering,*** University of California San Diego

Publications

1. **Zezhou Li**, Shiteng Zhao, Robert O. Ritchie, and Marc A. Meyers, Mechanical behavior of CoCrNi-based high-entropt alloys, **Progress in materials science**, 102 (2019) 296-345.

2. **Zezhou Li**, Shiteng Zhao, Senhat M. Alotaibi, Yong Liu, Bingfeng Wang, and Marc A. Meyers. "Adiabatic shear localization in the CrMnFeCoNi high-entropy alloy." **Acta Materialia** 151 (2018) 424-431.

3. **Zezhou Li**, Bingfeng Wang, Shiteng Zhao, Ruslan Z. Valiev, Kenneth S. Vecchio, and Marc A. Meyers. "Dynamic deformation and failure of ultrafine-grained titanium." **Acta Materialia** 125 (2017) 210-218.

4. **Zezhou Li**, Shiteng Zhao, Haoyan Diao, Peter K. Liaw, and Marc A. Meyers. "High-velocity deformation of Al 0. 3 CoCrFeNi high-entropy alloy: Remarkable resistance to shear failure." **Scientific Reports** 7 (2017) 42742.

5. Marc A. Meyers, **Zezhou Li**, Shiteng Zhao, Bingfeng Wang, Yong Liu, Peter K. Liaw, "Shear localization of fcc high-entropy alloys", the DYMAT Proceedings, (2018).

6. Bingfeng Wang, Ao Fu, Xiaoxia Huang, Bin Liu, Yong Liu, **Zezhou Li**, and Xiang Zan. "Mechanical properties and microstructure of the CoCrFeMnNi high entropy alloy under high strain rate compression." Journal of Materials Engineering and Performance 25, 7 (2016) 2985-2992.

7. Bingfeng Wang, Z. L. Liu, Xiaoyan Wang, and **Zezhou Li**. "An EBSD investigation on deformation-induced shear bands in a low nickel austenitic stainless steel under controlled shock-loading conditions." Materials Science and Engineering: A 610 (2014) 301-308.

8. Bingfeng Wang, Xiaoyan Wang, **Zezhou Li**, Rui Ma, Shiteng Zhao, Fangyu Xie, and Xiaoyong Zhang. "Shear localization and microstructure in coarse grained beta titanium alloy." Materials Science and Engineering: A 652 (2016) 287-295.

9. Bingfeng Wang, Rui Ma, Jindian Zhou, **Zezhou Li**, Shiteng Zhao, and Xiaoxia Huang. "Adiabatic shear localization in ultrafine grained 6061 aluminum alloy." Materials Science and Engineering: A 675 (2016) 221-227.

10. Marquez, Andrew M., **Zezhou Li**, Christopher H. Braithwaite, Timothy P. Weihs, Nicholas M. Krywopusk, David J. Gibbins, and Marc A. Meyers. "Fragmentation and mechanical performance of tailored nickel-aluminum laminate compacts." Materials Science and Engineering: A 727 (2018) 123-132.

11. Wei Huang, Nicholas A. Yaraghi, Wen Yang, Alexis Velazquez-Olivera, **Zezhou Li**, Robert O. Ritchie, David Kisailus, Susan M. Stover, Joanna McKittrick, A natural energy absorbent polymer composite: The equine hoof wall. Acta Biomaterialia, (2019) accepted.

12. Zhaowen Cui, Jingren Li, **Zezhou Li**, Shixuan Zeng, Hong Yan, Likun Jiang, Chengchang Jia, Performance study of copper matrix composite materials with CNTs, Al_2O_3 double reinforced by powder metallurgy method. Journal of Mechanical Engineering, 18 (2013) 18.

13. Ahmed Tiamiyu, Shiteng Zhao, **Zezhou Li**, Akindele ODESHI, and Szpunar Jerzy, Thermal and mechanical stability of austenite in metastable austenitic stainless steel, Metallurgical and Materials Transactions A. (2019) 1-18.

14. Jungmin Ha, Ekaterina Novitskaya, Natalie Lam, Maritza Sanchez, Yoon Hwa Kim, **Zezhou Li**, Won Bin Im, Olivia A. Graeve, Joanna McKittrick, Journal of Luminescence, **under review**.

In preparation

15. **Zezhou Li**, Shiteng Zhao, Bingfeng Wang, Shuang Cui, Renkun Chen, Ruslan Z. Valiev, Marc A. Meyers, Adiabatic shear localization in coarse- and ultrafine- grained titanium at cryogenic temperatures: thinner bands and smaller grains, **Acta Materialia**, **under review**.

16. Shiteng Zhao*, **Zezhou Li***, Wen Yang, Robert O. Ritchie, Marc A. Meyers, Dynamic behavior of as-processed CoCrFeMnNi high-entropy alloys, **in preparation**.

ABSTRACT OF DISSERTATION

Dynamic behavior of two advanced materials: ultrafine-grained titanium and high-entropy alloys

by

Zezhou Li
Doctor of Philosophy in Materials Science and Engineering

University of California, San Diego, 2019

Professor Marc A. Meyers, Chair

Dynamic deformation occurs when bodies are subjected to rapidly changing loads and can differ significantly from deformation that occurs under static or quasi-static situations. It is of great significance to understand the deformation and failure mechanisms of advanced materials, and there are potential applications in which dynamic deformation and failure can occur. Two classes of advanced materials, ultrafine-grained (UFG) (~500 nm and ~100 nm) titanium and high-entropy alloys (HEAs) ($Al_{0.3}$CoCrFeNi and CoCrFeMnNi) are the focus of this doctoral investigation.

The deformation and adiabatic shear localization at cryogenic temperatures (173 K and 77 K)

in ultrafine-grained (100 and 500 nm) titanium are investigated. In comparison with conventionally-grained titanium, the strength of ultrafine-grained titanium is higher due to the classic Hall-Petch effect while the strain-hardening rate approaches zero. Our results show that shear localization in dynamic deformation is also altered. The width of the shear band of coarse-grained titanium decreases from 30 μm at 293 K to 18 μm at 77 K (a 40% decrease). In contrast, for 100 nm titanium, the width of shear band decreases more significantly from 4 μm at room temperature to 1 μm (a 75% decrease) at cryogenic temperature (77 K). This difference is attributed to the combined effects of a decrease in the thermal conductivity and the specific heat capacity, and an increase in the thermal softening, which can lead to a band with thickness of 1 μm. These changes agree with the predictions of the Grady and Bai-Dodd theories. The dislocation evolution and the subgrain rotation mechanisms responsible for forming ultrafine- and nano-recrystallized grains are modeled. In addition, the Zener-Hollomon parameter is incorporated in the analysis to predict the critical dislocation density for shear localization and the recrystallized grain size in titanium .

The mechanical behavior of three single-phase face-centered-cubic (fcc) $Al_{0.3}CoCrFeNi$, annealed CoCrFeMnNi and as-processed CoCrFeMnNi high-entropy alloys (HEAs) was studied in both quasi-static and high strain-rate regimes. Based on Hall-Petch strengthening, solid-solution strengthening, order hardening, cutting forest dislocations, and twinning hardening mechanisms, a constitutive equation was proposed to describe the flow of the annealed CoCrFeMnNi high-entropy alloy under dynamic impact. The resistance to shear localization is being established by dynamically-loading hat-shaped specimens that induce forced shear localization. Adiabatic shear band formation required an imposed shear strain of ~7 for the annealed CoCrFeMnNi HEA and cannot be observed at a strain of 1.1 for the $Al_{0.3}CoCrFeNi$ HEA. The structural and mechanical response that give rise to a remarkable resistance to shear localization are characterized by a combination of (1) a high strain-hardening ability, enabled by solid solution hardening, forest dislocation hardening, order hardening, and twinning hardening, (2) a high strain-rate sensitivity and (3) modest thermal softening; these combination effects give rise to the remarkable resistance to shear localization. First, the low stacking-fault energies in as-received high-entropy alloys lead to the formation of twinned segments inside the coarse grains. Then, when the thermal softening overcomes strain hardening, the shear bands would form, and dynamic recrystallization occurs inside the segments for the further break-up of the grains. Classical Straker equation is applied to predict the critical shear strain for shear localization, which was quite comparable to the experimental values in the high-entropy alloys. It was revealed that the as-processed CoCrFeMnNi HEA was prone to shear localization due to the initially high dislocation density which results in a relatively low work-hardening effect.

The dynamic deformation of these two metallic materials leads to adiabatic shear band formation at extreme shear strains. The resultant of the ultrafine grain structure observed in these two materials with diverse structures (HCP for Ti and FCC for HEAs) is remarkably similar and reinforces the concept of rotational dynamic recrystallization as the mechanism responsible for localization.

Chapter 1. Introduction

Nanostructured materials have been the subject of widespread research over the past decades [1-4]. Due to the increased volume fraction of the intercrystalline regions (such as grain boundaries and triple junctions) shown in Fig. 1.1, the physical and mechanial properties of nanostructured materials can be significantly altered. For instance, as the grain size is reduced from the microcrystalline to the ultrafine-grained (100-1000 nm) and nanocrystalline (<100 nm) size, the slope of the Hall-Petch equation, based on the separation of the material into grain interior and grain-boundary larger, decreases as was pointed out by Meyers and Ashworth in 1982 [5]. A variety of models such as the grain-boundary dislocation source-sink model by Swygenhoven *et al.*[6], the thermally-activated grain boundary shearing model by Conrad *et al.* [7], and the grain boundary rotation and coalescence model by Haslam *et al.* [8] were proposed to understand the deformation mechanisms of nanocrystalline materials.

Over the past 20 years, the production of titanium and titanium alloys has matured more rapidly than perhaps any other structural material in the history of metallurgy [9]. Titanium and titanium alloys have enormous applications such as biomedical implants, airframes and tubing for heat exchangers. Thus, it is of great importance to examine their mechanical performance in some extreme conditions, such as cryogenic temperatures and high strain-rates. The mechanical response and shear localization mechanism of coarse-grained (CG) ~72 μm titanium were examined by Meyers *et al* [10, 11]. The equiaxed ultrafine-grained (UFG) ~0.2 μm grains inside the shear bands were formed by the rotational dynamic recrystallization mechanism [12, 13]. Nemat-Nasser *et al.* [14] and Chichili *et al.* [15] have studied the dynamic response of coarse-grained titanium at a wide range of temperatures and strain-rates. However, the dynamic behavior of UFG titanium still needs to be investigated.

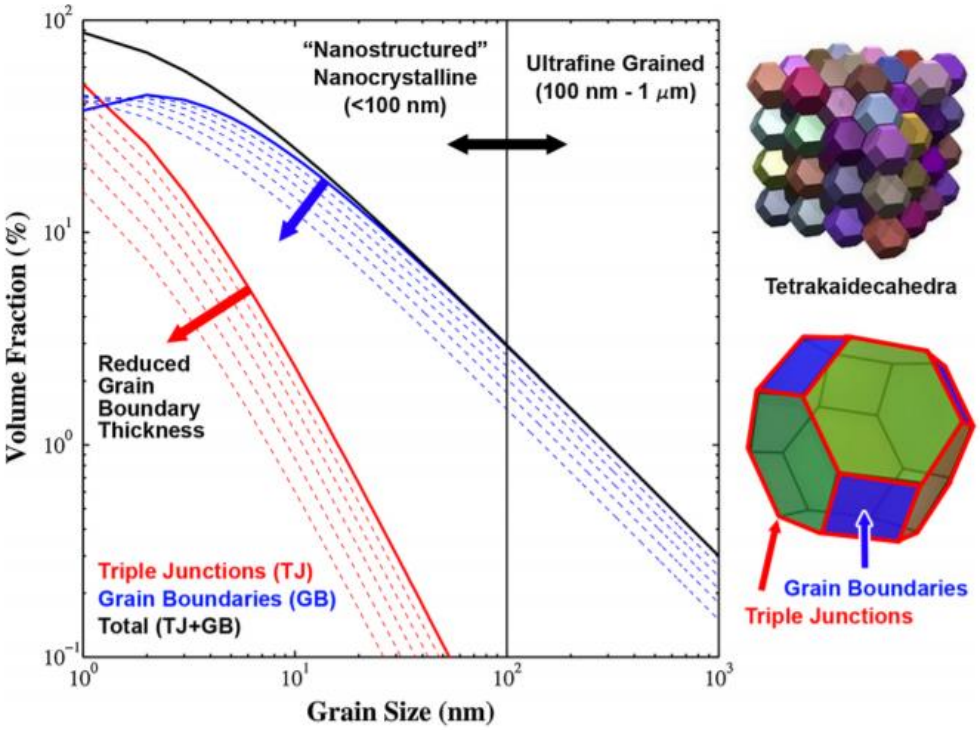

Figure 1.1. The increase in the volume fraction of grain boundaries and triple junctions as a function of grain size in the nanocrystalline (<100 nm) and ultrafine-grained (100 nm–1000 nm) regimes. These plots are based on space-filling tetrakaidecahedra grains with a grain boundary thickness of 1 nm (thick line), where the dotted lines show the evolution for grain boundary thicknesses of 0.9 nm to 0.5 nm in increments of 0.1 nm [4].

On the other hand, the mechanical properties required for metallic materials in structural applications can rarely be achieved by pure metals, and are usually obtained through the addition of alloying elements. Cantor *et al.* [16] pointed out that conventional alloy development strategy led to an enormous amount of knowledge about alloys based on one component, but to very little or no knowledge about alloys containing several main components in equal or near equal proportions. This motivated an initial attempt to investigate the unexplored central phase region of multicomponent alloy, concentrating particularly on multicomponent transition metal alloys which could form a single fcc phase. The single fcc CoCrFeMnNi alloy was synthesized by Cantor *et al.* [16] for the first time, and for this reason is known as the "Cantor alloy".

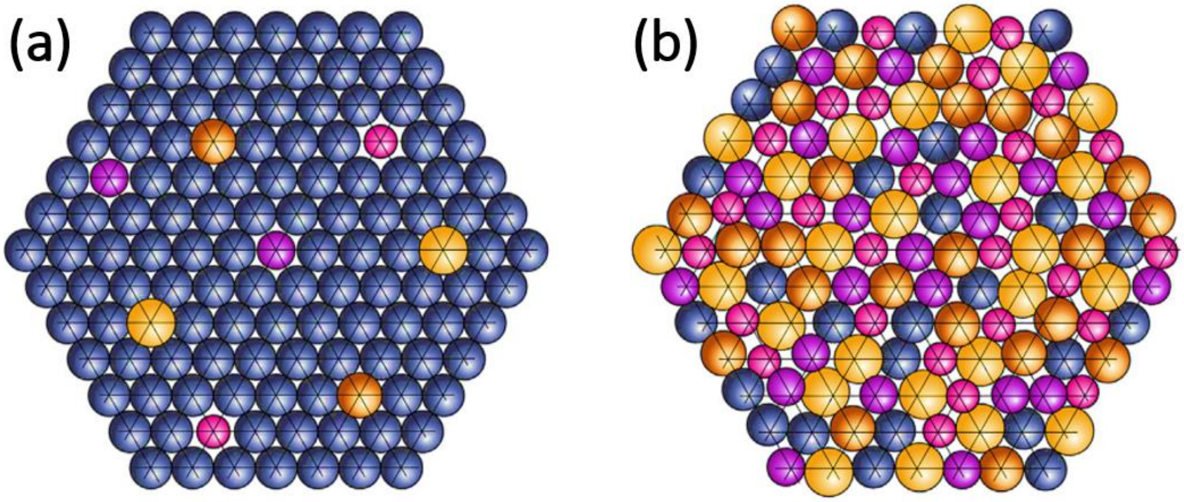

Figure 1.2. The effect of atom size difference on atom positions in (a) a dilute solution, where solute atoms are constrained to occupy lattice sites by surrounding solvent atoms and (b) a complex, concentrated solution, where there is no dominant atom species and atom positions usually deviate from mean lattice positions. The variability in atom positions in (b) contributes to an excess configurational entropy .

Ideal configurational entropy is based on the occupation of identical lattice sites with chemically different but equal-sized atoms. However, atoms with different sizes can bring uncertainty in atom locations, thus giving an excess entropy term. This effect may be small in dilute solutions, where the location of the minority atom is constrained by the surrounding majority atoms as shown in Fig. 1.2(a) [17]. The uncertainty in atom locations increases with increasing size differences and concentrations. In multi-principal element alloys, the lattice is expected to be highly strained, so that atoms are usually displaced from the average lattice sites (Fig. 1.2(b)), and this lattice distortion effect can be important.

The statistical-mechanics definition of entropy was developed by Boltzmann in 1870s [18] by analyzing the statistical behavior of the microscopic components of a system [19]. Boltzmann's hypothesis states that the entropy of a system is linearly related to the logarithm of the frequency of occurrence of a macro-state or, more precisely, the number, *W*, of possible micro-states corresponding to the macroscopic state of a system:

$$S = k \ln W = n \ln R \tag{1.1}$$

where $k = 1.38 \times 10^{-23}$ J/K is the Boltzmann's constant, *n* is the number of the components of the HEAs and *R* is the gas constant. Yeh *et al.* [20, 21] first proposed the high configurational-entropy effect of alloys with elements in equimolar proportions, which tend to stabilize high-entropy phases, such as a solid-solution phase. Fig. 1.3(a) shows the increase in the entropy of mixing with the number of elements for equimolar alloys. This mixing entropy readers a value of 3 Cal/K.mole for five elements because of the entropy term. Based on the effect of the entropy of mixing, the alloy world was divided into three fields, as shown in Fig. 1.3(b). Therefore, the alloy systems are divided into 3 categories: (1) Low-entropy alloys are traditional alloys; (2) medium-entropy alloys are the alloys with 2-4 major elements; (3) HEAs are the alloys with at least five major elements.

For an alloy system, the Gibbs free energy of mixing can be expressed as follows:

$$\Delta G_{mix} = \Delta H_{mix} - T\Delta S_{mix} \tag{1.2}$$

where ΔG_{mix} is the Gibbs free energy of mixing, ΔH_{mix} is the entropy, ΔS_{mix} is the entropy of mixing, and *T* is the absolute temperature. From the equation 1.2, we can see that if the ΔH_{mix} is kept constant, a higher entropy of mixing will lead to a lower Gibbs free energy, which makes the alloy system more stable. (No mismatch entropy due to grain size difference was considered in this situation.) However, the high-entropy effect of promoting the occurrence of the multi-phases was essentially found in the high-entropy alloys but should be less prevalent in the medium-entropy alloys.

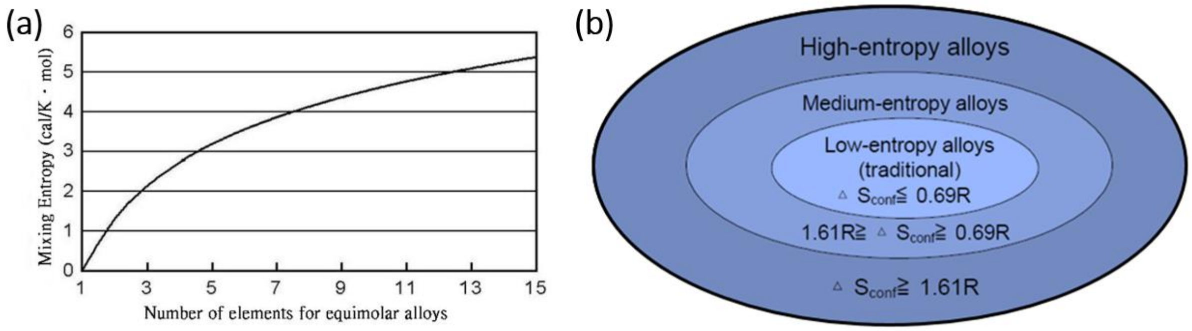

Figure 1.3. (a) Change of the mixing entropy with changing the number of equimolar elements in HEAs. (b) The alloy systems separated by the configuration entropy [20].

Chapter 2. Background

2.1 Adiabatic shear localization

2.1.1 Basic character and classification of shear bands

Adiabatic shear band is an important failure mechanism of materials under high strain-rate deformation. During plastic deformation, most of the plastic work is converted to heat in a very narrow region. Most materials including metals, ceramics, and some polymers exhibit thermal softening that leads to the decrease of their yield stress with increase of temperature. The thermal softening dominates the process of shear localization.

Morphology of shear localization is often observed as a narrow band undergoing a higher shear deformation than the surrounding areas. A typical shear band in coarse-grained pure titanium is shown in Fig. 2.1.1 [10]. The width of a shear band is often considered to be constant along its propagation direction although there exist small variations sometimes.

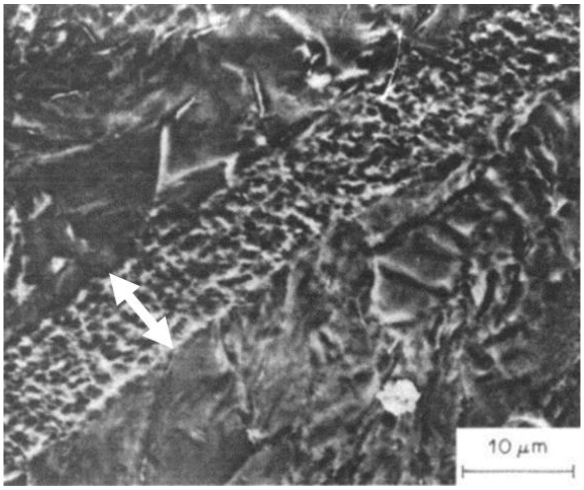

Figure 2.1.1 Scanning electron micrograph of the formation of the shear band in coarse-grained (CG) pure titanium [10].

Adiabatic shear bands have been observed under different dynamic loading conditions. Several main loading conditions, such as ballistic impact, explosive fragmentation, and dynamic penetration, are often related to the formation of the shear bands. Most of loading conditions for shear localization require shear or a combination of shear and compression. Almost no adiabatic shear banding occurs in tension for metals at ambient temperature. The reason is that the metals prefer the ductile fracture under tensile stress. Once thermal accumulation softens the material within a shear band, the tension stress can assist void nucleation and coalescence, leading to further fracture of the shear band.

According to the examination of the recovered microstructure, Backman and Finnegan [22] first classified adiabatic shear band into two types: “deformed” and “transformed” bands. Deformed shear band shows intensive deformation inside the shear band. The grains near the shear band are often distorted and rotated. In contrast, transformed shear band exhibits a totally new phase inside the band. In this case, the temperature inside the shear band usually reaches a value that is higher than a phase transformation point. When the deformation stops, the material within the shear band is quenched immediately during the cooling and maintains the transformed microstructure. Many of the bands originally considered to be “transformed” are indeed only recrystallized. The small recrystallized grain size could not be observed, and the bands were incorrectly classified as “transformed”. Therefore, detailed examination of microstructure with electron microcopy is needed to confirm whether it is “deformed shear band” or “transformed shear band”. Amounts of microstructural changes can happen within the shear bands due to the complex history of temperature and deformation. These microstructures may the products of the following process:

- Recovery
- Dynamic recrystallization
- Precipitate dissolution
- Phase transformation
- Amophization
- Melting

2.1.2 Material sensitivity to shear localization

The plastic deformation of crystalline and non-crystalline solids incorporates microscopically localized deformation modes that can be precursors to shear localization. Shear localization has been found to be an important deformation and fracture mode in metals, granular ceramics, polymers, and metallic glasses at high strains and high strain-rates [23]. Formation of shear localization is strongly dependent on material variables which include microstructure, physical parameters, and mechanical parameters.

Thermal softening, work hardening and strain-rate hardening are dominant factors in the formation of an adiabatic shear band. Generally, the shear stress τ , varied with several parameters: shear strain γ , strain-rate $\dot{\gamma}$, and temperature *T*. The constitutive equation of materials under high strain-rate deformation has a general form [24]:

$$\tau = f(\gamma, \dot{\gamma}, T) \tag{2.1.1}$$

The key parameters to govern shear localization are associated with hardening and softening mechanisms. Hardening of materials mainly consists of strain hardening and strain-rate hardening, which are defined as:

$$H = \frac{\partial \tau}{\partial \gamma} \text{ and } m = \frac{\partial \tau}{\partial \dot{\gamma}}, \tag{2.1.2}$$

respectively. The rate of thermal softening can be defined as:

$$\alpha = -\left(\frac{\partial \tau}{\partial \gamma} \right)_{T,\dot{\gamma}} \tag{2.1.3}$$

The thermal concentration is a prerequisite to the nucleation of adiabatic shear bands. Density of material ρ, specific heat capacity C_p, thermal conductivity λ and thermal diffusion rate $\chi = \lambda / (\rho \bullet C_p)$ govern the heating generation and heat diffusion process. It is obvious that a lower thermal conductivity of material is more suitable to initiate a shear band because the inhomogeneous heat can be easily produced in a narrow region. In addition, the low density and the low specific heat lead to a higher rate of temperature conversion. Therefore, materials with low heat capacity and low thermal conductivity will be prone to the formation of adiabatic shear bands. Low heat capacity of materials transfers more heat under the same input of plastic work and low thermal conductivity provides the material a slow diffusion rate of heat to surroundings. From the metals, pure titanium and titanium alloys have relatively lower value of thermal conductivity and heat capacity (for example, for pure titanium, $\lambda = 19$ W/m.K, C_p=523 J/kg.K). They have been found to be much easier to produce shear localization under high strain-rate deformation. In contrast, pure copper ($\lambda = 400$ W/m.K; C_p=385 J/kg.K) and pure aluminum ($\lambda = 238$ W/m.K; C_p=903 J/kg.K) are much less prone to adiabatic shear deformation.

However, physical properties, λ and C_p are not all the dominant factors for shear localization. In some polymers, the thermal conductivity is extremely low down to 10^{-1} W/m.K. The hardening effects from constitutive responses of materials compete with these softening effects. High strain-hardening and strain-rate-hardening may overcome thermal softening of materials and make localized deformation impossible.

Staker [24] discussed the competitive effects between strain-hardening and thermal-softening. He introduced a parameter to describe the competition the two effects:

$$P = \frac{\rho C_p n}{\left(-\frac{\partial \tau}{\partial T}\right)} \tag{2.1.4}$$

where n is the strain-hardening power index. Strain-rate hardening is another important effect on the formation of shear bands. Once localized deformation develops, the local strain-rate increases drastically. If the materials have relatively higher strain-rate sensitivity, the further localized deformation may be retarded. Zheng *et al.* [25] revealed that he thickest α-hcp lamellar in the transformed β-bcc matrix of Ti-6Al-4V alloy demonstrated the lowest possibility of the formation of adiabatic shear band due to the increment of strain hardening.

A quantitative description of the susceptibility to adiabatic shear banding (ASB), by Wright [26], has the following form:

$$\frac{\chi_{SB}}{a/m} = \min\left\{1, \frac{1}{n/m + \sqrt{n/m}}\right\} \tag{2.1.5}$$

where a is a nondimensional thermal softening parameter defined by $a = (-\partial\sigma / \partial T) / \rho C_p$, *n* is the strain hardening exponent and *m* is the strain-rate sensitivity. For a perfectly plastic material (no strain hardening), the susceptibility reduces to:

$$\chi_{SB} = \frac{a}{m} = \frac{\alpha\sigma_y}{\rho C_p m} \quad . \tag{2.1.6}$$

An increase in susceptibility to shear localization of UFG Fe was reported due to increase of the thermal softening effect [27].

However, the control method of shear band development was proposed by Sagapuram *et al.* [28]. They developed a passive geometric flow control of shear bands. The method is based on stopping the sliding phase by applying macroscopic constraints to the flow, resulting in a reduction or even removing shear flow localization at the meso- and macro- scales. Fig. 2.1.2.1 shows a separate constraint imposing on the free surface. The extent of sliding along the band in the second phase was represented by a parameter $\lambda = t_c / t_0$, where t_c represents the maximum thickness of flow localized chips. Their experiments show that applying different levels of constraints could lead to the significant decrease of λ , which in return could fully suppress shear localization. Figure. 2.1.2.2 shows the cutting of Mg AZ31B alloy by the passive geometric flow control methods. From different microstructure of optical microscopy, we can observe that by applying constraint, the material undergoes more continuous recrystallization inside of very localized shear formation. This method gives an extrinsic way to suppress shear localization during cutting.

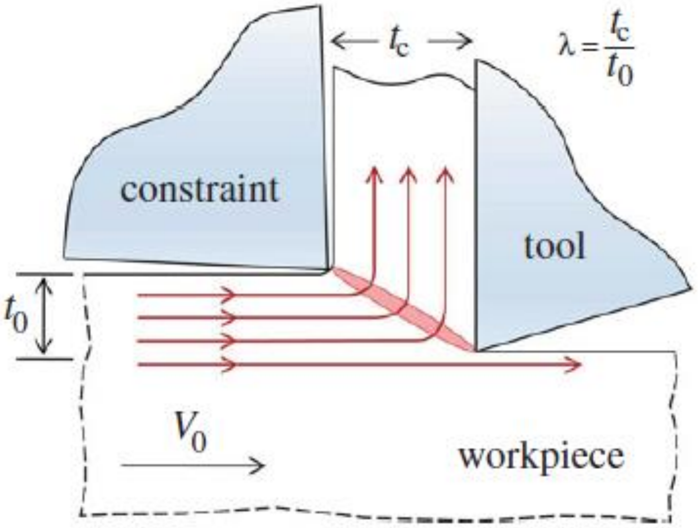

Figure 2.1.2.1. Schematic drawing of passive geometric flow control of shear bands. The degree of constraint on the flow is set by the parameter $\lambda = \frac{t_c}{t_0}$ [28].

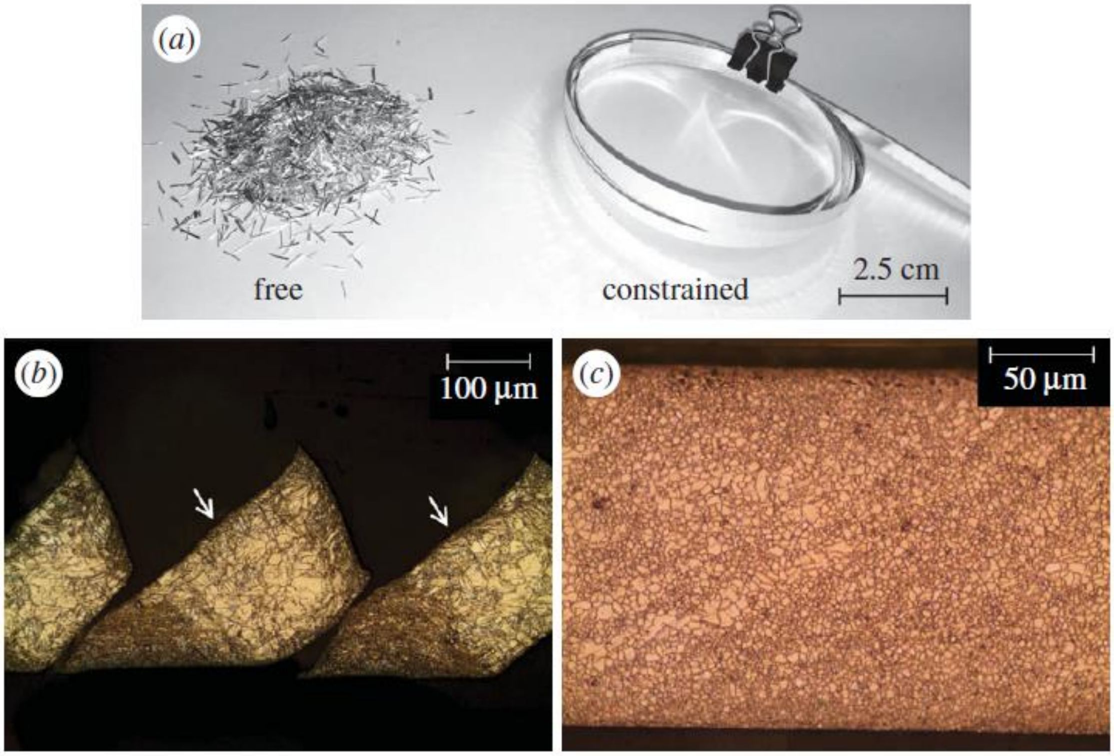

Figure. 2.1.2.2. Cutting of Mg AZ31B alloy by (b) the free surface and (c) constrained.

2.1.3 Formation and growth of the shear bands

The most direct response of instability of materials is the loss of resistance to the increasing load. Necking was considered as a typical unstable deformation in simple tension. The well-known Considere criterion for necking [29]:

$$\left(\frac{\partial\sigma}{\partial\varepsilon}\right)_{\dot{\varepsilon}} = \sigma_s \tag{2.1.7}$$

where σ is the true stress and ε is the true strain.

Recht [23] assumed that the shear localization occurs when:

$$\frac{d\tau}{d\gamma} = \left(\frac{\partial\tau}{\partial\gamma}\right)_{\dot{\gamma},T} + \left(\frac{\partial\tau}{\partial\dot{\gamma}}\right)_{\gamma,T}\frac{d\dot{\gamma}}{dT} + \left(\frac{\partial\tau}{\partial\gamma}\right)\frac{dT}{d\gamma} \le 0 \tag{2.1.8}$$

Recht [23] assumed that deformation was adiabatic and most of the plastic deformation concentrated into a narrow region once the unstable deformation started. The conversion of energy from strain energy to heat during the process was given as:

$$\rho C dT = \beta\tau d\gamma \tag{2.1.9}$$

where β is a conversion coefficient, usually taken as 0.9.

A number of models for shear localization were developed. In simple shear case, no geometric change happens in the cross section of the specimen. 1-D analysis can be used in the momentum and energy conversion relations [30]:

$$\rho\frac{\partial^2\gamma}{\partial t^2} = \frac{\partial^2\tau}{\partial y^2} \tag{2.1.10}$$

$$\tau\frac{\partial\gamma}{\partial t} = \rho C\beta\frac{\partial T}{\partial t} - \lambda\frac{\partial^2 T}{\partial y^2} \tag{2.1.11}$$

where y is the direction perpendicular to the shear direction. The general constitutive equation is given by equation 2.1.1. The mechanial and boundary condition may be a controlled shear stress or controlled velocity. The thermal boundary condition may be adiabatic or isothermal. A homogeneous solution of these solution can be obtained from stable plastic deformation. For adiabatic shear and constant velocity boundary conditions, the stable solutions are:

$$\dot{\gamma}_h = \dot{\gamma}_0 \tag{2.1.12}$$

$$\gamma_h = \dot{\gamma}_0 t \tag{2.1.13}$$

$$T_h = \frac{1}{\rho C}\int_0^t \tau_h \dot{\gamma}_0 dt + T_0 \tag{2.1.14}$$

where $\dot{\gamma}_h$, γ_h , T_h and τ_h are the shear strain-rate, strain, temperature and shear stress for homogeneous deformation; all of these parameters are function of time.

Bai [30] introduced linear perturbation analysis to a simple shear process to characterize the formation of the shear band. The basic idea of their model is to introduce a small perturbation solution superposed to the homogeneous stable solution. The examination of the development of small perturbation gives the criterion for localization deformation. The total solution can be expressed as:

$$\tau = \tau_h + \tau^{'} \qquad \gamma = \gamma_h + \gamma^{'} \qquad T = T_h + T^{'} \tag{2.1.15}$$

where "*h*" represents the homogeneous deformation and the prime represents the infinitesimal perturbations. Considering disturbances of the form $\gamma_a \exp(\alpha t + iky)$, it is possible to get characteristic equation:

$$\rho^2 C\alpha^3 + \rho\left[\left(-\frac{\partial\tau}{\partial T}\right)_h \dot{\gamma}_h + C\left(\frac{\partial\tau}{\partial\dot{\gamma}}\right)_h k^2\right]\alpha - \left[\tau_h\left(\frac{\partial\tau}{\partial T}\right)_h - \rho C\left(\frac{\partial\gamma}{\partial\gamma}\right)_h\right]h^2 = 0 \tag{2.1.16}$$

It is generally accepted that the wave number *k* represents a distribution of shear bands [30]. At the extreme case that instability grows at the highest rate, $k_{ex} = \infty$, the solution becomes:

$$\alpha_{ex} = \frac{1}{\frac{\partial \tau}{\partial \dot{\gamma}}} \left[\frac{\tau_h}{\rho C} \left(-\frac{\partial \tau}{\partial T} \right) - \frac{\partial \tau}{\partial \gamma} \right] \tag{2.1.17}$$

The physical meaning of this equation is that the shorter wavelength perturbations grow most rapidly. The relationship also indicates that thermal softening promotes the development of instability while strain hardening and strain-rate hardening retard it.

An estimate of the width of fully developed adiabatic shear bands may be made from equation 2.1.11 by considering what happens when $\frac{\partial T}{\partial t} = 0$, i.e., when the band has ceased to get any hotter [31, 32]. Then equation 2.1.11 becomes:

$$\tau \frac{\partial \gamma}{\partial t} = \lambda \frac{\partial^2 T}{\partial y^2} \tag{2.1.18}$$

The right-hand side of this equation may be approximated by $\frac{\lambda (T_b - T_m)}{\delta^2}$, where T_b is the temperature of the band, T_m is the temperature of the bulk metal, and δ is the half-width of the band. If further $T_b \gg T_m$, equation 2.1.11 may be solved for δ:

$$\delta = \left(\frac{\lambda T_b}{\tau_b \dot{\gamma}} \right)^{0.5} \tag{2.1.19}$$

where the subscript *b* refers to conditions inside the band. This equation predicts that the shear band width is inversely proportional to the square root of the strain rate. The higher the strain rate is, the narrower the bands would be. Table 2.1 presents a comparison of theoretical and experimental shear band width for five alloys by Dodd and Bai [31].

Table 2.1. Theoretical and experimental shear band widths.

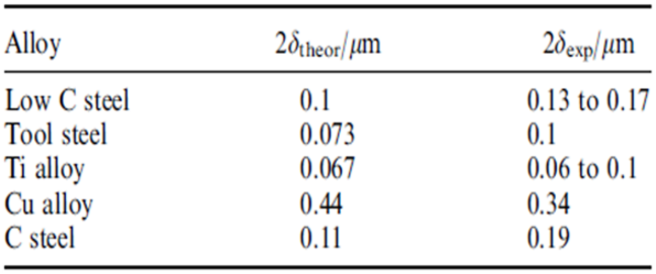

Alloy	$2\delta_{\mathrm{theor}}/\mu\mathrm{m}$	$2\delta_{\mathrm{exp}}/\mu\mathrm{m}$
Low C steel	0.1	0.13 to 0.17
Tool steel	0.073	0.1
Ti alloy	0.067	0.06 to 0.1
Cu alloy	0.44	0.34
C steel	0.11	0.19

A more rigorous (but still approximate) analysis was given by Grady and Kipp [33] as part of their continuing work on fragmentation caused by shock loading, expressed as:

$$a_0 = \left(\frac{9\rho^3 C_p{}^2 \chi^3}{\tau^3 (\frac{\partial \tau}{\partial T})^2 \dot{\gamma}} \right)^{0.25} \tag{2.1.20}$$

Being concerned with fragmentation, they studied the growth and interaction of shear bands both analytically and numerically as precursors of fracture. By including in their analysis inertial stresses generated by the redistribution of momentum necessitated by the sudden localization of deformation within narrow bands, they found the optimum width of shear band. There is an optimum width of shear band a_0 that has the maximum growth rate and minimum localization time in Fig. 2.1.3.1.

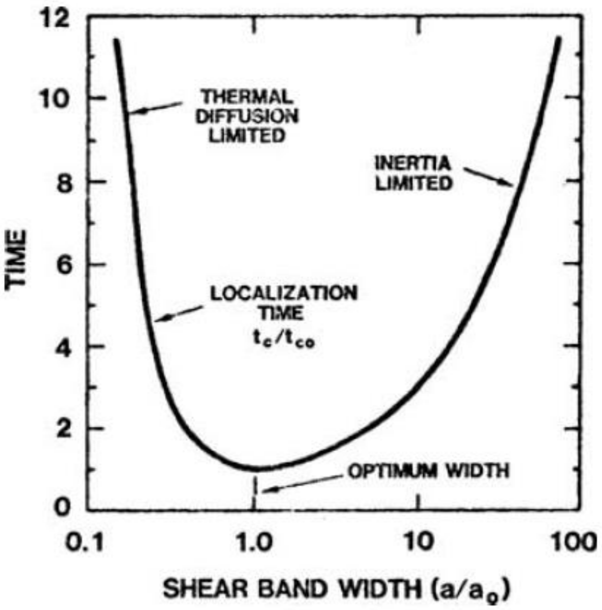

Figure 2.1.3.1 Graph showing there is a shear band width with minimum growth time [33].

Erlich *et al.* [34] first proposed a concept of “wave trapping”. Wu and Freund [35] developed this idea for the criterion of instability in shear localization. They considered a rate-independent material, $\tau = f(\gamma)$. Substituting the constitute equation into momentum conservation relation, one can get the disappearance of the gradient slope, $a(\gamma^*) = \sqrt{f'(\gamma)/\rho} = 0$. The physical meaning of $a(\gamma^*)$ is the velocity of the loading wave. During the homogenous plastic deformation, the plastic wave velocity is gradually reduced. The vanishing of wave velocity signifies that a critical condition arrives and beyond this point any increments will be trapped into shear localization region. The regions that satisfy the criterion don’t allow the loading wave to travel through it. There, all further increment of deformation is trapped into it.

Zhou *et al.* [36] conducted a group of impact experiments to pre-notched plates of the C300 steel and the Ti-6Al-4V alloy to examine the initiation and propagation of shear bands. Real-time temperature measurements both along shear band and perpendicular to the shear band were shown in Fig. 2.1.3.2.

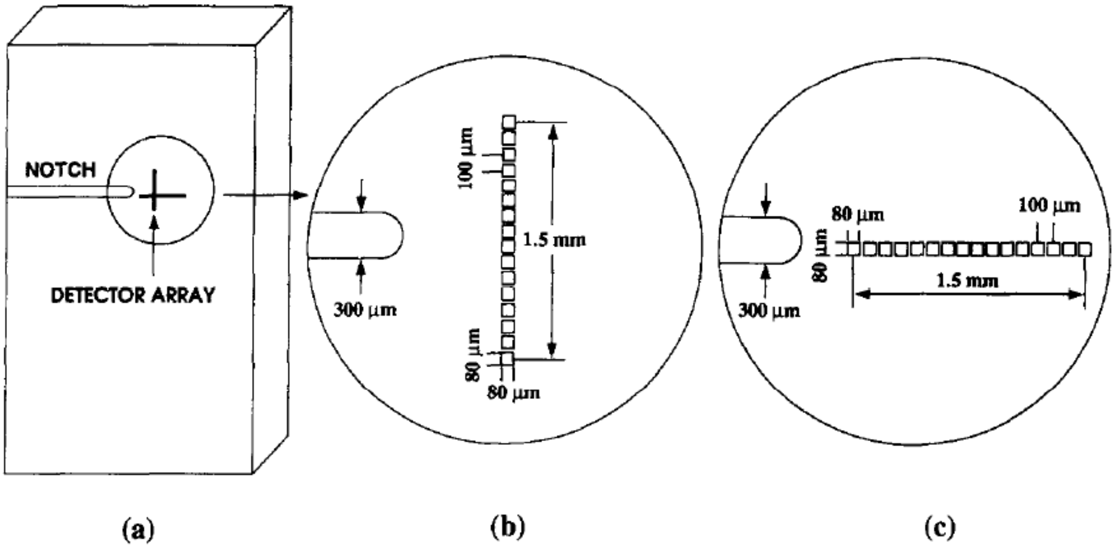

Figure 2.1.3.2. In-situ experiments of shear band propagation in the C-300 steel [33].

Shear band emanates from the notch tip and propagates rapidly in a direction nearly parallel to the direction of impact. When the impact velocity is higher than a critical value, the shear band propagates throughout the specimen. The shear band arrests inside the specimen when the impact velocity is below this critical value. In the latter case, a crack initiates and propagates from the tip of the arrested shear band at an angle to the direction of shear band propagation for the C-300 steel. Microscopic examinations of the shear band and crack surfaces reveal a ductile mode of shear failure inside the shear band and an opening mode of failure for the crack. The coexistence of shear banding and fracture events in the same specimen signifies a transition in the modes of failure for this material under the conditions as described. For Ti-6Al-4V alloy, the only mode of failure observed is shear banding. While the transition is induced by changes in loading conditions. This indicates that the failure behavior is related to the material property.

The temperature evolution was recorded and shown in Fig. 2.1.3.3. The temperature in different distances ahead of the notch-tip shows the temperature delay and inhomogeneity along a shear band. Zhou *et al.* [36] applied high-speed photography technique to examine the shear band speed for both C300 steel and Ti-6Al-4V alloy under different impact velocities. The velocity of shear band varied with the impact velocity of the projectile. Also, the transient velocity during shear band propagation under same impact velocity are different.

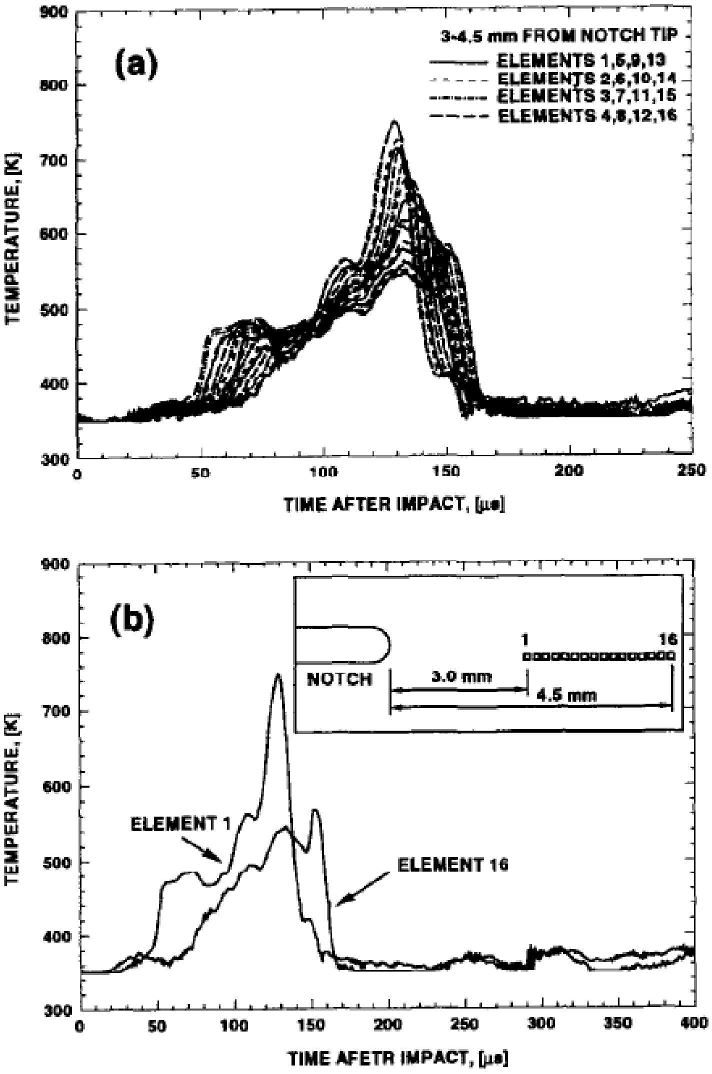

Figure 2.1.3.3 Temperature profiles at different distances from the notch tip, Ti-6Al-4V, V=64.5 ms^{-1} [33].

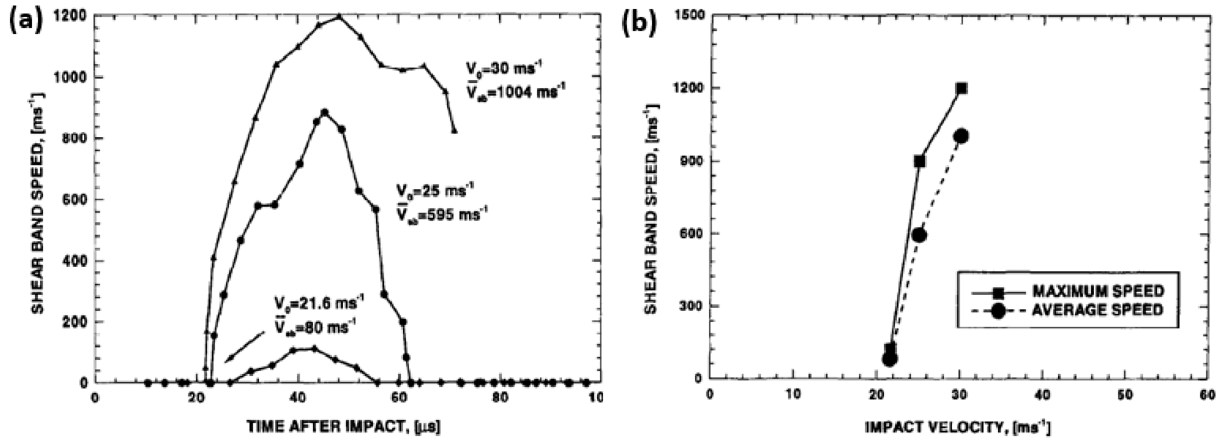

Figure 2.1.3.4 (a) Shear band speed histories for C-300 at different impact velocities. (b) Maximum and average shear band speeds as functions of impact velocity for C-300 steel [33].

Fig. 2.1.3.4(a) shows the velocities history of C-300 steel. They are initially quite low but accelertate very fast. The maxinmun of velocity of shear band in C-300 steel is 1000 m.s^{-1}. The drop of velocity is due to the unloading of shear band. Fig. 2.1.3.4(b) also shows that maximium speeds and average speeds (total band length divided by the time duration of extension) are quite similar.

2.2 Recovery, recrystallization and grain growth

Recrystallization is referred to a reconstruction of the grains during annealing of the deformed grains. It proceeds by generation and motion of high-angle grain boundaries removing the deformed microstructure. In contrast, recovery includes the rearrangement and annihilation of dislocations. The term “recrystallization”, is commonly used in a much broader way, by including all kinds of phenomena associated with grain boundary migration that lead to a lower free energy of the crystalline aggregate. Generally, recrystallization divides into two categories: one occurs during deformation (dynamic recrystallization, dynamic recovery) or subjected to cold formation during annealing treatment (static recrystallization, static recovery).

If recrystallization occurs during heat treatment of a deformed material, at the first, the generation of small grains is observed, which grow continuously and eventually replace the deformed microstructure. This process, characterized by nucleation and nucleus growth, is referred to primary recrystallization. Since the dislocation density in the material is not removed homogeneously but discontinuously at moving grain boundaries, it is also termed as discontinues recrystallization. In contrast, after large cold deformation or in case that grain boundary migration is strongly impeded, for instance by dispersion of a second phase, strong recovery can occur. During the process, even high-angel grain boundaries can be generated besides low-angel grain boundaries. The new microstructure was formed without migration of high-angel grain boundaries. The process occurs homogeneously throughout the microstructure and is referred as continuous recrystallization [37].

If the heat treatment is continued after complete primary recrystallization or in other essentially dislocation-free microstructure, the grain size usually increases. The grains then grow in two modes. Either the average grain size continuously increases, called continuous or normal grain growth. Or only a few grains grow rapidly, while the other grains grow slowly or not at all. The latter process is called discontinuous or abnormal grain growth. Only discontinuous grain growth is referred as secondary recrystallization. It leads to large grains and its occurrence is usually undesirable. Normal grain growth usually ceases, if the grain size becomes comparable to the smallest specimen dimension. In some cases, especially for thin sheet, discontinuous growth of a few grains is observed after continuous growth has come to an end. The process is referred to as tertiary recrystallization. The driving force for tertiary recrystallization is caused by the orientation dependence of the free surface energy.

Basically, there is always a driving force on a grain boundary if Gibbs free energy, G, of a crystal is reduced during the motion of the boundary. The free energy will be changed:

$$dG = -pdV \tag{2.2.1}$$

where dV is the swept volume. The term:

$$p = -dG / dV \tag{2.2.2}$$

is referred as driving force. In order to generate a recrystallization nucleus successfully from the deformed microstructure, three criteria have to be met: (1) Thermodynamic instability. Because of the low driving force for recrystallization, the nucleation rate due to thermal fluctuations is usually small. Therefore, one must assume that a supercritical nucleus is already present in the deformed microstructure, such as dislocation cell. (2) Mechanical instability. The grain boundary of the nucleus has to move in a defined direction, which requires a local imbalance of the driving forces. (3) Kinetic Instability. The surface of the nucleus, the grain boundary, must be mobile to make the nucleus grow.

If a grain boundary moves under the action of a driving force p, each atom gains free energy pb^3, where b^3 is the atomic volume. The velocity of a grain boundary is the displacement per unit time from the difference of thermally activated diffusional jumps from the shrinking to the growing grains, and vice versa:

$$\upsilon = bv_0 c_{vg} \left\{ \exp(-\frac{G_m}{kT}) - \exp(-\frac{G_m + pb^3}{kT}) \right\} \quad . \tag{2.2.3}$$

Here v_0 is the atomic vibrational frequency, G_m is the free activation energy for a diffusional jump through the grain boundary, and c_{vg} is the vacancy concentration in the grain boundary. In self diffusion, only a jump to an empty site in the grain boundary is possible. Because of the small driving forces of recrystallization, at typical recrystallization (T>0.4T), $pb^3 << kT$. Thus,

$$\upsilon \cong bv_0 c_{vg} \exp(-\frac{G_m}{kT}) \left\{ 1 - 1 + \frac{pb^3}{kT} \right\} = mp \tag{2.2.4}$$

where m is the mobility of the grain boundary.

The process of rotational dynamic recrystallization mechanism for the formation of equiaxed grains was modeled by Meyers *et al.* [38] using dislocation dynamic method, as shown in Fig. 2.2.1. Thermal softening is the first stage of this process, leading to processes of dynamic recovery and recrystallization with associated drops in the flow stress. Calculations reveal, for the first time, that the break-up of the elongated sub-grains and diffusive rotation of the grain boundaries can occur during the deformation process. Chen *et al.* [39] revealed the microstructural evolution inside the shear band of Ti-15Mo-3Al-2.7Nb-0.2Si alloy originally. The subgrains with grain size around 200-400 nm inside the shear band were recognized. The mechanism of formation of these subgrains, as dislocation slip on slip planes, subsequent formation of dislocation cells and final break-up of elongated subgrains, was proposed, and confirmed by experiments.

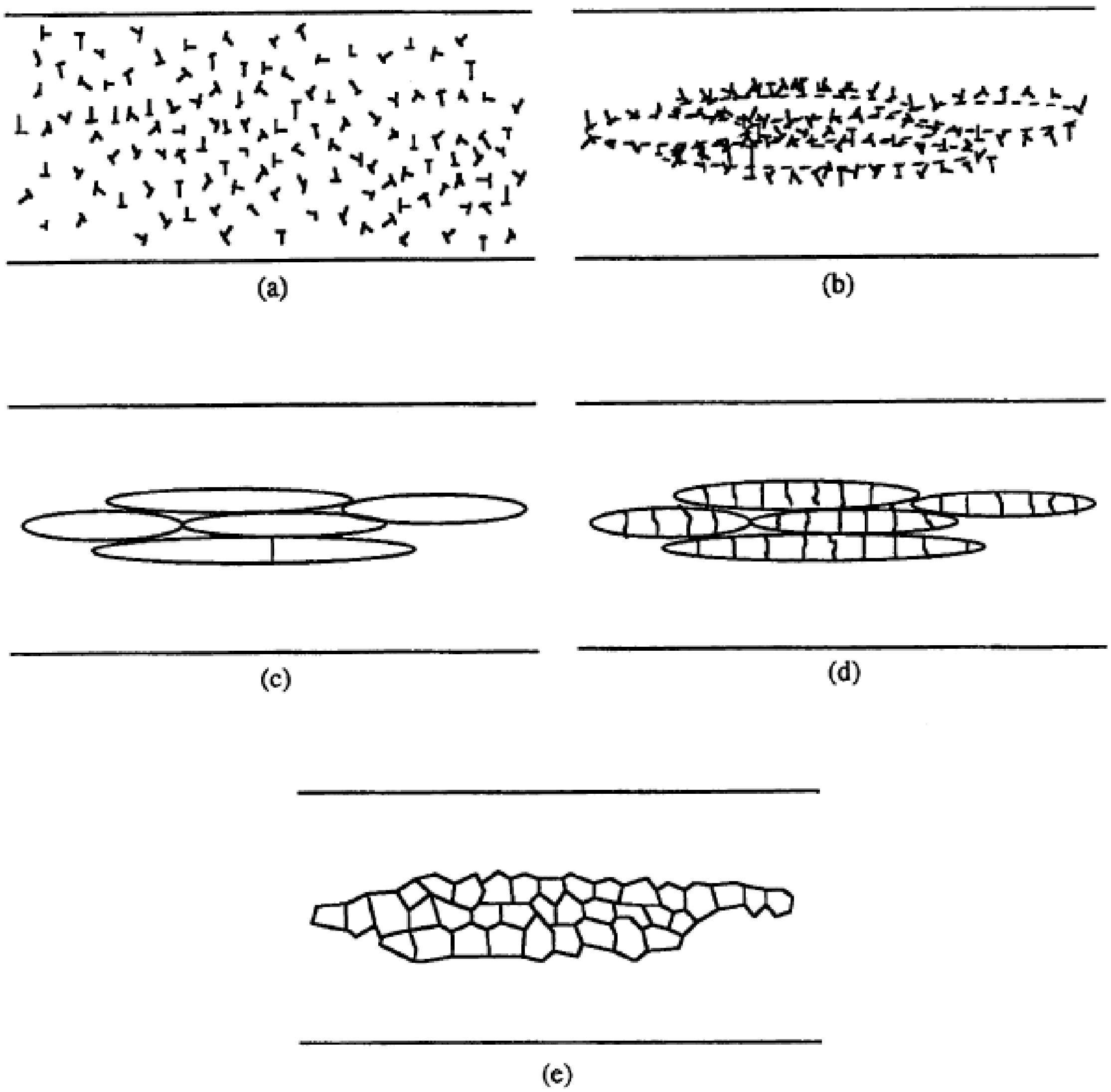

Figure 2.2.1 Schematic illustration of microstructural evolution during high-strain-rate deformation. (a) Randomly distributed dislocations; (b) Elongated dislocation cell formation (i.e. dynamic recovery); (c) Elongated subgrain formation; (d) Initial break-up of elongated subgrains; © Recrystallized microstructure [13].

Hines *et al.* [40] proposed a *progressive subgrain misorientation (PriSM) recrystallization* mechanism for the formation of submicron grains inside the adiabatic shear band, shown in Fig. 2.2.2. At the onset of shear band formation, an elongated dislocation cell structure begins to form in the direction of shear. The original grains begin to break up into a subgrain structure in order to accommodate the strain. There is a small degree of misorientation that develops between deforming subgrain regions. As deformation continues, these elongated cells become narrower and subdivide into more equiaxed cells to accommodate deformation and to obtain equilibrium with the increase of the flow stress. If the strain-rate or strain increases, the subgrain size will tend to decrease. This subgrain size decrease does not continue indefinitely, and eventually a critical subgrain diameter appears to occur where, after a given amount of deformation, the subgrain size is no longer inversely proportional to the strain. At this stage, since continued deformation no longer can reduce the subgrain size, the subgrain microstructure begins to rotate as a means of accommodating further deformation, resulting in highly misoriented, equiaxed regions. The large numbers of dislocations, which are present in the subgrain walls, can accommodate the rotation sufficiently to prevent gaps and cavities from forming when subgrains rotate away from each other (i.e., there are sufficient, geometrically necessary dislocations present to accommodate these rotations). After the deformation is completed, during the cooling stage, no additional dislocations are being added to the boundaries. The boundaries begin to be refined by reducing the excess dislocation dipoles through dislocation annihilation by dislocation climbing. If there is sufficient time during cooling for boundary refinement to occur, faceted high-angle boundaries will be created, and recrystallized grains could form.

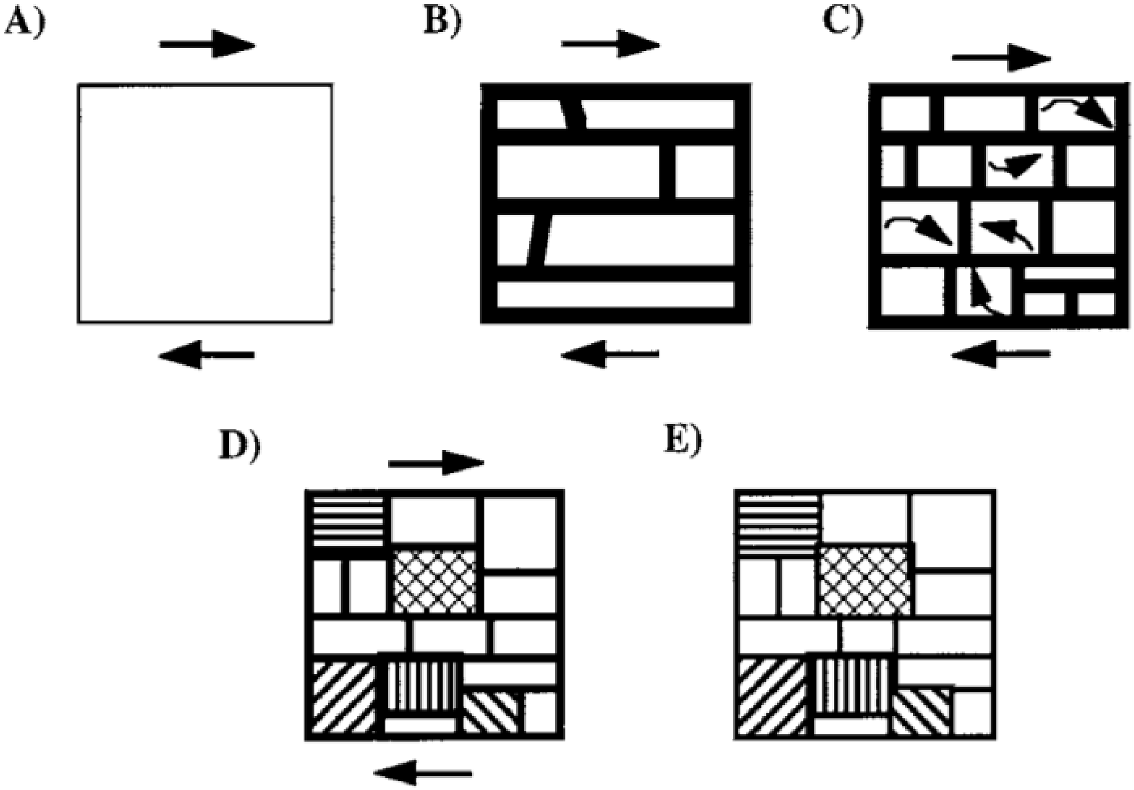

Figure 2.2.2. Schematic diagram of recrystallized grain evolution in an adiabatic shear band from the starting single crystal (A), to formation of elongated subgrains (B), to rotation of equiaxed subgrains (C), to high angle misorientations between some subgrains (D). The final stage is boundary refinement during cooling (C) [40].

2.3 Nanostructured materials

2.3.1 Pile-up break down

It was generally accepted for the pile-up break-down for nanocrystalline materials [2]. Fig. 2.3.1.1 shows the yield stress as a function with grain size for Cu, Fe, Ni, Ti and corresponding to Hall-Petch relationship curves. They all show the deviation from the conventional Hall-Petch curve when the grain size is below 100 nm. Nieh and Wadworth [40] derive the equation for the critical grain size that pile-up breaks down. The repulsive force by two edge dislocation in a pile up is represented as:

$$f = \frac{Gb^2}{2\pi\left(1-\nu\right)} \bullet \frac{1}{l} \qquad (2.3.1.1)$$

where G is the shear modulus, b is the Burgers vector and l is the distance between two dislocations. Assuming that the microhardness is 3 times of applied stress, $H = 3\sigma_{applied}$, and the applied shear stress is half of the applied shear stress ($f = \sigma_{applied}/2$), the equilibrium distance between two dislocations is

$$d = \frac{3Gb}{\pi(1-\nu)\bullet H} \quad . \qquad (2.3.1.2)$$

They proposed that when the grain size is smaller than this value, there will be no dislocation pile-ups, where the Hall-Petch relationship will break down.

The nanomaterials were represented by a composite material, which contains grain interior flow stress σ_G and grain boundary flow stress σ_{gb}. The flow stress was approximately estimated by [41]:

$$\sigma_y = A_G\sigma_G + A_{gb}\sigma_{gb} \tag{2.3.1.3}$$

where A_G and A_{gb} are the fraction of interior and boundary of the grain, respectively.

Meyers and Ahsworth [5] built an aggregate model to predict the stress of the nanomaterials based on Eqn. 2.3.1.3. Fig. 2.3.1.2 shows the model in which the spherical part with diameter d represents grain interior with grain boundary thickness t. The final form was derived as:

$$\sigma_y = \sigma_G + 8k_{MA}\left(\sigma_{gb} - \sigma_G\right)d^{-1/2} - 16k_{MA}^2 k_{MA}\left(\sigma_{gb} - \sigma_G\right)d^{-1/2} \tag{2.3.1.4}$$

where k_{MA} is a constant parameter. This model explains well the deviation of microhardness (or yield stress) from the conventional Hall-Petch curve in nanocrystalline materials.

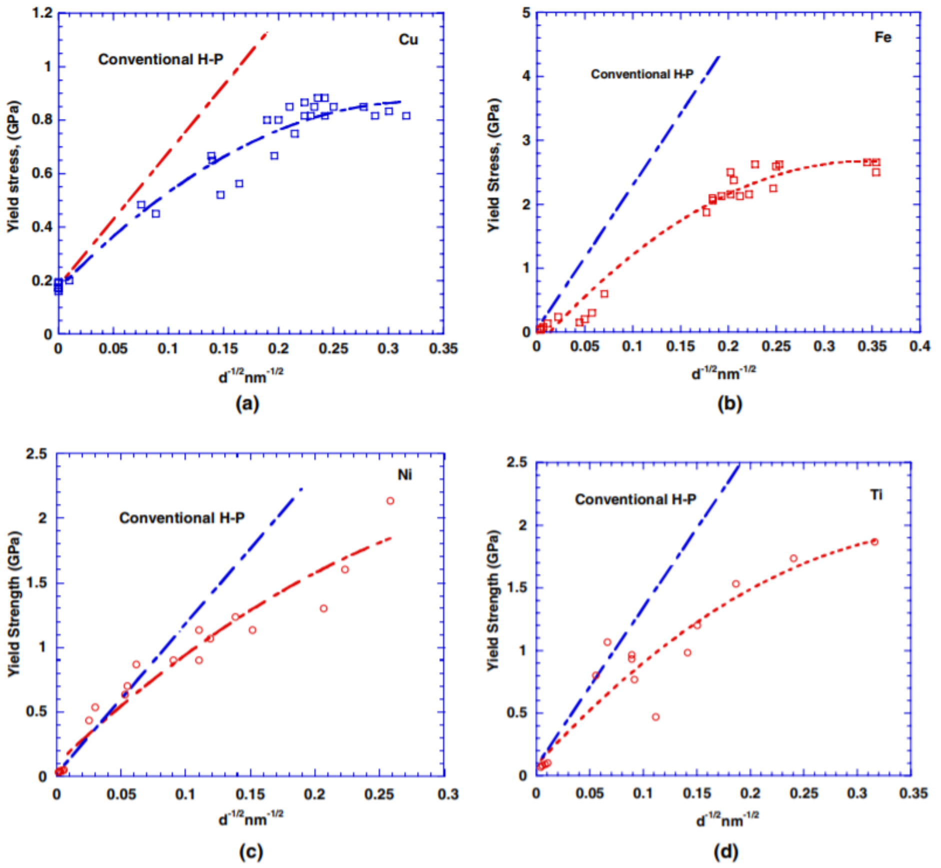

Figure 2.3.1.1. Plots showing the yield stress changes as a function of grain size with the conventional Hall-Petch curve: (a) Cu, (b) Fe, (c) Ni, (d) Ti [2].

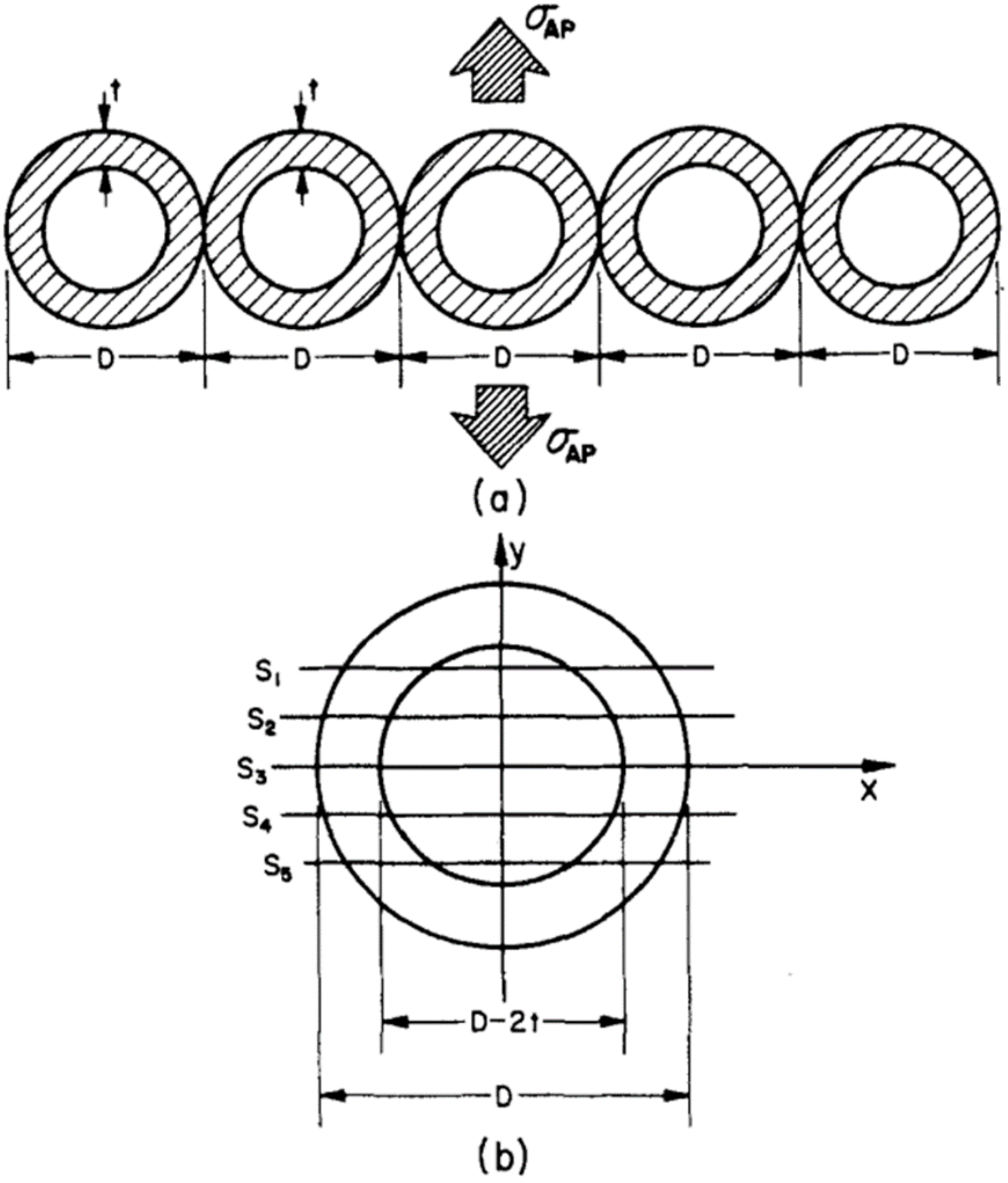

Figure 2.3.1.2. (a) The model contains bulk and grain boundary material. (b) Ideal representative nanograin with spherical diameter *D* and boundary thickness *t* [5].

2.3.2 Grain boundary sliding

Fig. 2.3.2 (a) shows the schematic drawing of grain boundary sliding mechanism under applied shear stress. Raj and Ashby [42] proposed that plastic deformation between neighboring grains occurs by diffusion alone. The diffusion path was shown by Fig. 2.3.2 (b). Taking the grain boundary diffusion and bulk diffusion into account, one can get the sliding rate as:

$$\dot{u} \approx \frac{2\delta\Omega D_B}{kT}\tau_\alpha\left(\frac{1}{h^2}\right) \tag{2.3.2.1}$$

where δ is the thickness of the grain boundary, Ω is the atomic volume, and h is the amplitude of the wave. If it was assumed that the grain boundary generates identical strain-rate and h is taken as $d/4$, one can get the strain-rate:

$$\dot{\gamma} = \frac{64\delta\Omega D_B}{kT}\left(\frac{1}{d^3}\right)\tau_\alpha \quad . \tag{2.3.2.2}$$

This can be simplified into the equation:

$$\dot{\gamma} = \left(\frac{1}{\eta_e}\right)\tau_\alpha \tag{2.3.2.3}$$

where η_e is an effective viscosity. The equation represents the Newtonian viscous flow. As the decrease of h, the strain-rate will increase, suggesting that shear localization tends to occur in the nano- materials.

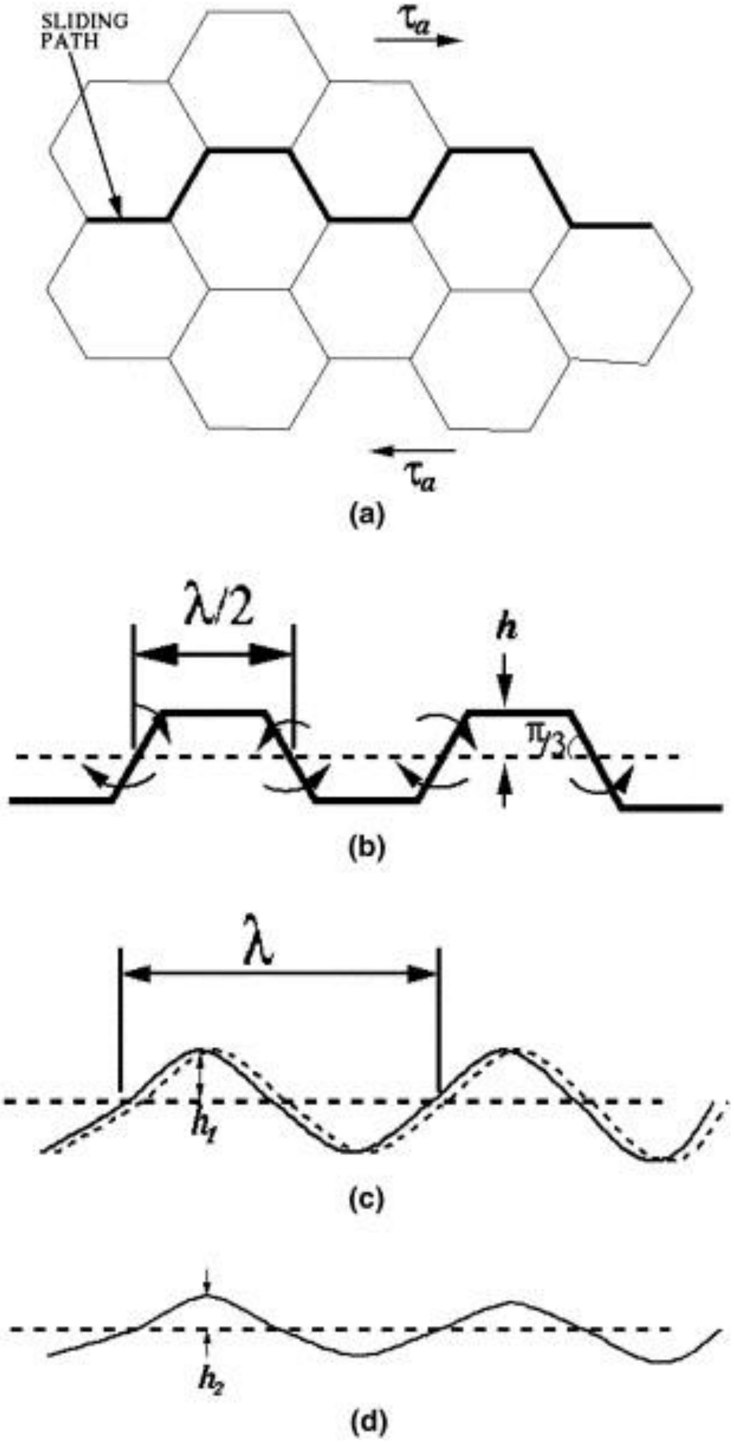

Figure. 2.3.2 (a) Schematic representation of grain-boundary sliding in polycrystal; (b) grain-boundary sliding path; (c) idealized sinusoidal path with diffusional migration of boundary according to Raj and Ashby [43]; (d) decrease in wave amplitude *h* with increasing plastic strain.

2.3.3 Grain- boundary rotation/ grain coalescence

Ma and coworkers [43, 44] reported possibility of rotation of nanograins. The planes with highest Schmid factor were represented by the short dark lines inside the grains in Fig. 2.3.3(a). The applied shear stress could make the neighboring nanograins rotating from the closer to the same orientation in Fig. 2.3.3 (b). The elimination of grain boundaries as represented by Fig. 2.3.3 (c) could provide the free path for dislocation motion. However, this leads to the strain softening and localization as observed in the nanocrystalline materials.

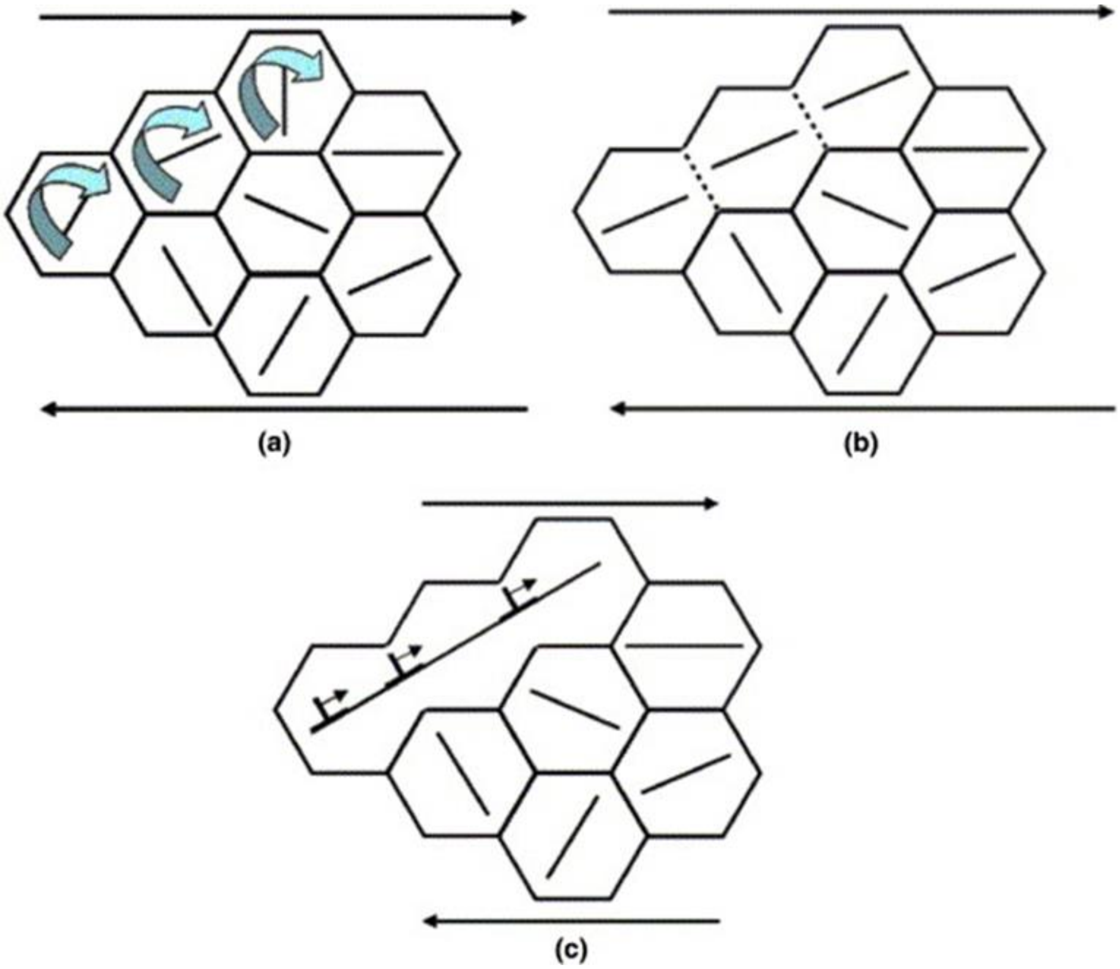

Figure. 2.3.3. Model of (a) the rotation of nanograins, (b) annihilation of grain boundary, and (c) coalescence of nanograins [2].

2.3.4 Twinning

Meyers and Lubarda have applied the Eshelby strain ellipsoid formalism to predict critical nucleus size of deformation twinning as follows [45]:

$$\gamma_c = \frac{5\pi}{4} \frac{G\gamma_{TB}}{\left(\tau_{twin}\right)^2} \tag{2.3.4}$$

The critical radius as a function of local shear stress has been applied for different materials in the Fig. 2.3.4. At the local shear stress of 500 MPa, the radius is above 50 nm. This indicates that other mechanisms should play a role for the deformation twinning.

Several other mechanisms were proposed: (a) the local stress concentrations may be larger than 500 MPa, providing smaller twinning nucleus size. (b) At the nanodomain, the increase of partial dislocations can aid the deformation twining. (c) The pre-existing stacking-fault can promote the twinning deformation.

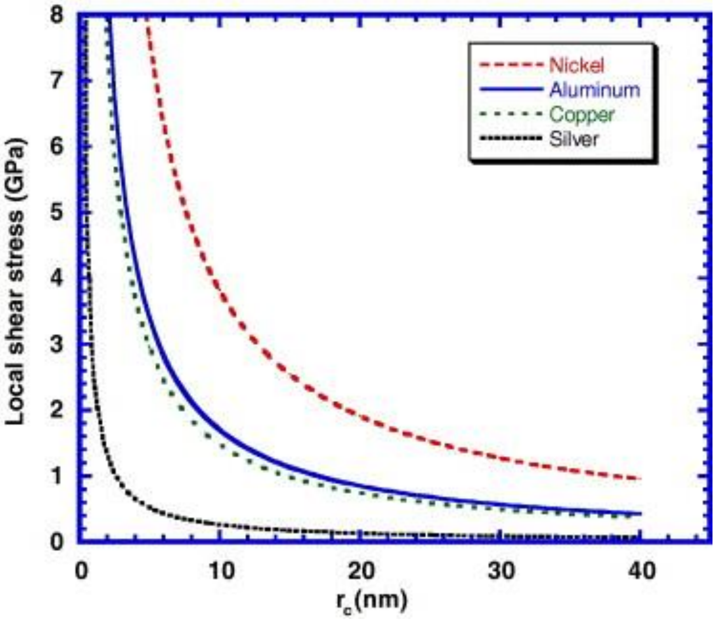

Figure. 2.3.4. Critical shear stress required for the activation of a twin nucleus as a function of size [46].

2.3.5 Grain boundary dislocation and annihilation

It was reported that dislocation cross slip, dislocation reaction and dislocation multiplication were prohibited in the nanocrystalline materials. It was prompted by molecular dynamics simulations [6] for new deformation mechanism in the nanocrystalline materials. One of example is that the nanocrystalline material can be deformed by grain boundary dislocation and annihilation. The grain boundaries obtaining dislocations are non-equilibrium boundaries. This provides the possibility of emission of dislocations from grain boundaries as shown in Fig. 2.3.5.

The emission of perfect dislocation and partial dislocations was assumed to be competition relationship. One requiring least stress would be activated. Asaro *et al.* [46], Liao *et al.* [47] and Zhu *et al.* [48] used an energetic analysis to demonstrate that the equilibrium separation of dislocation partials is larger in the nanocrystalline domain than that in a mono-crystal. This larger partial separation was favorable for stacking-fault formation and twinning formation. This has been mentioned in the section 2.3.4.

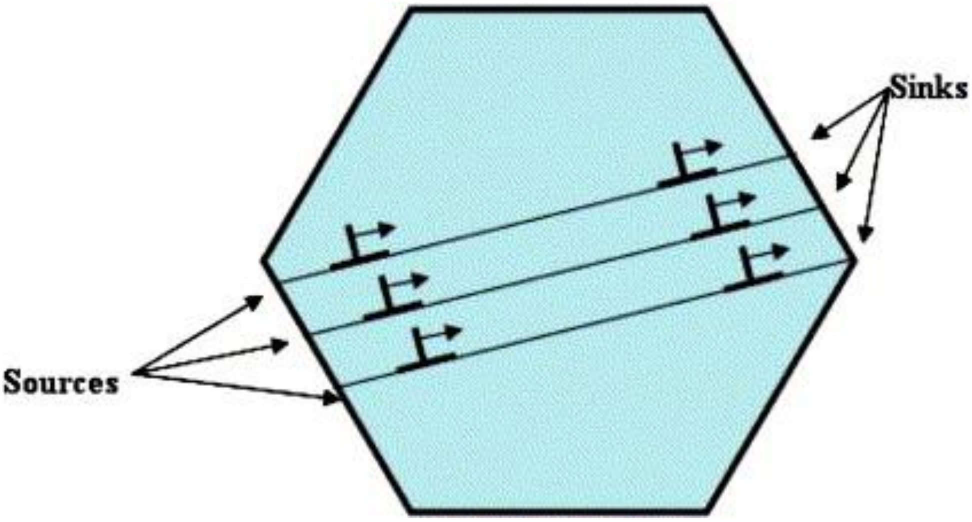

Figure 2.3.5. Model representing grain boundary source and sink.

2.3.6 Strain-rate sensitivity

The fcc materials are prone to forests dislocation strengthening. Thus, as a decrease of grain size, the activation volume decreases significantly, resulting in an increase of strain-rate sensitivity. When the grain size breaks down into a critical value, the increase of strain-rate sensitivity was not attributed to the grain boundary sliding, but rather to a change to the thermally-activated dislocation annihilation at grain boundaries. This indicates that the cutting of forest dislocations can not be dominant at nano- grain size due to the scale effect.

The strength of bcc materials normally comes from Peierls-Nabarro stress. This thermally activated process made bcc materials more sensitive to the temperature and strain-rate. As can been seen in Fig. 2.3.6, at coarse-grained size, the strain-rate sensitivity of bcc materials ~0.04 is about four times of that in fcc materials ~0.01. It becomes evident that, with the same Peierls barrier unchanged, the additive athermal contribution to the yield and flow stress due to Hall-Petch strengthening will become larger and larger as the grain size is reduced, rendering UFG bcc metals less rate sensitive [49].

In addition, the strain-rate sensitivity of Zn (as a representative of hcp metals) was also discovered to increase to a relatively high value ~0.15 with a grain size of 238 nm [50].

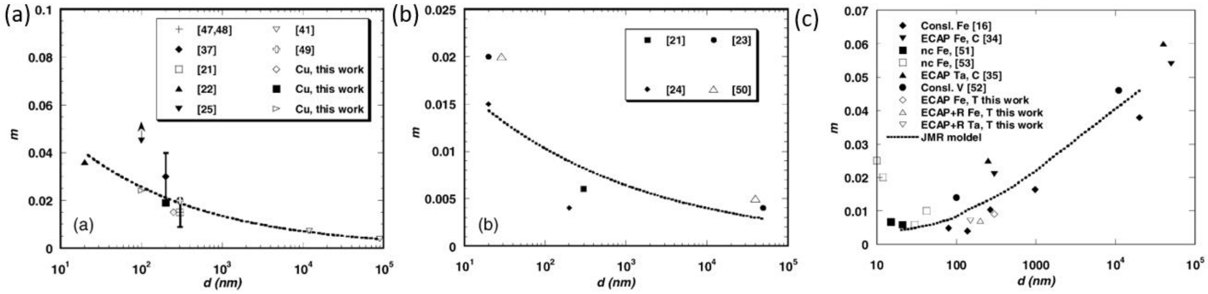

Figure 2.3.6. The strain-rate sensitivity in (a) fcc Cu (b) fcc Ni and (c) bcc iron and Ta with different grain sizes [50].

2.3.7 Shear band formation

Jia *et al.* [51] and Wei *et al.* [52] studied compression behavior of ultrafine-grained and nanocrystalline iron. They revealed that when the grain size is below 300 nm, the iron would easily deform by shear localization. Fig. 2.3.7 shows this obvious transition from uniform deformation (a) to non-uniform deformation in (b) representing low strain-rate deformation and (c) high strain-rate deformation. The 268 nm iron develops multiple shear bands instead of a single one, indicating easy initiation of shear bands in ultrafine-grained iron. Elongated grains with same width was revealed inside the shear bands. It was proposed that grain boundary sliding, or grain rotation leads to the softening of material in addition to more significant temperature rise softening under dynamic impact. Similar results have been observed in ultrafine-grained copper by Mishra *et al.* [53].

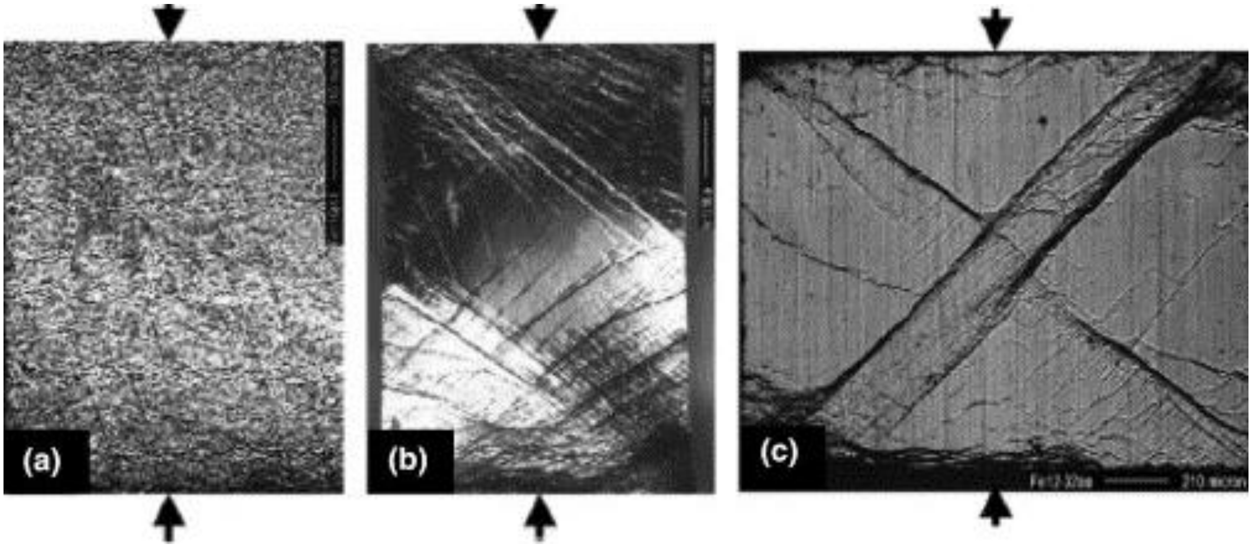

Figure 2.3.7. Change of deformation mode for ultrafine-grained Fe. (a) Uniformed deformation at low strain-rate compression with grain size 980 nm at the strain ~0.14. (b) Non-uniform low-rate deformation with grain size 268 nm. (c) Non-uniform high strain-rate deformation with grain size 268 nm [52].

2.3.8 Amorphization

Hua *et al.* [54] studied deformation mechanism of nanocrystalline (65 nm) NiTi superalloy in small scale. The initial material obtains B2 crystal structure demonstrated by selected area diffraction pattern. The superplasticity behavior was revealed in this NiTi micropillar loaded below the yield stress 2.1 GPa. This was attributed to the phase transformation between B2 crystal and B19’ martensite phase during loading and unloading.

A full stress-strain curve of micropillar was compressed to a nominal strain of ~0.2. The nanocrystalline NiTi shows no strain hardening. It has a first strain burst at the nominal strain of ~0.12, which corresponds to the formation of shear band. Then the shear band propagates gradually at the 45° to the loading direction until the failure. A combined microstructure of 11 nm nano-grains and amorphous phase was revealed inside the shear band. The temperature rise in the shear band was below the recrystallized temperature, which suggests a solid-state phase transformation to form the amorphous phase. This also confirms the discussion in section 2.3.7 that nanocrystalline material are easily deformed by the shear localization.

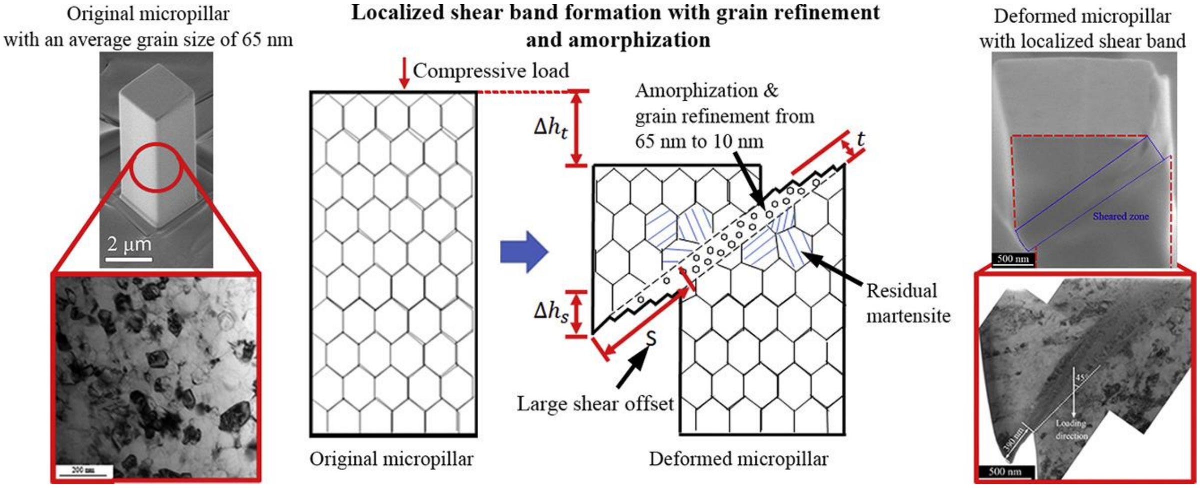

Figure 2.3.8. The uniaxial compression of nanocrystalline NiTi pillar with grain size 65 nm. The localized shear band obtains nano-grains and amorphous phase [55].

2.4 High-entropy alloys

2.4.1 Definition

The design strategy of high-entropy alloy (HEA) is based on five or more elements mixed in equiatomic or near equiatomic concentrations, such that the high configurational entropy promotes single-phase solid solution formation [20]. Cantor *et al.* [16] developed the CoCrFeMnNi HEA with the single face-centered-cubic (fcc) phase for the first time in 2004 and therefore this alloy is also known as the “Cantor alloy”. Recently, Gludovatz *et al.* [55] found that this CoCrFeMnNi HEA achieved remarkable damage-tolerance with a tensile strength above 1 GPa and fracture toughness exceeding 200 MPa·m$^{1/2}$ as shown in Fig. 2.4.1. Furthermore, its mechanical properties improved at cryogenic temperatures due to the transition of deformation mechanism from planar dislocation slip activities to mechanical nanotwinning. In-situ TEM experiments by straining a thin-foil on cracks revealed a synergy of multiple deformation mechanisms of this alloy, rarely achieved in other metallic systems, that included the easy motion of the Shockley partials, their interactions to form stacking-fault parallelepipeds, and arrest at planar slip bands of perfect dislocations. The multiple deformation modes of the Cantor alloy lead to high strength, high work-hardening rate and good ductility [56]. The mechanical properties, such as the creep mechanism [57], dynamic behavior [58], and tensile ductility [59], of the HEAs, attract enormous research attention.

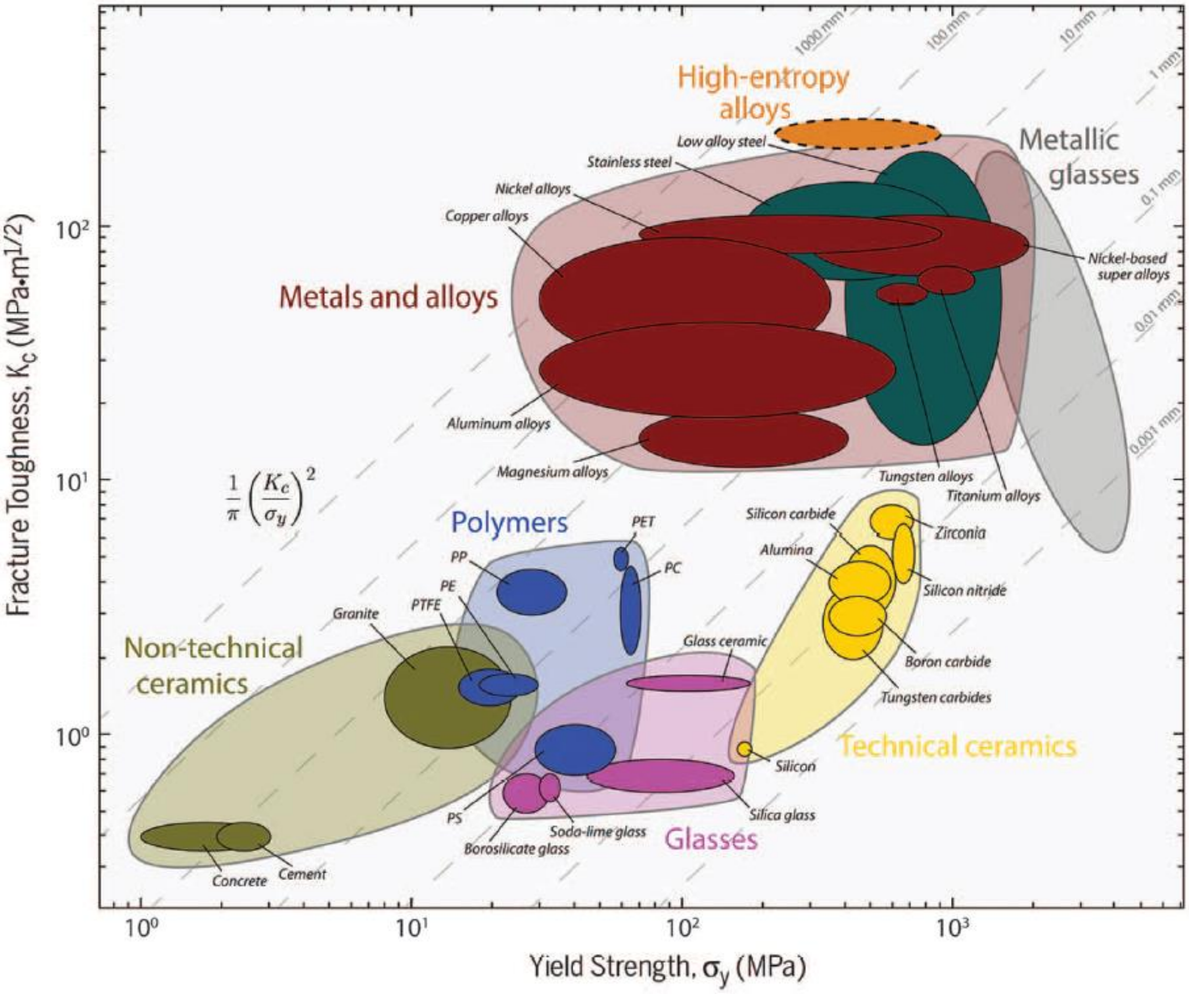

Figure 2.4.1. Ashby plot for HEAs compared with other materials describing the trade-off relationship between fracture toughness and yield strength [56].

2.4.2 Strengthening mechanisms

The strength of the materials is depending on their chemical compositions, crystal structure and microstructures. Theory of strengthening mechanisms in high-entropy alloys includes reduced grain size, precipitation, solid solution, order, phase transformation and so on. Due to the change of local environment of dislocation, a modified "Peierls-Nabarro" stress $\tau = \frac{1}{b}\left\{\frac{dE_{misfit}}{du}\right\}$ was applied by Patriarca *et al.* [60] to predict critical resolved shear stress for dislocation slip in CrMnFeCoNi high-entropy alloy.

Curtin and coworkers [61-62] pointed out that despite the Hall-Petch strengthening, the solid solution hardening and forest dislocation strengthening take dominant role on the strengthening of fcc solid solution. Fig. 2.4.2.1 demonstrates the validity of the solid solution strengthening model. Cheng and coauthors [63] developed interstitial oxygen strengthening of $ZrTiHfNb_{0.5}Ta_{0.5}O_x$ high-entropy alloys with combined high strength (~1GPa) and superior compressive ductility (~50%) at high temperature (700-800 °C).

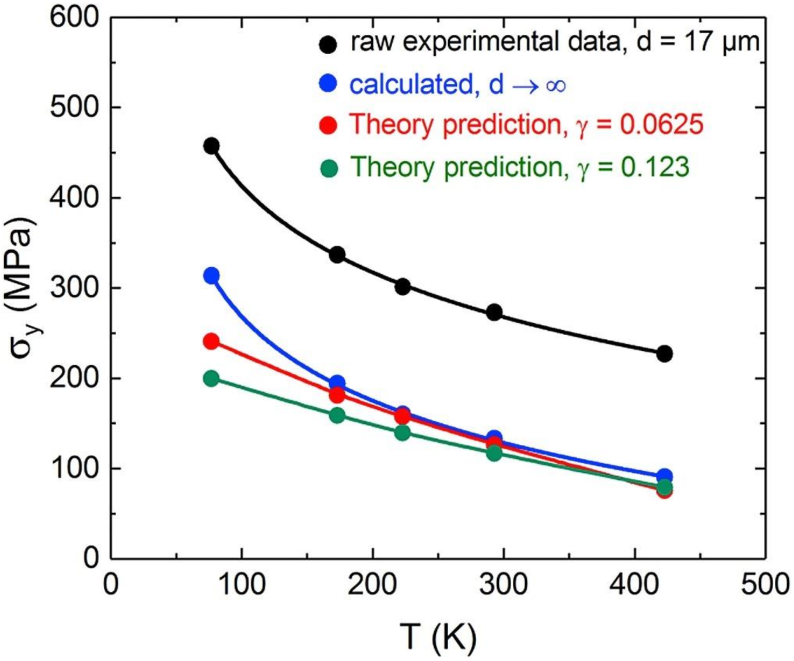

Figure 2.4.2.1. Yield stress with both predicted lines and experimental points [62].

In addition, amounts of scientific results demonstrates that deformation twinning, precipitation and phase transformation can play a significant role on both strength and ductility of the material. Ritchie, Geroge and coworkers [56] revealed profuse of nanotwins formation for the mode I fracture toughness testing, leading to highest toughness of CoCrNi-based high-entropy alloys. Raabe and coworkers [59] developed a dual-phase and transformation-induced metastable high-entropy alloys. The deformation mechanisms were represented in Fig. 2.4.2.3. This alloy obtains a combined high strength of 1000 MPa and failure strain of 0.4. More recently, Liu and cowerkers [64] developed a nanoparticle strengthening $(FeCoNi)_{86}$-Al_8Ti_6 high-entropy alloy. It shows an amazing engineering strength of 1500 MPa and an engineering strain of 0.5. They proposed the nanoparticle leads to a micro-band plasticity with the precipitation hardening effect.

Recently, it was revealed by both simulation and experiments that short-range order plays an important role on the mechanical behavior of high-entropy alloys. Using a Density Functional Theory (DFT) based Monte Carlo approach, Ding *et al.* [66] revealed a strong tendency for the formation of chemical short-range order in CrCoNi medium-entropy alloys, particularly around Cr atoms, which favor Ni and Co atoms as nearest neighbors. These neighbors cause an enhancement in the second and third shells of Cr. The DFT simulation results show that the degree of chemical short-range order varies from the random configuration up to the highest degree of order realized in the Monte Carlo approach simulations, leading to a large variation of the value of average intrinsic stacking fault energy shown in Fig. 2.4.2.2.(A). The value of average intrinsic stacking fault energy increases from −42.9 to 30 mJ m^{-2}, whereas the average extrinsic stacking-fault energy ranges between −27.8 and 66 $mJ \cdot m^{-2}$ as summarized in Figs. 2.4.2.2(B) and (C).

The study demonstrates the influence of local chemical short-range order on twinning, and even phase (fcc to hcp) transformation in CrCoNi medium-entropy solid-solution alloys, whose combination of strength, ductility, and toughness properties approaches the best on record.

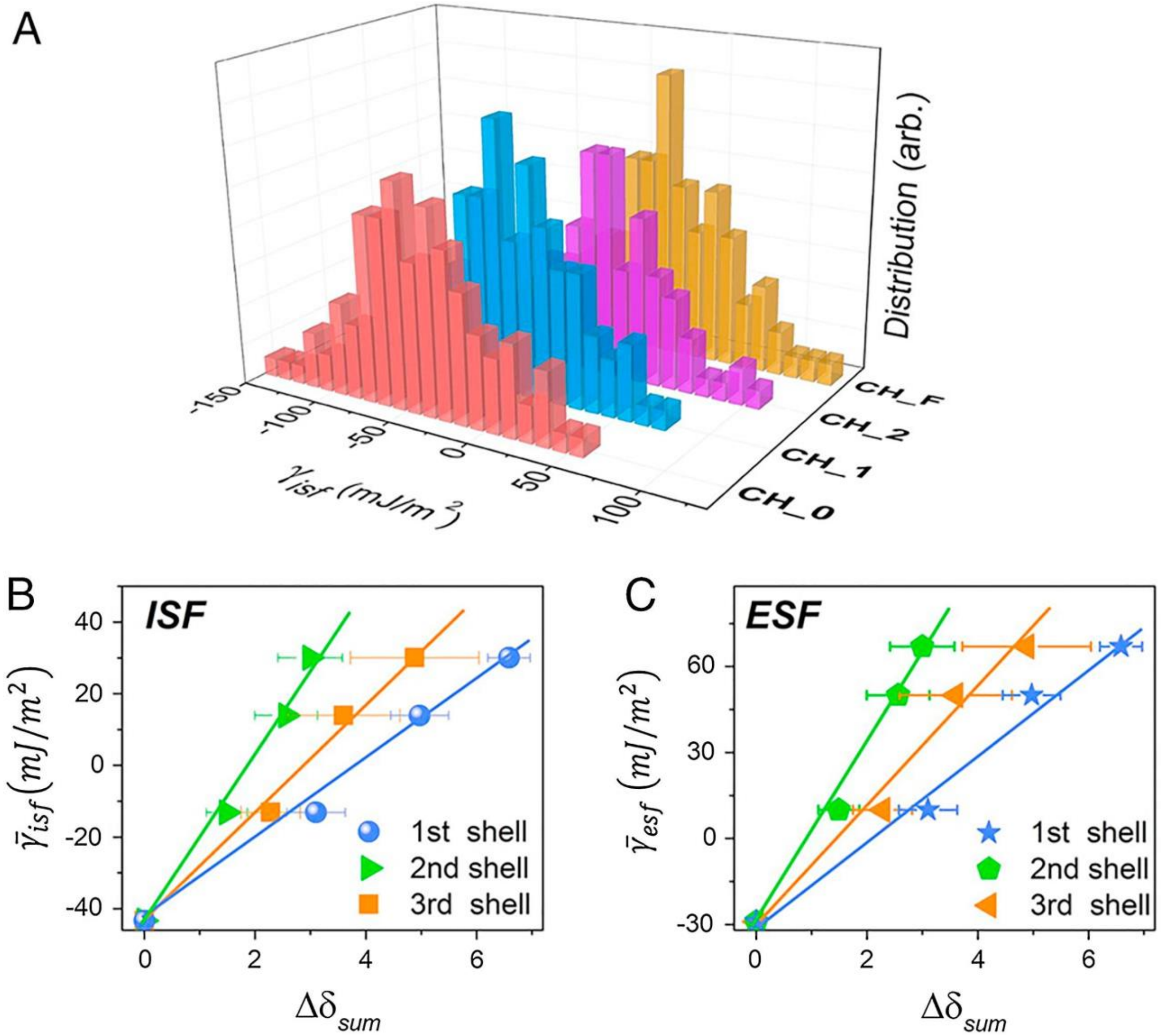

Figure. 2.4.2.2. Stacking fault energy variation with local chemical ordering. (A) Distribution of intrinsic stacking fault energy, γ_{isf}, for equimolar CrCoNi alloys in four specific states, i.e., CH_0, CH_1, CH_2 and CH_F, which expand from random solid solution to the highest degree of chemical ordering. Totally 108 stacking faults were considered for analysis in each group. The average energy, intrinsic stacking fault energy γ_{isf} and extrinsic stacking fault energy γ_{esf} in (B) and (C), respectively, among those four groups were correlated with the total nonproportional number of local atomic pairs, $\Delta\delta_{sum}$ for the first, second and third nearest-neighbor shells [33]. The conclusion here is that the stacking-fault energy of the CrCoNi alloy is strongly dependent on the degree of local chemical order.

As discussed, Ding *et al.* [65] applied the simulation method to demonstrate that short-range order in CoCrNi alloy can influence the stacking-fault energy of the materials, which in turn influence the twinning behavior and even phase transformation of fcc CoCrNi medium-entropy alloys. Also, it was reported that the presence of MnNi Clusters could suppress intrinsic stacking-fault energy in the CoCrFeMnNi alloy. Recently, Lu *et al.* [66] observed the oxygen ordering hardening of high-entropy alloys for a high strength and ductility.

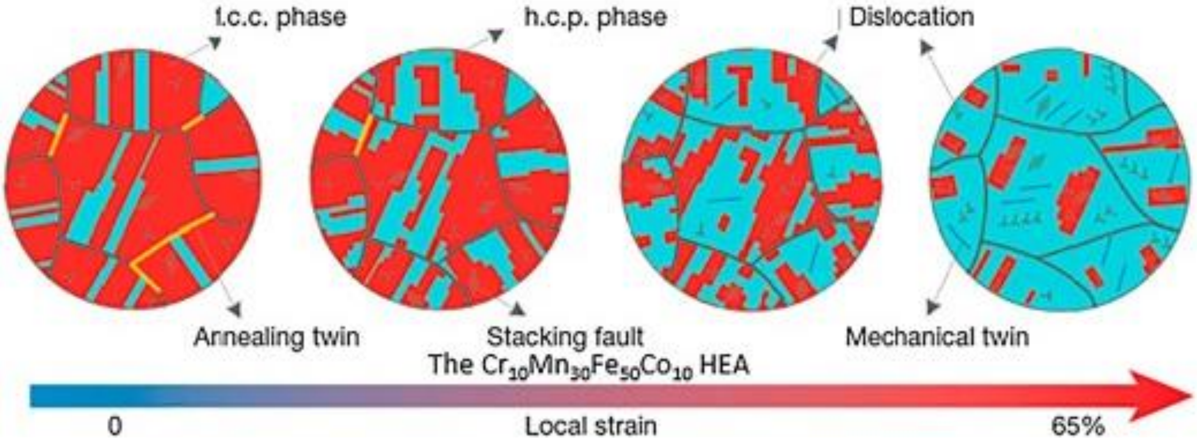

Figure. 2.4.2.3. Deformation map for the $Cr_{10}Mn_{30}Fe_{50}Co_{10}$ high-entropy alloy under the tension, noting that formation of hcp phases and mechanical twins to provide strength of the materials [60].

Chapter 3. Materials and Experimental Procedures

3.1 Description of materials

Ultrafine-grained pure titanium, the $Al_{0.3}CoCrFeNi$ alloy and the CoCrFeMnNi alloy are examined for my research, their basic properties are listed below:

Table. 3.1.1. Grain size and crystal structure of the as-received materials.

Materials	Grain Size	Crystal structure
UFG titanium	~500 nm	hcp
UFG titanium	~100 nm	hcp
$Al_{0.3}CoCrFeNi$ HEA	~500 μm	fcc
CoCrFeMnNi HEA	~10 and ~50 μm	fcc

3.2 Quasi-static and dynamic compression

The split Hopkinson pressure bar is employed to investigate dynamic behavior of materials. An elastic wave propagates through a cylindrical or rectangular sample and induces a corresponding dynamic process. The five major parts assembled to build a split Hopkinson pressure bar system are listed as follows [67]:

1. Two long and symmetrical bars;

2. Bearing and aligned fixtures to allow the bars and striking projectile to move freely while retaining precise axial alignment;

3. Compressed gas launcher/gun tube or alternate propulsion device for accelerating a projectile, termed the striker bar, to produce a controlled compressive pulse in the incident bar;

4. Strain gages mounted on both bars to measure the stress-wave propagation;

5. Associated instrumentation and data acquisition system to control, record, and analyze the stress-wave data in the bars.

Fig. 3.2.1 presents the schematic plot of the split Hopkinson pressure bar. A striker bar is pushed by a compressed-air driven gas gun. The striker generates elastic waves, which propagate through an incident bar to the sample, and then reach a transmitted bar. Two pairs of sensitive strain gauges are attached on the transmitted and incident bar, respectively. A momentum trap is placed and aligned after the rear end of the transmitted bar in order to stop the movement. All parts are fixed by a set of aligned fixtures. The pulse shape of transported waves is presented at the lower part of Fig. 3.2.1. The wave ε_I propagates from the incident bar, and then reaches the cylindrical sample. Here a reflected wave ε_R forms due to the impedances corresponded to two different materials of the incident bar and the sample. This reflected wave can be measured by the strain gages attached on the incident bar and used for investigating the dynamic responses of the tested samples. After the wave ε_T propagates through the transmitted bar, the rest of the energy is trapped by a momentum trap usually made of Pb or other soft materials. The dynamic strain rate of the split Hopkinson pressure bar can reach several thousand per second. The strain rate usually is not constant due to the work hardening as shown in Fig. 3.2.2.

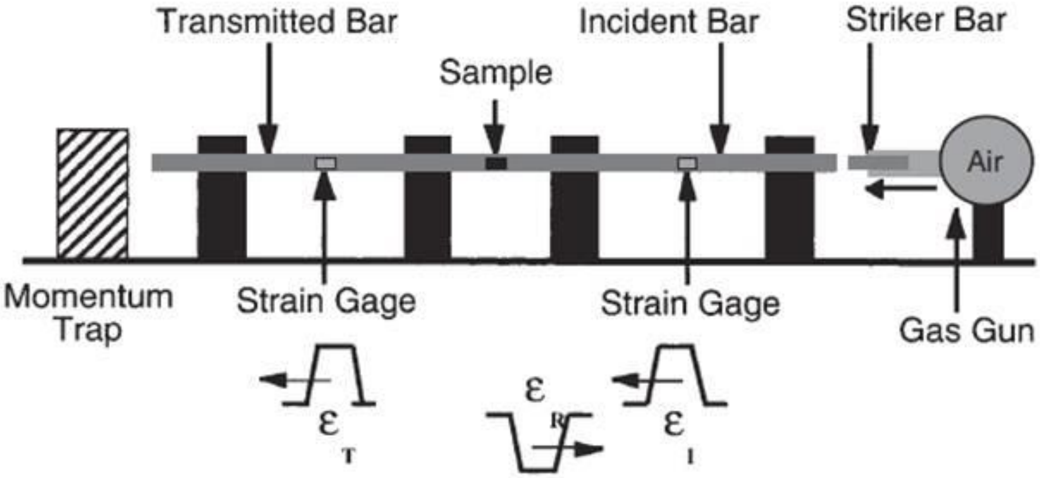

Figure 3.2.1. The split Hopkinson pressure bar system [68].

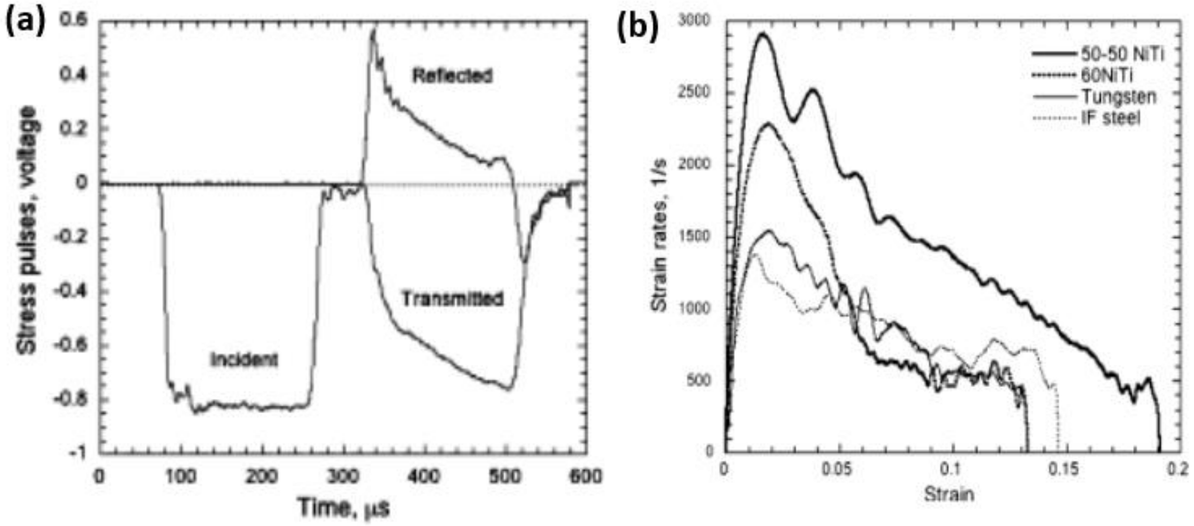

Figure 3.2.2. (a) Stress vs. time plot of 50-50 NiTi super-elastic alloy at room temperature. (b) Strain rate vs. strain curves of metals show the strain hardening induced inhomogeneous strain rate [68].

Therefore, a variety of pulse-shaping methods are proposed in order to achieve a constant strain-rate and dynamic stress equilibrium in samples to obtain reliable mechanical properties of the materials [3]. By applying pulse-shaped incident wave, the constant strain-rate can be obtained. For example, Fig 3.2.3 presents incident and reflected waves after applied pulse shapers placed at the front end of the incident bar (transmitted pulse shaper). The pulse shaper alters the incident shock wave and increases the rise time. This method results in a flat and smooth reflected wave, demonstrating a constant strain-rate is obtained.

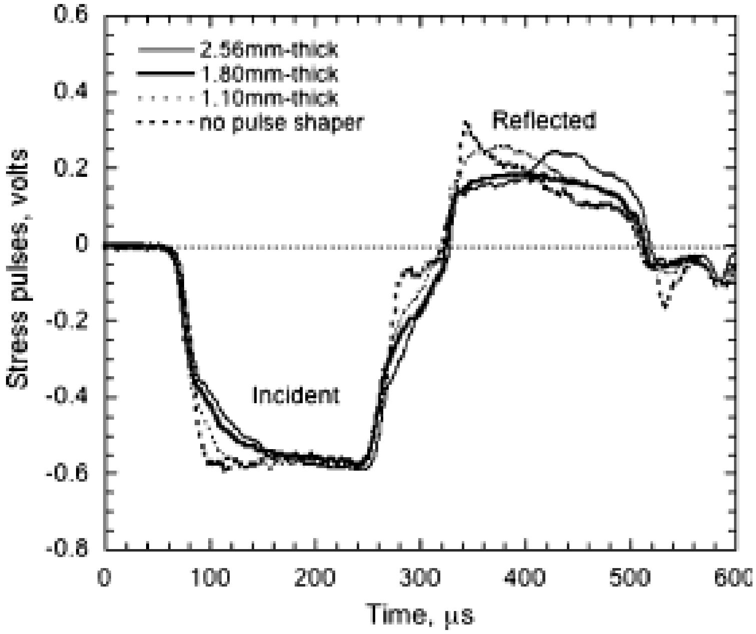

Figure 3.2.3. Incident and reflected waves with different thicknesses of pulse shapers [68].

The measured strains ε_I, ε_T, ε_R corresponded to incident, transmitted, and reflected waves can be written in an equation:

$$\varepsilon_T = \varepsilon_I - \varepsilon_R \quad , \tag{3.2.1}$$

due to the energy conservation. The dynamic stress $\sigma(t)$, strain $\varepsilon(t)$, and strain rate $\dot{\varepsilon}(t)$, are calculated based on one-dimensional stress wave theory [68, 69]:

$$\sigma(t) = E\frac{A_0}{A}\varepsilon_T(t) \tag{3.2.2}$$

$$\varepsilon_T(t) = \frac{2C_0}{L_0} \int \varepsilon_R(t)dt \tag{3.2.3}$$

$$\dot{\varepsilon}(t) = \frac{2C_0}{L_0} \varepsilon_R(t) \tag{3.2.4}$$

where E is the Young's modulus of the pressure bars; A is the cross-sectional area of the bars; A_o and L_o are the initial cross-sectional area and length of the sample, respectively; C_o is the bulk sound speed of bars. These equations provide the basic information (stress, strain, and strain-rates) which can be obtained from the split Hopkinson pressure bar tests.

3.3 Forced shear setup with hat-shaped specimen

The hat-shaped specimens are widely used to induce the shear localization of materials shown in Fig. 3.3. The stopper ring is used to control the shear displacements of the specimen. The term ‘forced localized shear’ is used to emphasize the geometry in hat-shaped specimens. The origin of localization is rooted in the initial conditions of loading and geometry of the specimen. This localized shear is not created by instability in uniformly strained material, and will be observed in many materials using hat-shaped specimens. Different geometries are applied to induce the shear bands to study shear localization of UFG pure titanium, the $Al_{0.3}CoCrFeNi$ HEA and the CoCrFeMnNi HEA.

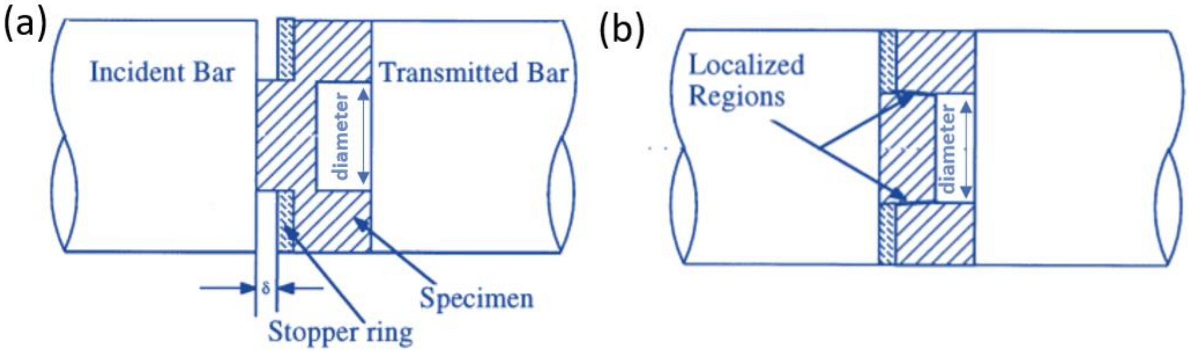

Figure 3.3. The hat-shaped specimen right in the middle of two the bars: (a) before the impact; and (b) after the impact.

3.4 Optical microscopic observation

The specimens before and after deformation were mounted and polished. The chemical etching solution was used for these materials before microstructural examination. Several etchants for the samples were selected and listed in Table 3.4. Optical Microscope was used to examine the microstructure of the specimen with the magnification ranging from 10 to 1000 times.

Table 3.4. Etchants for the samples.

Materials	Component I	Component II	Component III	Component IV
UFG titanium	2 %, HF	3 %, HNO_3	5 %, HCl	90 %, H_2O
$Al_{0.3}CoCrFeNi$ HEA	-	5 %, HNO_3	15 %, HCl	80 %, ethanol

3.5 Microhardness measurement

Microhardness measurement is an important tool to examine the material properties [70]. The simplest way of determining the resistance of a metal to plastic deformation is through a hardness test. The description of the procedures used in testing is given in ASTM Standard E92-72. The Vickers hardness (HV) is computed from the equation and is equal to the load divided by the area of the depression:

$$HV = \frac{2P\sin(\alpha/2)}{d^2} = \frac{1.8544P}{d^2} \quad , \tag{3.5.1}$$

where *P* is the applied load (in kgf), *d* is the average length of the diagonals (in mm), and *α* is the angle between the opposite faces of the indenter (136°). The surface has to be grounded and polished. After the indentation, both diagonals of impression are measured, and their average is taken. The indenting load varies from 10 g to 1 kg and the loading duration is 15 seconds.

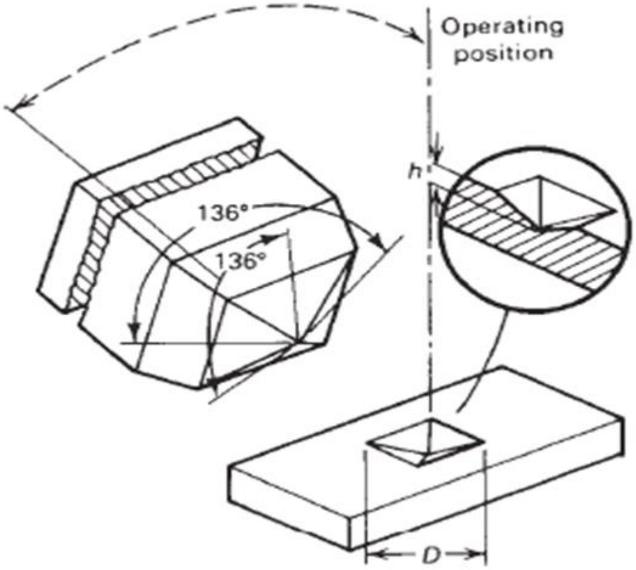

Figure 3.5. Schematic drawing of the square-based diamond pyramidal indenter used for the Vickers test and an example of the indentation it produces [71].

3.6 Scanning electron microscopy (SEM)

Scanning electron microscope (SEM) allows researchers to observe and investigate microstructure of materials down to even nano-scale. It is applicable to a variety of materials such as metals, ceramics and polymers. In 1935, Knoll proposed the concept of a scanning electron microscope [71]. Two years later, in 1938, Van Ardenne constructed a first scanning transmission electron microscope [72]. Later on, lots of scientific advances were developed and improved. The first commercial model SEM was built by A.D.G. Stewart at Cambridge Scientific Instrument Co. [73].

The basic components of modern SEMs are shown in Fig. 3.6(a). Inside the Microscope column, an electron gun provides electron beams which are used to scan the specimen. An electron beam passes through electron lenses made of magnetic materials and are controlled by the scan coils as shown in Fig. 3.6.1(a). A computer system as shown in Fig. 3.6.1(a) is used to acquire electron data converted it to SEM images, and recently, for all the modern SEM, the digitalized imaging system is essential to the commercial model. The electron beams come from the electron gun which is a LaB_6 filament, or a file emission source as shown in Fig. 3.6.1(b). The two electron-lens are made of magnetic materials using for focusing the electron beam. After focusing, the electron beam passes through an aperture, and then goes through the magnification controlled scan coils. The electron beam scans the specimen and generates several different types of electrons such as secondary electrons, backscattered electrons, and Auger electrons. The secondary (SE) and backscattered electrons (BSE) are utilized to compose the SEM images. Due to their distinct electronic properties, the SEM images produced by secondary electrons are suitable for investigating the topography of the sample. However, the backscattered electrons show different gray levels of areas corresponding roughness and elemental differences as well. The BSE image does not clearly show the roughness compared to the SE image due to the lack of shadows of the rough edges.

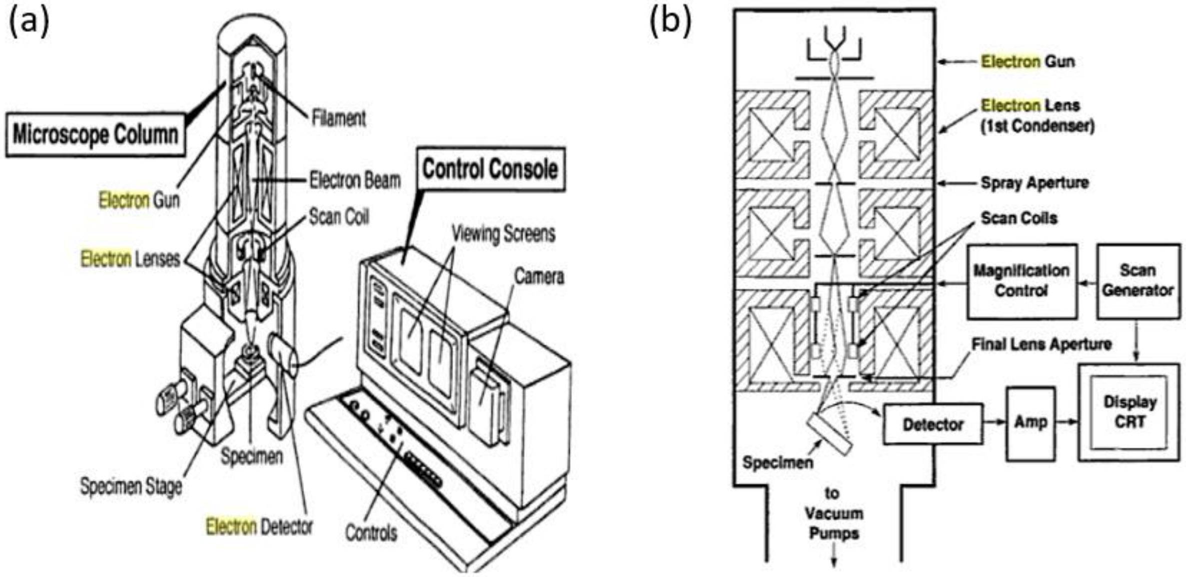

Figure 3.6.1. (a) Components of the scanning electron microscopy (SEM); (b) schematic drawing showing the components in the SEM chamber.

3.6.1 Energy dispersive X-ray spectroscopy (EDS)

Energy dispersive x-ray spectroscopy (EDS) is a sensitive, nondestructive analysis for studying the chemical composition. It can provide both quantitative and qualitative information of the composed materials. Recently, most of the modern SEMs integrated EDS system for the fast and in-situ analysis. SEM and EDS integrated a popular and powerful micro-analysis instrument [74]. The principle of EDS, developed by Fitzgerald *et al*. in 1968 [75], bases on the intrinsic semiconductivity of the micorcalorimeter which provides a high energy resolution for analyzing a variety of different x-ray energies. Specific x-rays are ignited by the electron beam of SEM, and then passed through the outer vacuum window where the ED spectrometer is placed behind the window and shielded by a heat isolating chamber. An intrinsic semiconductor, the microcalorimeter, is aligned and positioned behind Al-coated parylene windows which are used for filtering the IR irradiation in the SEM chamber. In this microcalorimeter, electron-hole pairs are created while the intrinsic semiconductor absorbs the incident x-ray, and then these charge pulses are converted to voltage steps by a charge-to-voltage preamplifier [74]. These voltage steps are then utilized for analyzing the chemical components of the specimen.

3.6.2 Micro-orientation measurement

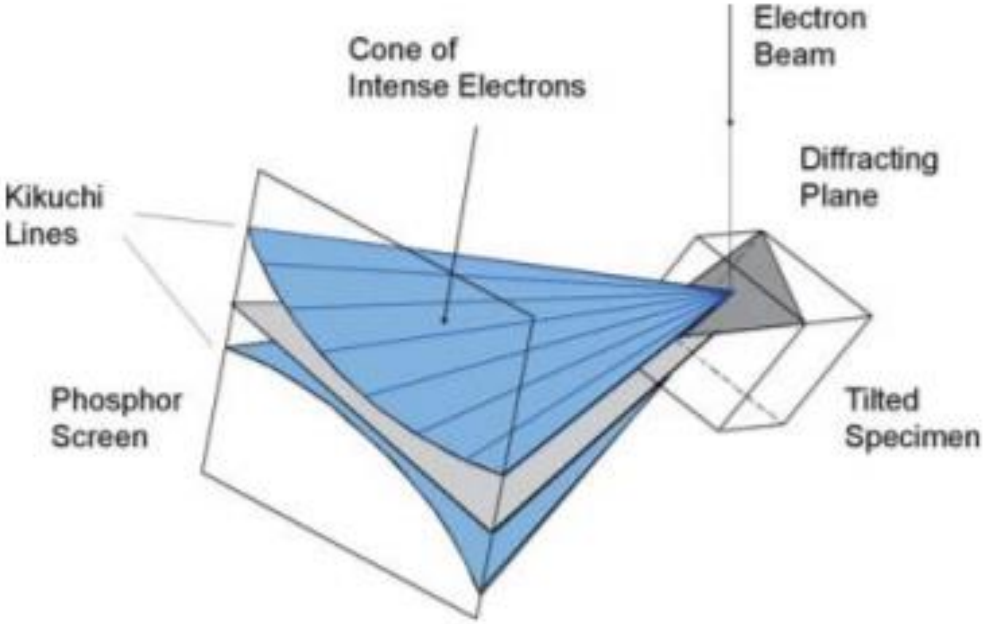

Figure 3.6.2. Schematic drawing of the diffracting cones with respect to the reflecting plane, the specimen, and the phosphor screen [77].

Fig. 3.6.2 contains a schematic drawing of the incident beam on the specimen with a given unit cell orientation and a specified diffracting plane giving rise to backscattered “Kikuchi” diffraction [76]. The two diffracting cones are the edges of the Kikuchi band, and the plane through the center of these cones is the geometric projection of the diffracting plane onto the phosphor screen. This pattern analysis of Kikuchi pattern is routinely carried out using sophisticated software algorithms to produce extremely rich data sets that can be interrogated for crystallographic texture, grain orientation, grain shape, and local deformation structure.

3.7 Transmission electron microscopy (TEM)

Transmission electron microscopes (TEM) utilizes transmitted electrons to project a magnified image at the rear side of the specimen. Due to the extremely short wavelength of electrons, the resolution of the electron microscope can have a significant increase, compared with SEM. Each electron has its own property and can be used in many different electron microscopes, or to quantify the components of the materials. For instance, the secondary electrons and backscattered electrons are used for SEM, and the transmitted electrons are utilized in TEM.

The basic components inside the TEM chamber are basically the same as what is inside the SEM, however the arrangement of these parts is significantly different. Fig. 3.7 shows the schematic drawing of TEM. The specimen is placed in between two electronic lenses, and the image is shown at the rear side of the object [77]. In crystalline specimens, the use of the primary beam (bright field) or a Bragg-reflected beam on-axis (dark field) gives rise to diffraction contrast, which is important for the imaging of crystal defects. When Bragg-diffracted beams also pass through the aperture, crystal-structure imaging reveals projections of atomic rows.

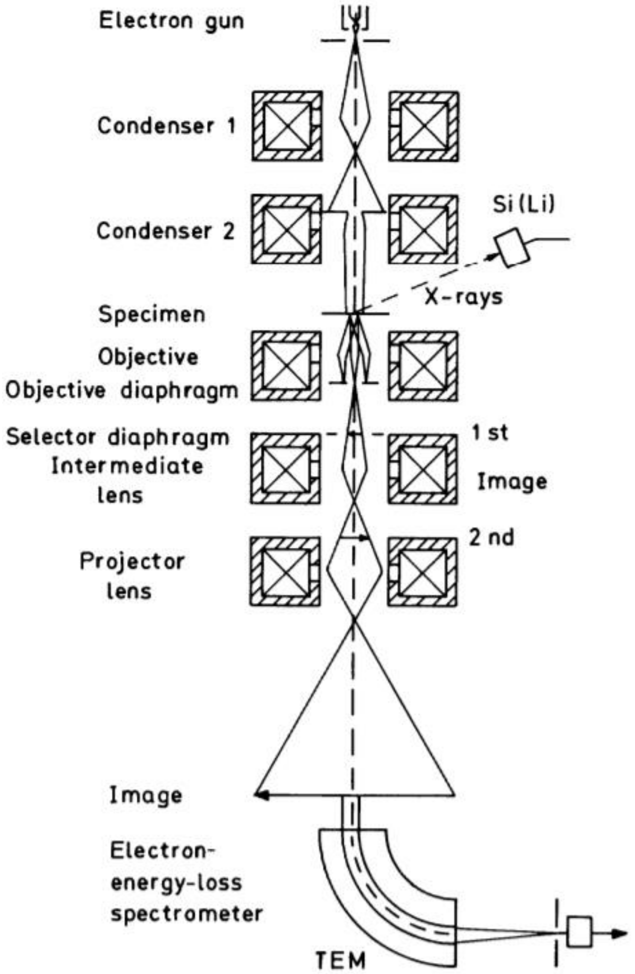

Figure 3.7. Schematic ray path for a transmission electron microscope (TEM).

3.8 X-ray diffractometer

X-ray diffractometer is a powerful methodology for qualitative analysis. Due to the constructional diffraction phenomena of the Bragg's law, $2d\sin\theta = n\lambda$, where d is the interplanar spacing and λ is the wavelength, in Fig. 3.8, for a specific crystalline structure, it has an identical diffraction pattern corresponding to each crystallographic phase and plane [78]. These basic crystal structures construct most of the crystalline structures in the nature. Different elemental crystals have their own crystal structures and lattice parameters. Some materials may have the same crystal structure, for instance, the Al0.3CoCrFeNi HEA and the CoCrFeMnNi HEA obtain the face-centered cubic (fcc) structure, but their lattice parameter is different due to their distinct atomic size. These special features allow for the x-ray diffractometer to do a qualitative analysis.

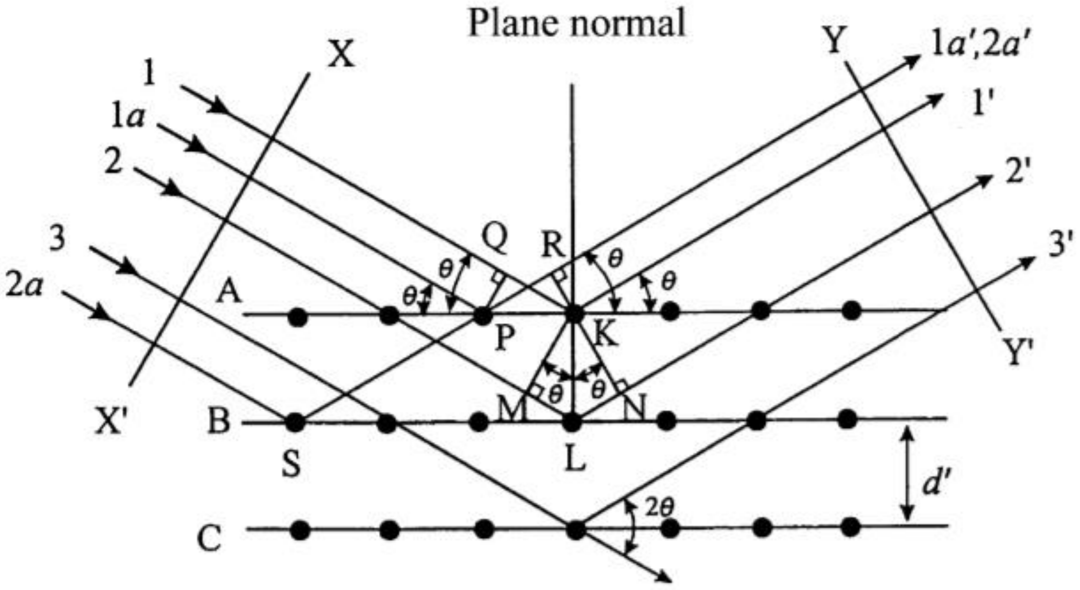

Figure 3.8. Schematic diagram of diffraction of X-rays by a crystal (Bragg condition).

Chapter 4. Dynamic response of CG and UFG titanium

4.1 Introduction

Synthesis of nanocrystalline materials can be used by either bottom-up or top-down methods [79, 80]. In the bottom-up method, the materials were built up layer by layer , such as electrodeposition, sputtering, and chemical vapor deposition. The top-down method breaks up bulk materials into small scale. For example, severe plastic methods are applied to make ultrafine-grained or nanocrystalline materials widely.

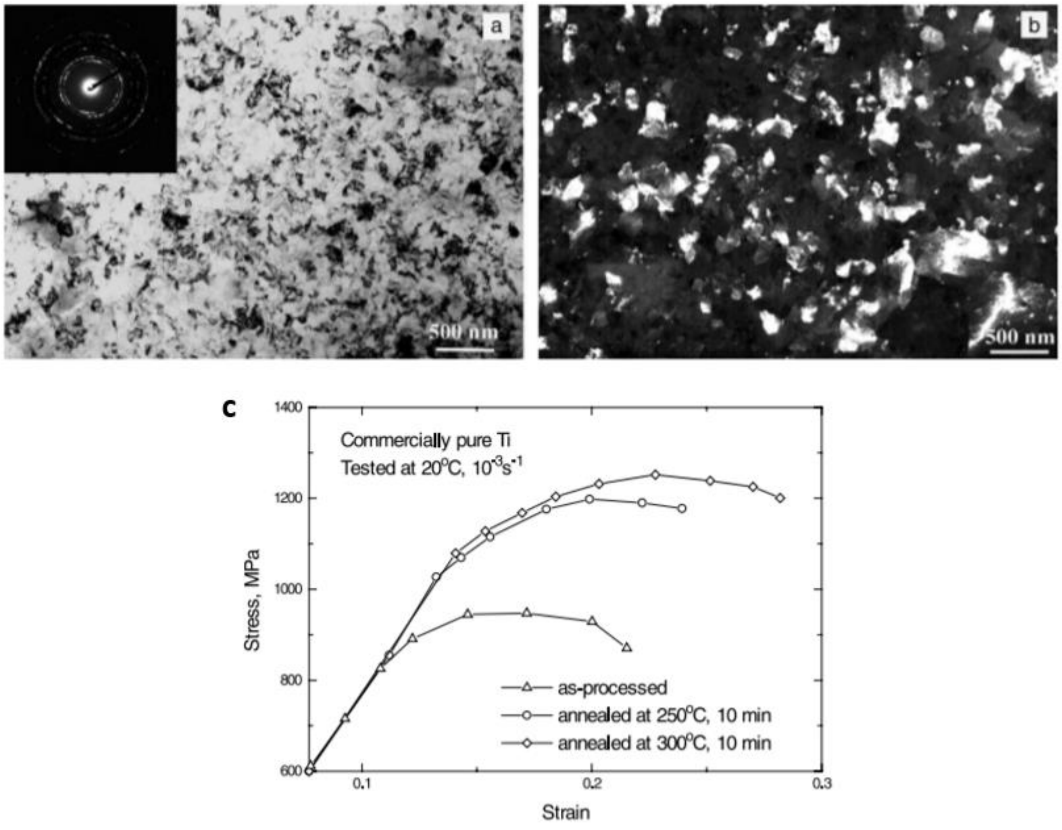

Figure. 4.1. (a) Bright- and (b) Dark- field images of microstructure of high-pressure torsion processed commercial pure titanium annealed at 250 °C for 10 min. (c) Mechanical response of high-pressure torsion processed and post-annealed commercial pure titanium [82].

Figs. 4.1(a,b) show the microstructure of high-pressure torsion processed pure titanium annealed at 250 °C for 10 min [81]. The grain size breaks down into ~100 nm. The material shows the ultimate strength of 950 MPa and 14% elongation. After annealed at 250 °C and 300 °C for 10 min, the grain size grows, and the dislocation density decreases. The ultrafine-grained titanium then shows excellent ultimate strength over 1100 MPa and ~30 % elongation. Titanium and its alloys have important technological applications such as biomedical implants, airframes and tubing for heat exchangers. Since the mechanical response has been improved significantly after annealing, further application of ultrafine-grained titanium is very promising.

4.2 Experiments

To investigate the dynamic mechanical response of CG (~10 μm) and UFG (~500 nm and ~100nm) titanium, the split Hopkinson pressure bar was applied. Cylinder specimens, were deformed at room temperature (293 K) and low temperatures (173 K and 77 K). Hat-shaped specimens were used to generate high shear strain in a localized region, thus inducing "forced shear localization" [82]. All the cryogenic temperature tests were performed inside an enclosed chamber (containing liquid nitrogen). The temperature inside the chamber was measured by the thermocouples when it was stable. Focused ion beam (FIB) technique was used to accurately extract the TEM sample from examined samples. Representative FIBed sample was presented in Fig. 4.2. The shear bands were formed for 500 nm titanium at room temperature. The advantage of this technique is that the sample can be accurately made in the right position. The FIBed TEM samples were then characterized by the model JEOL-2800 TEM and Tecnai G^2 Sphera FEI TEM operating at 200 kV.

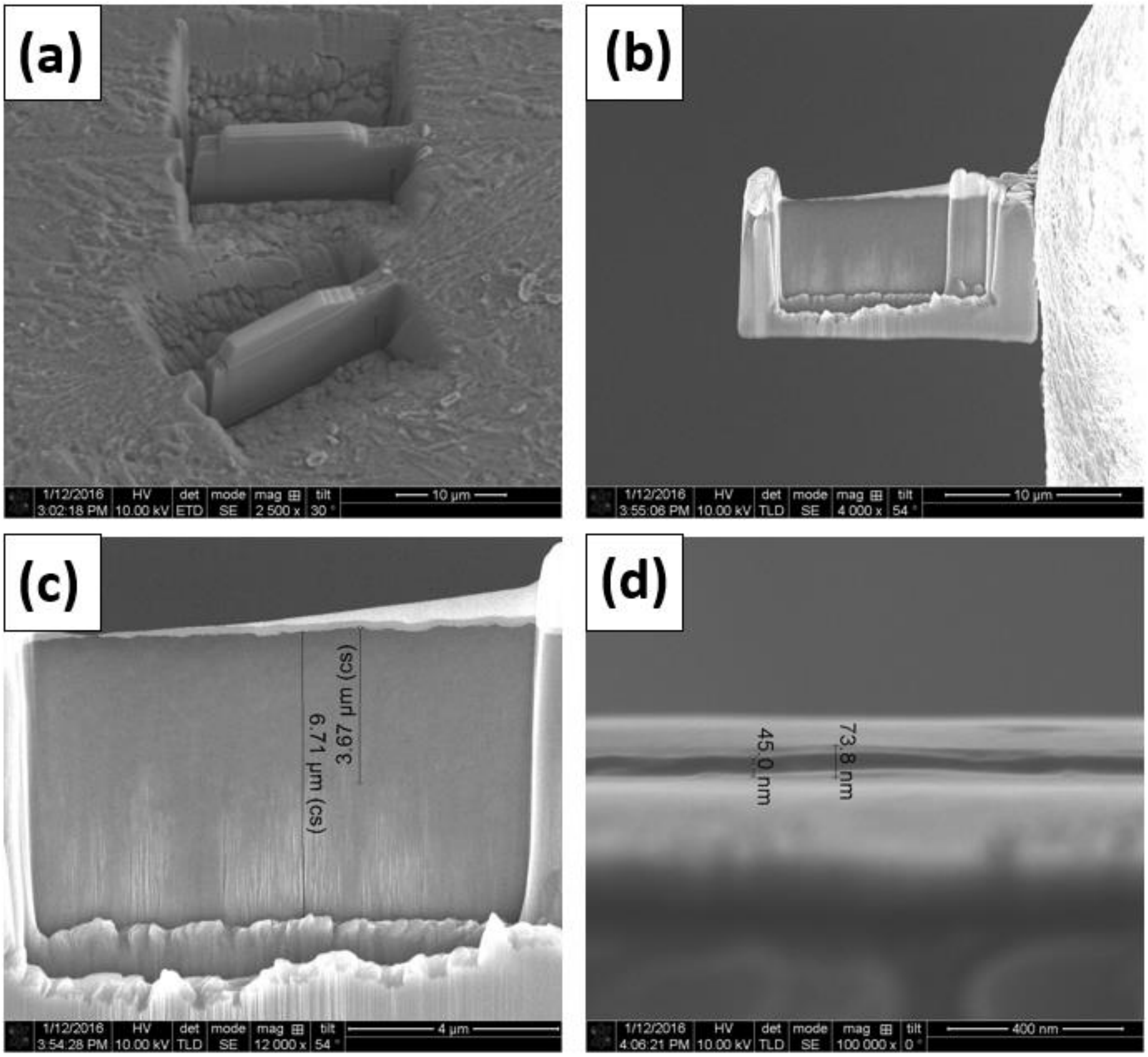

Figure. 4.2. (a) SEM image showing focused ion beam position right in the middle of shear bands; (b) TEM sample attached to a holder grid; (c) the sample was about 8 µm in length and 6 µm in width. (d) The thickness of TEM sample was less than 100 nm.

4.3 Results

4.3.1 Microstructure

Fig. 4.3.1(a1) shows the average grain size of the 500 nm UFG titanium. The low dislocation density inside the grains and accumulated dislocations near the grain boundaries in Fig. 4.3.1(a1) indicate that the materials underwent dynamic recovery and recrystallization processes during severe plastic deformation. A higher magnification image in Fig. 4.3.1(b1) shows that the grains still contain dislocations. The corresponding selected-area diffraction (SAD) pattern in Fig. 4.3.1(c1) shows the polycrystal structure. Fig. 4.3.1(a2) shows another as-received UFG titanium with average grain size 100 nm. Fig. 4.3.1(b2) shows the equiaxed configuration of grains. The high-resolution image in Fig. 4.3.1(c2) confirms its initial hcp crystal structure.

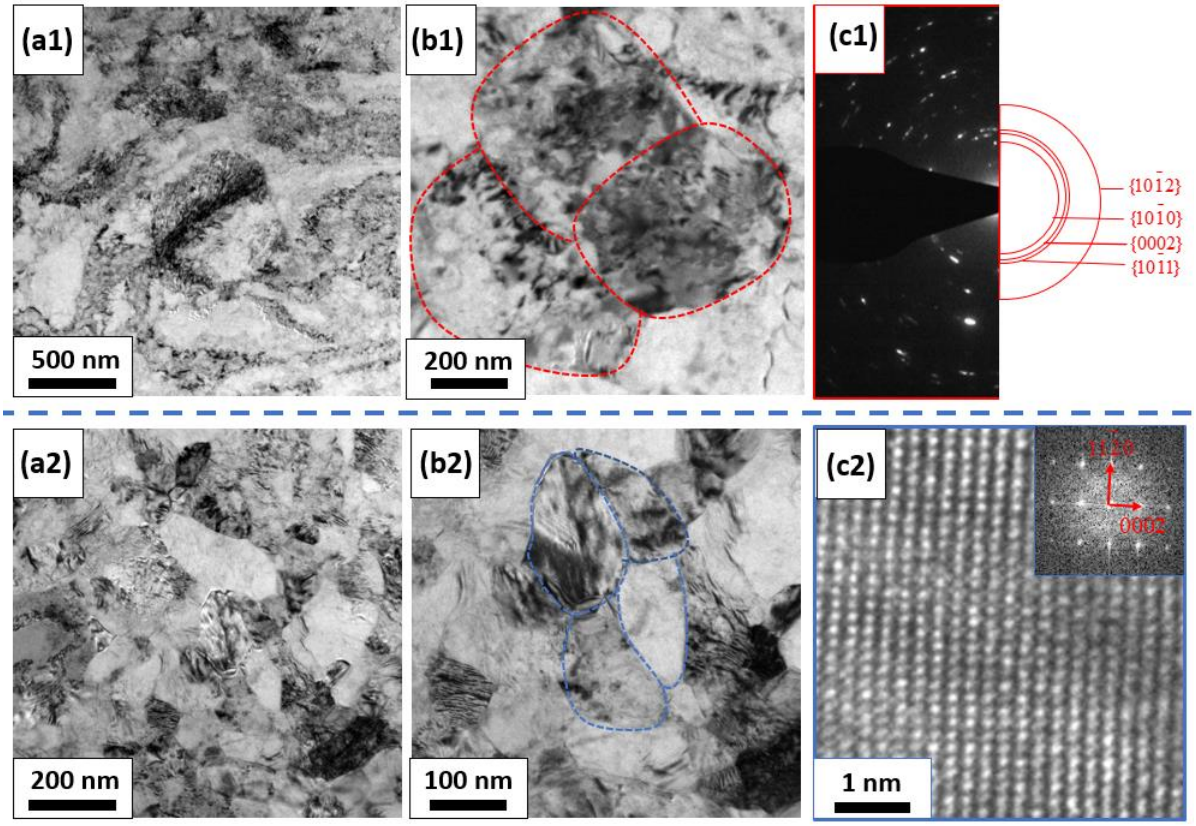

Figure 4.3.1. (a1) Transmission electron microscopy image showing Ti with average grain size of 500 nm; (b1) microstructure of ultrafine-grained Ti; (c1) selected area diffraction (SAD) pattern in (a1). (a2) Transmission electron microscopy image showing Ti with average grain size of 100 nm; (b2) microstructure of ultrafine-grained grains; (c2) high-resolution TEM image showing hcp crystal structure of Ti.

4.3.2 Mechanical response of UFG titanium

Fig. 4.3.2.1(a) shows the compressive stress-strain curves of UFG 100 nm titanium at different strain-rates [11, 83, 84]. After an initial stage of rapid strain hardening, the strain-hardening rate beyond a strain of ~0.04 is significantly reduced. This is the characteristic of nanocrystalline and UFG materials, which often show low strain-hardening rate. Fig. 4.3.2.1(b) further shows that the strain-hardening rate of UFG (~100 nm) titanium under dynamic-loading follows the same trend. In contrast, the flow stress of CG titanium under dynamic impact continues to increase [11]. The density of dislocations in a nanocrystalline metal saturates due to dislocation annihilation at grain boundaries. They tend to lose their defect accumulation ability and hence the capacity for strain-hardening. Flat compression curves have been observed for UFG pure titanium made by ECAP [85]. Elias *et al.* [86] also reported a low strain-hardening rate for UFG (~200 nm) titanium after a strain of 0.05.

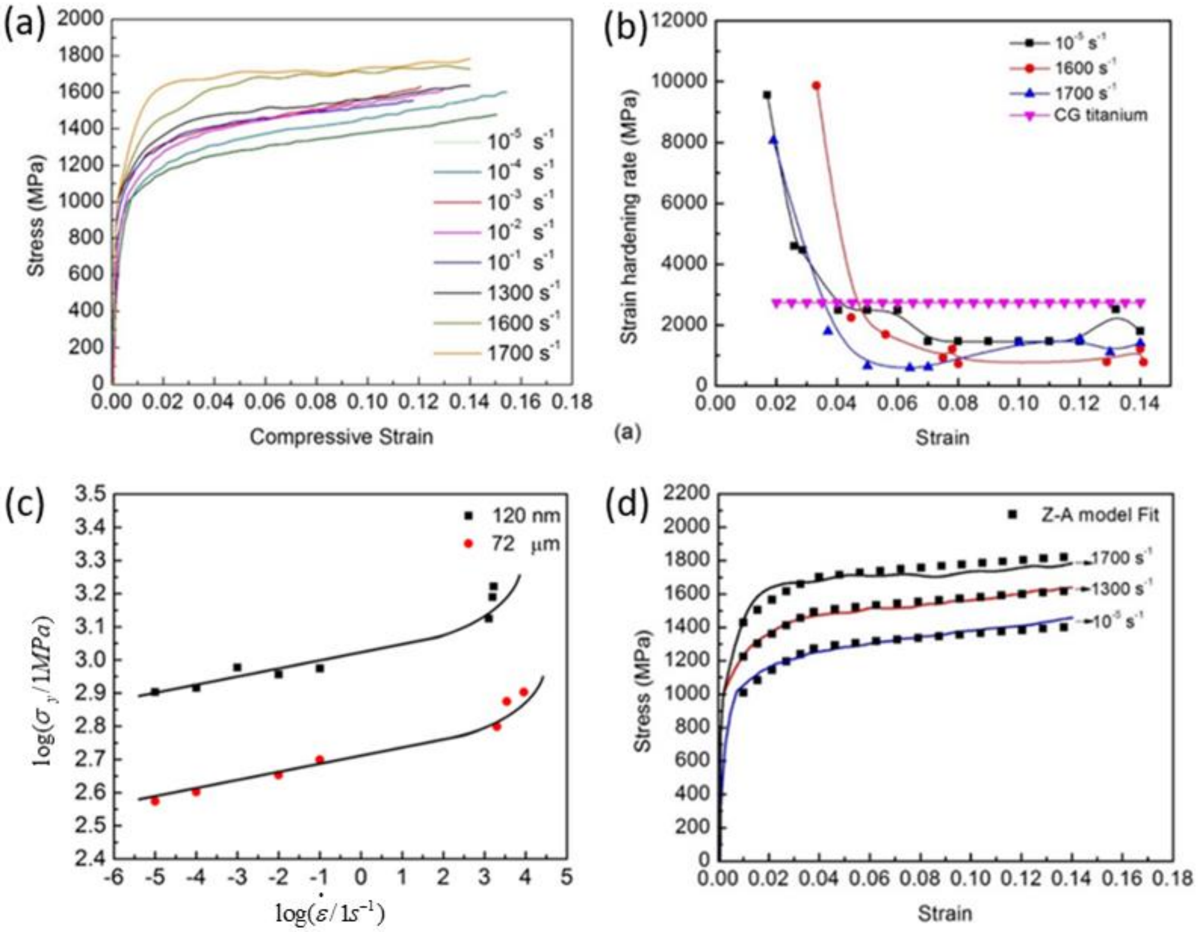

Figure 4.3.2.1. (a) Stress-strain relationships of UFG titanium cylindrical samples at different strain-rates. (b) Strain-hardening rate as a function of strain. (c) Strain-rate sensitivity of CG titanium and UFG titanium. (d) Stress-stress relationship and Zerilli-Armstrong constitutive equation fit to experimental results at strain rates 10^{-5} s^{-1}, 1300 s^{-1} and 1700 s^{-1}.

The strain-rate dependence of the yield stress for two grain sizes (72 μm and 100 nm) are shown in Fig. 4.3.2.1(c). The strain-rate sensitivity, defined as $m = \partial \log \sigma / \partial \log \dot{\varepsilon}$, is 0.027 between 10^{-4} s^{-1} and 10^{3} s^{-1} for both UFG titanium and CG titanium [11]. At the higher strain-rate, there is an increase in *m*. The activation volume parameter concept provides insight into the deformation mechanisms [87]. which is expressed as:

$$\upsilon^{*} = \frac{kT}{m\sigma_{y}} \tag{4.3.2.1}$$

where *T* is the temperature, σ_y is the yield stress, and *k* is the Boltzmann constant. It can be seen from equation 4.3.2.1 that the activation volume υ^{*} is inversely proportional to both strain-rate sensitivity and yield stress. The yield stress of UFG titanium is approximately twice that of coarse-grained pure titanium. The activation volume of UFG titanium is ~$40b^3$, where b=0.289 nm is the Burgers vector in hexagonal titanium. This represents a significant reduction in the activation volume, compared with ~$80b^3$ for coarse-grained CP titanium [84]. The influence of the cutting of forest dislocations decreases for UFG materials. This results in a decrease of the activation volume related to its low strain-hardening response.

Zerilli and Armstrong [88, 89] developed physically-based constitutive equations based on the general mechanical responses for fcc, bcc and hcp metals. The Zerilli-Armstrong equation is based on the framework of thermally-activated dislocation motion, where both the work-hardening rate and strain-rate sensitivity are influenced by the temperature. This equation was applied by Meyers *et al.* [45] to describe the mechanical response of hexagonal materials and is modified below to account for two regimes:

$$\sigma=\begin{cases}\sigma_G+k_s d^{-1/2}+C_1\left(\frac{\dot{\varepsilon}_0}{\dot{\varepsilon}}\right)^{-C_3T}+\frac{C_2}{e^{-C_4T}}\varepsilon^{n_1},\varepsilon\in(0,\varepsilon_0)\\ \sigma_G+k_s d^{-1/2}+C_1\left(\frac{\dot{\varepsilon}_0}{\dot{\varepsilon}}\right)^{-C_3T}+\frac{C_2}{e^{-C_4T}}\varepsilon_0^{\ n_1}+\frac{C_5}{e^{-C_4T}}(\varepsilon-\varepsilon_0)^{n_2},\varepsilon\in(\varepsilon_0,\varepsilon)\end{cases}\tag{4.3.2.2}$$

where σ_G represents the athermal part of the stress required for plastic deformation. The second term in the right-hand side represents the Hall–Petch relationship (also considered athermal). The third and fourth terms represent the increase of the yield stress related to an increase of strain rate $\dot{\varepsilon}$ and plastic strain ε, respectively (thermal part). As discussed, in the first stage of plastic deformation, for a strain less than 0.04, dislocations are still the carriers of plastic deformation for the UFG titanium. For the nearly zero post-yield work-hardening range ($\varepsilon\geq0.04$), the experimentally determined parameters, C_5 and n_2, are changed to describe its low strain-hardening ability. This provides the fifth term. For UFG 100 nm titanium, σ_G =0 MPa, k_s=6 MPa •mm$^{-1/2}$ [2], C_1=420 MPa, C_2=2200 MPa, C_3=8.05$\times$10^{-3} K^{-1}, C_4=6.8$\times$10^{-4} K^{-1}, C_5=655 MPa, $\dot{\varepsilon}_0$ =1700 s^{-1}, n_1=0.33 and n_2=0.8. The validity of the constitutive equations is further assessed by comparing the experimental and predicted results in Fig. 4.3.2.1(d).

Vickers microhardness tests were performed on the bulk samples, and the values of microhardness were converted to the yield stress by $\sigma_y=H_V/3$. The results in Fig. 4.3.2.2(a) show that the yield stress of UFG titanium increases with decreasing grain size but tends to deviate from the conventional Hall-Petch slope. Meyers *et al.* [2] showed that the Hall-Petch slope decreases from 12.5 GPa.nm$^{1/2}$ to 4.38 GPa.nm$^{1/2}$ in the nano- range. The decrease in the Hall-Petch slope was mainly attributed to different deformation mechanisms gradually becoming dominant.

Fig. 4.3.2.2(b) shows the true stress - true strain curves of CG and UFG titanium under high strain-rates at various temperatures. It is apparent that the yield stress of both UFG and CG titanium increases with decreasing temperature and increasing strain-rate. In contrast with clear strain hardening of CG titanium. [90], the flow stress is relatively flat, and no significant strain-hardening behavior is observed for UFG titanium at either room or low temperatures.

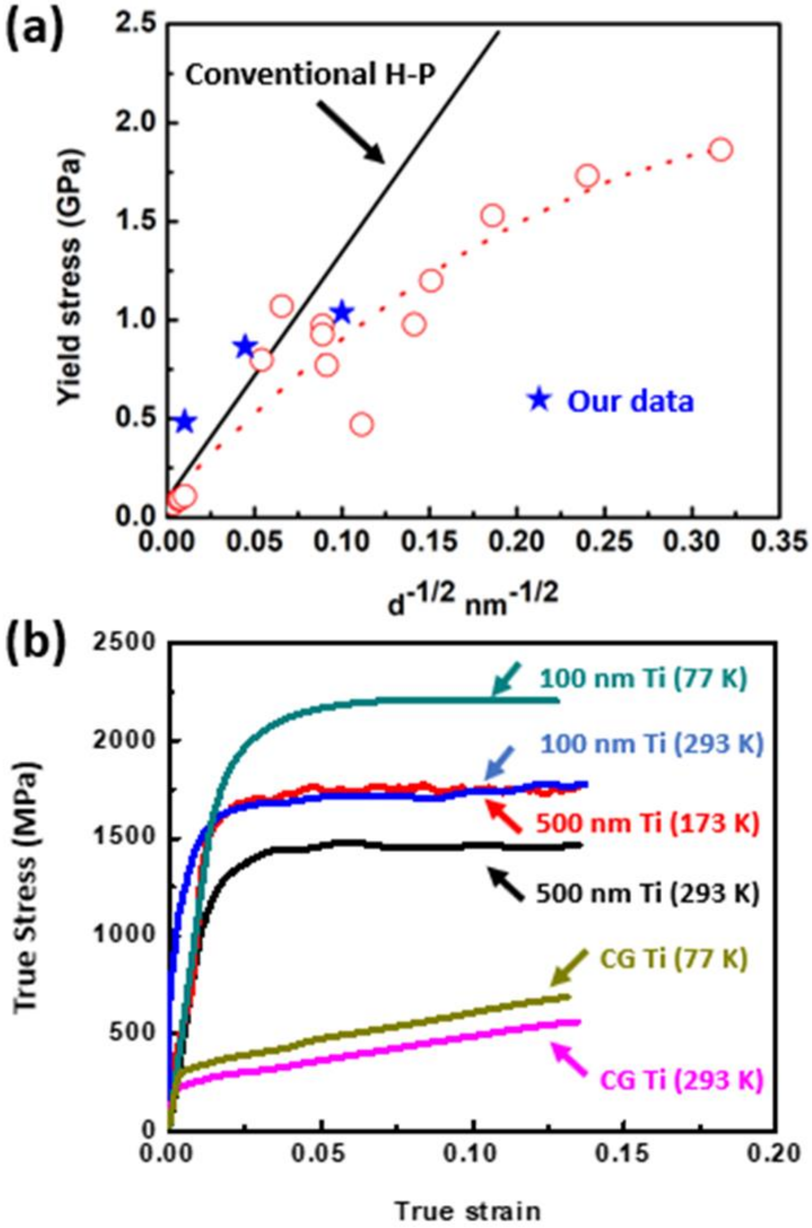

Figure 4.3.2.2. (a) Microhardness Hall-Petch relationship of titanium. (b) Stress-strain curves of Ti with different grain sizes under dynamic loading strain-rates ~10^3 s^{-1}.

4.3.3 Mechanical response of shear band

To examine the grain size and temperature effects on shear localization of titanium, the hat-shaped samples were tested at room temperature (293K) and low temperatures (173 K and 77 K).

The shear stress versus shear strain curves in the adiabatic shear bands (ASB) for the samples are shown in Fig. 4.3.3 [91]. It should be noticed that the true shear strain is established by the displacement divided by the width of shear region in the hat-shaped specimen. With increasing strain, the flow stress begins to fluctuate due to the competition between strain-hardening, strain-rate-hardening and thermal softening. When thermal softening effect becomes dominant, the stress decreases sharply and a complete adiabatic shear band **(**ASB) is generated. Fig. 4.3.3 indicates that the samples tested at low temperatures were loaded under higher shear stress, in comparison with the samples tested at room temperature.

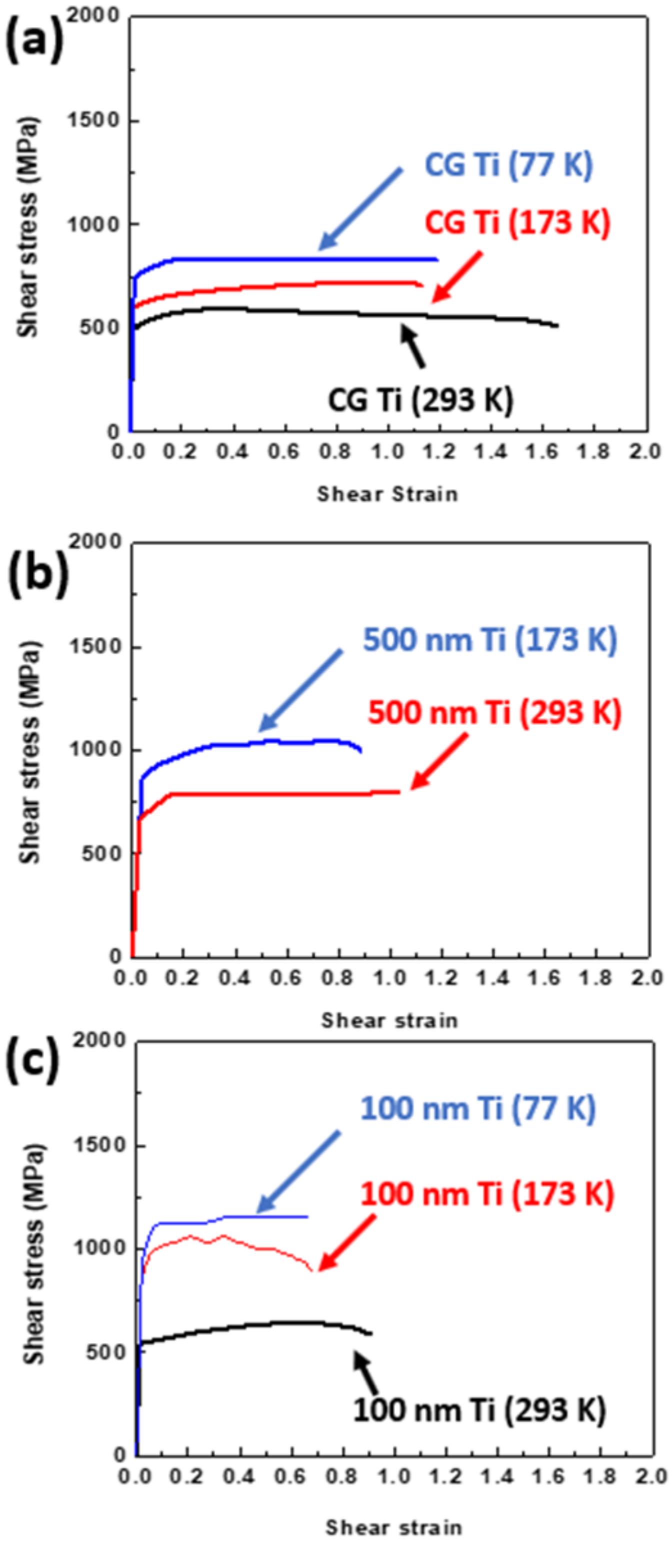

Figure 4.3.3. (a) Shear stress and shear strain plots in shear region for CG titanium. (b) Shear stress and shear strain plots in shear region for UFG 500 nm titanium. (c) Shear stress and shear strain plots in shear region for UFG 100 nm titanium.

Assuming adiabatic heating, it is possible to estimate the temperature rise within the shear band. Taking into account that a fraction β of the work done is converted into heat, temperature rise ΔT is [3]:

$$\Delta T = \frac{\beta}{\rho C_p} \int_{\gamma_s}^{\gamma_e} \tau d\gamma \quad . \tag{4.3.3.1}$$

The initial conditions are $\beta = 0.9$, $C_{p(T=273K)} = 520$ J/(kg·K), $C_{P(T=173K)} = 430$ J/(kg·K), $C_{P(T=77K)} = 210$, and $\rho = 4500$ kg/m^3. By using the stress-strain data in Fig. 4.3.3, a temperature rise of at least 300 K can be reached for all of the tested samples as determined from Eqn. 4.3.3.1. Using the in-situ infrared detector, at the onset of the load drop, Guo *et al.* [92] reported that severe strain localization happened first before the shear band temperature rises to ~800 K for coarse-grained titanium. Since the width of shear band is significantly lower than the shear region of hat-shaped specimens, the actual local shear strain in the shear band is indeed much larger than the values. Zhao *et al.* [93, 94] reported that large shear stress can even cause the amorphization in silicon under shock compression.

A quantitative description of the susceptibility to adiabatic shear banding (ASB), by Wright [25], has the following form:

$$\frac{\chi_{SB}}{a/m} = \min\left\{1, \frac{1}{n/m + \sqrt{n/m}}\right\} \tag{4.3.3.2}$$

where a is a nondimensional thermal softening parameter defined by $a = (-\partial\sigma/\partial T)/\rho C_p$, n is the strain hardening exponent, and m is the strain-rate sensitivity. For a perfectly plastic material (no strain hardening), the susceptibility reduces to:

$$c_{SB} = \frac{a}{m} = \frac{a\ s_y}{r\ C_p m} \qquad (4.3.3.3)$$

where $\alpha = 0.002$ K^{-1} is the thermal softening parameter evaluated under isothermal conditions and σ_y is the yield strength [11]. The susceptibility to ASB of the UFG (100 nm) titanium can thus be estimated to be ~30 using the following parameters: σ_y = 0.97 GPa, m = 0.027 [84]. For the CG titanium, σ_y = 0.4 GPa, $\alpha = 0.001$ K^{-1}, m = 0.027 [11] results in a susceptibility to ASB of ~6, five times lower than that for the UFG (100 nm) titanium. A similar increase in susceptibility to shear localization of UFG Fe was also reported by Wei *et al.* [27].

4.3.4 Microhardness of adiabatic shear band

Microhardness tests were performed both inside and away from the shear bands of the samples. The average hardness values as a function of distance to the shear band were plotted in Figs. 4.3.4. As approaching to the shear band, the microhardness increases due to the decrease of the grain size inside the shear band. Such microhardness difference between the shear band and matrix was caused by the formation of recrystallized grains inside the shear band, which was also reported by Meyers *et al.* [11].

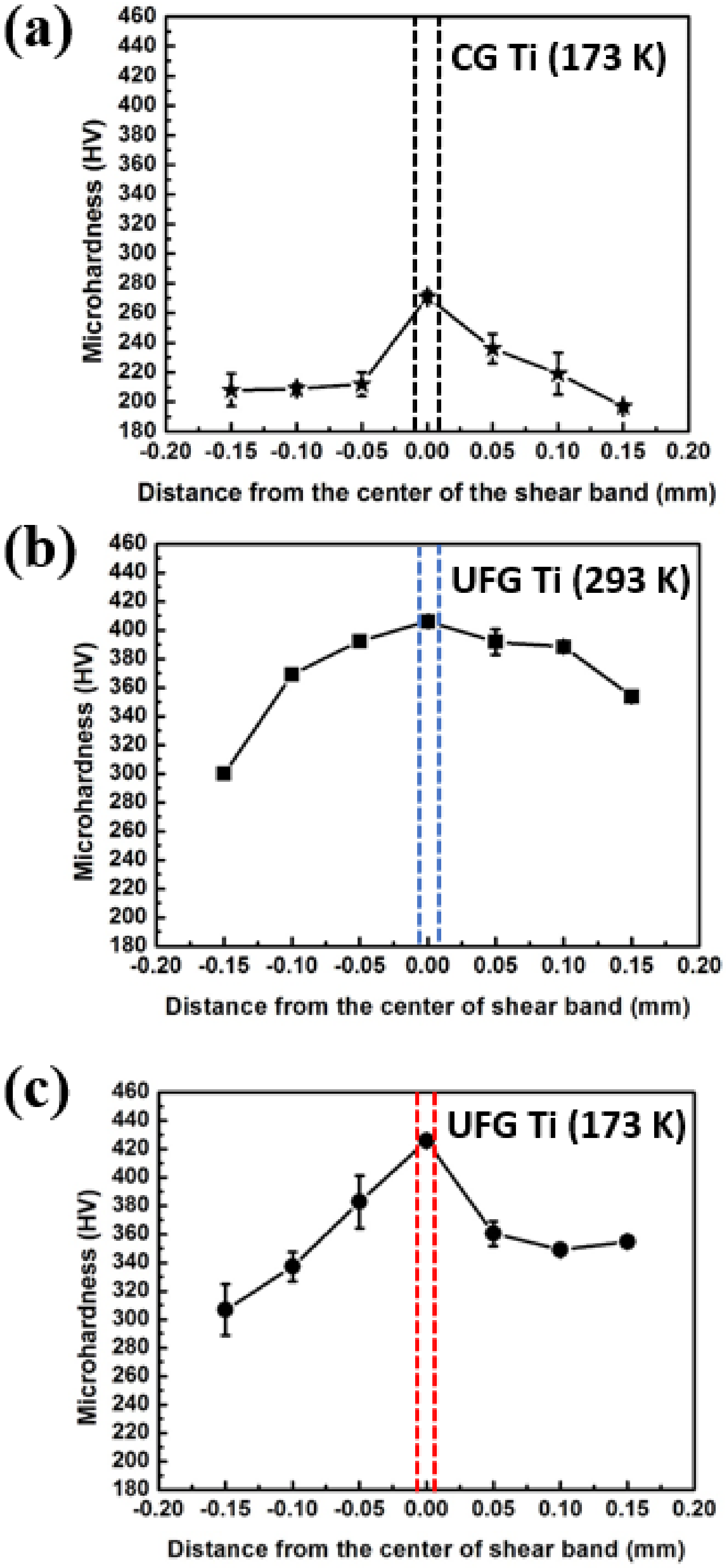

Figure 4.3.4. Microhardness of shear bands for CG titanium at (a) 173 K and UFG titanium at (b) 293 K and (c) 173 K.

4.3.5 Microstructure evolution of ASB

Fig. 4.3.5.1 shows TEM micrographs from the shear bands. The corresponding selected area diffraction (SAED) patterns for each image demonstrate the preponderance of randomly distributed recrystallized grains. The selected area diffraction (SAED) patterns do not suggest strong texture, due to the apparent absence of concentrated intensity in the ring pattern. The shear bands contain both elongated and equiaxed grains in Fig. 4.3.5.1(a1), which are much smaller than the grains in the matrix. Entangled dislocations are found inside the grains. The average grain size inside the shear band of CG titanium at 77 K is 140 nm as observed in Fig. 4.3.5.1(c1), which is much smaller than the average grain size of 250 nm inside shear band formed at room temperature of CG titanium [11] in Fig. 4.3.5.1(a1).

The UFG titanium also exhibits a tendency for a decrease in grain size when decreasing temperatures. Fig. 4.3.5.1(a2) shows elongated grains breaking up to the recrystallized subgrains. A higher magnification image in Fig. 4.3.5.1(b2) illustrates the formation of equiaxed grains. Fig. 4.3.5.1(c2) shows that UFG subgrains with average grain size of 120 nm with deformation initiated at 77 K. Fig. 4.3.5.1(a3) shows the formation of nano-bundles during the shear deformation in UFG 100 nm titanium at 293 K. The red arrow shows a series of nano-bundles ranging from 30 nm to 80 nm. Significant nanocrystalline subgrains were observed inside the shear bands. Figs. 4.3.5.1(b3,c3) illustrate the formation of extremely small nanograins inside the shear bands at cryogenic temperatures. No deformation twins are found inside any of shear bands, further evidence of dynamic recrystallization.

Figs. 4.3.5.2 shows the higher magnification images of subgrains inside the shear bands. Very fine recrystallized grains are the dominant feature. Fig. 4.3.5.2(a1) shows that the UFG elongated dislocation cells were formed in the shear band at room temperature for CG titanium. The dark-field image of Fig. 4.3.5.2(b1) shows the subgrains with grain size around 140 nm formed in the shear band at 77 K. The dislocations inside the grain are the evidence of on-going deformation. Fig. 4.3.5.2(a2) shows the break-up of elongated grains in the shear band of UFG 500 nm titanium at 293 K. Recrystallized grain boundaries and triple points were observed in Fig. 4.3.5.2(b2) in the shear band at 173 K, and the grains have narrow and faceted boundaries, which are the characteristics of the recrystallization [39, 95]. Fig. 4.3.5.2(a3) shows the formation of both nano-bundles and recrystallized equiaxed grains in the shear band of UFG 100 nm titanium at 293 K. The dark-field image of shear band in Fig. 4.3.5.2(b3) demonstrates the formation of extreme small nanogrians inside the shear band at 77 K.

The grain size distribution inside the shear bands for the different materials and initial deformation temperatures are depicted in Fig. 4.5.5.3 and Table 4.3.5. There are clearly two trends: (1) as the initial grain size is decreased, so it is the recrystallized grain size in the shear band; (2) as the initial temperature is decreased, so is the grain size in the shear band.

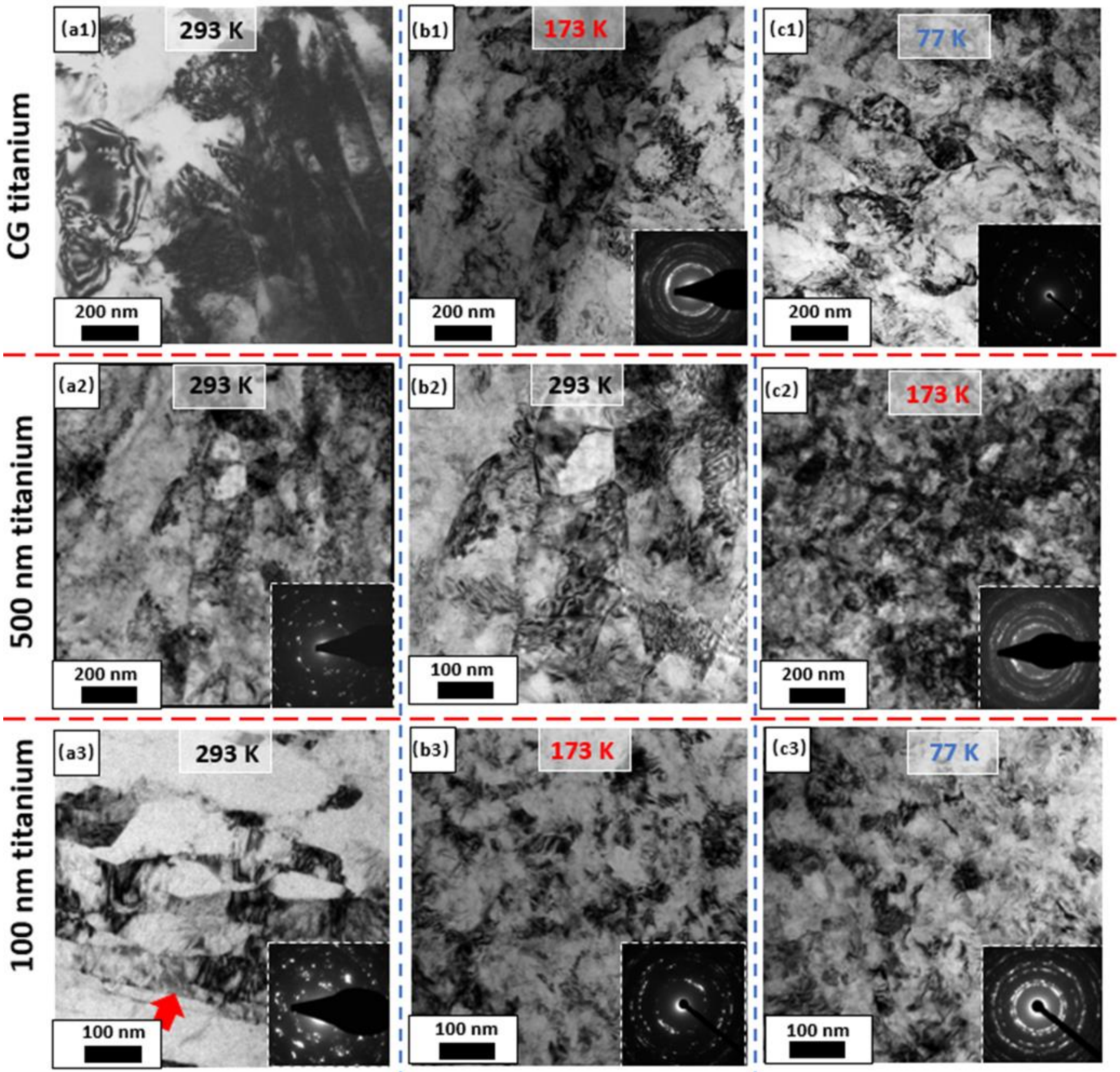

Figure 4.3.5.1. TEM images of the shear band formed in CG titanium at (a1) 293 K, (b1) 173 K, (c1) 77 K. TEM images of the shear band formed in UFG 500 nm titanium at (a2) 293 K, (b2) 293 K, (c2) 77 K. TEM images of the shear band formed in UFG 100 nm titanium at (a3) 293 K, (b3) 173 K, (c3) 77 K.

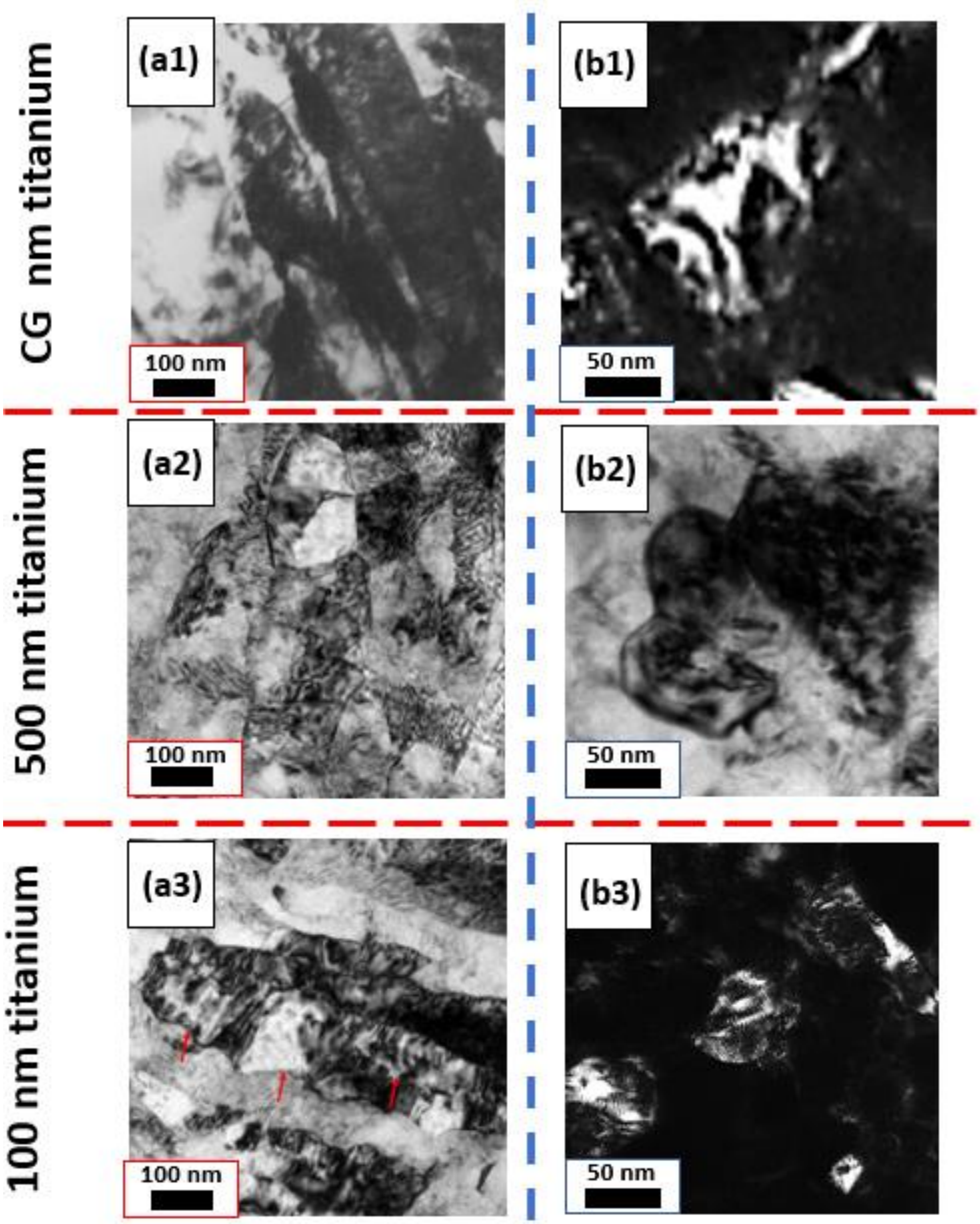

Figure 4.3.5.2. Microstructure inside the shear bands for CG Ti at (a1) 293 K and (b1) 77 K. Microstructure inside the shear bands for UFG 500 nm Ti at (a2) 293 K and (b2) 173 K. (a3) Microstructure inside the shear bands for UFG 100 nm Ti at 293 K. The red arrows show the formation of recrystallized subgrains in the elongated nano-bundle. (b3) Dark-field image shows the formation of equiaxed subgrains in shear band at 77 K.

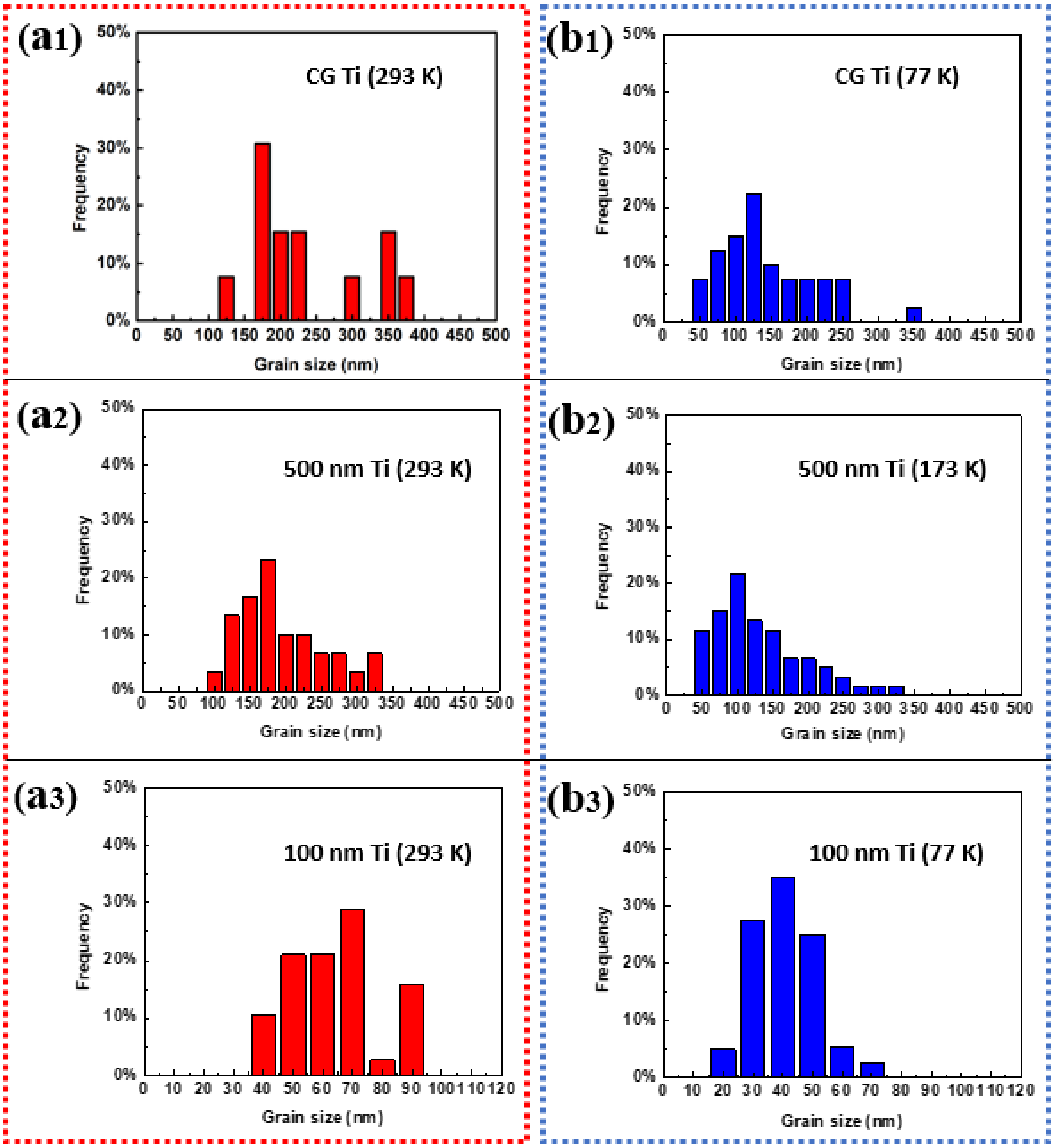

Figure 4.3.5.3. Grain size distribution in shear bands in CG titanium at (a1) 293 K and (b1) 77K. Grain size distribution in shear bands in UFG 500 nm titanium at (a2) 293 K and (b2) 173 K. Grain size distribution in shear bands in UFG 100 nm titanium at (a3) 293 K and (b3) 77 K.

Table 4.3.5. The width of shear bands and average recrystallized grain size inside the shear bands.

	293 K	173 K	77 K
CG Ti	30 µm (250 nm)	25 µm (190 nm)	18 µm (140 nm)
500 nm Ti	15 µm (180 nm)	5 µm (120 nm)	
100 nm Ti	4 µm (60 nm)	2 µm (50 nm)	1 µm (36 nm)

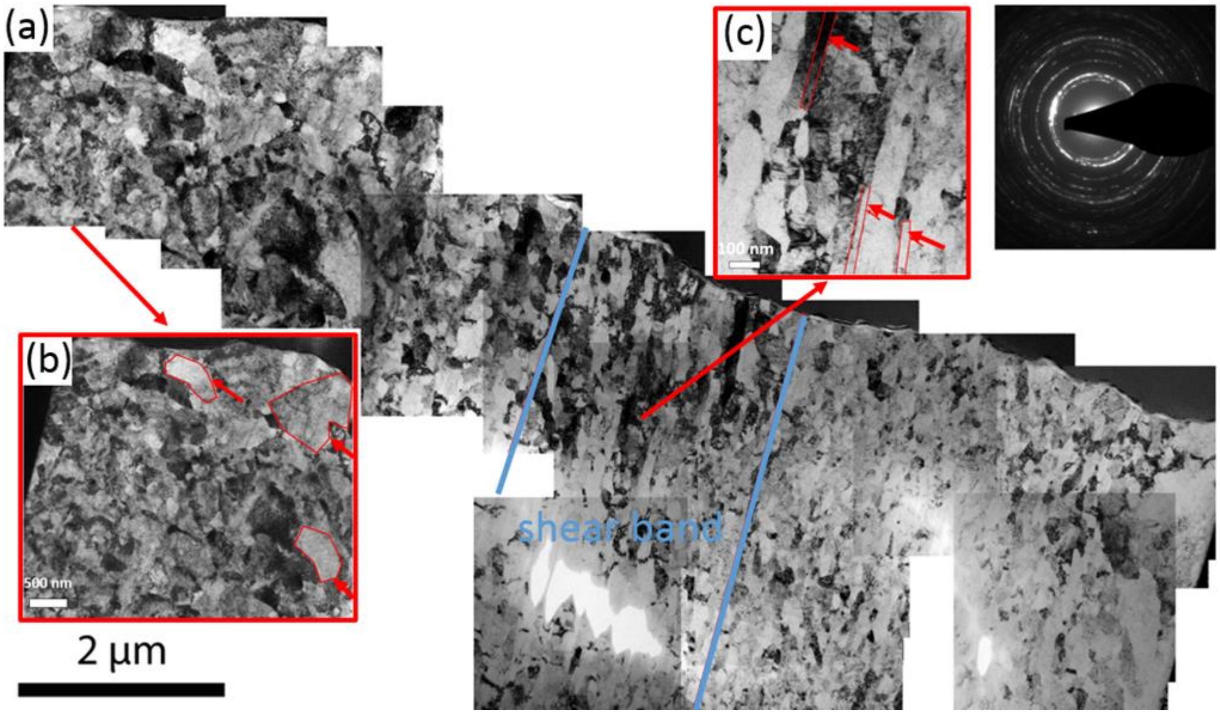

Figure 4.3.5.4. TEM images of the microstructure (a) of the sample B (perpendicular to shear band), (b) near the shear band, (c) inside the shear band. (Shear direction nominally perpendicular to the foil; misorientation is possible).

TEM was carried out on the samples B and C to study microstructural features of the shear bands formed at room temperature for UFG 100 nm titanium. Fig. 4.3.5.4(a) provides an overall view of sample B (the shear band lies between the blue lines). The microstructures within and outside the shear band are quite distinct. The continuous sharp diffraction ring pattern indicates that the microstructure is randomly oriented, with no strong texture. Lins *et al*. [96] showed that the shear band in an interstitial-free steel displays a strong heterogeneous character from the center of the shear band to its edges. Fig. 4.3.5.4(b) shows both the nominally equiaxed UFG matrix and abnormally grown coarse grains with low dislocation density (see arrow). The abnormal grain growth is due to the temperature rise near and in the shear band and the thermal instability of the UFG titanium. The elongated grains, which were less severely deformed, were formed along the edge of the shear band. Fig. 4.3.5.4(c) shows a mixture of elongated and equiaxed grains inside the shear band. The grain boundaries are clearly delineated. The thickness of the elongated grains varies, which may be due to the inhomogeneous shear stress distribution inside the shear band. Some very narrow elongated grains (see arrow) are formed, which may further break down to form nanograins upon further deformation. This evolution process was described in several studies [11, 13].

Fig. 4.3.5.5(a) shows the microstructure of sample C. It shows the randomly distributed nanostructured grains. The dark field image of Fig. 4.3.5.5(b) shows that the nanograins tend to flow in one direction (shown by arrows) under shear deformation inside the shear band. Fig. 4.3.5.5(c) highlights a high magnification image of a nanograin with grain size ~40 nm, corresponding to the breakdown of the narrow and elongated grains as detailed in Fig. 4.3.5.5(c).

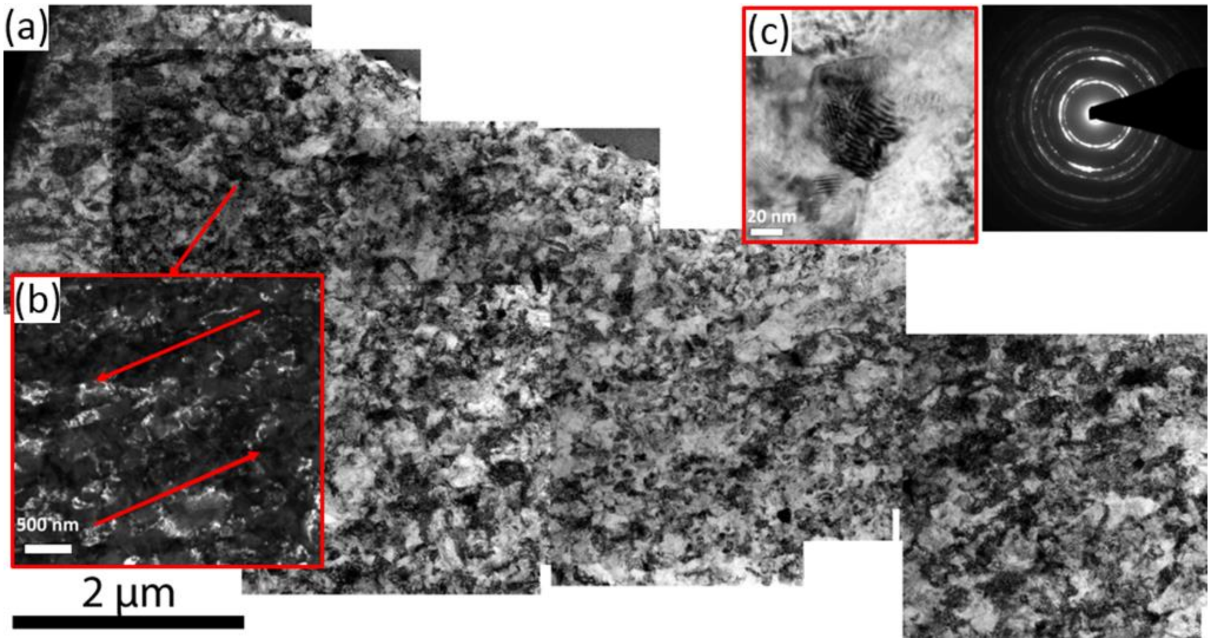

Figure 4.3.5.5. TEM images of (a) the microstructure of the sample C (inside shear band), (b) the dark-field microstructure, (c) the equiaxed grains. (Shear direction indicated in dark-field micrograph (b)).

In Fig. 4.3.5.4, the FIB cutting direction is perpendicular to the shear band; therefore, the sample is only partially in the shear band (shown between two blue lines). The matrix of UFG titanium can also be seen. Both elongated UFG grains and recrystallized nanosized grains can be observed. Fig. 4.3.5.5, on the other hand, only shows the microstructure right in the middle of the shear band, since the FIB cutting direction is parallel to the shear band. Only fully recrystallized nanograins are seen. The temperature rise in the middle of the shear band is higher than that at its edges, providing more thermal energy to form recrystallized equiaxed nanograins. Different applied shear strains and inhomogeneous temperature distribution occur during the formation of the shear band, as demonstrated by finite element simulation of formation and failure of the shear band [97]. This leads to different shear direction and different microstructures in different regions as shown in Figs. 4.3.5.4 and 4.3.5.5. As indicated by the TEM diffraction ring patterns in Figs.

4.3.5.4 and 4.3.5.5, the recrystallized grains are nearly randomly distributed, and do not show strong texture inside the shear band.

4.3.6. Cooling of the shear bands

It is important to establish the cooling times for the shear bands with different thickness. Assuming a constant rate of heat generation in the thin shearing zone, then the solution of the heat equation for the hat-shaped specimens can be reduced to [98]:

$$\rho C_p \frac{\partial T}{\partial t} = \lambda \nabla^2 T \tag{4.2.4}$$

where T is temperature, C_P is specific heat capacity and λ is thermal conductivity. Since the shear band is very narrow and axially symmetric, one-dimensional calculation that considers a shear zone is in an infinite medium can be carried out. Assuming a constant rate of heat generation in the thin shearing zone, then the solution of the heat equation for the hat-shaped specimen can be reduced to [98]:

$$T(x,t) = \frac{\delta(T_m - T_0)}{\sqrt{4\pi\chi t}} e^{-(x-R_i)^2/4\chi t} \qquad (R_i - \frac{\delta}{2} < x < R_i + \frac{\delta}{2}) \tag{4.2.5}$$

where T_0 and T_m are the initial temperature and the maximum temperature within the shear band after the deformation; t, δ and R_i are the cooling time, the width of shear bands and the distance from the center of shear band to the center of the hat-shaped specimen; χ is the heat diffusivity. $\Delta T = T_m - T_0 = 500\,\text{K}$ is assumed for each shear band and x is equal to R_i in the middle of shear band. $\chi_{T=293K} = \lambda_{500nmTi} / (\rho \cdot C_{p(T=293K)}) = 5.17 \times 10^{-6}$ m^2/s and $\chi_{T=173K} = \lambda_{500nmTi} / (\rho \cdot C_{p(173K)}) = 6.41 \times 10^{-6}$ m^2/s were built for 500 nm titanium.

$\chi_{T=293K} = \lambda_{100nmTi} / (\rho \cdot C_{p(T=293K)}) = 2.22 \times 10^{-6}$, $\chi_{T=173K} = \lambda_{100nmTi} / (\rho \cdot C_{p(T=173K)}) = 1.75 \times 10^{-6}$ and $\chi_{T=77K} = \lambda_{100nmTi} / (\rho \cdot C_{p(T=77K)}) = 5.5 \times 10^{-6}$ were built for 100 nm titanium. The fast cooling-rate of shear bands at room and low temperatures shown in Fig. 4.3.6 is responsible for retaining the ultrafine- and nano- grain size inside the shear band and not allowing the grains to grow during cooling. Although there are differences among the different initial conditions, the cooling to ambient temperature occurs within 20 μs for most specimens. These calculations confirm that the grains inside the shear band are formed by the rotational dynamic recrystallization process, and not by static migrational recrystallization during cooling.

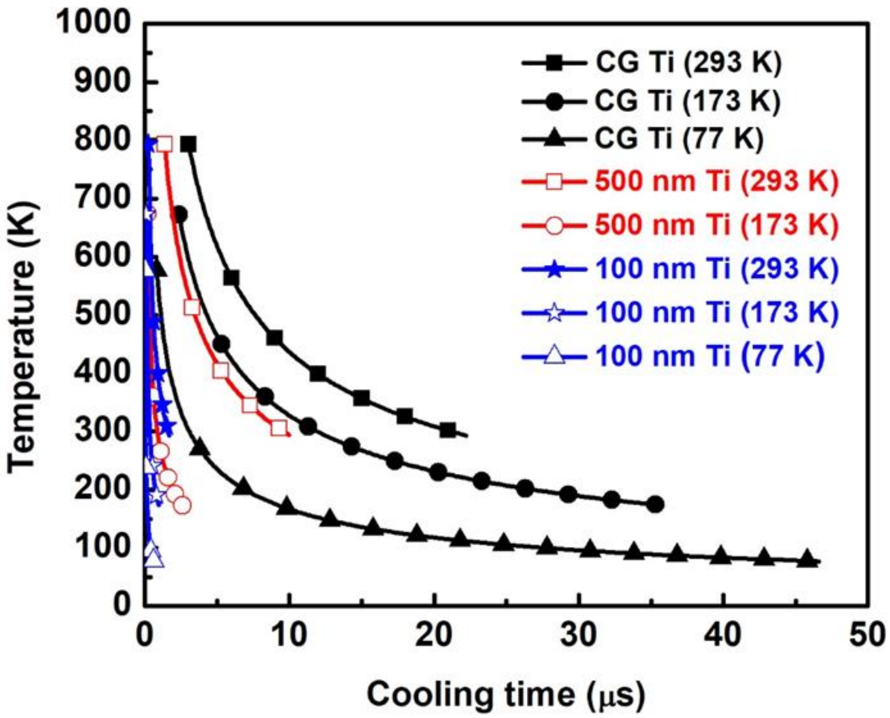

Figure 4.3.6. Temperature in the middle of the shear bands as a function of cooling time for CG and UFG titanium.

4.3.7 Fracture of the shear band

The formation of an ASB precedes the failure mechanisms by void and crack formation. Xue *et al.* [99] observed both elongated and equiaxed voids that preceded failure of the shear band. Both morphologies are observed inside the shear bands, depending on how the separation of the two parts occurs. If only tension is applied, the two parts separate by forming voids in the shear band; these voids grow until their diameters reach the band thickness. The elongated dimples are a characteristic of shear failure, due to elongated and coalesced voids. The formation of elongated voids when the failure has a strong shear component is explained by Meyers and Chawla [70].

Fig. 4.3.7(a) shows a microvoid in sample with maximum displacement of 1 mm between the shear band and its surrounding; this indicates that microvoids can be nucleated at the edge of the shear band. Fig. 4.3.7(b) shows the ductile ligaments (see arrow) along the shear band in sample. The ductile ligaments indicate the coalescence of microvoids. The shear failure surface of the sample with maximum displacement of 1.15 mm was observed by SEM shown in Fig. 4.3.7(c). The fracture surface contains both ductile features such as dimples, and brittle features such as cleavage patterns, indicating that brittle and ductile fracture modes might take place simultaneously. A microstructure consisting of elongated dimples, shows similar characteristics to other HCP materials, such as Re, Hf and Ti-6Al-4V alloy [100]. The coalescence of voids, leading to cracks, was observed along the shear band in rhenium in high-strain-rate deformation [101]. Similar elongated shear dimples were observed in the fracture surface of polycrystalline hafnium [102].

A schematic illustration of ASB fracture is shown in Fig. 4.3.7(d). Microvoids can be nucleated inside shear band or at its edges, followed by their coalescence and the formation of microcracks; this leads to the formation of a mixture of ductile and brittle failure. The formation of cracks between sheets of dimples along the shear band can lead to more rapid fracture of the ASB and a more brittle fracture.

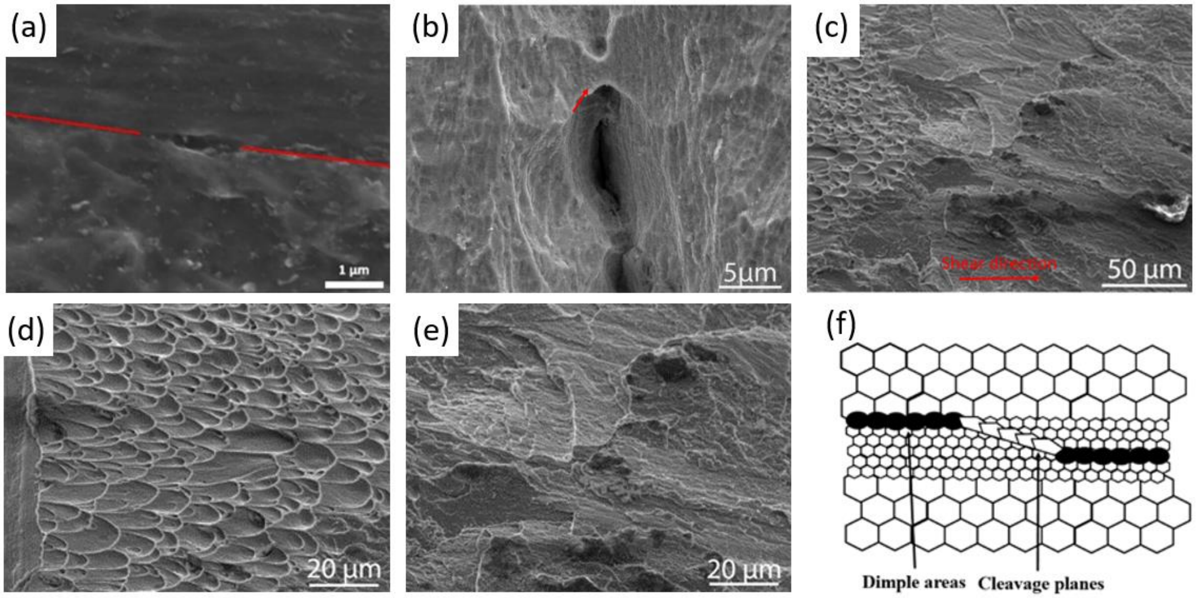

Figure 4.3.7. SEM images of the sample with max-displacement 1 mm showing (a) dimples along the shear band, (b) alignment between dimples and fracture surface, and of the sample with max-displacement 1.15 mm (c) ductile areas and cleavage plane, (d) dimples areas, (e) cleavage planes. (f) Schematic illustration of ASB failure of UFG 500 nm titanium.

4.4 Discussion

4.4.1 Width of shear band

The shear bands for CG titanium are shown in Figs. 4.4.1.1(a1,b1,c1). It decreases from ~30 μm at 293 K to ~18 μm at 77 K. In comparison, the shear-band width decreases from ~15 μm at 293 K in Fig. 4.4.1.1(a2) to ~5 μm at 173 K in Fig. 4.4.1.1(c2) for UFG 500 nm titanium. Shear band bifurcation (within the red dashed lines) was observed at low temperature as shown in Fig. 4.4.1.1(b2). Xue *et al.* [99] observed this important feature of shear bands in the exploding cylinder geometry, which was geometrically necessary under high strain-rate deformation. For the UFG 500 nm titanium, the width of the shear band is slightly lower at room temperature in comparison with CG titanium as illustrated in Fig. 4.4.1.2. In contrast, the width decreases much more significantly at low temperatures. In addition, there is an obvious drop in the width of shear bands for UFG 100 nm titanium as shown in Figs. 4.4.1.1(a3,b3,c3). It decreases in a significant way from 4 to 1 μm as shown in Fig. 4.4.1.1(c3). Two theories were proposed to predict the shear-band width; they are used here to evaluate the effects of temperature and grain size.

The Bai-Dodd equation [103] predicts the width, *δ*, of the shear bands as:

$$\delta = 2\left(\frac{\lambda T}{\tau \dot{\gamma}}\right)^{1/2} \tag{4.4.1.1}$$

where λ is the thermal conductivity; T, $\dot{\gamma} = 10^5\ \mathrm{s}^{-1}$ and τ are the absolute temperature, shear strain-rate and shear stress inside the shear band. Alternatively, Grady [40,41] found that the shear-band thickness at minimum dissipation corresponded to a maximum shear-band growth rate. He derived the following expression of the width of shear band, incorporating the thermal softening parameter $\alpha_{CG} = \frac{1}{\sigma_y}\frac{\partial \sigma}{\partial T}$ [104]:

$$\delta = \left(\frac{16\ \lambda^3}{\tau^3 \alpha^2\ C_p \dot{\gamma}}\right)^{1/4} \tag{4.4.1.2}$$

where ρ is the density, C_p is the specific heat capacity, and $\dot{\gamma} = 10^5$ s^{-1} [83]. These two classic models predict a reduced width δ with increasing strength, strain-rate, thermal softening, specific heat capacity, and decreasing thermal conductivity. The sub-sections below show how these parameters vary for the materials under study. They are affected by grain size and temperature.

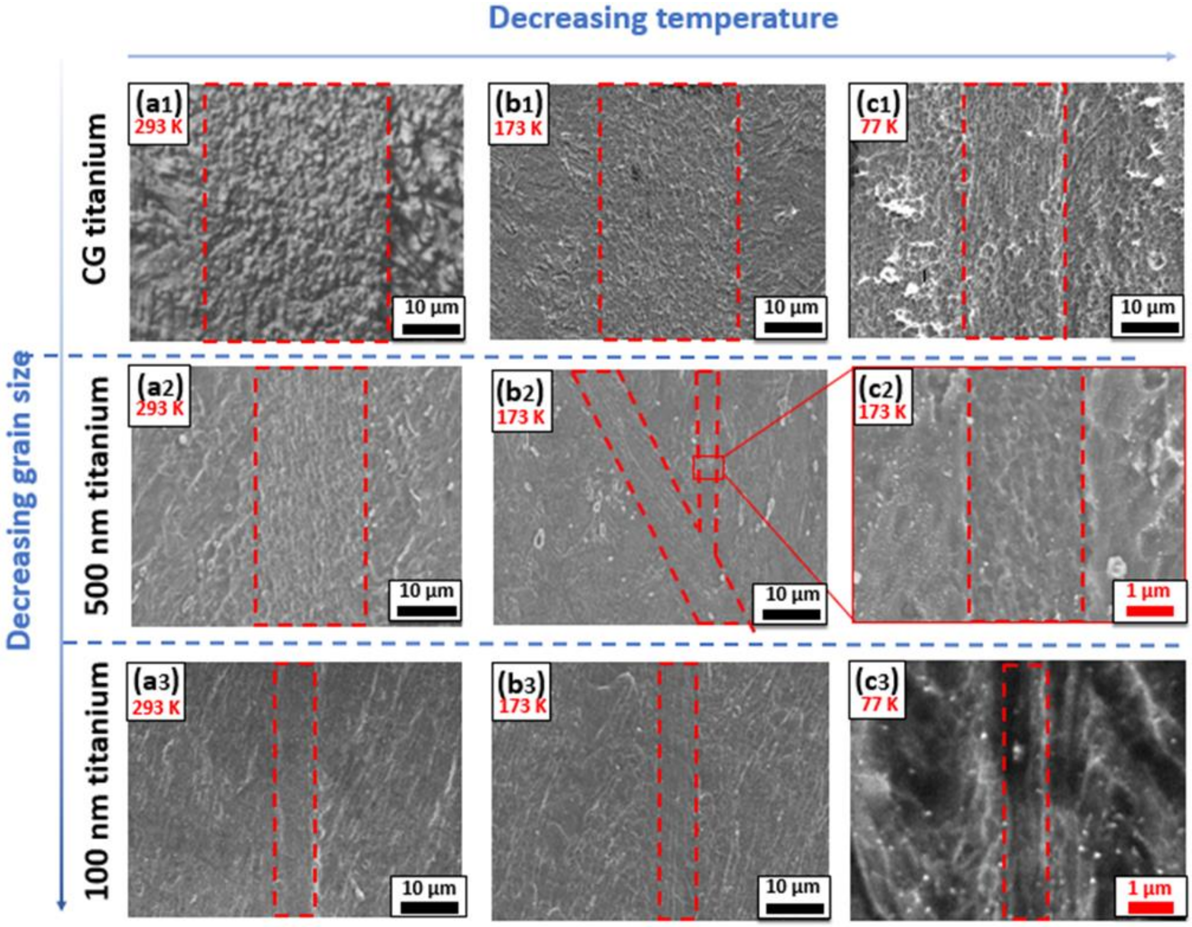

Figure 4.4.1.1. SEM images showing the width of shear bands in different titanium at different temperatures.

4.4.1.1 effect of thermal conductivity.

Thermal conduction in solids includes electron conduction and phonon condition. In general, in pure metals, the main contribution to thermal conductivity comes from electrons [105, 106]. The measured electrical resistivity of the UFG 500 nm titanium disks was $0.59 \pm 0.01\, \mu\Omega$. Thus, applying Wiedemann-Franze law, the electronic thermal conductivity of UFG pure titanium was reduced from 22 W.m^{-1}.K^{-1} [5] to 12.12 W.m^{-1}.K^{-1} (~45% deduction) as shown in Fig. 4.4.1.2.

Guo *et al.* [107] examined the thermal conductivity of nanostructured titanium by scanning thermal microscopy that allowed it to be mapped down to the submicron scale. The analysis showed that the thermal conductivity decreased to 5.2 W.m^{-1}.K^{-1} for nanostructured Ti from 22 W.m^{-1}.K^{-1} for coarse-grained Ti. A large volume fraction of grain boundaries and high density of dislocations within the nanograins act as barriers for electron motion. In addition, it was reported that the thermal conductivity of titanium did not change significantly when decreasing the temperature to 77 K [108].

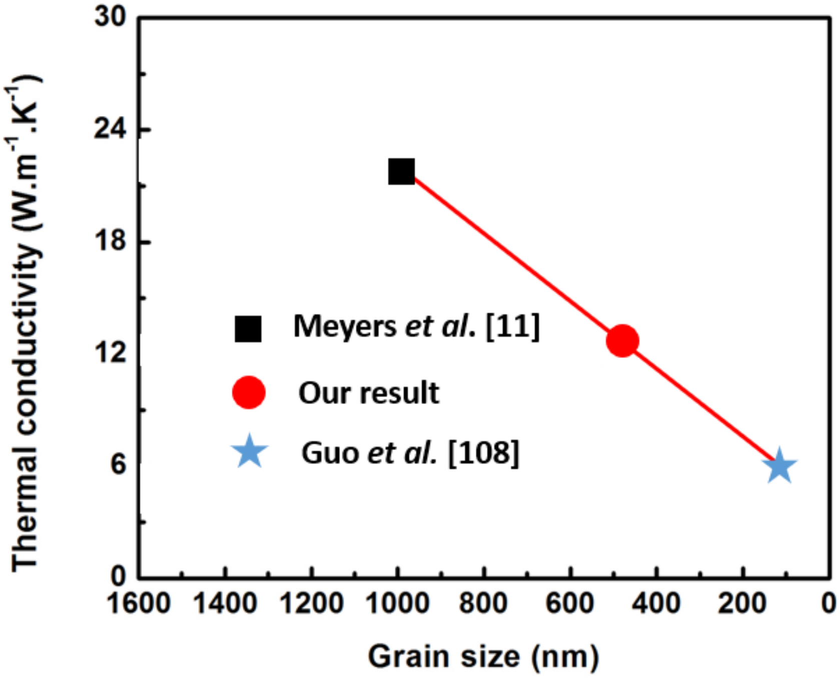

Figure 4.4.1.2. Relationship of the thermal conductivity of titanium with different grain sizes [11,108].

4.4.1.2 Effect of heat capacity.

Heat capacity of metals is contributed by lattice vibration. Debye [109] assumed that the range of frequencies of vibration available to the oscillators was the same as that available to the elastic vibrations in a continuous solid. The lower limit of the wavelengths of these vibrations was determined by the interatomic distances in the solid. He obtained the following expression for the heat capacity of solids under constant volume:

$$C = 9R\left(\frac{T}{\theta_D}\right)^3 \int_0^{\theta_D/T} \frac{x^4 e^{-x}}{(1-e^{-x})^2} dx \tag{4.1.1.3}$$

where $x = h\upsilon / kT$ (h is the Planck's constant), R = 8.314 J/(K·mol) and the Debye frequency is v_D= 8.75×1012 s-1. $\theta_D = hv_D / k$ = 420 K is the characteristic Debye temperature for titanium [110]. Fig. 4.4.1.3 shows that the specific heat capacity for both CG and UFG titanium decreases with decreasing temperature due to the lower population of thermally excited phonon modes [111]. Thus, $C_{T=293K} = 520$ J/(kg·K) decreases to a very low value of $C_{T=77K} = 210$ J/(kg·K). It predicts a narrower region at cryogenic temperatures. Thus, $C_{T=293K} = 520$ J/(kg·K) decreases to a much lower value of $C_{T=77K} = 210$ J/(kg·K) at 77 K. The decrease of specific heat capacity will cause a more rapid increase of temperature for the same deformation energy and contribute to a narrower shear region.

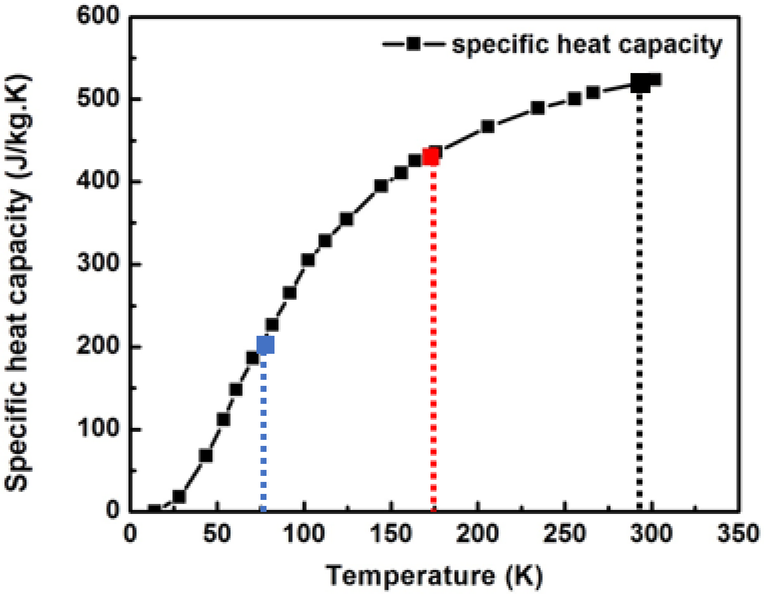

Figure 4.4.1.3. Specific heat capacity of titanium.

4.4.1.3 Effect of thermal softening.

The thermal softening parameter was defined as:

$$\alpha = -\frac{1}{\sigma_y}\left(\frac{\partial \sigma}{\partial T}\right)_{\gamma,\dot{\gamma}}, \tag{4.4.1.4}$$

as described. Fig. 4.4.1.4 describes the strain-softening effect of CG and UFG titanium [112]. With the increase of temperature, the yield stress decreases. To a first approximation, the strain softening of UFG 100 nm titanium ($\alpha_{UFG} \approx 0.002$) is larger than that of CG Ti ($\alpha_{CG} \approx 0.001$) at 77 K [51].

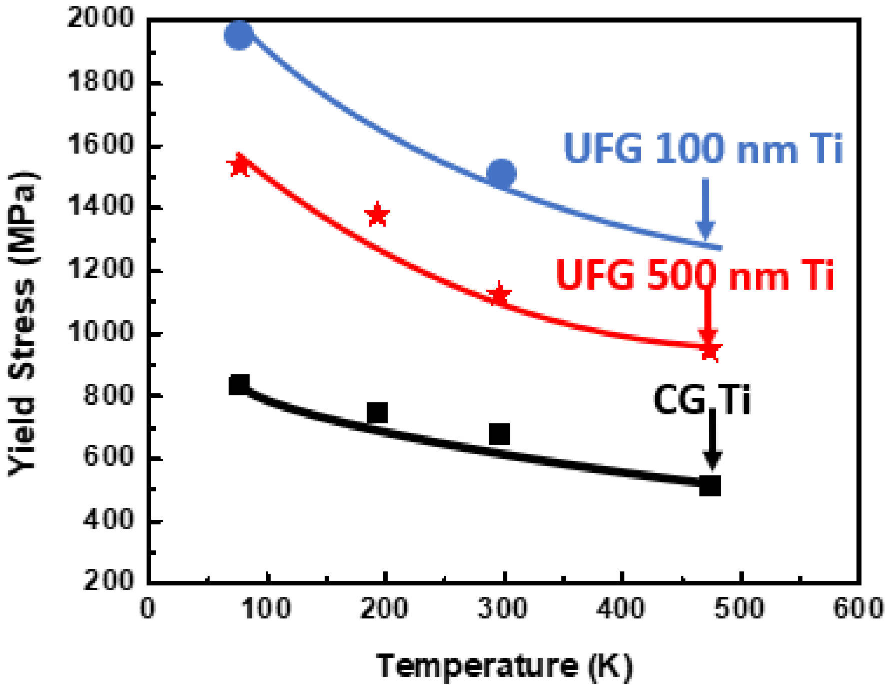

Figure. 4.4.1.4. Thermal softening effect of CG and UFG titanium [113].

4.4.1.4 Combined effects on shear-band width

Here we discuss these three effects and apply them to the Grady-Kipp and Bai-Dodd Eqns. First, the reduction of the thermal conductivity of nanostructured titanium at room temperature as shown in Fig. 4.1.1.2, leading to the decrease of the width of shear band from equation 4.4.1.1. It was also reported that the thermal conductivity of titanium did not change significantly when decreasing the temperature to 77 K. The lower specific heat capacity at cryogenic temperature transfers more heat under the same input of plastic work, and low thermal conductivity provides the material a slow diffusion rate of heat to the surroundings. In addition, the increase of the thermal softening parameter contributes to the narrower width of shear band according to equation 4.4.1.2. Also, increased thermal softening and decreased strain hardening can make UFG material more prone to shear localization. Thus, the higher thermal softening effect of UFG titanium at 77 K as shown in Fig. 4.4.1.5 also contributes to the decrease of width of shear bands.

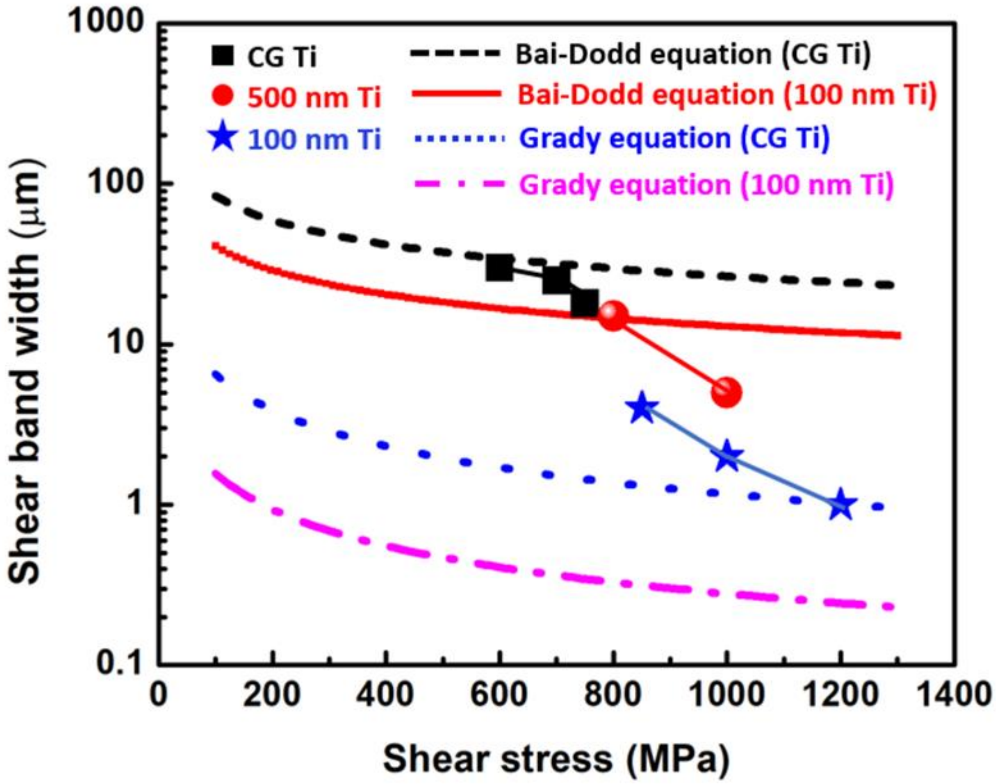

Figure 4.4.1.5. Width of the shear band in pure titanium for different grain sizes and temperatures. The full lines represented Bai-Dodd [104] and Grady equation [105] predictions applied for CG and UFG 100 nm titanium.

4.4.2 Dislocation evolution during deformation for CG and UFG 500 nm titanium

Meyers *et al* [13], and Hines and Vecchio [38, 39] demonstrated that migrational recrystallization could not account for the grains generated inside the shear band and proposed complementary rotational recrystallization mechanisms. Whereas Meyers *et al.* [13] used a dislocation energetics approach, Hines and Vecchio [38] and Hines *et al.* [39] implemented a continuum mechanics analysis. The sequence of events shown in Fig. 4.4.2.1 leading to the formation of equiaxed nanograins is expected to occur. The formation of elongated grains is due to the dislocation motion instead of dynamic recrystallization. In essence, the equiaxed grains shown in Fig. 4.4.2.1(a) are deformed into elongated grains as shown in Fig. 4.4.2.1(b). Fig. 4.4.2.1(c) shows that dislocations are accumulated in subgrain boundaries inside the elongated grains. The elongated grains then break up to finer subgrains. Once the elongated subgrains are achieved, further break up by dislocation generated at the grain boundaries is due to geometrically-necessary dislocations required to accommodate further plastic deformation. The relaxation of elongated subgrains into an equiaxed crystalline structure can occur by minor rotations of the grain boundaries in Fig. 4.4.2.1(d).

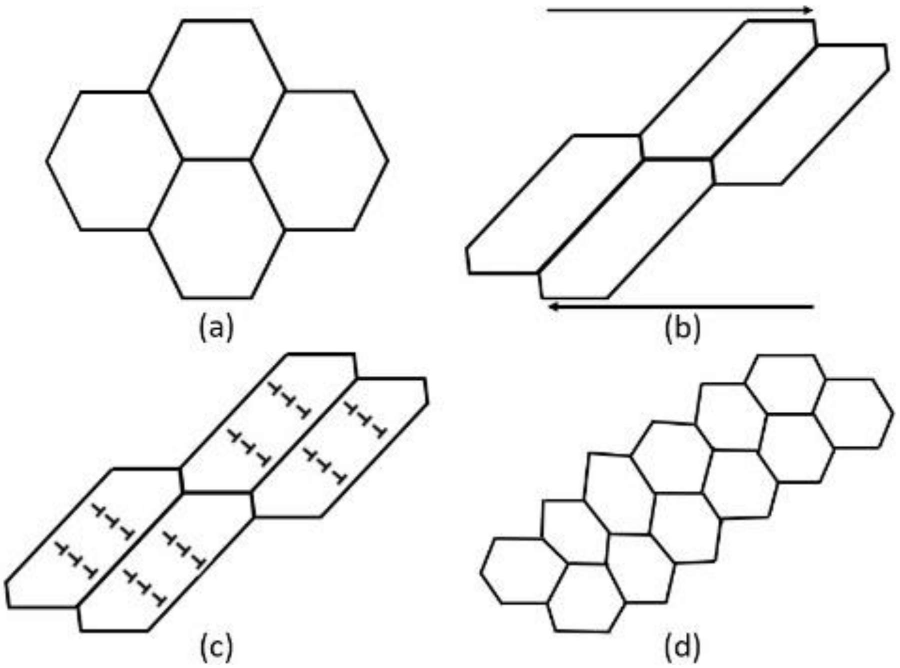

Figure 4.4.2.1. Schematic illustration of microstructural evolution inside the shear band according to the rotational dynamic recrystallization mechanism: (a) randomly distributed equiaxed grains; (b) formation of elongated grains through plastic deformation (shear direction indicated by arrows); (c) dislocations accumulation forming subgrain boundaries; (d) breakup of elongated grains, reorientation of grain boundaries and formation of equiaxed nanosized grains.

According to the rotational dynamic recrystallization mechanism, formation of a new grain requires local grain-boundary segments to tilt about 30° during the last stage of the deformation process (from Figs. 4.4.2.1(c) to 4.4.2.1(d)) [13]. The time needed for these processes is given by:

$$t = \frac{LkTf(\theta)}{4\delta\eta D_{b0}\exp(-Q_b / RT)} \tag{4.4.2.1}$$

where t is time, L is the average subgrain diameter, δ is grain-boundary thickness, η is the grain boundary energy, D_{b0} is a constant related to grain boundary diffusion, Q_b denotes the activation energy for grain boundary diffusion, θ is the subgrain misorientation, and $f(\theta)$ can be described as follows:

$$f(\theta) = \frac{3\tan(\theta) - 2\cos(\theta)}{3 - 6\sin(\theta)} + \frac{2}{3} - \frac{4\sqrt{3}}{9}\ln\frac{2+\sqrt{3}}{2-\sqrt{3}} + \frac{4\sqrt{3}}{9}\ln\frac{\tan(\theta) - 2 - \sqrt{3}}{\tan(\theta) - 2 + \sqrt{3}} \tag{4.4.2.2}$$

For UFG titanium, $\delta = 1.5\times10^{-9}$ m, $\eta = 0.675$ J/m^2, $D_{b0} = 1.4 \times 10^{-3}$ m^2/s, $Q_b = 151$ kJ/mol, $k = 1.38\times10^{-23}$ J/K, $R = 8.314$ J/(K·mol), and $T = 900$ K [113-115]. The kinetic curves for the rotational dynamic recrystallization mechanism in a shear band can be obtained by incorporating the parameters into equations 4.4.2.1 and 4.4.2.2, as shown in Figs. 4.4.2.2(a) and (b). A decrease in the activation energy for grain-boundary diffusion [84] and increase of grain-boundary thickness accelerate the formation of equiaxed grains by the grain-boundary diffusion process. In Fig. 4.4.2.2(a), the nanograin size, L, is varied from 40 nm to 100 nm at $T = 900$ K $\approx 0.46T_m$. Fig. 4.4.2.2(b) indicates that the increase of temperature helps the grain boundary diffusion process. The rate of rotation decreases with increasing angle and asymptotically approaches 30° as $t \to \infty$. The calculations predict significant rotations of the boundary within the deformation time. Thus, rotational recrystallization can also take place during plastic deformation (2×10^{-4} s). This does not exclude the possibility of further coalescence of nanograins inside the shear band. Since the deformation mechanisms in nanocrystalline titanium are different from the ones in coarse-grained titanium, the discussion below provides deeper insight into the formation of nanograins inside the shear band.

The driving force for the migration of a grain boundary can be simply estimated by equating the force acting on a curved segment of the boundary, *dS*, due to the grain-boundary energy $\eta = 0.675$ J/m^2 [115]. Assuming a two-dimensional geometry, for simplicity, the total force acting on the grain boundary in the y-direction (seen in Fig. 4.4.2.2(c)) is:

$$F = 2\eta \sin\frac{d\theta}{2} \approx \eta d\theta \tag{4.4.2.3}$$

Therefore,

$$force / area = \frac{\eta d\theta}{R d\theta} \approx \eta d\theta \tag{4.4.2.4}$$

The velocity of the grain boundary is proportional to the force acting on the segment *dS*:

$$v \propto \frac{\eta}{R} = M\,\frac{\eta}{R} \tag{4.4.2.5}$$

where *M*, the grain boundary mobility has an Arrhenius-type temperature dependence [116]:

$$M = M_0 \exp\left(\frac{-Q_m}{RT}\right) \tag{4.4.2.6}$$

For titanium [117], $M_0 = 4.3 \times 10^{-6}$ m^4/J/s and Q_m =179 KJ/mole.

Grain-boundary velocity is plotted against the grain size at 900 K in Fig. 4.4.2.2(d). For a grain size of 40 nm (v = 6 nm/s), a grain boundary movement of 6 nm at 900 K can be expected in 1 s. This cannot be sufficient to reorganize the deformed grain configuration. For a shear band, the cooling takes place in time scales of fractions of milliseconds. For 0.2 ms and a grain size of

40 nm, a displacement of 1.2×10^{-3} nm is obtained. Thus, the calculation shows that no significant grain growth by grain-boundary migration takes place after a nanocrystalline size of 40 nm is reached. However, growth of equiaxed nanograins might occur by grain rotation during shear deformation inside the band.

Mishra *et al.* [53] reported that the similarity of structure evolution in SPD and shear-band formation is related to the hypothesis that both processes are regulated by a similar mechanism with two significant differences: the time is shorter and temperature is higher in shear-band formation. The Zener-Hollomon (ZH) parameter is defined as [118]:

$$Z = \dot{\varepsilon} \exp\left(\frac{-Q_d}{RT} \right) \tag{4.4.2.7}$$

where R is the gas constant and Q_d is the related activation energy for deformation. At a constant Z, the resultant grain size in SPD and dynamic deformation is the same; this is clear from the opposing effects of $\dot{\varepsilon}$ and T in equation 4.1.15. Li *et al.* [119] reported that finer copper grains were formed in deformation at a temperature of 77 K at high strain rates, on the order of 10^2 s^{-1}, than under quasi-static conditions. This increased the ZH parameter of the process and consequently decreased the resulting grain size. Extending the proposal of Mishra *et al.* [53], they reported that the recrystallized grain size was inversely related to the ZH parameter.

In fact, a different grain refinement mechanism inside the shear band for nanocrystalline titanium may operate at the high Zener-Hollomon parameter deformation conditions. For nanocrystalline titanium, as grain size decreases, an increasing amount of grain-boundary sliding can occur. Using MD simulation, Schiøtz *et al.* [120] reported that grain-boundary sliding dominates the plastic deformation instead of dislocation motion, due to the larger volume fraction of grain-boundaries when the grain size is under 10 nm. Thus, with further increase of the ZH parameter, the grain size inside the shear band may reach a steady-state value of several nanometers, where most plastic deformation is due to grain-boundary sliding instead of dislocation motion. The ZH parameter was applied to predict critical dislocation density and recrystallized grain size in the following discussion.

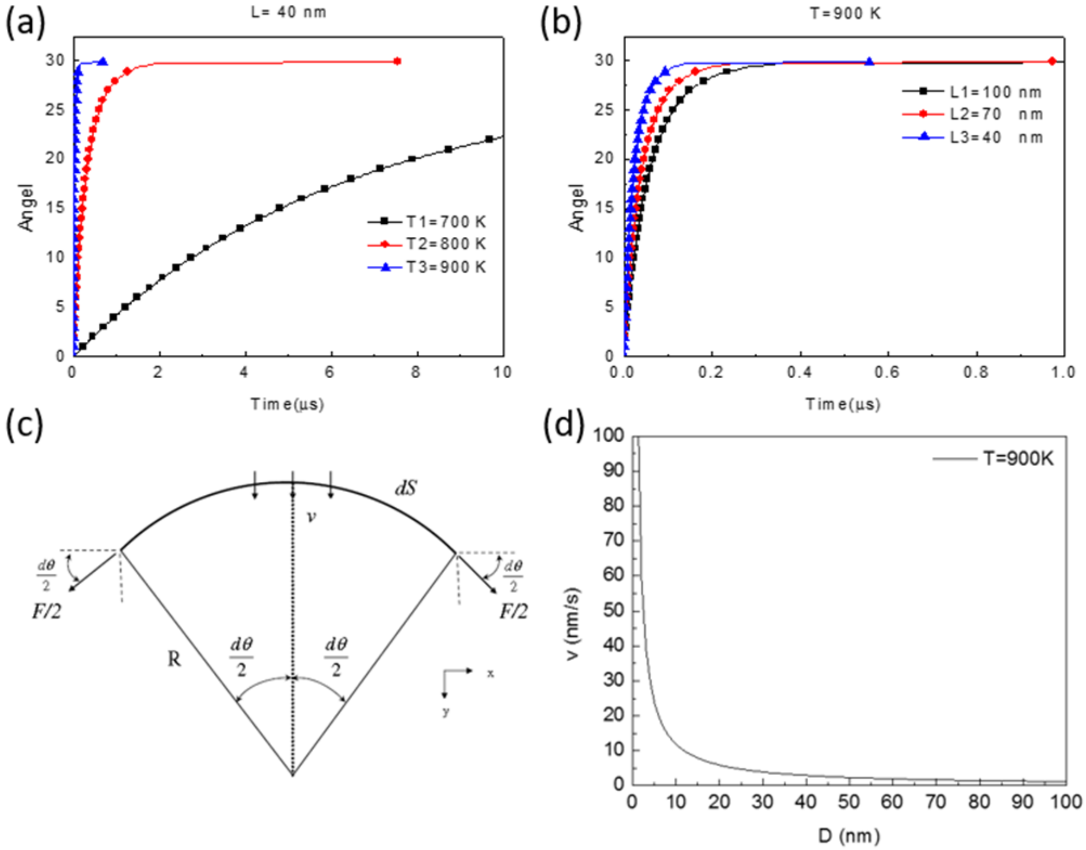

Figure 4.4.2.2. Angle of rotation of grain boundary during the deformation process as a function of time for (a) different grain sizes (40, 70, and 100 nm) at T=900 K and (b) different temperatures (700, 800, and 900 K) for grain size L=40 nm. (c) Schematic showing force acting on the grain boundary with radius of curvature R. (d) Grain-boundary velocity as a function of radius R typical of shear band deformation process at 900 K.

The evolution of dislocation density with plastic deformation is the result of the combined effects of dislocation generation and annihilation [121] :

$$\dot{\rho} = \dot{\rho}_{gen} - \dot{\rho}_{ann} \tag{4.4.2.8}$$

where $\dot{\rho}_{gen}$ and $\dot{\rho}_{ann}$ represent dislocation generation and annihilation rates, respectively.

Mecking and Kocks [122] proposed that the evolution of the dislocation density during plastic deformation is due to the competition between cutting forest dislocations and dynamic recovery of dislocations, and obtained the following expression:

$$\frac{d\rho}{d\gamma} = k_h\sqrt{\rho} - f_s\rho \tag{4.4.2.9}$$

where k_h is a hardening factor and f_s is a softening parameter. The cutting of forest dislocations leads to strain hardening and the annihilation of dislocations by dynamic recovery results in strain softening. Thus, it is possible to estimate the dislocation density at the recrystallization temperature (~0.4 T_m) , often considered as required for shear localization.

Meyers *et al.* [12] proposed the critical dislocation density for shear localization, where the strain energy for randomly distributed dislocations and ellipsoid configuration dislocations (forming subgrains) is equal. It is possible to estimate the dislocation density at the recrystallized temperature (~0.4 T_m) for shear localization. The energy of randomly distributed dislocations is:

$$E_1 = \rho_d\left(\frac{\varpi G b^2}{4\pi}\right)\ln\left(\frac{\alpha_0}{2b\rho_d^{1/2}}\right) \tag{4.4.2.10}$$

where ϖ is the constant depending on the character of the dislocation, G is the shear modulus, b is Burgers' vector, α_0 is a constant which accounts the core energy of the dislocation, and ρ is the dislocation density, which can be estimated throughout the plastic deformation process from the Kocks-Mecking equation. The energy of low-angle grain boundary arrays of the same density, arranged in ellipsoidal subgrain, is:

$$E_2 = \rho_d \left(\frac{\varpi G b^2}{4\pi} \right) \ln \left[\frac{e\alpha_0}{4\pi b} \left(\frac{S}{V} \right) \frac{1}{\rho_d} \right] \tag{4.4.2.11}$$

where S and V are surface area and volume of ellipsoid. At a critical dislocation density or temperature, the structure transforms from homogeneous to cellular. Thus, the critical dislocation density obtained from $E_1 = E_2$ can be used to calculate the width of ellipsoid subgrains, W:

$$W = \frac{3e\rho^{-1/2}}{4} \quad . \tag{4.4.2.12}$$

Zener-Hollomon parameter [118], Z, was initially used to describe the relationship between flow stress and strain-rates and temperature as mentioned. The strain-rate inside the shear band is about 10^5 s^{-1}, the activation energy for deformation is 150 kJ and the temperature rise inside the shear band is assumed to be 500 K, the recrystallized temperature for Ti. Mishra *et al.* [53], Derby [123] and Li *et al.* [119] found that the recrystallized grain size is proportional to the value ln Z:

$$d_R (\ln Z)^B = A \tag{4.4.2.13}$$

By incorporating eqn. (4.4.2.13) to eqn. (4.4.2.12) and assuming the width of the ellipsoid equal to the size of recrystallized grains (W=d_R), one can obtain the critical dislocation density for shear localization for titanium:

$$\rho_c = \left[\frac{3e}{4} \left(\frac{(\ln Z)^B}{A} \right) \right]^2 \tag{4.4.2.14}$$

where the fitting parameters A and B for CG and UFG 500 nm titanium are summarized in the Table 4.4.2. Figs. 4.4.2.10(b1,b2) show the predicted recrystallized grain size d_R and the critical dislocation density for shear localization for CG and UFG 500 nm titanium under different (ln Z) values. Once the critical dislocation is established, by assuming an initial dislocation density of

$6*10^{12}$ m^{-2}, one can obtain the parameters k_h and f_s through the classic Taylor equation ($\tau = \tau_0 + \alpha_0 Gb\sqrt{\rho}$, where τ_0 is the yield shear stress, α_0 is a constant taken as 0.09, G=45 GPa is the shear modulus, and b is the Burgers vector). Table 4.4.2 shows other fitting parameters for the Kocks-Mecking theory. Figs. 4.4.2.10(a1,a2) show that the rate of change of dislocation density first increases and then decreases gradually to zero.

Once the subgrain configuration forms with a width (W), it tends to break into segments which rotate to accommodating further deformation. Assuming static migrational recrystallization during the cooling of the shear band, Meyers *et al.* [13] demonstrated that the recrystallized grain size of CG titanium inside the shear band could not reach the nanocrystalline region assuming static migrational recrystallization during the cooling of the shear band, thus demonstrating that the migrational recrystallization mechanism can't account for the formation of recrystallized grains inside the shear band. The temperature rise inside the shear bands can rise to the recrystallization temperature (between 0.4 T_m–0.5 T_m) for both CG and UFG titanium. Once the elongated subgrains are achieved, they further break up into subgrains. According to the rotational dynamic recrystallization mechanism, the formation of a new equiaxed grain requires local grain-boundary segments to tilt about 30° within the deformation process [13]. The time needed for these processes can be expressed by Equation 4.4.2.1

For UFG titanium, the parameters for equation 4.4.2.2. [83] are the same as mentioned. The kinetic curves for the rotational dynamic recrystallization mechanism in a shear band can be obtained by integrating the parameters into equations 4.4.2.1 and 4.4.2.2. The results show that it can rotates 30° within 20 μs for a grain size of 200 nm. The rate of rotation increases with decreasing grain size.

Table 4.4.2. Constants for the Kocks-Mecking model and critical dislocation density for shear localization.

Parameters	k_{forest}	$f_{recovery}$	*Critical dislocation density*
CG Ti (173 K)	**3.63*10^8**	**33.8**	**1.15*10^14**
CG Ti (77 K)	**3.81*10^8**	**26.2**	**2.12*10^14**
500 nm Ti (293 K)	**4.01*10^8**	**35.4**	**1.28*10^14**
500 nm Ti (173 K)	**4.50*10^8**	**26.5**	**2.89*10^14**

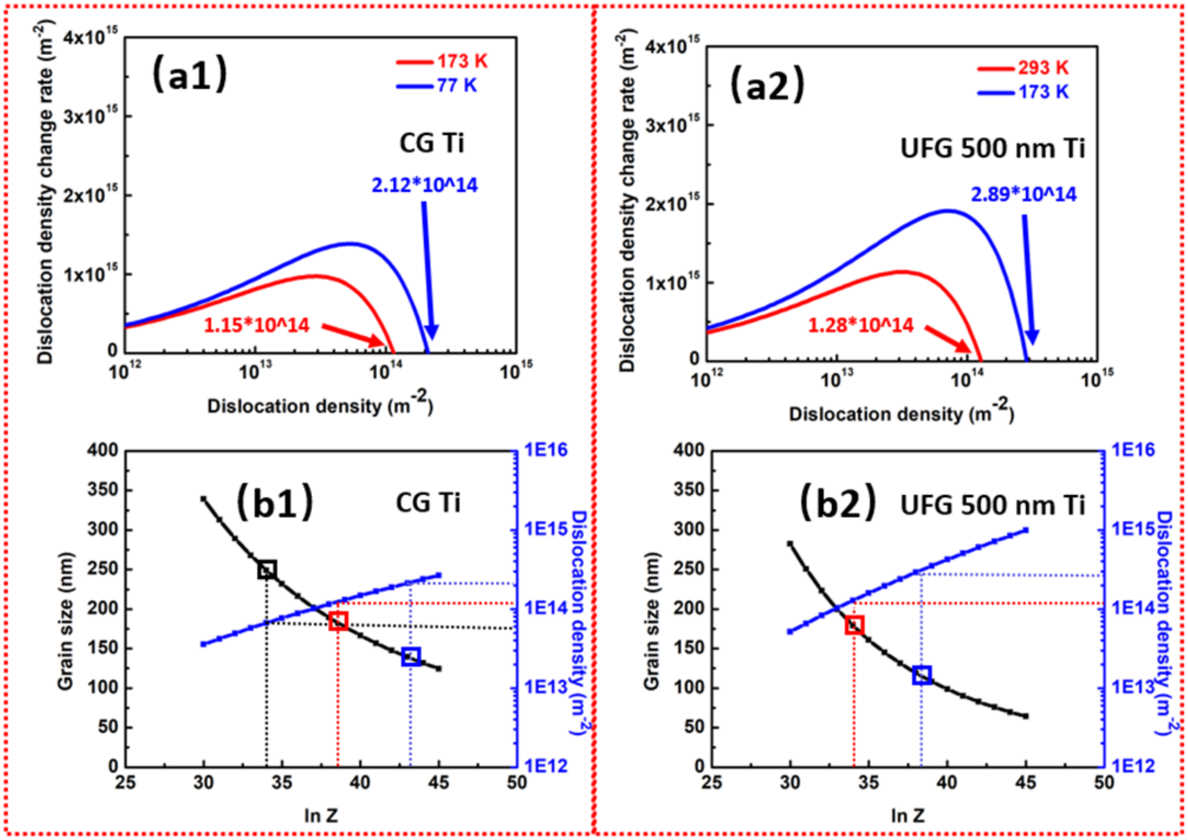

Figure 4.4.2.3. (a1,a2) Change of dislocation density with the variation of dislocation density. (b1,b2) Relationship between critical dislocation density and subgrain size with Zener-Hollomon parameter (ln Z) [119].

A model that is realistic has to predict the effects of initial deformation temperatures and grain size on the microstructure within the shear band. The observations in the past sections indicate that the width of shear band decreases with initial grain size as shown in Fig. 4.4.2.4(a), and that the recrystallized grain size decreases with the width of shear band as shown in Fig. 4.4.2.4(b). Under the same displacement of hat-shaped specimens for each material, the obvious decrease of width of shear bands at cryogenic temperatures leads to the much larger local shear strain inside the shear bands, which is thought to be responsible for the formation of smaller grain size.

The local shear strains were estimated as follows. A displacement of 1.2 mm and shear-region thickness of 0.15 mm for CG grained titanium, a displacement of 0.5 mm and shear-region thickness of 0.25 mm for UFG (500 nm) titanium and a displacement of 0.4 mm and shear-region thickness of 0.3 mm for UFG (100 nm) titanium were imposed in the specimens. Thus, local shear strain γ_{local} for shear bands was estimated by the equation ($d_{total} = d_{uniform}\gamma_{uniform} + \delta_{local}\gamma_{local}$). The calculated local shear strain for different shear bands was represented in Fig. 4.4.2.4(c). These are first-order estimates and the realistic local shear strain should be much smaller than the calculated ones.

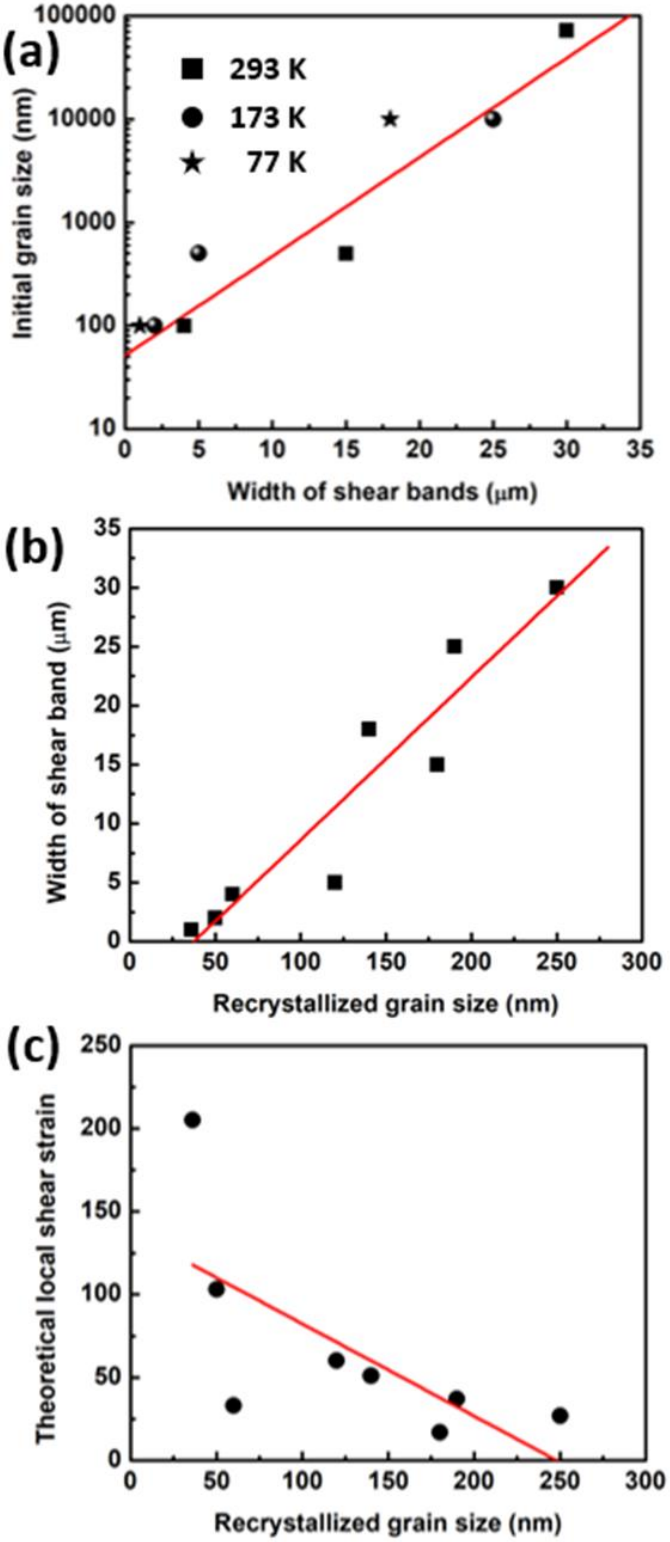

Figure 4.4.2.4. (a) Width of shear band as function of initial grain size. (b) Recrystallized grain size as a function of shear band width. (c) Recrystallized grain size as a function of estimated local shear strain.

4.4.3 Dislocation evolution during deformation for UFG 100 nm titanium

Due to the tiny grain size of UFG 100 nm titanium, a very small shear displacement could impose large shear strain on grains. This has been demonstrated by observation of amounts of nano-bundles inside the shear bands of UFG 100 nm titanium. Once UFG 100 nm titanium initiates the recrystallization, the low angel grain boundaries will form insides these nano-bundles. For low-angle grain boundary, the angel of misorientation is related to the spacing between the edge dislocations, the relationship can be approximately as following [124]:

$$\theta = \frac{b}{s} \tag{4.4.3.1}$$

where the Burgers vector b is taken as 0.289 nm for titanium, and s is the spacing between dislocations. To assume the maximum degree of the low-angle grain boundary 15°, one can get the critical dislocation density for recrystallization inside the shear band. Since the subgrain size in the shear band of UFG 100 nm at 77 K is about 1/3 of the initial grain size, we here assume that two low angel grain boundaries would form inside a single nano-bundle. Thus, the critical dislocation density is determined to be 10^{16} m-^{2}. This value is much higher than the critical dislocation density for recrystallization in CG titanium. But it can be achieved easily due to its small grain size. The schematic drawing showing dynamic recrystallization process of UFG 100 nm at 77 K is presented in Fig. 4.4.3.1.

Once the low-angle grain boundary forms, the grain tend to rotate to form equiaxed grains due to energy gradients as shown in Figs. 4.4.3.1(b) and (c). Harris *et al.* [125] proposed the possibility of grain rotation is driven by the aggregate energy gradient with respect to misorientation, for all of the grain boundaries surrounding a particular grain:

$$\frac{d\Theta}{dt} = M\sum_i A_i \frac{d\gamma_i}{d\Theta} \ , \tag{4.4.3.2}$$

where Θ is the instant orientation of grain to the initial reference grain and M is mean diffusion velocity. For the initial configuration shown in Fig. 4.4.3.1(b), the time need to rotate one grain represented in Fig. 4.4.3.1(c) is estimated by:

$$\Delta t \approx (\frac{kT}{D_{gb}})\frac{\Delta\Theta}{(\frac{A_i\Delta\gamma_i}{R(Rd\Theta)\Delta\Theta})} \tag{4.4.3.3}$$

where D_{gb}≈10^{-13} m^2/s is the grain boundary diffusion coefficient for UFG titanium at 800 K [126]. R is about half of the grain size, $Rd\Theta$ represents the length of the rotation grain boundary, and $A_i=W(Rd\Theta)=2R(Rd\Theta)$ is the area of the rotation grain boundary. The aggregate energy gradient, which establishes the driving force of grain rotation, is taken to be 300 mJ/m^2 degree with grain rotating from low-angel 15° to high-angle of 45° [127]. The duration time of a rotation of 30° to form a equiaxed grain in Fig. 4.4.3.1(c) is estimated to be ~0.05 μs, which is far less than the deformation time. With further decreasing subgrain size, the nano-grain can rotate in a faster speed. This calculation confirms the grain rotation model proposed by Meyers [13]. When the grain is smaller than 10 nm, the grain boundary dislocation can play an important role on grain rotation [128]. Zhu *et al.* [129] reported significant increase of geometric dislocations near the shear band in CG titanium, which should also make a contribution to plastic deformation in the nanostructured titanium.

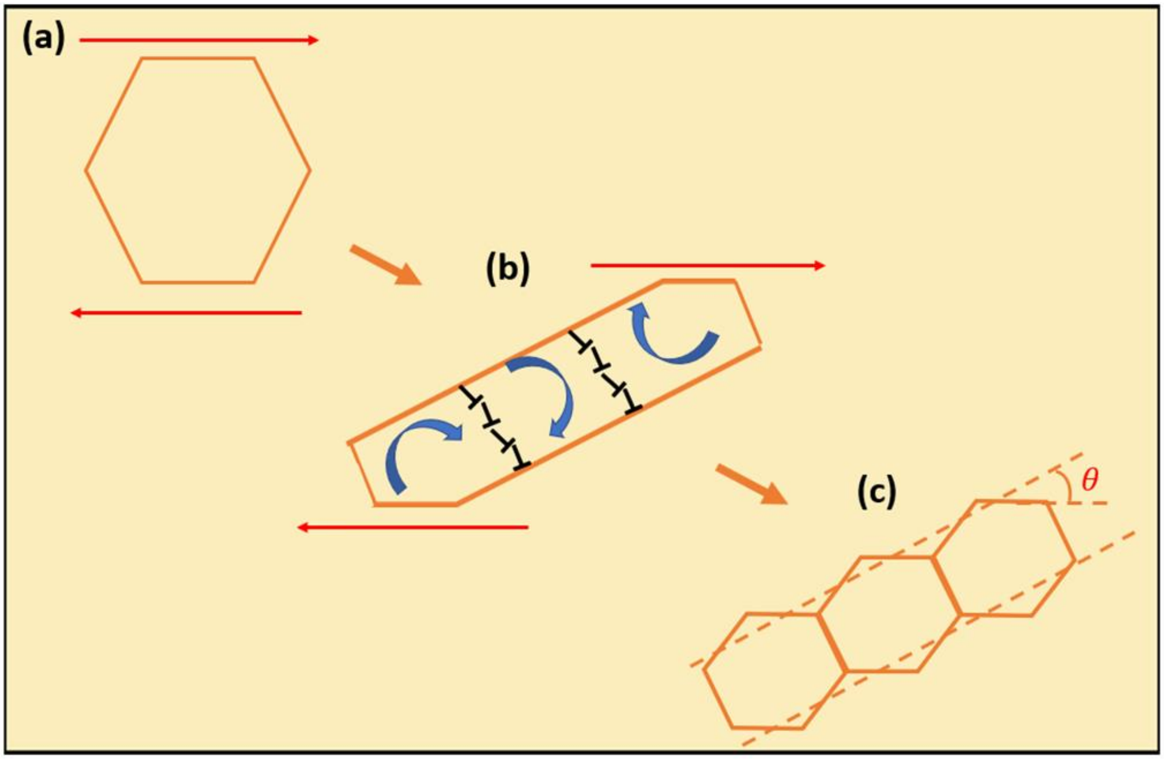

Figure 4.4.3.1. Schematic drawing showing the shear-rotational dynamic recrystallization mechanism for UFG 100 nm to form recrystallized equiaxed nanograins. (a) Original ultrafine-grains; (b) formation of low-angle grain boundaries and subsequent grain rotation under the applied shear stress; (c) formation of recrystallized equiaxed nanograins through grain-boundary rotation by an angle.

4.4.4 Effect of Zener-Hollomon parameter

Since the UFG titanium didn't exhibit the obvious ductile-to-brittle transition under dynamic impact, we would expect that the extreme narrow shear band should form with further decreasing temperatures and increasing strain-rates. The ultrafine- and nano- shear bands have been observed under severe plastic deformation or high strain-rate impact [27]. But not all of materials follow this significant tendency of reduced thickness of shear bands at cryogenic temperatures. Many other factors, such as the thermal conductivity, thermal softening parameter and microvoids, could influence the width of shear bands.

The Zener-Hollomon effect [119] on the recrystallization grain size in the shear bands of titanium is presented in Fig. 4.4.4. The fitting parameters for equation 4.4.2.14 are summarized in Table 4.4.4. Similar grain refinement behavior has been observed by Li *et al.* [130] and Mishra *et al.* [131]. The recrystallized nanocrystalline grains in the shear bands have already been observed. For a larger value of ln Z, the formation of smaller nanograins and even phase formation (when the temperature reaches hcp to bcc titanium transition temperatures) would be possible. In addition, Sun *et al.* [132] reported that the deformation twinning propensity in UFG Ti decreased monotonously with decreasing grain size down to 50 nm by dynamic plastic deformation. Due to a large stacking-fault energy (>300 mJ.m^{-2}) of titanium, no deformation or recrystallized twinning was observed inside shear bands in titanium. Thus, the presence of twins before shear localization could also break up and evolve to the recrystallized boundaries inside the shear bands. When the grain size breaks into a few nanometers, other deformation mechanisms such as grain boundary dislocation generation and annihilation and grain boundary sliding may be triggered. But this needs to be confirmed by experiments. This grain refinement mechanism brings the insight into making nanocrystalline materials [133, 134].

Chapter 4, in part, is a reprint of the materials as it appears in “Dynamic deformation and failure of ultrafine-grained titanium, Acta Materialia 2017 125: 210-218”. This work was coauthored by Zezhou Li, Bingfeng Wang, Shiteng Zhao, Ruslan Z Valiev, Kenneth S Vecchio, Marc A Meyers. The dissertation author was the primary author of this paper.

Chapter 4, in part, is currently being submitted as it appears in “The Effects of Ultra-Fine-Grained Structure and Cryogenic Temperature on Adiabatic Shear Localization in Titanium, Acta

Materialia". This work was coauthored by Zezhou Li, Shiteng Zhao, Bingfeng Wang, Shuang Cui, Renkun Chen, Ruslan Z. Valiev, Marc A. Meyers. The dissertation author was the primary investigator and primary author of this paper.

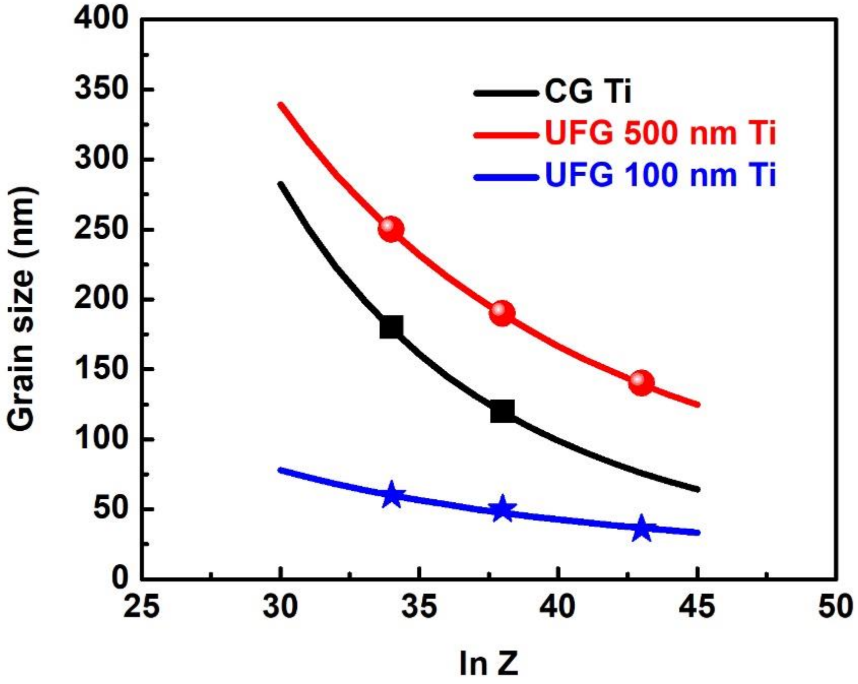

Figure 4.4.4. The relationship of Zener-Hollomon parameter with the average recrystallized grain size for titanium.

Table 4.4.4. Parameters for the relationship of Zener-Hollomon parameter with the average recrystallized grain size for titanium.

	A	B
CG Ti	**1.51*10^6**	**2.47**
UFG 500 nm Ti	**6.96*10^7**	**3.65**
UFG 100 nm Ti	**9.88*10^4**	**2.1**

Chapter 5. Dynamic response of the Al$_{0.3}$CoCrFeNi high-entropy alloy

5.1 Background

Figure 5.1.1 shows the arc-melting equipment and corresponding copper mold. The Al$_{0.3}$CoCrFeNi high-entropy alloy was fabricated by vacuum-induction melting with the Al, Co, Cr, Fe and Ni elements to cast a plate with dimensions: 127 mm × 305 mm × 19 mm. Then the plate underwent the hot-isostatic-pressing (HIP) at 1204 °C and 103 MPa for 4 hours to reduce defects formed during the casting and cooling processes. Samples were cut from the center of the bulk materials and underwent homogenization at 1,200 °C for 2 hours, followed by water quench [135].

Figure 5.1.1. Arc-melting method to make high-entropy alloys [136].

Tang *et al.* [136] reviewed the Al alloying effect on crystal structure, microstructures and mechanical properties of AlxCoCrFeNi systems. They revealed that the Al element can be served as the potential BCC stabilizer in 3d transitional elements based high-entropy alloys. An fcc high-entropy alloy have good ductility but low strength. With alloying Al elements, the Al-based high-entropy alloys become stronger but somewhat lose ductility. In Fig. 5.1., with x ratio increasing from 0 to 3, the microhardness increases from 100 HV to 700 HV [137]. For low contents of Al, only fcc phase presents without any brittle phase such as intermetallic phases. The presence of bcc phase mainly contributes to the hardening of the alloys. In addition, Al obtains larger atomic metallic radius, which could lead to more severe lattice-strain distortion. Wang *et al.* [138] examined Al alloying effect on mechanical response of $Ni_{1.5}CoFeCu_{1-x}Al_xV_{0.5}$ HEA. They discovered that the yield stress increases significantly with the increase of Al contents due to the presence of more BCC phase and Al oxide.

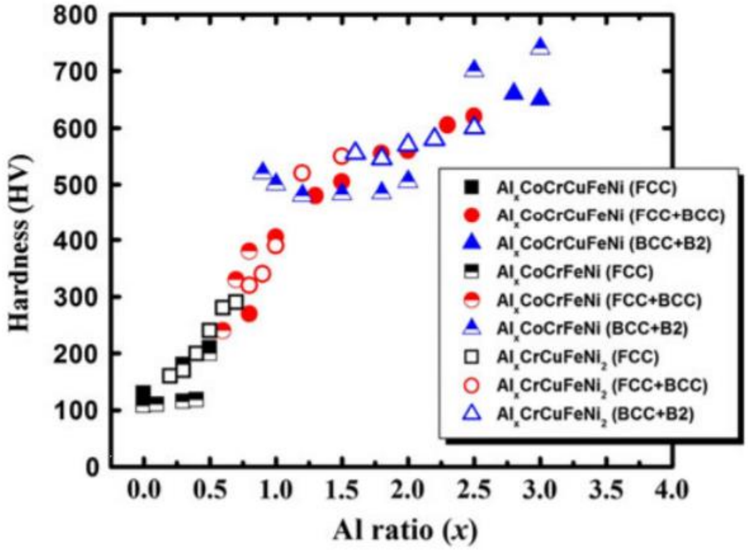

Figure 5.1.2. Microhardness of $Al_xCoCrCuFeNi$, $Al_xCoCrFeNi$ and $Al_xCoCrFeNi_2$ high-entropy alloys and corresponding phase [137].

5.2 Microstructure of the $Al_{0.3}CoCrFeNi$ HEA

The alloy contains coarse-grained grains with size ~ 500 μm and large annealing twins shown in Fig. 5.2(a) [138]. The single phase (fcc) $Al_{0.3}CoCrFeNi$ alloy, as demonstrated by neutron-diffraction pattern [139] in Fig. 5.2(b), contains two elements (Cr and Fe) that crystallize with the body-centered cubic (bcc) structure, two elements (Ni and Al) as face-centered cubic (fcc) and one (Co) as hexagonal close-packed (hcp). This single phase fcc crystal structure is consistent with the XRD analysis of $Al_xCoCrFeNi$ (x in molar ratio, x=0-2.0) high-entropy alloy [140]. The elemental maps of the $Al_{0.3}CoCrFeNi$ high-entropy alloy in Fig. 5.2(c) show that the distribution of Al, Co, Cr, Fe and Ni within the analyzed volume is homogeneous with no indication of segregation or clustering at the atomic scale. The atom probe tomography (APT) results of Fig. 5.2(d) show the concentrations of the different elements along with the black arrow, which represents the nominal alloy composition.

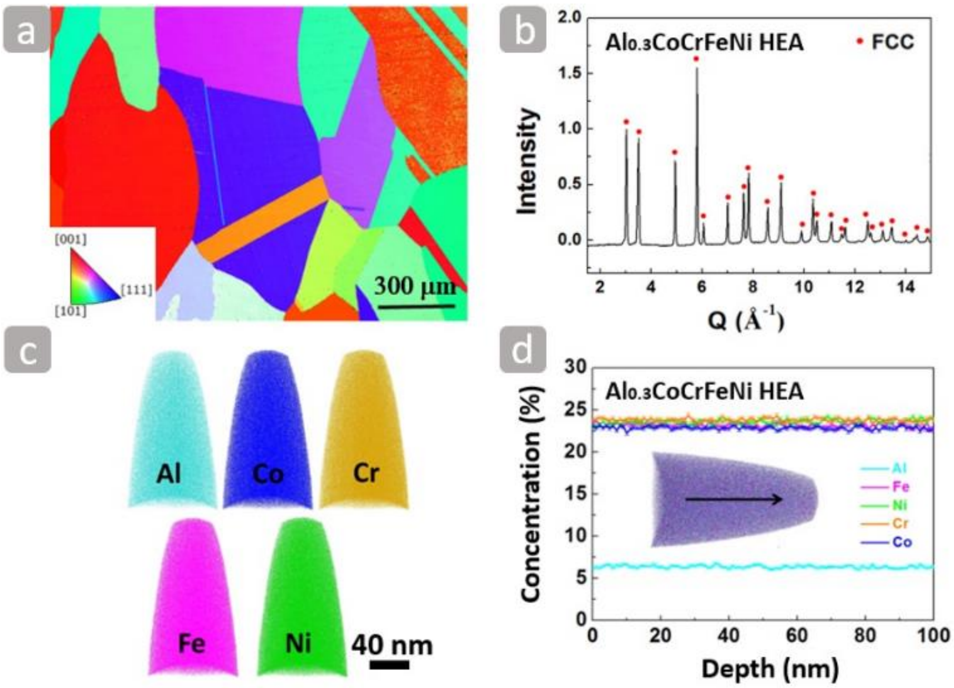

Figure 5.2. (a) Electron backscattered diffraction (EBSD)-inverse pole figure (IPF) showing the microstructure of the $Al_{0.3}CoCrFeNi$ high-entropy alloy with annealing twins. (b) Neutron-diffraction pattern of the $Al_{0.3}CoCrFeNi$ high-entropy alloy. (c) APT analysis showing the homogeneous distribution of Al, Co, Cr, Fe, and Ni elements. (d) APT results of one-dimensional element concentration taken along the black arrow [136].

5.3 Mechanical behavior

The compressive true stress-true strain curves at room temperature are plotted in Fig. 5.3(a). The $Al_{0.3}CoCrFeNi$ high-entropy alloy has a high strain-hardening ability during plastic deformation both at quasi-static and high strain rates. The stress-strain curve of coarse-grained (CG) (grain size $\sim$ 75 μm) pure aluminum [141] is also shown in Fig. 5.3(a) for comparison. Fig. 5.3(b) shows changes of strain hardening rate θ (defined by $\frac{\mathrm{d}\sigma}{\mathrm{d}\varepsilon}$) as a function of true strain for the alloy and CG pure Al at a strain rate of 10^{-2} s^{-1}. The strain-hardening rate of the alloy (above 1000 MPa) is significantly higher than that of CG pure Al. Fig. 5.3(b) shows a negative-slope region followed by a positive-slope region. Such transition is due to a change in the deformation mechanism from dislocation slip-dominated plastic deformation to twinning-dominated plastic deformation.

Work hardening suppresses both necking (in tension) and localization (in shear). Both the phenomena are interconnected. Lu *et al.* [142] showed that nanocrystalline copper exhibited much higher ductility when the grain boundaries are nanotwins. The cause of the high strain hardening in low-SFE fcc alloys, particularly high-Mn steels, has been widely discussed [143]. This high strain-hardening effect is due to the interstitial C atoms of C–Mn dipoles interacting strongly with dislocations or mechanical twins providing barriers to dislocation motion with increasing dislocation storage and thus decreasing their mean free path [144]. In the case of dynamic deformation, thermal softening plays an additional role. Xiong *et al.* [145] reported a maximum temperature increase of 55 K for a twin-induced plastic (TWIP) steel deformed at a high rate of 2400 s^{-1}. This temperature rise was not sufficient to form an adiabatic shear band. In single-phase high-entropy alloys, the lattice is locally distorted because of the occupation of the same crystallographic sites by atoms with different sizes. This local distortion effect is an essential strengthening mechanism [146]. The combination of several strengthening mechanisms such as solid solution hardening, forest dislocation hardening, as well as twinning can lead to an excellent work hardening ability. The yield stress σ_y of the alloy increases from 216 MPa to 503 MPa when the strain rate increases from 10^{-4} s^{-1} to 1.8×10^{2} s^{-1}. The corresponding strain-rate sensitivity m (defined by $\frac{\log \sigma_y}{\log \dot{\varepsilon}}$) is about 0.053 as shown in Fig. 5.3(c). The strain-rate sensitivity of the pure Al is about 0.028, which is only half of that of the alloy [147]. In order to study the thermal softening, the dynamic response at 1800 s^{-1} and different temperatures was examined. The thermal softening parameter $\frac{\mathrm{d}\sigma_y}{\mathrm{d}T}$ shown in Fig. 5.3(d) is ~ - 0.4 MPa/K.

The propensity to shear localization can be quantified from the constitutive response. The Johnson-Cook model is the most common phenomenological constitutive equation used to describe the plastic behavior of materials. A modified Jonson-Cook constitutive equation [11] is used here :

$$\sigma = (\sigma_0 + B\epsilon^n)(1 + C\log\frac{\dot{\varepsilon}}{\dot{\varepsilon}_0})(\frac{T}{T_r})^\lambda \tag{5.3.1}$$

where σ_0 is the yield stress, $\dot{\varepsilon}_0$ (10^{-4} s^{-1}) is a reference strain rate and T_r (293K) is a reference temperature. A, B, n, C and λ are experimentally determined parameters: σ_0 = 216 MPa, B = 1000, C = 0.145, $n = 1.2$, $\lambda = -0.18$, $T_r = 293$ K. The work of the deformation can be used to calculate an (adiabatic) temperature rise:

$$\mathrm{d}T = \frac{\beta}{\rho C_p}\sigma \mathrm{d}\varepsilon \tag{5.3.2}$$

where ρ is the density and C_p is the heat capacity. The parameter β, which is the efficiency of the conversion of the strain energy into heat, is usually taken as 0.9. The density of the $\mathrm{Al_{0.3}CoCrFeNi}$ high-entropy alloy was measured to be 7860 kg/m^3. The specific heat C_p is approximated to be 460 J/kg · K by using a weight averaging method $C_p = w_i \sum_{i=1}^{5} C_{pi}$ (w_i is the weight percent and C_{pi} is the specific heat for each element of the alloy). A relationship between the temperature and plastic strain, at a fixed strain rate, is obtained by substituting equation 5.3.1 into equation 5.3.2:

$$T = \left[T_r^{-\lambda+1} + \frac{1+C log\frac{\dot{\varepsilon}}{\dot{\varepsilon}_0}}{\rho C_p T_r^\lambda} \times 0.9(1-\lambda)\varepsilon(\sigma_0 + \frac{B\varepsilon^n}{n+1})\right]^{\frac{1}{1-\lambda}} \tag{5.3.3}$$

The temperature at an extreme high strain rate of 10^4 s^{-1} and true strain of 0.5 is only 402 K, representing a temperature rise of 109 K.

Joseph *et al.* [148] reported that both arc-melted and direct laser sintered $Al_{0.3}CoCrFeNi$ alloy samples (with FCC structure) exhibited a yield strength of 200 MPa, excellent strain hardening, and had tensile failure strain above 1. Li *et al*. [149] discovered that tensile strength and elongation of the FCC $Al_{0.3}CoCrFeNi$ alloy increased with decreasing temperatures and reached 1010 MPa and 68% at 77 K. The Charpy impact energy of the $Al_{0.3}CoCrFeNi$ alloy was approximately 413 J at room temperature and 328 J at 77 K. This superior ductility and ultrahigh Charpy impact toughness of this alloy are the result of mechanial nanotwinning instead of planar slip dislocations [150]. This has been also observed by Gludovatz *et al.* [55] in the CrMnFeCoNi high-entropy alloy. Deformation-induced nanotwinning delays the onset of necking instability (i.e., localized plastic deformation that can lead to premature failure) to higher strains.

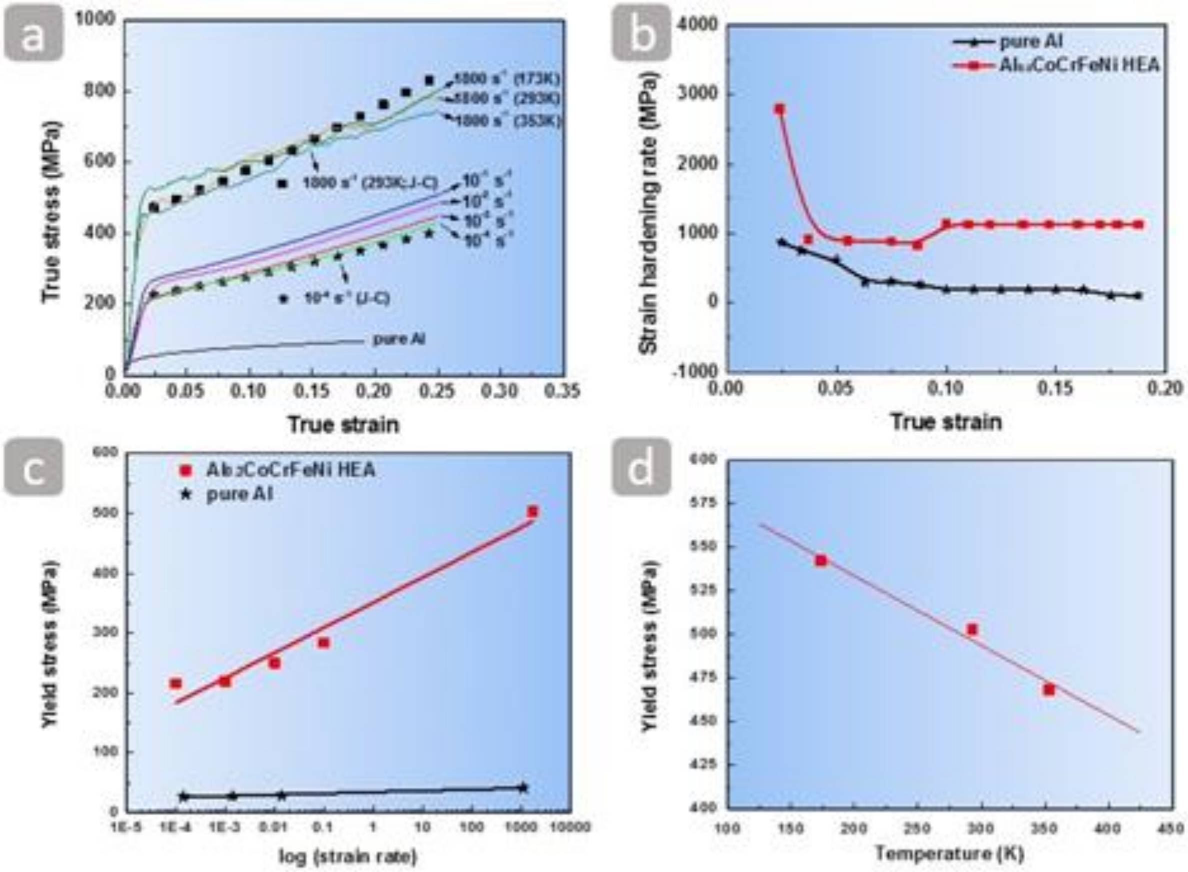

Figure 5.3. (a) True stress-true strain curves of the Al$_{0.3}$CoCrFeNi high-entropy alloy at different strain rates (with Jonson-Cook model fitting curves) and true stress-true strain curve of the CG pure aluminum at the quasi-static 10^{-2} s^{-1}. (b) Strain-hardening rate as a function of true strain of the Al$_{0.3}$CoCrFeNi high-entropy alloy and pure aluminum at the strain rate 10^{-2} s^{-1}. (c) Yield stress as a function of log ($\dot{\varepsilon}$). (d) Thermal softening of the Al$_{0.3}$CoCrFeNi high-entropy alloy at 1800 s^{-1}.

5.4 Resistance to shear localization

In order to understand the strain hardening mechanisms of the Al$_{0.3}$CoCrFeNi high-entropy alloy, it is important to establish the microstructure evolution of deformed samples. This was examined at strain rates of 10^{-4} s^{-1} and 1800 s^{-1} by transmission electron microscopy (TEM) and is shown in Fig. 5.4.1. Fig. 5.4.1(a) shows tangles of randomly distributed dislocations in the sample deformed at 10^{-4} s^{-1}, revealing that forest dislocations can lead to steady strain-hardening during plastic deformation. Fig. 5.4.1(b) indicates that the high density of dislocations tends to align in one direction and entangle under dynamic loading. Such a high dislocation density configuration has been also observed for the laser-induced shock compression of monocrystalline copper [151]. Mechanical twins form in many metallic materials, especially those with low stacking-fault energy (SFE). Some fcc single phase materials with high SFE (such as Al and Ni) may not easily form twins except under extreme conditions, such as low temperatures and high strain rates [152]. Fig. 5.4.1(c) shows that the parallel bands are mechanical twins, which suggests that mechanical twinning is an important plastic deformation mechanism in the $Al_{0.3}CoCrFeNi$ high-entropy alloy at high strain rates. Fig. 5.4.1(d) summarizes the deformation mechanism of the $Al_{0.3}CoCrFeNi$ HEA under dynamic loading, indicating that the dislocation slip and twinning can lead to the excellent strain-hardening ability [153].

Chapter 5, in full, is a reprint of the materials as it appears in “High-velocity deformation of $Al_{0.3}CoCrFeNi$ high-entropy alloy: Remarkable resistance to shear failure, Scientific Reports, 2017 7:42742”. This work was coauthored by Zezhou Li, Shiteng Zhao, Haoyan Diao, Peter K. Liaw, Marc A. Meyers. The dissertation author was the primary author of this paper.

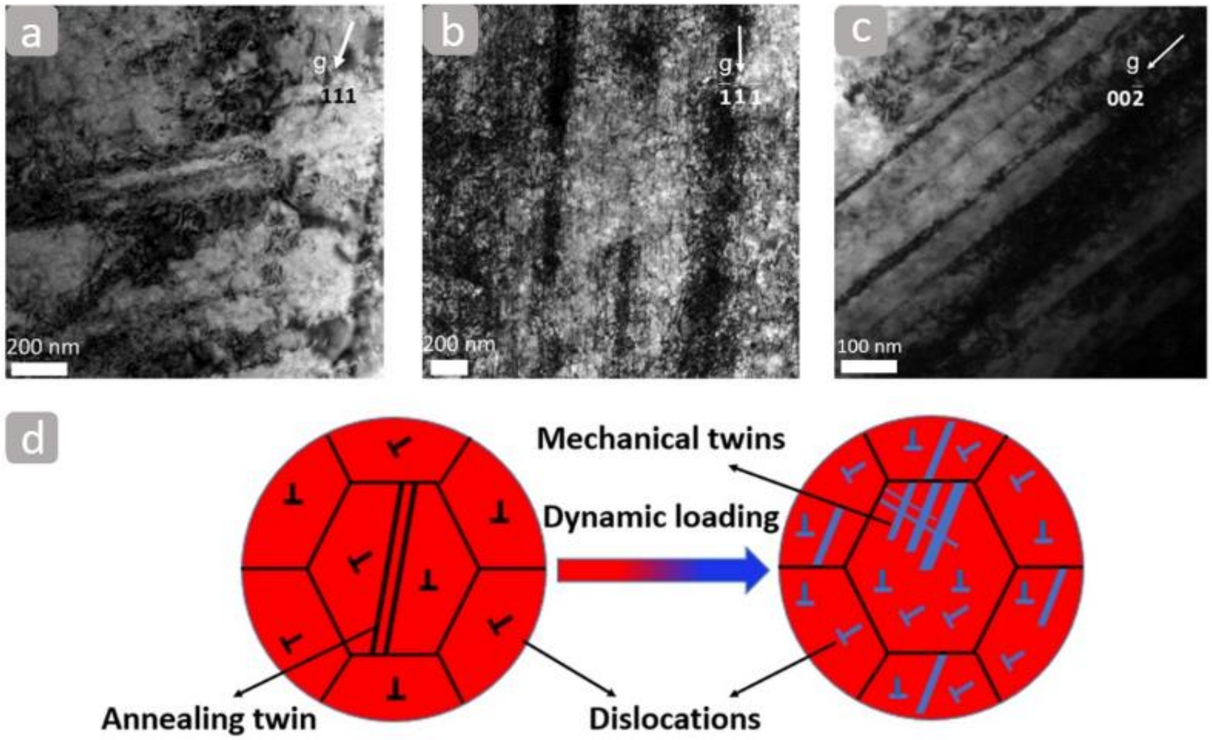

Figure 5.4.1. TEM bright-field images of the deformed samples at the strain rates of (a) 10^{-4} s^{-1}; (b) and (c) 1800 s^{-1}. (d) Schematic sketches showing the deformation mechanisms of the $Al_{0.3}CoCrFeNi$ high-entropy alloy under dynamic loading.

Proportionality between the twin-boundary energy and the stacking-fault energy (SFE) has been reported for most metals [45]. Some fcc single phase materials with high SFE [154, 155] (Al with SFE ≈ 86 mJ/m^2 and Ni with SFE ≈ 100-130 mJ/m^2) may not easily form twins except under extreme conditions, such as low temperatures and high strain rates. Kumar *et al.* [156] reported low SFE (below 30 mJ/m^2) of the $Al_{0.1}CoCrFeNi$ alloy. He attributed it to the larger atomic size difference between Al and other elements in the alloy. Low stacking-fault energy values (~30 mJ/m^2) have been reported in NiFeCrCoMn alloy [157]. Hence, one would expect that addition of Al would cause a high lattice strain per atomic percent in CrFeCoNi as compared to Mn. Mishra *et al.* [158] proposed that lattice strain in HEAs might play an important role in dislocation core energy which in turn will have a bearing on stacking-fault formation and its energy. The lattice strain in HEAs raises the base energy of the crystal and thereby reduces the additional energy required to nucleate dislocations and twins. Since $Al_{0.1}CoCrFeNi$ has ~1.2 wt.% of Al, it is assumed that Al addition might have caused a decrease in SFE from ~30 mJ/m^2 to a lower value. Thus, it is proposed that the SFE of $Al_{0.3}CoCrFeNi$ is lower than that of the $Al_{0.1}CoCrFeNi$ alloy, leading to the formation of profuse mechanical twins in high strain-rate deformation.

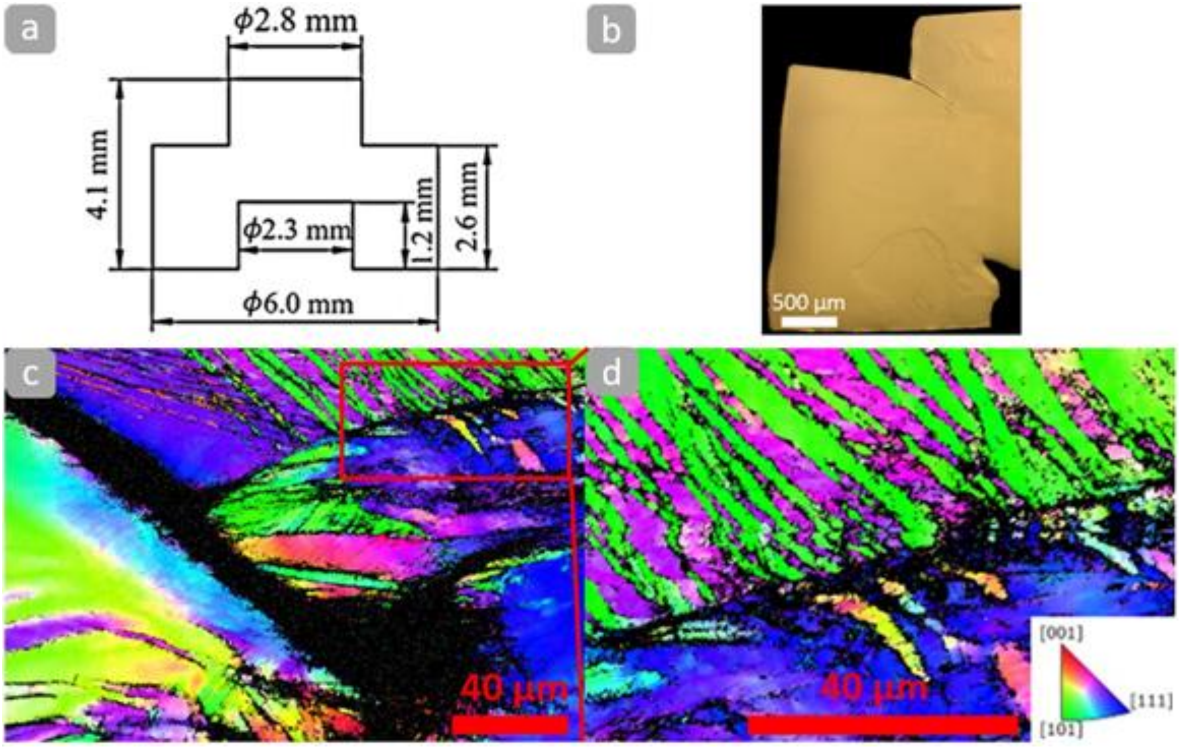

Figure 5.4.2. (a) Dimension of the hat-shaped sample. (b) Optical microscopy image of the deformed hat-shaped sample. (c) EBSD image near the deformation tip. (d) EBSD image showing deformation twins near the deformation tip.

Shear localization has been found to be an important and sometimes dominant deformation and fracture mode in metals, granular ceramics, polymers, and metallic glasses at high strains and strain rates. For metals, thermal softening is the first stage of this process, leading to processes of dynamic recovery and recrystallization with associated drops in the flow stress. Calculations by Meyers *et al.* [13] revealed that the break-up of the elongated sub-grains and diffusive rotation of the grain boundaries can occur during the deformation process. The complex interrelationships between stress, strain, strain rate and temperature, have been used for pursuing a better design of materials with the objective of postponing and even avoiding localized shear deformation.

An adiabatic shear band can form when the material starts to "soften". The condition for instability is $\frac{d\tau}{d\gamma} \leq 0$, is obtained from the general function $\tau = f(\gamma, \dot{\gamma}, T)$:

$$\frac{d\tau}{d\gamma} = (\frac{\partial\tau}{\partial\gamma})_{\dot{\gamma},T} + (\frac{\partial\tau}{\partial\dot{\gamma}})_{\gamma,T}\frac{\partial\dot{\gamma}}{\partial\gamma} + (\frac{\partial\tau}{\partial T})_{\gamma,\dot{\gamma}}\frac{dT}{d\gamma} \leq 0 \tag{5.4.1}$$

The normal stress and strain shown in equation 5.4.1 at a constant strain rate of 10^4 s^{-1} can be converted to the corresponding shear stress and shear strain [91] by: $\tau = \frac{\sigma}{2}$ and $\gamma = \sqrt{2e^{2\varepsilon} - 1} - 1$. For a shear strain of 1.1, at constant $\dot{\gamma}$ and T, $\frac{\partial\dot{\gamma}}{\partial\gamma} = 0$, the strain hardening parameter is ~ 440 MPa, and the thermal softening parameter is ~ - 0.2 MPa/K. Consequently, $\frac{dT}{d\gamma} = 175\ K^{-1}$. Neglecting the second term in equation 5.4.2:

$$\frac{d\tau}{d\gamma} = \left(\frac{\partial\tau}{\partial\gamma}\right) + \left(\frac{\partial\tau}{\partial T}\right)\frac{dT}{d\gamma} \approx 440 - 0.2 \times 175 = 405\ \text{MPa} \gg 0 \tag{5.4.2}$$

Thus, shear instability is not predicted from the constitutive response of this alloy.

The resistance of the $Al_{0.3}CoCrFeNi$ alloy to shear localization was then experimentally studied by dynamically-loading a hat-shaped sample to induce forced shear localization. The dimension of the hat-shaped sample is shown in Fig. 5.4.2(a). Fig. 5.4.2(b) shows the optical image of the deformed hat-shaped sample. The electron backscatter diffraction (EBSD)-inverse pole figure (IPF) mapping in Fig. 5.4.2(c) indicates that the hat-shaped sample was highly deformed under high strain rates but not fractured. The formation of mechanical twins can be observed in Fig. 5.4.2(d) near the deformation tip. No observable shear band can be identified in the hat-shaped sample at an imposed shear strain of ~ 1.1. The microstructure is severely deformed in the "forced" shear region. Xu *et al.* [159] studied shear localization and recrystallization in dynamic deformation of a CG single fcc 8090 Al-Li alloy and observed a recrystallized equiaxed structure with an average grain size of ~ 0.2 μm. Dynamic recrystallization, which has been widely observed inside adiabatic shear bands, is absent in the shear region of the hat-shape sample, indicating the alloy continues to harden under dynamic loading instead of softening by recrystallization. Jiao *et al.* [160] reported pile-ups around the indents in the $Al_{0.3}$CoCrFeNi high-entropy alloy and observed a highly localized severe plastic deformation under the nanoindentation. However, they did not mention shear bands. Indeed, pile-ups are a natural result of indentations because of the volume constraining requirement. Tang *et al.* [161] found that the grain size of the $Al_{0.3}$CoCrFeNi high-entropy alloy decreased severely from ~350 μm to nanocrystalline size due to dynamic recrystallization via high-pressure torsion processing method. These observations indicate that dynamic recrystallization of this alloy can happen under severe plastic deformation. However, adiabatic shear localization of this alloy can only be activated by higher strains and temperatures than the ones imposed by our experiments. The enlarged Fig. 5.4.2(d) with a ~ 36 % twin area fraction and a ~ 2.4 μm average twin thickness confirms that their formation can play an important role on high strain-rate deformation. Consequently, the dislocation slip and twin-twin reaction can lead to the excellent strain-hardening ability; this, in turn, results in the its extraordinary resistance to shear localization.

Fig. 5.4.3 shows the excellent performance of the $Al_{0.3}$CoCrFeNi HEA studied here, in comparison with other alloys. Our results suggest that the $Al_{0.3}$CoCrFeNi high-entropy alloy maintains the remarkable mechanical properties at high strain rates, rendering it to be of great potential for impact-protection (ballistic) applications.

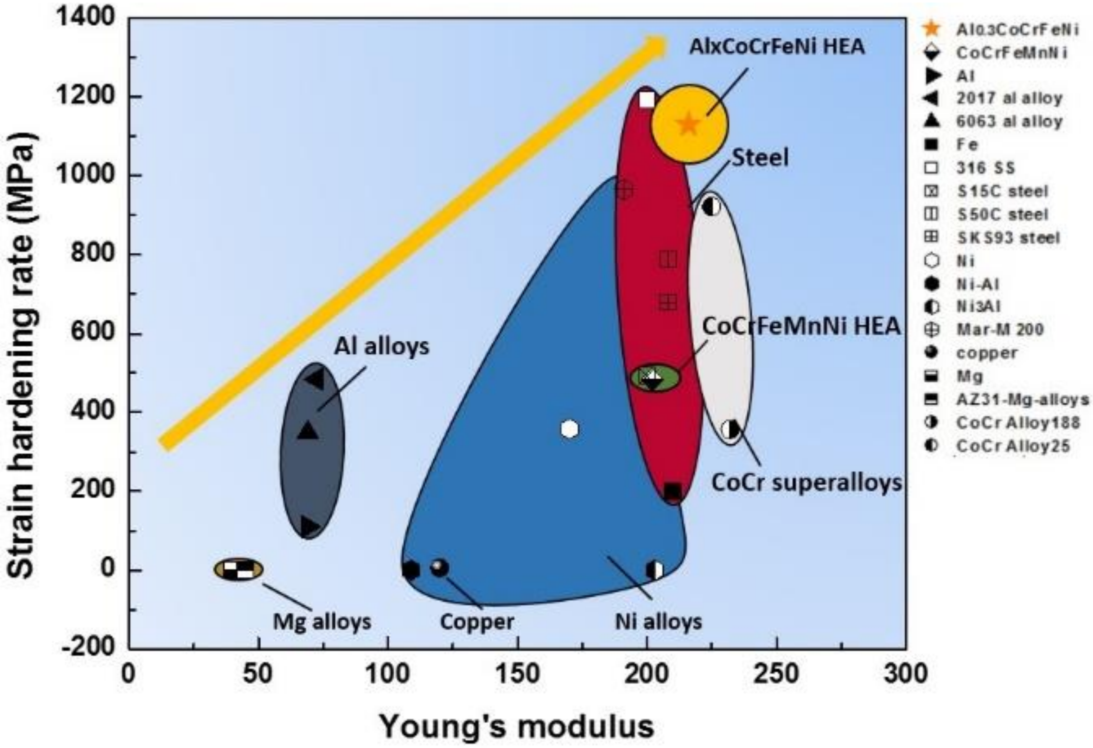

Figure. 5.4.3. Plot comparing the strain-hardening rate (at a compressive true strain of 0.2) as a function of Young's modulus for $Al_{0.3}$CoCrFeNi HEA and other structural materials [58, 131, 162-175]. (The strain hardening rate of the structural materials was calculated to be zero at the condition when the materials are fractured at a true strain of 0.2).

Chapter 5, in full, is a reprint of the materials as it appears in "High-velocity deformation of $Al_{0.3}$CoCrFeNi high-entropy alloy: Remarkable resistance to shear failure, Scientific Reports, 2017 7:42742". This work was coauthored by Zezhou Li, Shiteng Zhao, Haoyan Diao, Peter K. Liaw, Marc A. Meyers. The dissertation author was the primary author of this paper.

Chapter 6. Dynamic response of the CoCrFeMnNi high-entropy alloy

6.1 Dynamic behavior of the annealed CoCrFeMnNi high-entroy alloy

6.1.1. Microstructure of the CoCrFeMnNi high-entroy alloy

The as-received CoCrFeMnNi high-entropy alloy was prepared by spark plasma sintering (SPS) method. Fig. 6.1.1.1 shows the initial microstructure of this alloy, which obtains coarse-grained grains. The low-stacking fault energy ~20 mJ/m^2 of the Cantor alloy has been reported by Zaddach *et al.* [157], which could promote the formation of annealed twins during the synthesis process. The XRD result in Fig. 6.1.2 shows that this alloy obtains a single fcc crystal structure, while three elements (Cr, Mn and Fe) obtain the body-centered cubic (bcc) crystalline structure, element Ni has a face-centered cubic (fcc) structure and one (Co) presents hexagonal close-packed (hcp) structure.

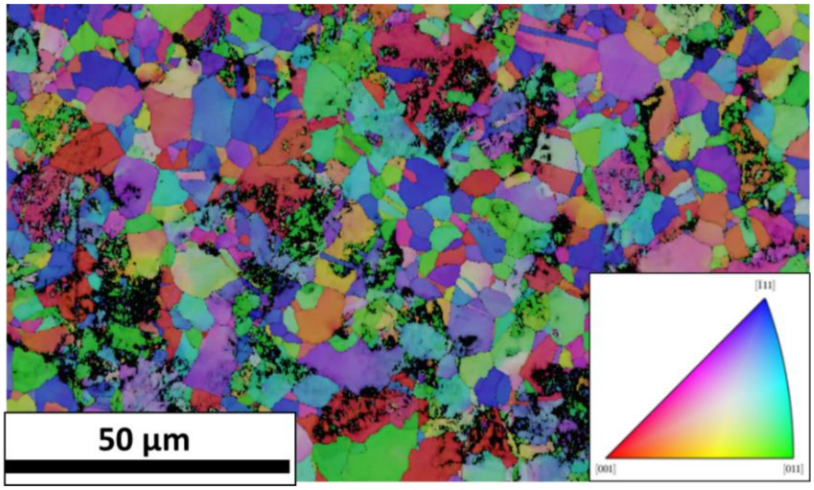

Figure 6.1.1.1. EBSD (electron backscatter diffraction) image depicting the initial microstructure of the as-received CoCrFeMnNi HEA.

The powders as represented in Fig. 6.1.1.2 were prepared by gas-atomisation [176]. The powder with a particle size under 200 mesh was mechanically milled by using ball milling equipment. The weight ratio between powder and stainless-steel balls is 1:10, and ethanol was incorporated during the milling. Spark plasma sintering was applied to consolidate the milled powder.

Fig. 6.1.1.3. shows the chemical composition of as-received materials. The chemical contents of Co, Cr, Fe, Mn and Ni elements are near the nominal composition 20% with each element. No obvious segregation was observed in the as-received high-entropy alloy. Such a homogeneous distribution of 5 elements has also been reported by Bing *et al.* [58].

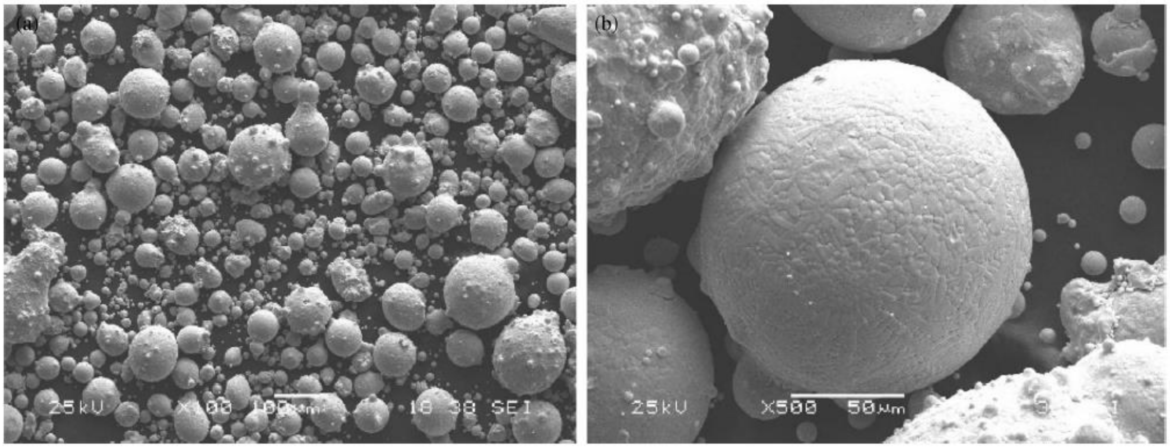

Figure 6.1.1.2. Images showing gas-atomised CrMnFeCoNi high-entropy alloy powders: (a) morphology of powders; (b) surface of powders [176].

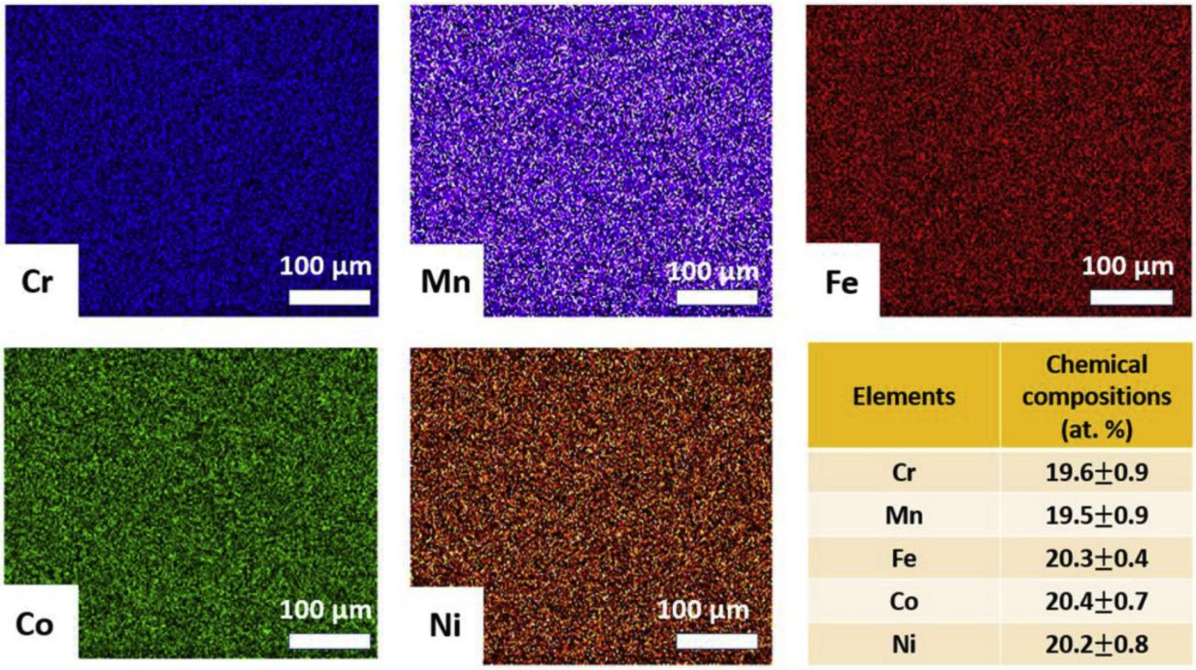

Elements	Chemical compositions (at. %)
Cr	19.6±0.9
Mn	19.5±0.9
Fe	20.3±0.4
Co	20.4±0.7
Ni	20.2±0.8

Figure 6.1.1.3. Elementary distribution and chemical composition by Energy-dispersive X-ray spectrometry [178].

6.1.2 Lattice constants for the CoCrFeMnNi high-entropy alloy

The lattice constant of this alloy is measured by both X-ray diffraction and selected area diffraction pattern methods. In Fig. 6.1.2(a), the degree for the Bragg diffraction planes can be recognized [177]. The wavelength of Cu K-alpha is 1.5406 Å. By applying the classical Bragg diffraction equation $2d\sin\theta = \lambda$, one can get the *d* spacing of diffraction planes. Thus, a lattice constant planes can be derived from the lattice spacing in fcc crystal. In comparison, the selected area diffraction pattern inside the shear bands is conducted by a corrected TEM. The lattice constant by XRD method was 2.076 Å while that by the selected area diffraction pattern by TEM was 2.058 Å in Table 6.1. The reference lattice constant of this alloy is also 2.076 Å. This difference may originate from severe deformed microstructure inside the shear band.

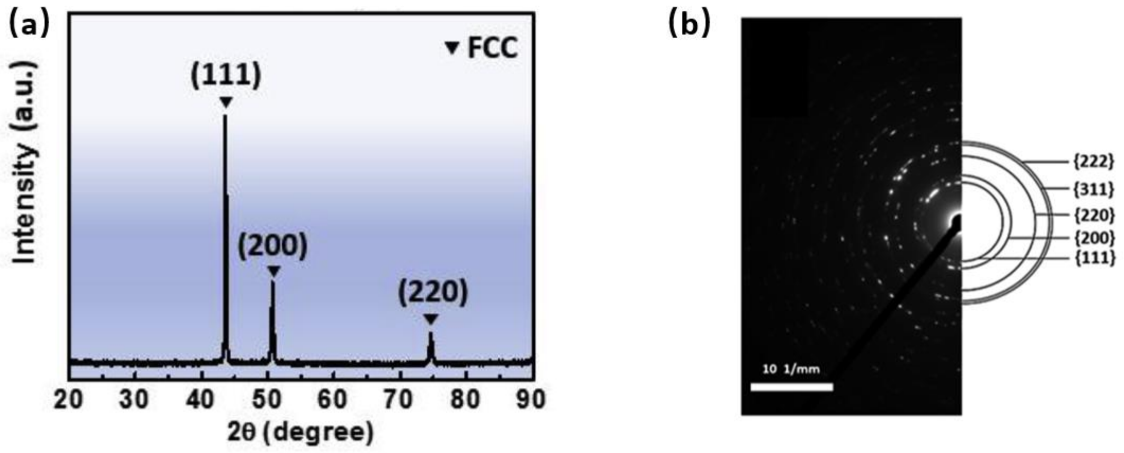

Figure 6.1.2. (a) X-ray diffraction pattern of the alloy using Cu-Kα radiation. (b) Selected area diffraction pattern of the high-entropy alloy inside the shear band.

Table 6.1. *d*-spacings (in Å) of the different (hkl) planes of the fcc CrMnFeCoNi HEA measured by different testing methods.

Methods	***d* (111)**	***d* (200)**	***d* (220)**
XRD (X-ray diffraction)	2.076	1.801	1.273
TEM (selected area diffraction)	2.058	1.780	1.223
XRD (X-ray diffraction)	2.076	1.798	1.271

6.1.3 Mechanical behavior of the CoCrFeMnNi high-entroy alloy

Fig. 6.1.3 shows mechanical response of the Cantor alloy at various strain-rates. The strain-hardening rate keeps ~1100 MPa at a true 0.2. In both quasi-static and dynamic compression condition, the strength of this alloy increases gradually with increasing strain. The strain-hardening rate (measured by slope of the curve at a true strain of 0.2) is ~1100 MPa, which is as similar as that of the $Al_{0.3}$CoCrFeNi HEA [138]. This strain hardening is maintained at 1600 s^{-1}, evidence that no localization is taking place. This same resistance to shear localization behavior has been reported for the $Al_{0.3}$CoCrFeNi HEA; it is attributed to good strain-hardening ability, caused by the solid-solution hardening, forest-dislocation hardening, as well as mechanical twinning under dynamic impact.

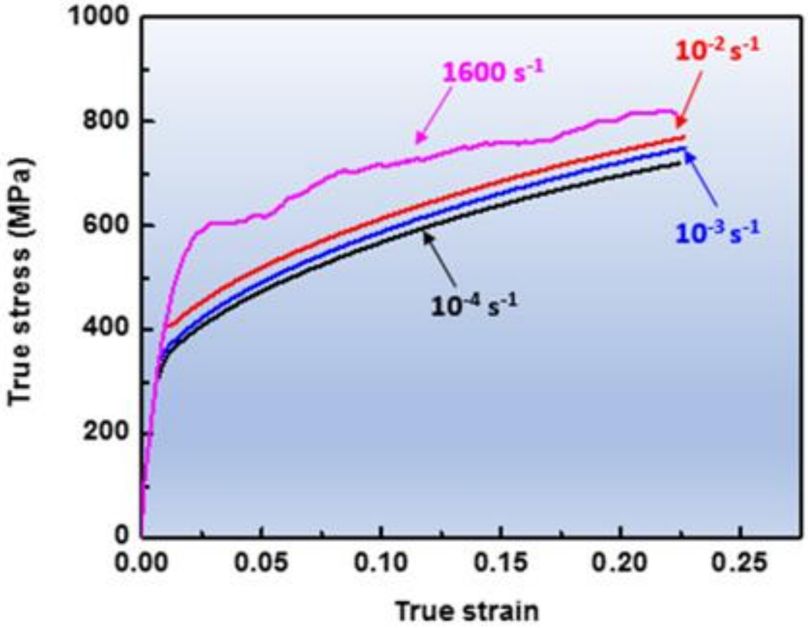

Figure 6.1.3. Mechanial behavior of the Cantor alloy at quasi-static and dynamic strain-rates.

6.1.4 Strengthening and shear localization mechanisms in the Cantor alloy

The hat-shaped specimens are loaded to induce the forced shear band. Fig. 6.1.4.1(a) shows the dimensions of the hat-shaped specimen, which was deformed at room temperature to induce a forced shear band using a split-Hopkinson pressure bar. A series of dynamic-loading experiments on hat-shaped specimens using stopper rings to control the displacement (0.7 mm, 1.14mm, 1.57 mm and 2 mm) are performed. However, among these specimens, a clear shear band was only found at a very large imposed shear strain of ~7. The corresponding shear stress vs. shear strain curve is illustrated in Fig. 6.1.4.1(b). The work of deformation can be used to calculate an (adiabatic) temperature rise inside the shear band: ($dT = \frac{0.9}{\rho C_p}\sigma d\varepsilon$. where ρ =7900 kg/m^3 is the density [178] and C_p is the specific heat capacity). The specific heat capacity C_p of the Cantor alloy is approximated to be 450 J/(kg·K) by using a weight averaging method $C_p = \omega_i \sum_{i=1}^{5} C_{pi}$ (ω_i is the weight percent and C_{pi} is the specific heat capacity for each element of the alloy). Fig. 6.1.4.1(b) shows that the temperature can rise to about 700 K inside the shear band, which approaches the recrystallization temperature for the Cantor alloy, $0.4T_m$, its melting temperature being 1553 K. Fig. 6.1.4.1(c) shows the microstructure inside and near the shear band. The shear band width is about 10 μm. Staker [24] proposed an expression for critical shear strain for shear localization (neglecting the effect of strain-rate hardening):

$$\gamma_c = \frac{\rho C_p n}{-\frac{\partial \tau}{\partial T}} \qquad (6.1.4.1)$$

where ρ is the density, C_p is the specific heat capacity, and n is the strain-hardening power index for the constitutive equation ($\tau = \tau_0 + K\gamma^n$, where τ_0 is the yield stress and K is the constant), and $\frac{\partial \tau}{\partial T}$ is the thermal-softening parameter. Equation 6.1.4.1, which is the same as the equation 2.1.4, expresses the competition of strain hardening and thermal softening prior to shear localization. Fig. 6.1.4.1(d) shows the predicted critical shear strain for shear localization in these metals using Eq. 6.1.4. Fig. 6.1.4(b) shows that the adiabatic shear band is formed only at a very large shear strain ~7. It should be noted that the imposed shear deformation region has a width of over 50 µm whereas the adiabatic shear band has a width of ~10 µm. Therefore, the combination of the excellent strain-hardening ability and moderate thermal-softening effect of the Cantor alloy postpones shear localization to higher degree of shear deformation.

Fig. 6.1.4.3(a) shows the microstructure inside the adiabatic shear band. It indicates that the Cantor alloy goes through significant grain refinement. The corresponding dark-field image in Fig. 6.1.4.3(b) confirms the nanostructured recrystallized grains inside the shear band. In addition, multiple nanotwins were observed inside the recrystallized grains in Fig. 6.1.4.3(c). Due to the sluggish diffusion of the high-entropy alloys [179], the recrystallized grains inside the shear band cannot be formed by migrational dynamic recrystallization mechanism. The elongated grains are proposed to be formed under severe shear deformation at the first and then break up into small ultrafine-grained grains. Small grain-boundary rotations of these grains to form equiaxed structure inside the shear band are required, where the driving force is the minimization of the overall energy. Fig. 6.1.4.3(d) shows the equiaxed refined grains with entangled dislocations, indicating that dislocations can still be the carriers of plastic deformation at a relatively high temperature inside the shear band. Figs. 6.1.4.3(e) and 6.1.4.3 (f) depict the formation of nanotwins in the recrystallized grains.

To reveal the superior strengthening mechanism in Cantor alloy, the microstructure before shear localization was revealed. Fig. 6.1.4.2(a) shows the microstructure near the tip of the shear zone for the hat-shaped deformation, which was subjected to a shear strain of ~2.5. It was observed that the HEA deforms severely just near the tip of shear region. A magnified EBSD image in Fig. 6.1.4.2(b) shows the significant amounts of deformation twinning. A TEM sample in this region confirms the formation of slip bands and deformation twins in Fig. 6.1.4.2(c). Until occurrence of shear localization, the crystallized grains with recrystallized twins were observed in Fig. 6.1.4.2(d). A magnified grain with annealed twin was shown in Fig. 6.1.4.2(e). The diffraction pattern in Fig. 6.1.4.2(f) demonstrates the twining structure in fcc crystal structure.

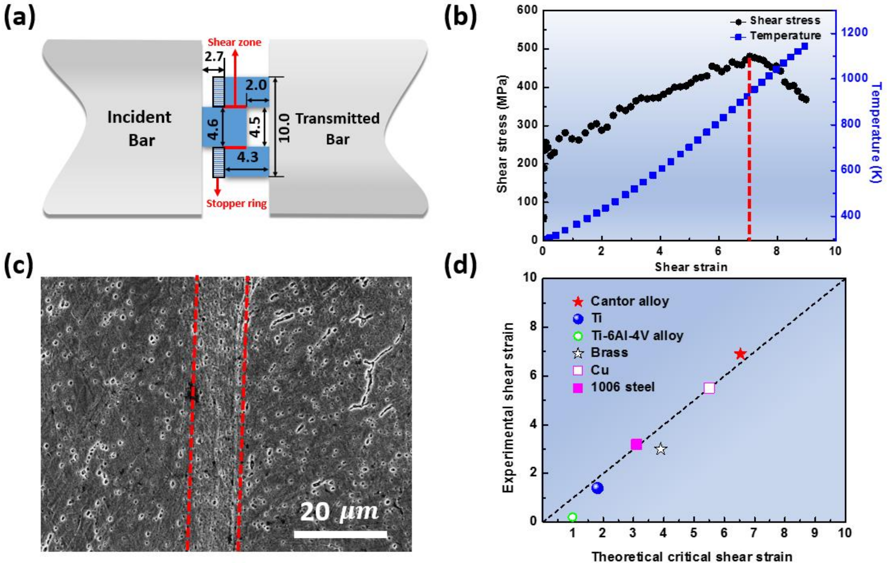

Figure 6.1.4.1. (a) Schematic drawing of dynamic loading of the hat-shaped specimen with the stopper ring (in mm) by the split-Hopkinson pressure bar; (b) shear stress, strain and temperature evolution of the shear band; (c) scanning electron microscope (SEM) image of the shear band. (d) predicted critical shear strain for shear localization [25].

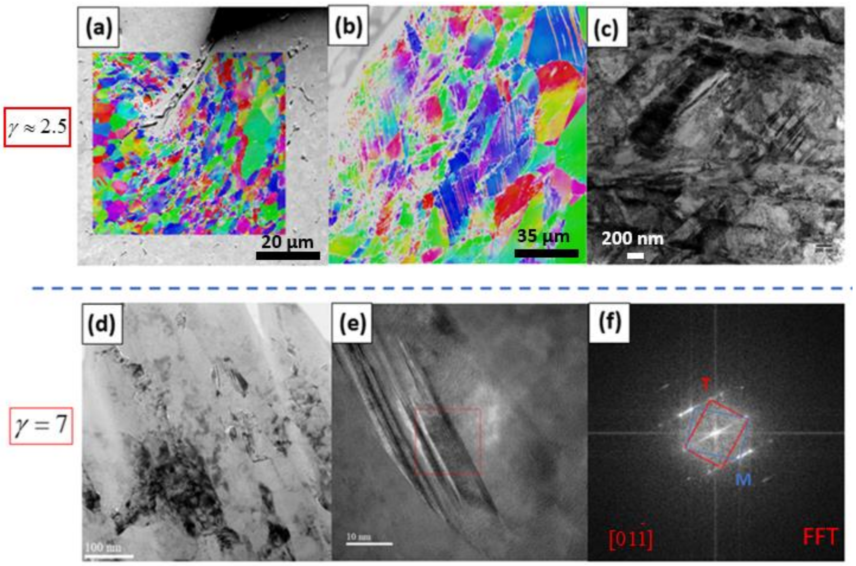

Figure 6.1.4.2. (a,b,c) Microstructure of the Cantor alloy deformed at a shear strain of 2.5. (d,e,f) Microstructure of recrystallized grains with annealed twins in the shear bands at s strain ~7.

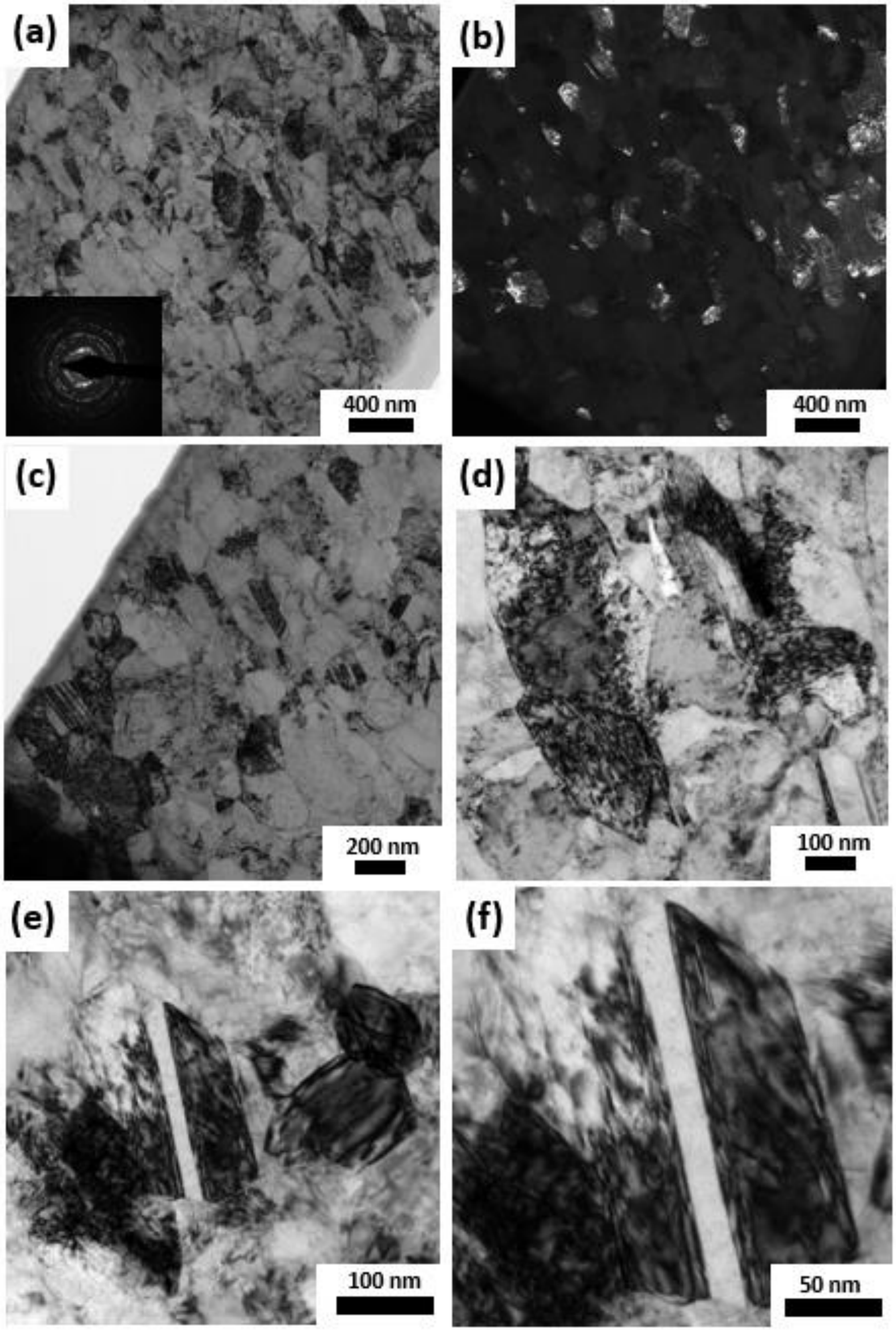

Figure 6.1.4.3. (a) Bright-field TEM image of the microstructure inside the shear band; (b) corresponding dark-field TEM image of (a); (c) recrystallized grains with dislocations and twins; (d) recrystallized grains with dislocations; (e) recrystallized equiaxed grains; (f) the nanotwin inside one recrystallized grain.

Hyun *et al.* [180] examined the lattice distortion effect in CrMnFeCoNi high-entropy alloy by both experiments and theory. The density functional theory and experimental results all show that the lattice distortion in this homogenized alloy is relatively small (<0.1%), explaining recent success of theoretical simulations assuming undistorted crystal lattices. However, they suggest that local lattice distortion can be an order higher than the mean value, which can play a unignorable role on the solid solution strengthening. The yield strength of high-entropy alloy is determined by both Hall-Petch strengthening and solid-solution strengthening. During the deformation, both solid-solution strengthening and cutting forest dislocation provides significant work-hardening rate of this alloy. Until deformation twinning coming, the "dynamic Hall-Petch" [181] effect starts, resulting a synergic effect of strength and ductility in this alloy under dynamic impact.

The yield stress of CrMnFeCoNi high-entropy alloy is based on Hall-Petch strengthening and solid-solution strengthening mechanisms as follows:

$$\sigma_y = \sigma_{HP}(d) + \sigma_{SS}\left(T, \dot{\varepsilon}\right) \tag{6.1.4.2}$$

where $\sigma_{HP}(d) = \sigma_o + k_{HP} d^{-1/2}$ represents Hall-Petch stress and $\sigma_{SS}\left(T, \dot{\varepsilon}\right)$ represents the solid-solution stress. It was reported that σ_o is 125 MPa and k_{HP} is 677 MPa. µm$^{-1/2}$ for the Cantor alloy [182]. Since the average grain size of this alloy is 8 µm, the theoretical Hall-Petch stress $\sigma_{HP}(d)$ is 294 MPa. Curtin and coworkers represent the solid-solution stress in fcc crystal as:

$$\sigma_{ss}(T, \dot{\varepsilon}) = M\tau_{y0} \exp(-\frac{kT}{0.55\Delta E_b(T)} \ln\left(\frac{\dot{\varepsilon}_0}{\dot{\varepsilon}}\right)) \text{ when } \frac{\sigma_{ss}(T)}{\sigma_{y0}(T)} \le 0.5 \tag{6.1.4.3}$$

where M is assumed to be 3, $\dot{\varepsilon}_0$ is 10^{-3} s^{-1} and T is room temperature. They assumed the low-energy wavy dislocation configuration as it moves through the random field of solutes. τ_{y0} is the zero-temperature yield stress about 104 MPa. The strain-rate for the shear band is around 10^5 s^{-1}. Thus, the solid solution stress is 33 MPa. Combined with Hall-Petch relationship, one can get the normal yield stress: 372 MPa. The theoretical shear yield stress is about half of the normal yield stress 165 MPa, corresponding well to the yield stress in Fig. 6.1.4.4.

During the deformation, the forest dislocations continue to strengthen the alloy as follows:

$$\sigma\left(T,\dot{\varepsilon},\varepsilon_p,d\right)=\sigma_{HP}(d)+\sigma_{SS}\left(T,\dot{\varepsilon}\right)+\sigma_f(T,\dot{\varepsilon},\varepsilon_p) \qquad (6.1.4.4)$$

where $\sigma_f=\alpha MGb\sqrt{\rho}$ is the classical Talyor hardening equation [183]. The solid solution stress was not changed with plastic strain by theory, but the fiction stress increases due to higher dislocation density. In addition, due to low stacking-fault energy, the deformation twinning plays an important role on the strengthening and ductility under dynamic impact. Thus, we incorporate the twinning boundary stress to the Eqn. 6.1.4.4:

$$\sigma\left(T,\dot{\varepsilon},\varepsilon_p,d\right)=\sigma_{HP}(d)+\sigma_{SS}\left(T,\dot{\varepsilon}\right)+\sigma_f(T,\dot{\varepsilon},\varepsilon_p)+\sigma_{twin}\,. \qquad (6.1.4.5)$$

The deformation twins are recognized to have “dynamic Hall-Petch” effect, where the twin boundary works as obstacles for dislocation motion [184,185]. At a true shear strain of 2.5, the twin spacing is measured to be 77 nm and twin fraction is 43% by combined EBSD and TEM methods. With the further increase of the shear strain, the twin spacing decreases and twin fraction increases. Thus, we can get the theoretical value of dislocation density and shear stress by the constitutive Eqn. 6.1.4.5, which is represented in Fig. 6.1.4.4.

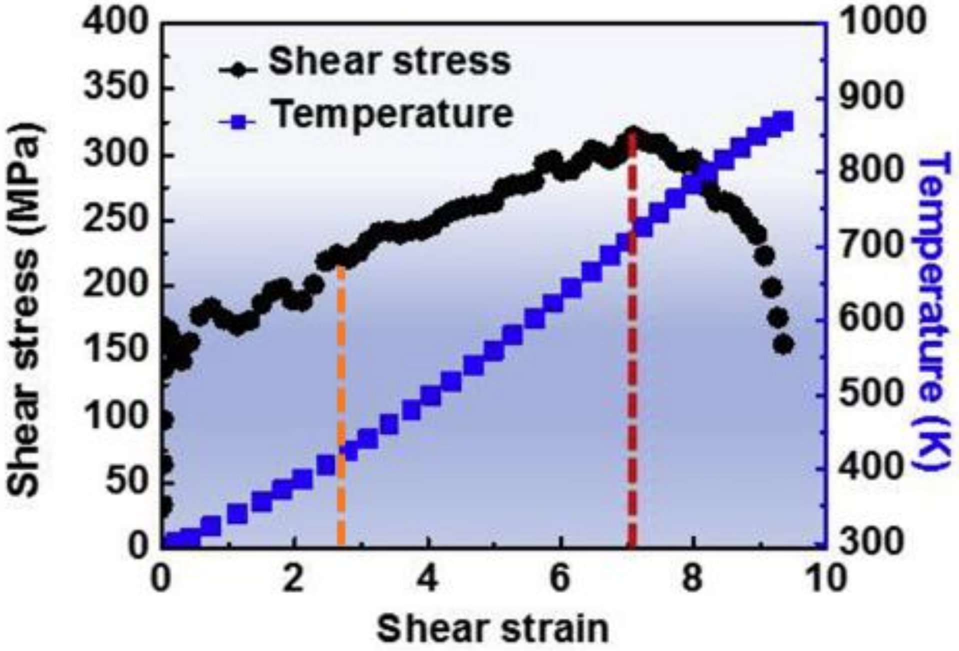

Figure 6.1.4.4. The shear-strain curve and corresponding star predicted by the constitutive model.

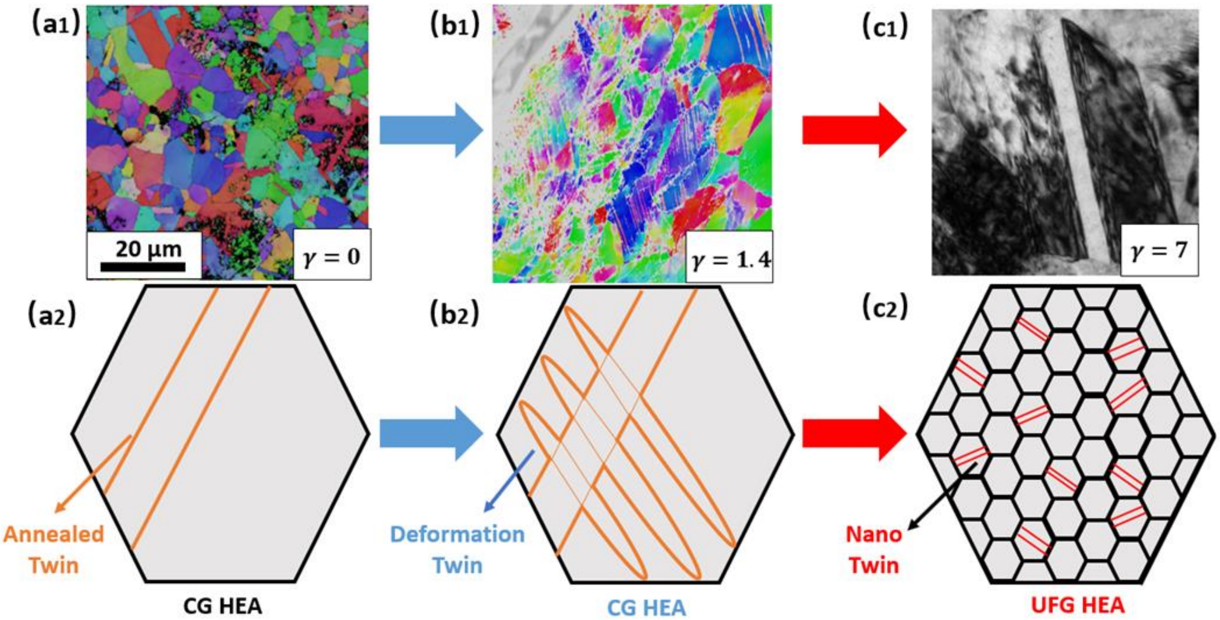

Figure 6.1.4.5. (a1,b1,c1) Images describe the evolution of microstructure under dynamic impact. (a2,b2,c2) Schematic drawing shows the corresponding strengthening mechanism and shear localization mechanism of low-stacking energy HEA.

Figs. 6.1.4.5 summaries the microstructural evolution before and after shear localization. The initial microstructure obtains annealed twins. Under dynamic loading, deformation twinning takes the lead at early stage. When thermal softening overcomes strain hardening, the shear band starts to form. Dynamic recrystallization occurs between twinning segments inside the grains. Although the alloy was severely deformed, shear localization was not thought to occur until an obvious thermal temperature rise. Thus, the softening was a result of thermal softening instead of the microstructural softening.

Longère *et al.* [186] pointed out that for very late onset of dynamic recrystallization, the initiation of shear band is mainly controlled by thermal softening, whereas for early dynamic recrystallization onset, the initiation of shear band is proposed to be dominant by microstructural softening. Between these two extreme conditions, thermal softening and microstructural softening both play an important role. This explains that even for the same material, different microstructure can indeed influence the shear localization behavior. This will be discussed in more detail in the following section 6.2.

6.2 Dynamic behavior of the as-processed CoCrFeMnNi high-entroy alloy

6.2.1. Microstructure

The as-received CoCrFeMnNi rod is 10 mm in diameter and 20 cm in length. The X-ray diffraction pattern confirms a single fcc crystal structure. The initial microstructure in Figs. 6.2.1.1(a,b) gives the insight that the initial sample was severely deformed. The change of misorientation inside the grains indicates the activity of dislocation motion and even twinning behavior. A higher yield stress but relatively low strain-hardening rate would be expected due to the severely deformed microstructure. The TEM images in Fig. 6.2.1.2 show the severely deformed microstructure. Fig. 6.2.1.2(a) shows the accumulation of dislocations. The diffraction pattern in Fig. 6.2.1.2(b) confirms its fcc crystal structure. The dislocation structure in Figs. 6.2.1.2(c,d) shows a very wavy microstructure. This may be attributed to heterogeneously distributed energy barriers for dislocation motion in solutes.

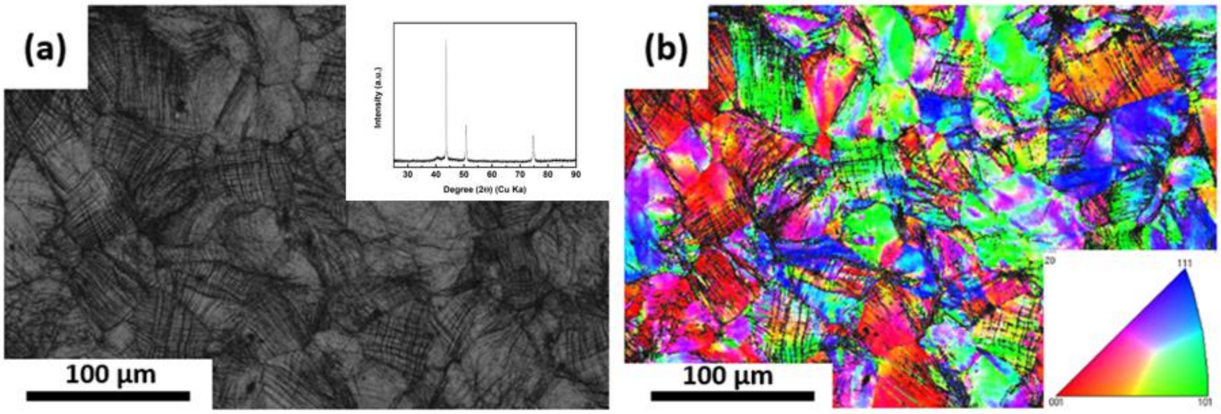

Figure 6.2.1.1. The initial microstructure in the transverse direction. (a) Backscattered electron (BSE) image of the microstructure and X-ray diffraction pattern; (b) Electron backscatter diffraction (EBSD) image.

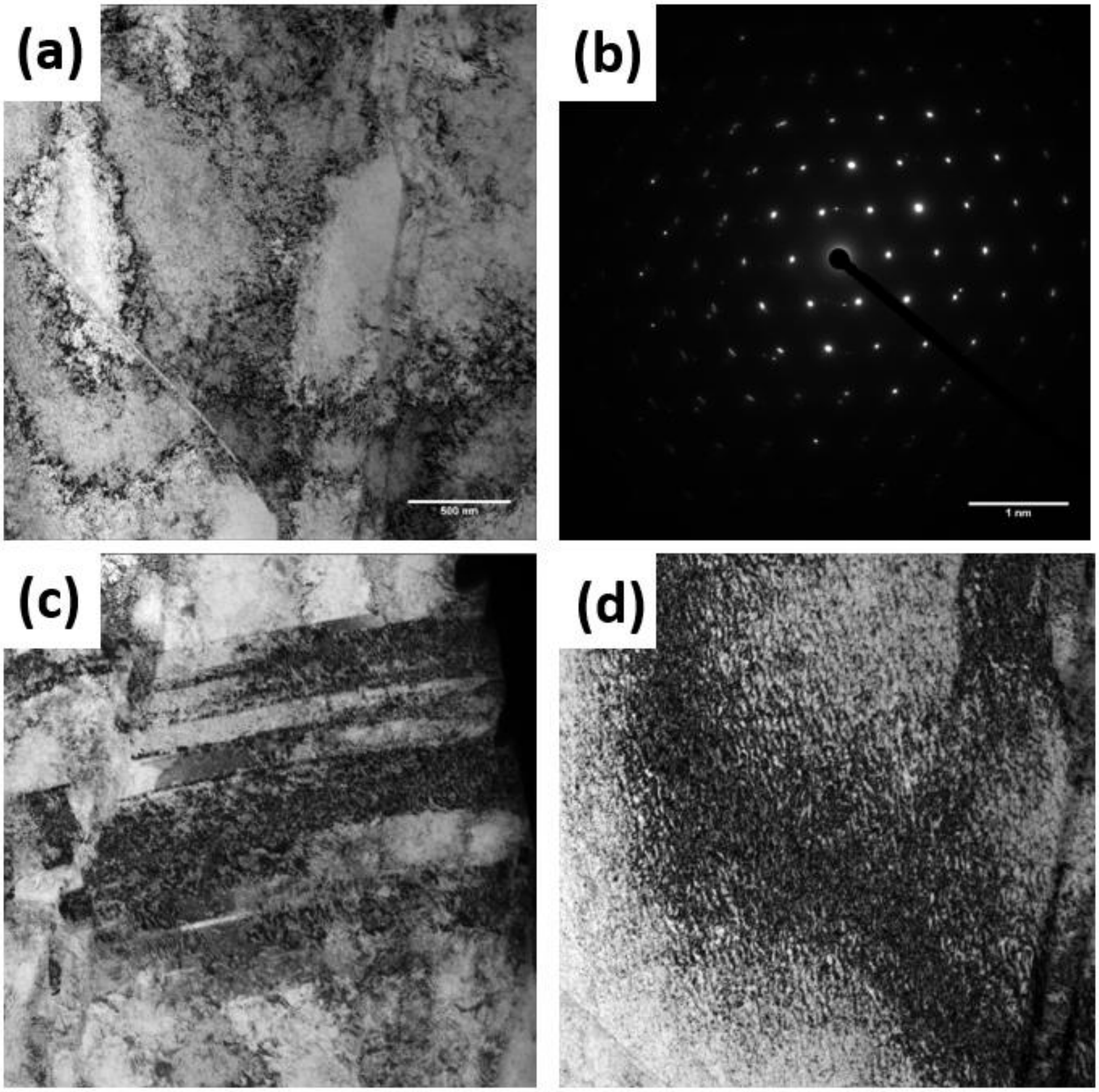

Figure 6.2.1.2. (a) TEM images showing the severely deformed initial microstructure. (b) Selected diffraction pattern showing the fcc structure. (c) Slip bands obtains dislocations. (d) Wavy dislocations.

6.2.2. Mechanical response

Fig. 6.2.2(a) depicts mechanical response of this material. Unlike the same alloy as discussed in part 6.1, this material reaches low strain-hardening rate after rapid initial strain hardening. This indicates that microstructure itself can influence the mechanical behavior of materials significantly. Fig. 6.6.2(b) shows that the alloy obtains obviously superior strain-hardening rate, which is over 1000 MPa, under dynamic impact. At quasi-static strain-rate 10^{-3} s^{-1}, the strain-hardening rate gradually reaches zero at a true strain of 0.2. However, the material does not fracture at this point. This means a balance of dislocation generation and annihilation.

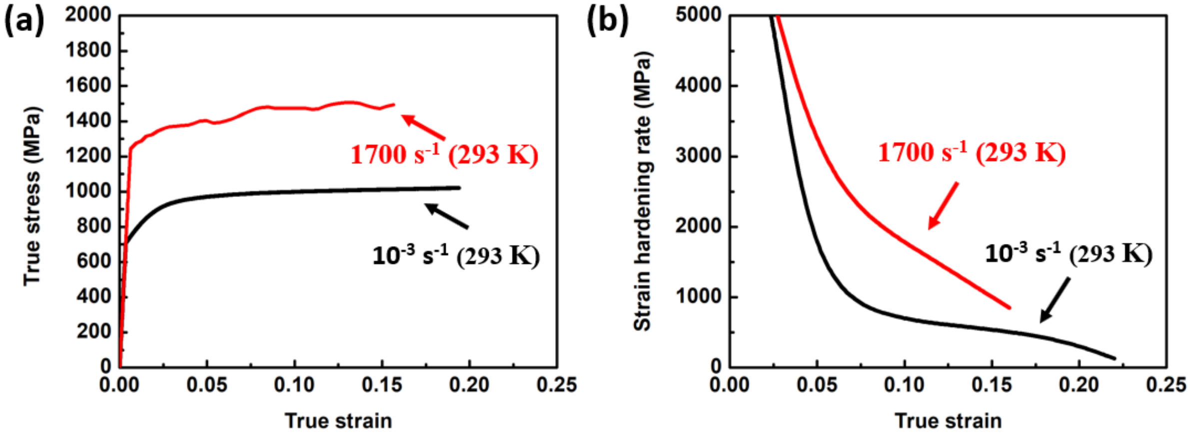

Figure 6.2.2. (a) Mechanical response of the CrMnFeCoNi Cantor HEA in compression, noting that the material can still continuously deform without shear fracture. (b) The strain-hardening rate of the material as a function of true strain.

By applying in-situ TEM, Ritchie and coauthors [184] reveal the strengthening mechanisms of CrCoNi-based medium- and high- entropy alloys at 93 K. It incorporated glide of partial and full dislocations, deformation twinning, multiple cross-slip and interaction between dislocation and grain boundary. Since the low-temperature effect counterparts with high strain-rate effect, similar behavior would be expected in this alloy under dynamic impact.

6.2.3 Width of shear bands

The results in dynamic impact of hat-shaped samples were summarized in Fig. 6.2.3.1. The alloy localizes in a shear strain of 1.5 at room temperature and 0.8 at 77 K. Due to a relatively large dislocation density initially, the dislocation density reaches critical crystallization value in a fast speed at low temperature. This is consistent with the results on the cryogenic temperature influence on titanium in chapter 5. Since the low temperature influence on the width of shear bands was not significant in the copper, it was proposed that the materials with very high thermal conductivity may not be so sensitivity to the development of shear bands.

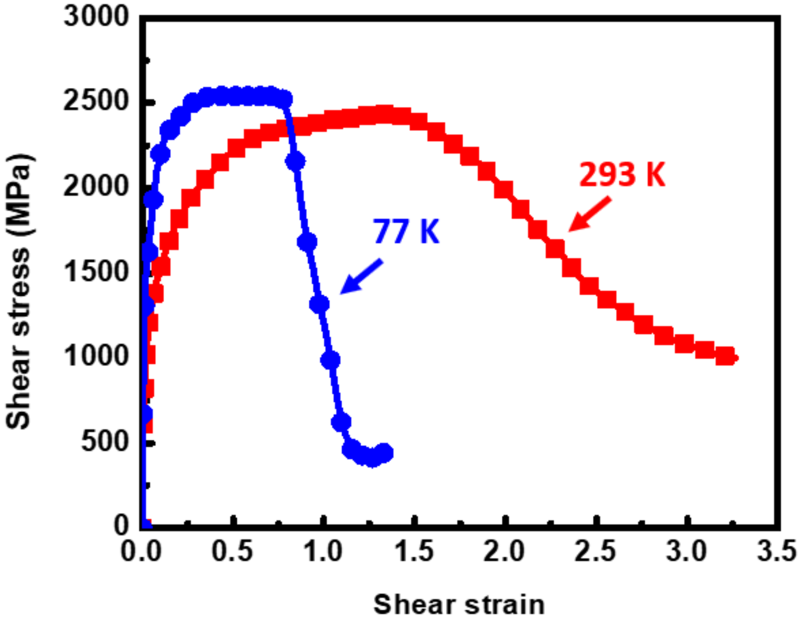

Figure 6.2.3.1. Shear stress and shear strain curves in shear bands occurring at 293 K and 77 K. The shear strain-rates are ~6*10^5 s^{-1} for both.

The shear band formed at 77 K in Fig. 6.2.3.2(e) obtains a narrower band width than that formed at room temperatures in Fig. 6.2.3.2(a). Under very similar shear strain-rates, the applied shear stress was increased, and specific heat capacity was reduced significantly at cryogenic temperature. This would cause the decrease of shear band as discussed in part 4.4.1. Correspondingly, the recrystallization grain size inside the shear band is smaller at low temperature.

Staker [24] predicted the critical shear strain for shear localization as mentioned:

$$\gamma_c = \frac{\rho C_p n}{-\frac{\partial \tau}{\partial T}} \quad . \tag{6.2.3}$$

This is the same with Eqn. 6.1.4.1. The thermal-softening parameter was -0.1 MPa/K, the density is 7.9 kg/m^3 and heat capacity is 450 J/(kg.K). n=0.0364 is fitting parameter of the powder index for the constitutive equation ($\tau = \tau_0 + K\gamma^n$) as mentioned. Thus, a theoretical critical shear strain of 1.3 was achieved, which corresponds well to the experimental result in Fig. 6.2.3.1.

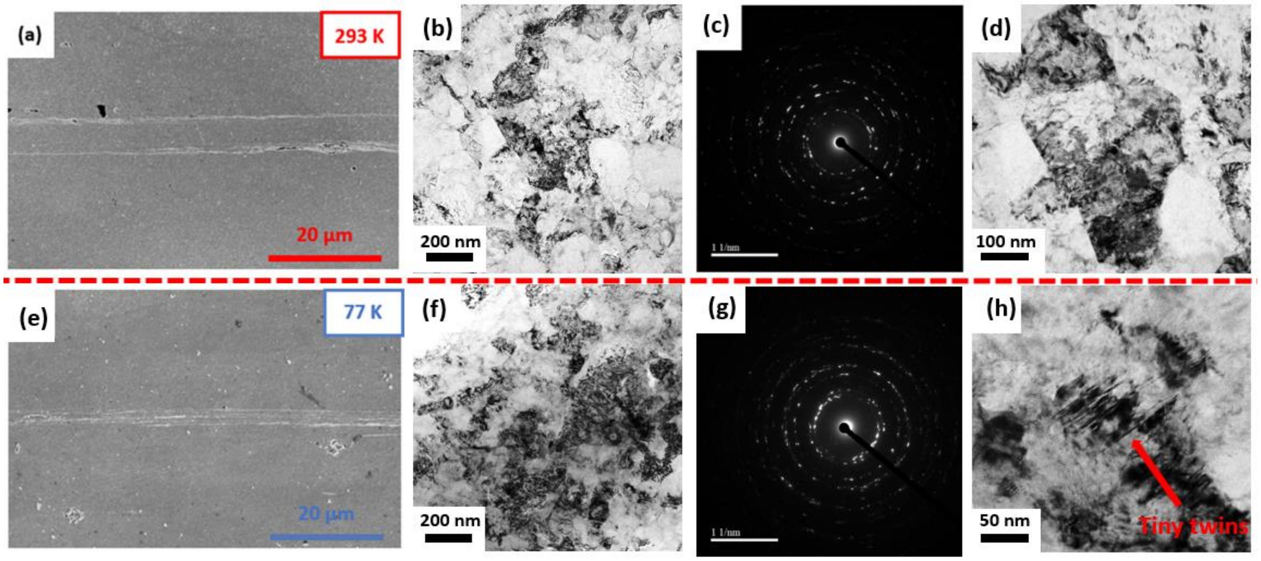

Figure 6.2.3.2 (a) Secondary electron microscopy (SEM) image of shear band formed at 293 K; (b,c,d) corresponding TEM images showing the formation of ultra-fine grains. (e) SEM image of shear band formed at 77 K. (f,g,h) Corresponding TEM images showing formation of ultra-fine and nano- grains. Some of grains contains nanotwins pointed by the red arrow in (h).

Figs. 6.2.3.2 (b) and (f) show the microstructures inside the shear bands formed at room temperature and low temperature, respectively. The corresponding diffraction patterns in Figs. 6.2.3.2 (c) and (g) depict a polycrystal fcc structure. Fig. 6.2.3.2 (d) shows obviously larger recrystallization grains than the ones formed in the shear band at 77 K. This is also attributed to higher applied shear stress in the low temperature, which is quite the same as the results in CG and UFG titanium. It is interesting that although the initial microstructure is severely deformed, all of grains have been recrystallized to a state with low dislocation density.

6.3 Summary of the chapter

Based on the experimental results and discussion, a resistance mechanism of shear localization was suggested. The alloys obtaining high strain-hardening rate, low thermal softening effect and high heat capacity are less prone to shear localization [182, 187]. Fig. 6.3 shows a summary of dynamic response of high-entropy alloys. The as-annealed Cantor alloy exhibits very promising dynamic impact properties. As discussed in part 6.1.4, for very late dynamic recrystallization onset, the initiation of shear band is mainly controlled by thermal softening. From our results, the as-annealed CrMnFeCoNi high-entropy alloys can indeed suppress shear localization, mainly due to its high strain-hardening rate and relatively low thermal-softening.

Miracle [188] pointed that although we have studied a serial of high-entropy alloy systems during last 15 years, we have not scratched the surface of it yet. He suggests creating new alloy systems with uncommon elements groupings [188], which could result in unexpected mechanical, chemical and physical properties.

Chapter 6, in part, is a reprint of the materials as it appears in “Adiabatic shear localization in the CrMnFeCoNi high-entropy alloy, Acta Materialia 2018 151: 424-431.” And “Mechanical properties of high-entropy alloys with emphasis on face-centered cubic alloys, Progress in materials science 2019 102:296-345”. This work was coauthored by “Zezhou Li, Shiteng Zhao, Senhat M Alotaibi, Yong Liu, Bingfeng Wang, Marc A Meyers” and “Zezhou Li, Shiteng Zhao, Robert O Ritchie, Marc A Meyers”, respectively. The dissertation author was the primary author of two paper.

Chapters 6, in part is currently being prepared for submission for publication of the material. Shiteng Zhao*, Zezhou Li*, Wen Yang, Robert O. Ritchie, Marc A. Meyers will be the coauthors. The dissertation author was the primary investigator and primary author of this paper.

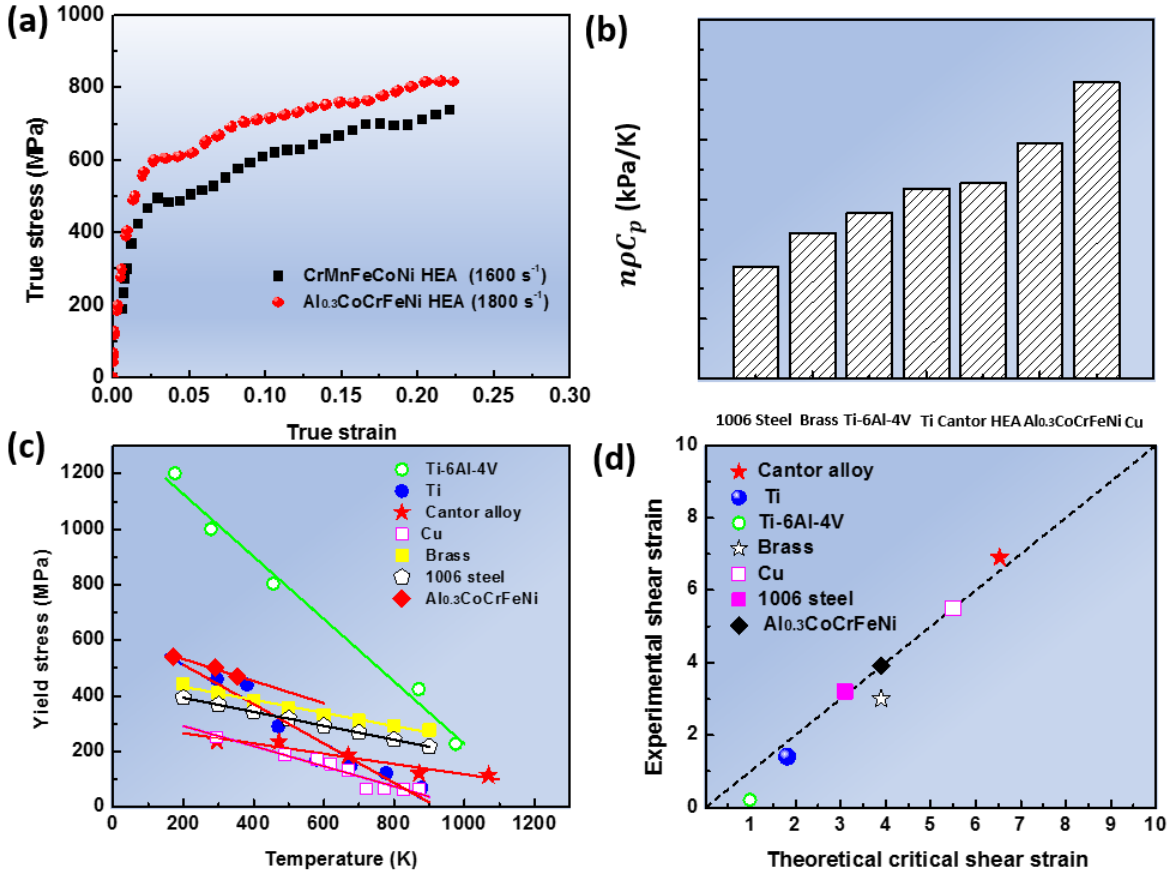

Figure 6.3. (a) Mechanical response of $Al_{0.3}CoCrFeNi$ HEA and the Cantor alloy under high strain-rates; (b) the value of $\rho C_p n$ for pure Ti, Ti-6Al-4V alloy, 1006-Steel, Copper, Brass, $Al_{0.3}CoCrFeNi$ HEA and the Cantor alloy; (c) thermal-softening effect of different materials; (d) predicted and experimental critical shear strain for shear localization [187].

Chapter 7. Summary and perspectives

7.1 Dislocation dynamics in ultrafine-grained titanium

(1) The strength of UFG titanium is significantly higher compared with CG titanium due to the Hall-Petch effect. In comparison with CG titanium, the strain-hardening rate of the UFG titanium is significantly lower due to the reduced dislocation activation volume and larger incidence of grain boundaries. The strain-rate sensitivity of UFG titanium does not change significantly with temperature, in agreement with CG titanium, indicating no significant change of deformation mechanisms.

(2) The width of the shear band of CG titanium does not change too much when decreasing temperature. In contrast, the width of shear band in UFG 500 nm titanium decreases from (~15 μm) formed at room temperature to ~ 5 μm at low temperature (173 K). The width of shear band of UFG 100 nm titanium decreases to ~ 1 μm at low temperature (77 K), which is one quarter of that (~ 4 μm) formed at room temperature. The combined effect of the decrease of thermal conductivity, the decrease of specific heat capacity and the increase of thermal-softening parameter for UFG titanium can lead to decreased widths according to Bai-Dodd and Grady's equations, and is indeed experimentally observed.

(3) A dislocation-based Kocks-Mecking model is proposed to describe the dislocation evolution prior to dynamic recrystallization for CG and UFG 500 nm titanium. The dislocation density in UFG titanium increases gradually until it reaches the critical value marked by a balance

between dislocation generation and annihilation. Once the temperature rises into the recrystallization value (~0.4 T_{melting}), the randomly distributed dislocations start to form an elongated ellipsoid configuration which on their turn breaks down to subgrains.

(4) The formation of nanograins inside the shear bands is explained in terms of the rotational dynamic recrystallization mechanism, which is expanded to incorporate the differences observed for the different initial conditions (grain size, initial deformation temperature, and shear strain).

(5) A reduction in the recrystallized grain size inside the shear bands for both CG and UFG titanium is observed for the initial deformation temperature in the cryogenic region. This is caused by a higher dislocation density reached at the onset of recrystallization due to higher accumulation rates in the first stage of deformation, at sub-ambient temperatures.

(6) The Zener-Hollomon parameter was used to predict the recrystallized grain size and critical dislocation density for shear localization. Additionally, the larger local shear strain in the shear bands at cryogenic temperatures, because of the decrease of width, also contributes to a more severe plastic deformation, inducing smaller grain size inside the shear band.

7.2 Strengthening mechanism in CoCrNi-based high-entropy alloys under dynamic impact

The second part of the investigation focused on mechanical response and shear localization of two compositions of fcc high-entropy alloys: $Al_{0.3}CoCrFeNi$ and CoCrFeMnNi.

(1) Mechanical response and microstructural evolution of an annealed $Al_{0.3}CoCrFeNi$ high-entropy alloy were investigated, with emphasis on the high strain-rate regime. The yield stress

σ_y increases from 216 MPa to 503 MPa with increasing strain-rate from 10^{-4} s^{-1} to 1800 s^{-1}, showing a significant strain-rate sensitivity of 0.053. The strain-hardening rate of the alloy is also significantly higher than a CG pure Al and retained in the dynamic regime. The TEM images and EBSD analysis of dislocations and mechanical twinning reveal that (1) the high strain-hardening ability enabled by solid solution hardening, forest dislocation hardening and twinning hardening, (2) the high strain-rate sensitivity and (3) modest thermal softening give rise to the high resistance to shear localization.

(2) The mechanical behavior of the single phase (fcc) CoCrFeMnNi high-entropy alloy (HEA) is examined in the dynamic regime. A series of experiments by dynamic-loading hat-shaped specimens using stopper rings to control the displacement are performed, and the alloy resists adiabatic shear formation up to a very large imposed shear strain of ~7. It is proposed that the combination of the excellent strain-hardening ability and moderate thermal-softening effect retards shear localization. Recrystallized ultrafine-grained grains (diameters of 100-300 nm) with twins are revealed inside the shear band. It is therefore proposed that the combination of the excellent strain-hardening ability and general thermal-softening effect of these two kinds of high-entropy alloys gives rise to remarkable resistance to shear localization, which makes HEAs an excellent candidate for impact resistance applications.

(3) Based on Hall-Petch strengthening, solid-solution strengthening, cutting forest dislocations, and twinning hardening mechanisms, a constitutive equation was proposed to describe the flow of the annealed CoCrFeMnNi high-entropy alloy under dynamic impact.

(4) The as-processed Cantor alloy shows relatively low strain-hardening rate, which makes

the materials more sensitive to the shear localization. As a result, this alloy localizes at a true shear strain of ~1.5. It indicates that microstructures indeed influence the mechanical properties of high-entropy alloys. This can be very useful to improve the mechanical properties of high-entropy alloys with different thermal and mechanical treatments.

7.3. Width of shear bands

We applied the Bai-Dodd [31] equation in our study to predict width of shear bands:

$$\delta = \left(\frac{\lambda T_b}{\tau_b \dot{\gamma}} \right)^{0.5} \tag{7.3.1}$$

where the subscript *b* refers to conditions inside the shear band.

A more rigorous (but still approximate) analysis was given by Grady and Kipp [33] as part of their continuing work on fragmentation caused by shock loading, expressed as:

$$\delta = \left(\frac{9\lambda^3}{\tau^3 (\frac{\partial \tau}{\partial T})^2 C_p \dot{\gamma}} \right)^{0.25} \tag{7.3.2}$$

The width of the shear band of CG titanium does not change too much when decreasing temperature. In contrast, the width of shear band of UFG 500 nm titanium decreases from (~15 μm) formed at room temperature to ~ 5 μm at a low temperature (77 K). The width of shear band of UFG 100 nm titanium decreases to ~ 1 μm at low temperature (77 K), which is one quarter of that (~ 4 μm) formed at room temperature. The combined effect of the decrease of thermal conductivity, the decrease of specific heat capacity and the increase of thermal-softening parameter on UFG titanium can explain the decreased widths according to Bai-Dodd and Grady-Kipp's equations and is indeed experimentally observed.

Similar results have been revealed in the as-processed Cantor alloys. Since the influence of low-temperature on the width of shear bands was not significant in the coarse-grained titanium and copper, it was proposed that the materials with very high thermal conductivity may be less sensitivity to the development of shear bands. However, this still needs to be examined by more experiments because thermal conductivity can also vary with decreasing temperatures.

7.4 Perspectives

Based on our results and discussion, there are still a lot of room in the study of dynamic properties in nanostructured materials and high-entropy alloys.

(1) The dislocation evolution model that was proposed before and during shear localization in both coarse-grained and ultrafine-grained titanium has been confirmed by experimental results. Due to a more obvious strain softening effect, dynamic properties of nanocrystalline titanium with grain size less than 100 nm would be attractive for further study.

(2) The annealed CoCrFeMnNi high-entropy alloy with low-stacking fault energy exhibits a high strain-hardening rate at both quasi-static and high strain-rates. Deformation mechanisms of this alloy have been examined by EBSD and TEM to reveal this high work-hardening ability. Also, the constitutive equation was be built to describe its mechanical behavior. The yield strength of the materials was proposed by Hall-Petch relationship and solid-solution strengthening. During

dynamic deformation, the material was mainly strengthened by forest dislocation and deformation twinning. This gives the indication of high work-hardening rate in this alloy under dynamic impact.

(3) The critical shear strain for shear localization was predicted by the classical Staker equation. The equation is based on the competition among strain-hardening, strain-rate sensitivity and thermal-softening. From Fig. 7.4, the study on impact resistant high-entropy alloys gives the conclusion that the material with high strain hardening-rate, high specific heat capacity, high density and low thermal-softening effect would be less prone to shear localization. Although the strain-rate hardening effect is ignored in this classical equation, the high strain-rate sensitivity needs to be incorporated for a more rigorous examination. This would be a worthwhile extension of the Staker equation.

(4) A model for evolution of shear localization for materials with low stacking-fault energy was proposed. The material forms deformation twins easily under dynamic impact. Then, when shear localization occurs, dynamic recrystallization happens easily inside the segmented grains. Due to its low stacking fault energy, the recrystallization twins are easily found inside the recrystallized grains. A specific model for rotational dynamic recrystallization in alloys with low stacking-fault energy needs to be developed.

(5) It is now concluded that mechanical properties of high-entropy alloys were not just dependent on the number of mixed elements. Very careful simulation and experiments need to be carried out to examine and reveal how the elements themselves and even microstructures could influence the mechanical and other properties of high-entropy alloys.

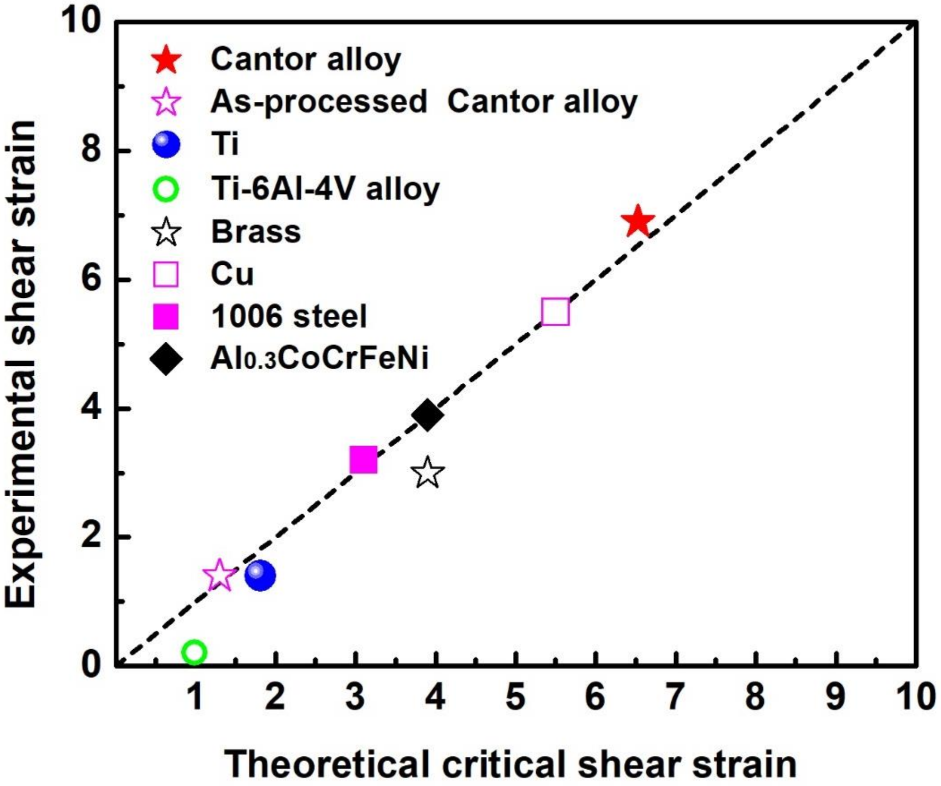

Figure. 7.4. Summary of critical shear strain for shear localization in our materials and other structural materials [186].

References

[1] Gleiter H. Nanostructured materials: basic concepts and microstructure. Acta Materialia. 2000;48:1-29.

[2] Meyers MA, Mishra A, Benson DJ. Mechanical properties of nanocrystalline materials. Progress in materials science. 2006;51:427-556.

[3] Meyers MA. Dynamic behavior of materials: John wiley & sons. 1994.

[4] Hahn EN, Meyers MA. Grain-size dependent mechanical behavior of nanocrystalline metals. Materials Science and Engineering: A. 2015;646:101-34.

[5] Meyers MA, Ashworth E. A model for the effect of grain size on the yield stress of metals. Philosophical Magazine A. 1982;46:737-59.

[6] Van Swygenhoven H, Derlet P, Frøseth A. Nucleation and propagation of dislocations in nanocrystalline fcc metals. Acta Materialia. 2006;54:1975-83.

[7] Conrad H, Narayan J. On the grain size softening in nanocrystalline materials. Scripta materialia. 2000;11:1025-30.

[8] Haslam A, Moldovan D, Phillpot S, Wolf D, Gleiter H. Combined atomistic and mesoscale simulation of grain growth in nanocrystalline thin films. Computational materials science. 2002;23:15-32.

[9] Banerjee D, Williams J. Perspectives on titanium science and technology. Acta Materialia. 2013;61:844-79.

[10] Meyers M, Pak H-R. Observation of an adiabatic shear band in titanium by high-voltage transmission electron microscopy. Acta Metallurgica. 1986;34:2493-9.

[11] Meyers M, Subhash G, Kad B, Prasad L. Evolution of microstructure and shear-band formation in α-hcp titanium. Mechanics of Materials. 1994;17:175-93.

[12] Meyers M, LaSalvia J, Nesterenko V, Chen Y, Kad B, McNelley T. Recrystallization and related phenomena. Proc Rex, Monterey. 1997;279.

[13] Meyers MA, Nesterenko VF, LaSalvia JC, Xue Q. Shear localization in dynamic deformation of materials: microstructural evolution and self-organization. Materials Science and Engineering:

A. 2001;317:204-25.

[14] Nemat-Nasser S, Guo W, Cheng J. Mechanical properties and deformation mechanisms of a commercially pure titanium. Acta materialia. 1999;47:3705-20.

[15] Chichili D, Ramesh K, Hemker K. The high-strain-rate response of alpha-titanium: experiments, deformation mechanisms and modeling. Acta Materialia. 1998;46:1025-43.

[16] Cantor B, Chang I, Knight P, Vincent A. Microstructural development in equiatomic multicomponent alloys. Materials Science and Engineering: A. 2004;375:213-8.

[17] Miracle DB, Senkov ON. A critical review of high entropy alloys and related concepts. Acta Materialia. 2017;122:448-511.

[18] Gaskell DR, Laughlin DE. Introduction to the Thermodynamics of Materials: CRC press; 2017.

[19] Ruffa A. Thermal potential, mechanical instability, and melting entropy. Physical Review B. 1982;25:5895.

[20] Yeh JW, Chen SK, Lin SJ, Gan JY, Chin TS, Shun TT, et al. Nanostructured high-entropy alloys with multiple principal elements: novel alloy design concepts and outcomes. Advanced Engineering Materials. 2004;6:299-303.

[21] Yeh JW, Chen YL, Lin SJ, Chen SK. High-entropy alloys–a new era of exploitation. Materials Science Forum: Trans Tech Publ; 2007. p. 1-9.

[22] Backman ME, Finnegan SA. The propagation of adiabatic shear. Metallurgical Effects at High Strain Rates: Springer; 1973. p. 531-43.

[23] Recht R. Catastrophic thermoplastic shear. Journal of Applied Mechanics. 1964;31:189-93.

[24] Staker M. The relation between adiabatic shear instability strain and material properties. Acta Metallurgica. 1981;29:683-9.

[25] Zheng C, Wang F, Cheng X, Liu J, Liu T, Zhu Z, Yang K, Peng M, Jin D. Capturing of the propagating processes of adiabatic shear band in Ti–6Al–4V alloys under dynamic compression. Materials Science and Engineering: A. 2016;658:60-7.

[26] Wright TW. The physics and mathematics of adiabatic shear bands: Cambridge University Press. 2002.

[27] Wei Q, Kecskes L, Jiao T, Hartwig K, Ramesh K, Ma E. Adiabatic shear banding in ultrafine-grained Fe processed by severe plastic deformation. Acta Materialia. 2004;52:1859-69.

[28] Sagapuram D, Viswanathan K, Mahato A, Sundaram NK, M'Saoubi R, Trumble KP, et al. Geometric flow control of shear bands by suppression of viscous sliding. Proceedings of the Royal Society A: Mathematical, Physical and Engineering Sciences. 2016;472:20160167.

[29] Considère A. Mémoire sur l'emploi du fer et de l'acier dans les constructions, Annales des ponts et chaussées I sem. 1885.

[30] Bai Y. Thermo-plastic instability in simple shear. Journal of the Mechanics and Physics of Solids. 1982;30:195-207.

[31] Dodd B, Bai Y. Width of adiabatic shear bands. Materials Science and Technology. 1985;1:38-40.

[32] Dodd B, Bai Y. Adiabatic shear localization: frontiers and advances: Elsevier. 2012.

[33] Grady D, Kipp M. The growth of unstable thermoplastic shear with application to steady-wave shock compression in solids. Journal of the Mechanics and Physics of Solids. 1987;35:95-119.

[34] Erlich D, Curran D, Seaman L. Further Development of a Computational Shear Band Model. SRI INTERNATIONAL MENLO PARK CA. 1980.

[35] Wu F, Freund L. Deformation trapping due to thermoplastic instability in one-dimensional wave propagation. Journal of the Mechanics and Physics of Solids. 1984;32:119-32.

[36] Zhou M, Rosakis A, Ravichandran G. Dynamically propagating shear bands in impact-loaded prenotched plates—I. Experimental investigations of temperature signatures and propagation speed. Journal of the Mechanics and Physics of Solids. 1996;44:981-1006.

[37] Gottstein G. Physical foundations of materials science: Springer Science & Business Media; 2013.

[38] Meyers MA, Nesterenko VF, LaSalvia JC, Xue Q. Shear localization in dynamic deformation of materials: microstructural evolution and self-organization. Materials Science and Engineering: A. 2001;317:204-25.

[39] Chen XW, Sun K, Wang FC. Revealing microstructual evolution of adiabatic shear band in

Ti-15Mo-3Al-2.7Nb-0.2Si alloy. Rare Metal and Materials and Engineering. 2008;37:1756-59.

[40] Hines JA, Vecchio KS, Ahzi S. A model for microstructure evolution in adiabatic shear bands. Metallurgical and Materials Transactions A. 1998;29:191-203.

[41] Nieh T, Wadsworth J. Hall-Petch relation in nanocrystalline solids. Scripta Metallurgica et Materialia. 1991;25:955-8.

[42] Benson DJ, Fu H-H, Meyers MA. On the effect of grain size on yield stress: extension into nanocrystalline domain. Materials Science and Engineering: A. 2001;319:854-61.

[43] Li JC. High-Angle Tilt Boundary—A Dislocation Core Model. Journal of Applied Physics. 1961;32:525-41.

[44] Wang Y, Chen M, Zhou F, Ma E. High tensile ductility in a nanostructured metal. Nature. 2002;419:912.

[45] Ma E. Watching the nanograins roll. Science. 2004;305:623-4.

[46] Meyers M, Vöhringer O, Lubarda V. The onset of twinning in metals: a constitutive description. Acta Materialia. 2001;49:4025-39.

[47] Asaro RJ, Krysl P, Kad B. Deformation mechanism transitions in nanoscale fcc metals. Philosophical Magazine Letters. 2003;83:733-43.

[48] Liao X, Srinivasan S, Zhao Y, Baskes M, Zhu Y, Zhou F, et al. Formation mechanism of wide stacking faults in nanocrystalline Al. Applied physics letters. 2004;84:3564-6.

[49] Zhu Y, Liao X, Srinivasan S, Zhao Y, Baskes M, Zhou F, et al. Nucleation and growth of deformation twins in nanocrystalline aluminum. Applied physics letters. 2004;85:5049-51.

[50] Wei Q, Cheng S, Ramesh K, Ma E. Effect of nanocrystalline and ultrafine grain sizes on the strain rate sensitivity and activation volume: fcc versus bcc metals. Materials Science and Engineering: A. 2004;381:71-9.

[51] Zhang X, Wang H, Scattergood R, Narayan J, Koch C, Sergueeva A, et al. Studies of deformation mechanisms in ultra-fine-grained and nanostructured Zn. Acta Materialia. 2002;50:4823-30.

[52] Jia D, Ramesh K, Ma E. Effects of nanocrystalline and ultrafine grain sizes on constitutive behavior and shear bands in iron. Acta Materialia. 2003;51:3495-509.

[53] Wei Q, Jiao T, Ramesh K, Ma E, Kecskes L, Magness L, et al. Mechanical behavior and dynamic failure of high-strength ultrafine grained tungsten under uniaxial compression. Acta Materialia. 2006;54:77-87.

[54] Mishra A, Martin M, Thadhani N, Kad B, Kenik EA, Meyers M. High-strain-rate response of ultra-fine-grained copper. Acta Materialia. 2008;56:2770-83.

[55] Hua P, Chu K, Sun Q. Grain refinement and amorphization in nanocrystalline NiTi micropillars under uniaxial compression. Scripta Materialia. 2018;154:123-6.

[56] Gludovatz B, Hohenwarter A, Catoor D, Chang EH, George EP, Ritchie RO. A fracture-resistant high-entropy alloy for cryogenic applications. Science. 2014;345:1153-8.

[57] Zhang Z, Mao M, Wang J, Gludovatz B, Zhang Z, Mao SX, et al. Nanoscale origins of the damage tolerance of the high-entropy alloy CrMnFeCoNi. Nature communications. 2015;6:10143.

[58] Lee D-H, Seok M-Y, Zhao Y, Choi I-C, He J, Lu Z, et al. Spherical nanoindentation creep behavior of nanocrystalline and coarse-grained CoCrFeMnNi high-entropy alloys. Acta Materialia. 2016;109:314-22.

[59] Wang B, Fu A, Huang X, Liu B, Liu Y, Li Z, et al. Mechanical properties and microstructure of the CoCrFeMnNi high entropy alloy under high strain rate compression. Journal of Materials Engineering and Performance. 2016;25:2985-92.

[60] Li Z, Pradeep KG, Deng Y, Raabe D, Tasan CC. Metastable high-entropy dual-phase alloys overcome the strength–ductility trade-off. Nature. 2016;534:227.

[61] Patriarca L, Ojha A, Sehitoglu H, Chumlyakov Y. Slip nucleation in single crystal FeNiCoCrMn high entropy alloy. Scripta Materialia. 2016;112:54-7.

[62] Varvenne C, Luque A, Curtin WA. Theory of strengthening in fcc high entropy alloys. Acta Materialia. 2016;118:164-76.

[63] Chen Y, Li Y, Cheng X, Xu Z, Wu C, Cheng B, Wang M. Interstitial strengthening of refractory ZrTiHfNb$_{0.5}$Ta$_{0.5}$O$_x$ (x= 0.05, 0.1, 0.2) high-entropy alloys. Materials Letters 2018;228:145-147.

[64] Laplanche G, Bonneville J, Varvenne C, Curtin W, George EP. Thermal activation parameters of plastic flow reveal deformation mechanisms in the CrMnFeCoNi high-entropy alloy. Acta Materialia. 2018;143:257-64.

[65] Yang T, Zhao Y, Tong Y, Jiao Z, Wei J, Cai J, et al. Multicomponent intermetallic nanoparticles and superb mechanical behaviors of complex alloys. Science. 2018;362:933-7.

[66] Ding J, Yu Q, Asta M, Ritchie RO. Tunable stacking fault energies by tailoring local chemical order in CrCoNi medium-entropy alloys. Proceedings of the National Academy of Sciences. 2018;115:8919-24.

[67] Lei Z, Liu X, Wu Y, Wang H, Jiang S, Wang S, et al. Enhanced strength and ductility in a high-entropy alloy via ordered oxygen complexes. Nature. 2018;563:546.

[68] Vecchio KS, Jiang F. Improved pulse shaping to achieve constant strain rate and stress equilibrium in split-Hopkinson pressure bar testing. Metallurgical and materials transactions A. 2007;38:2655-65.

[69] Kuhn H, Medlin D. ASM Handbook. Volume 8: Mechanical Testing and Evaluation. ASM International, Member/Customer Service Center, Materials Park, OH 44073-0002, USA, 2000 998. 2000.

[70] Follansbee P, Frantz C. Wave propagation in the split Hopkinson pressure bar. Journal of Engineering Materials and Technology. 1983;105:61-6.

[71] Chawla KK, Meyers M. Mechanical behavior of materials: Prentice Hall. 1999.

[72] Knoll M. Aufladepotentiel und sekundäremission elektronenbestrahlter körper. Z tech Phys. 1935;16:467-75.

[73] Von Ardenne M. Das elektronen-rastermikroskop. Zeitschrift für Physik A Hadrons and Nuclei. 1938;109:553-72.

[74] Stewart A. The origins and development of scanning electron microscopy. Journal of Microscopy. 1985;139:121-7.

[75] Watt IM. The principles and practice of electron microscopy: Cambridge University Press. 1997.

[76] Fitzgerald R, Keil K, Heinrich KF. Solid-state energy-dispersion spectrometer for electron-microprobe X-ray analysis. Science. 1968;159:528-30.

[77] Schwartz AJ, Kumar M, Adams BL, Field DP. Electron backscatter diffraction in materials science: Springer. 2000.

[78] Reimer L. Transmission electron microscopy: physics of image formation and microanalysis: Springer. 2013.

[79] Waseda Y, Matsubara E, Shinoda K. X-ray diffraction crystallography: introduction, examples and solved problems: Springer Science & Business Media. 2011.

[80] Valiev RZ, Islamgaliev RK, Alexandrov IV. Bulk nanostructured materials from severe plastic deformation. Progress in materials science. 2000;45:103-89.

[81] Valiev RZ, Langdon TG. Principles of equal-channel angular pressing as a processing tool for grain refinement. Progress in materials science. 2006;51:881-981.

[82] Sergueeva A, Stolyarov V, Valiev R, Mukherjee A. Advanced mechanical properties of pure titanium with ultrafine grained structure. Scripta Materialia. 2001;45:747-52.

[83] Chen Y-J, Meyers M, Nesterenko V. Spontaneous and forced shear localization in high-strain-rate deformation of tantalum. Materials Science and Engineering: A. 1999;268:70-82.

[84] Li Z, Wang B, Zhao S, Valiev RZ, Vecchio KS, Meyers MA. Dynamic deformation and failure of ultrafine-grained titanium. Acta Materialia. 2017;125:210-8.

[85] Lopes FPD, Lu CH, Zhao S, Monteiro SN, Meyers MA. Room temperature dynamic strain aging in ultrafine-grained titanium. Metallurgical and Materials Transactions A. 2015;46:4468-77.

[86] Jia D, Wang Y, Ramesh K, Ma E, Zhu Y, Valiev R. Deformation behavior and plastic instabilities of ultrafine-grained titanium. Applied physics letters. 2001;79:611-3.

[87] Elias CN, Meyers MA, Valiev RZ, Monteiro SN. Ultrafine grained titanium for biomedical applications: An overview of performance. Journal of Materials Research and Technology. 2013;2:340-50.

[88] Lu L, Schwaiger R, Shan Z, Dao M, Lu K, Suresh S. Nano-sized twins induce high rate sensitivity of flow stress in pure copper. Acta Materialia. 2005;53:2169-79.

[89] Zerilli FJ, Armstrong RW. Dislocation-mechanics-based constitutive relations for material dynamics calculations. Journal of applied physics. 1987;61:1816-25.

[90] Zerilli FJ, Armstrong RW. Description of tantalum deformation behavior by dislocation mechanics based constitutive relations. Journal of applied physics. 1990;68:1580-91.

[91] Long F-W, Jiang Q-W, Xiao L, Li X-W. Compressive deformation behaviors of coarse-and

ultrafine-grained pure titanium at different temperatures: a comparative study. Materials Transactions. 2011;52:1617-22.

[92] Culver RS. Thermal instability strain in dynamic plastic deformation. Metallurgical effects at high strain rates: Springer; 1973. p. 519-30.

[93] Guo Y, Ruan Q, Zhu S, Wei Q, Chen H, Lu J, et al. Temperature Rise Associated with Adiabatic Shear Band: Causality Clarified. Physical Review Letters. 2019;122:015503.

[94] Zhao S, Kad B, Remington BA, LaSalvia JC, Wehrenberg CE, Behler KD, et al. Directional amorphization of boron carbide subjected to laser shock compression. Proceedings of the National Academy of Sciences. 2016;113:12088-93.

[95] Zhao S, Hahn E, Kad B, Remington B, Wehrenberg C, Bringa E, et al. Amorphization and nanocrystallization of silicon under shock compression. Acta Materialia. 2016;103:519-33.

[96] Andrade U, Meyers M, Vecchio K, Chokshi A. Dynamic recrystallization in high-strain, high-strain-rate plastic deformation of copper. Acta metallurgica et materialia. 1994;42:3183-95.

[97] Lins J, Sandim H, Kestenbach H-J, Raabe D, Vecchio K. A microstructural investigation of adiabatic shear bands in an interstitial free steel. Materials Science and Engineering: A. 2007;457:205-18.

[98] Teng X, Wierzbicki T, Couque H. On the transition from adiabatic shear banding to fracture. Mechanics of Materials. 2007;39:107-25.

[99] Nemat-Nasser S, Isaacs JB, Liu M. Microstructure of high-strain, high-strain-rate deformed tantalum. Acta Materialia. 1998;46:1307-25.

[100] Xue Q, Meyers M, Nesterenko V. Self-organization of shear bands in titanium and Ti–6Al–4V alloy. Acta Materialia. 2002;50:575-96.

[101] Bai Y, Xuc Q, Xu Y, Shen L. Characteristics and microstructure in the evolution of shear localization in Ti-6A1-4V alloy. Mechanics of materials. 1994;17:155-64.

[102] Koeppel B, Subhash G. Influence of cold rolling and strain rate on plastic response of powder metallurgy and chemical vapor deposition rhenium. Metallurgical and Materials Transactions A. 1999;30:2641-8.

[103] Subhash G, Pletka B, Ravichandran G. Plastic deformation of hafnium under uniaxial compression. Metallurgical and Materials Transactions A. 1997;28:1479-87.

[104] Dodd B, Bai Y. Width of adiabatic shear bands formed under combined stresses. Materials science and technology. 1989;5:557-9.

[105] Grady D. Dissipation in adiabatic shear bands. Mechanics of materials. 1994;17:289-93.

[106] Philips'Gloeilampenfabrieken O. A method of measuring specific resistivity and Hall effect of discs of arbitrary shape. Philips Res Rep. 1958;13:1-9.

[107] van der Pauw LJ. A method of measuring the resistivity and Hall coefficient on lamellae of arbitrary shape. Philips technical review. 1958;20:220-4.

[108] Guo F, Zhu K, Trannoy N, Lu J. Examination of thermal properties by scanning thermal microscopy in ultrafine-grained pure titanium surface layer produced by surface mechanical attrition treatment. Thermochimica Acta. 2004;419:239-46.

[109] Hidnert P. Thermal expansion of titanium. J Res Natl Bur Stand. 1943;30:101.

[110] Debye P. Zur theorie der spezifischen wärmen. Annalen der Physik. 1912;344:789-839.

[111] Gaskell D. Introduction to the Thermodynamics of Materials, 5th Edn. New York: Taylor and Francis group, LLC. 2008.

[112] Kelley K. Specific heats at low temperatures of titanium and titanium carbide. Industrial & Engineering Chemistry. 1944;36:865-6.

[113] Sun X, Guo Y, Wei Q, Li Y, Zhang S. A comparative study on the microstructure and mechanical behavior of titanium: Ultrafine grain vs. coarse grain. Materials Science and Engineering: A. 2016;669:226-45.

[114] Sauvage X, Wilde G, Divinski S, Horita Z, Valiev R. Grain boundaries in ultrafine grained materials processed by severe plastic deformation and related phenomena. Materials Science and Engineering: A. 2012;540:1-12.

[115] Perez RA, Nakajima H, Dyment F. Diffusion in α-Ti and Zr. Materials Transactions. 2003;44:2-13.

[116] Roth T, Suppayak P. The surface and grain boundary free energies of pure titanium and the titanium alloy Ti□ 6Al□ 4V. Materials Science and Engineering. 1978;35:187-96.

[117] Humphreys FJ, Hatherly M. Recrystallization and related annealing phenomena: Elsevier;

2012.

[118] Hoseini M, Pourian MH, Bridier F, Vali H, Szpunar JA, Bocher P. Thermal stability and annealing behaviour of ultrafine grained commercially pure titanium. Materials Science and Engineering: A. 2012;532:58-63.

[119] Zener C, Hollomon JH. Effect of strain rate upon plastic flow of steel. Journal of applied physics. 1944;15:22-32.

[120] Li Y, Zhang Y, Tao N, Lu K. Effect of the Zener–Hollomon parameter on the microstructures and mechanical properties of Cu subjected to plastic deformation. Acta Materialia. 2009;57:761-72.

[121] Schiøtz J, Jacobsen KW. A maximum in the strength of nanocrystalline copper. Science. 2003;301:1357-9.

[122] Taylor GI. The mechanism of plastic deformation of crystals. Part I.—Theoretical. Proceedings of the Royal Society of London Series A, Containing Papers of a Mathematical and Physical Character. 1934;145:362-87.

[123] Kocks U, Argon A, Ashby M, Chalmers B, Christian J, Massalski T. PROG MATER SCI. Prog Mater Sci. 1975;19:1-281.

[124] Derby B. The dependence of grain size on stress during dynamic recrystallisation. Acta metallurgica et materialia. 1991;39:955-62.

[125] Cai W, Nix WD. Imperfections in crystalline solids: Cambridge University Press; 2016.

[126] Harris K, Singh V, King A. Grain rotation in thin films of gold. Acta Materialia. 1998;46:2623-33.

[127] Sushko GB, Verkhovtsev AV, Yakubovich AV, Schramm S, Solov'yov AV. Molecular dynamics simulation of self-diffusion processes in titanium in bulk material, on grain junctions and on surface. The Journal of Physical Chemistry A. 2014;118:6685-91.

[128] Wang Y, Ye H. On the tilt grain boundaries in hcp Ti with [0001] orientation. Philosophical Magazine A. 1997;75:261-72.

[129] Wang L, Teng J, Liu P, Hirata A, Ma E, Zhang Z, et al. Grain rotation mediated by grain boundary dislocations in nanocrystalline platinum. Nature communications. 2014;5:4402.

[130] Zhu C, Livescu V, Harrington T, Dippo O, Gray III GT, Vecchio KS. Investigation of the shear response and geometrically necessary dislocation densities in shear localization in high-purity titanium. International Journal of Plasticity. 2017;92:148-63.

[131] Li Y, Tao N, Lu K. Microstructural evolution and nanostructure formation in copper during dynamic plastic deformation at cryogenic temperatures. Acta Materialia. 2008;56:230-41.

[132] Mishra A, Kad B, Gregori F, Meyers M. Microstructural evolution in copper subjected to severe plastic deformation: Experiments and analysis. Acta Materialia. 2007;55:13-28.

[133] Sun JL, Trimby PW, Yan FK, Liao XZ, Tao NR, Wang JT. Grain size effect on deformation twinning propensity in ultrafine-grained hexagonal close-packed titanium. Scripta Materialia. 2013;69:428-31.

[134] Lu K, Lu L, Suresh S. Strengthening materials by engineering coherent internal boundaries at the nanoscale. Science. 2009;324:349-52.

[135] Yan F, Zhang H, Tao N, Lu K. Quantifying the microstructures of pure Cu subjected to dynamic plastic deformation at cryogenic temperature. Journal of Materials Science & Technology. 2011;27:673-9.

[136] Li Z, Zhao S, Diao H, Liaw P, Meyers M. High-velocity deformation of $Al_{0.3}$CoCrFeNi high-entropy alloy: remarkable resistance to shear failure. Scientific reports. 2017;7:42742.

[137] Tang Z, Gao MC, Diao H, Yang T, Liu J, Zuo T, et al. Aluminum alloying effects on lattice types, microstructures, and mechanical behavior of high-entropy alloys systems. JOM. 2013;65:1848-58.

[138] Wang P, Cheng X, Cai H, Xue Y, Zhang Y. Influence of increasing Al concentration on phase, microstructure and mechanical behaviors of $Ni_{1.5}CoFeCu_{1-x}Al_xV_{0.5}$ high entropy alloys. Materials Science and Engineering: A. 2017;708:523-36.

[139] Haoyan D, Louis J.S, Zhi T, Takeshi E, Liaw PK, Local Structures of High-Entropy Alloys (HEAs) on Atomic Scales: An Overview. JOM. 2015;67:2321-2325.

[140] Guo W, Dmowski W, Noh J-Y, Rack P, Liaw PK, Egami T. Local atomic structure of a high-entropy alloy: an X-ray and neutron scattering study. Metallurgical and Materials Transactions A. 2013;44:1994-7.

[141] Wang W-R, Wang W-L, Wang S-C, Tsai Y-C, Lai C-H, Yeh J-W. Effects of Al addition on the microstructure and mechanical property of AlxCoCrFeNi high-entropy alloys. Intermetallics.

2012;26:44-51.

[142] Xu J, Li J, Shi L, Shan D, Guo B. Effects of temperature, strain rate and specimen size on the deformation behaviors at micro/meso-scale in ultrafine-grained pure Al. Materials Characterization. 2015;109:181-8.

[143] Lu L, Chen X, Huang X, Lu K. Revealing the maximum strength in nanotwinned copper. Science. 2009;323:607-10.

[144] Hadfield RA. Hadfield's manganese steel. Science. 1888;12:284-6.

[145] Steinmetz DR, Jäpel T, Wietbrock B, Eisenlohr P, Gutierrez-Urrutia I, Saeed–Akbari A, et al. Revealing the strain-hardening behavior of twinning-induced plasticity steels: Theory, simulations, experiments. Acta Materialia. 2013;61:494-510.

[146] Xiong Z-p, Ren X-p, Bao W-p, Li S-x, Qu H-t. Dynamic mechanical properties of the Fe–30Mn–3Si–4Al TWIP steel after different heat treatments. Materials Science and Engineering: A. 2011;530:426-31.

[147] Zhang Y, Zuo TT, Tang Z, Gao MC, Dahmen KA, Liaw PK, et al. Microstructures and properties of high-entropy alloys. Progress in Materials Science. 2014;61:1-93.

[148] Yamada H, Ogasawara N, Shimizu Y, Horikawa K, Kobayashi H, Chen X. Effect of high strain rate on indentation in pure aluminum. Journal of Engineering Materials and Technology. 2013;135:021010.

[149] Joseph J, Jarvis T, Wu X, Stanford N, Hodgson P, Fabijanic DM. Comparative study of the microstructures and mechanical properties of direct laser fabricated and arc-melted AlxCoCrFeNi high entropy alloys. Materials Science and Engineering: A. 2015;633:184-93.

[150] Li D, Li C, Feng T, Zhang Y, Sha G, Lewandowski JJ, et al. High-entropy $Al_{0.3}CoCrFeNi$ alloy fibers with high tensile strength and ductility at ambient and cryogenic temperatures. Acta Materialia. 2017;123:285-94.

[151] Li D, Zhang Y. The ultrahigh charpy impact toughness of forged AlxCoCrFeNi high entropy alloys at room and cryogenic temperatures. Intermetallics. 2016;70:24-8.

[152] Meyers MA, Gregori F, Kad B, Schneider M, Kalantar D, Remington B, et al. Laser-induced shock compression of monocrystalline copper: characterization and analysis. Acta Materialia. 2003;51:1211-28.

[153] Chen M, Ma E, Hemker KJ, Sheng H, Wang Y, Cheng X. Deformation twinning in nanocrystalline aluminum. Science. 2003;300:1275-7.

[154] Diao H, Feng R, Dahmen K, Liaw P. Fundamental deformation behavior in high-entropy alloys: An overview. Current Opinion in Solid State and Materials Science. 2017;21:252-66.

[155] Hammer B, Jacobsen K, Milman V, Payne M. Stacking fault energies in aluminium. Journal of Physics: Condensed Matter. 1992;4:10453.

[156] Carter C, Holmes S. The stacking-fault energy of nickel. Philosophical Magazine. 1977;35:1161-72.

[157] Kumar N, Ying Q, Nie X, Mishra R, Tang Z, Liaw P, et al. High strain-rate compressive deformation behavior of the Al 0.1 CrFeCoNi high entropy alloy. Materials & Design. 2015;86:598-602.

[158] Zaddach A, Niu C, Koch C, Irving D. Mechanical properties and stacking fault energies of NiFeCrCoMn high-entropy alloy. JOM. 2013;65:1780-9.

[159] Mishra R, Kumar N, Komarasamy M. Lattice strain framework for plastic deformation in complex concentrated alloys including high entropy alloys. Materials Science and Technology. 2015;31:1259-63.

[160] Xu Y, Zhong W, Chen Y, Shen L, Liu Q, Bai Y, et al. Shear localization and recrystallization in dynamic deformation of 8090 Al–Li alloy. Materials Science and Engineering: A. 2001;299:287-95.

[161] Jiao Z-M, Ma S-G, Yuan G-Z, Wang Z-H, Yang H-J, Qiao J-W. Plastic deformation of Al0. 3CoCrFeNi and AlCoCrFeNi high-entropy alloys under nanoindentation. Journal of Materials Engineering and Performance. 2015;24:3077-83.

[162] Tang Q, Huang Y, Huang Y, Liao X, Langdon T, Dai P. Hardening of an $Al_{0.3}$CoCrFeNi high entropy alloy via high-pressure torsion and thermal annealing. Materials Letters. 2015;151:126-9.

[163] Yasuda HY, Shigeno K, Nagase T. Dynamic strain aging of $Al_{0.3}$CoCrFeNi high entropy alloy single crystals. Scripta Materialia. 2015;108:80-3.

[164] Gludovatz B, George EP, Ritchie RO. Processing, microstructure and mechanical properties of the CrMnFeCoNi high-entropy alloy. JOM. 2015;67:2262-70.

[165] Tiamiyu A, Basu R, Odeshi A, Szpunar JA. Plastic deformation in relation to microstructure

and texture evolution in AA 2017-T451 and AA 2624-T351 aluminum alloys under dynamic impact loading. Materials Science and Engineering: A. 2015;636:379-88.

[166] Ye T, Li L, Guo P, Xiao G, Chen Z. Effect of aging treatment on the microstructure and flow behavior of 6063 aluminum alloy compressed over a wide range of strain rate. International Journal of Impact Engineering. 2016;90:72-80.

[167] Bao WP, Xiong ZP, Ren XP, Wang FM. Effect of strain rate on mechanical properties of pure iron. Advanced Materials Research: Trans Tech Publ; 2013:21-5.

[168] Seetharaman V, Krishnan R. Influence of the martensitic transformation on the deformation behaviour of an AISI 316 stainless steel at low temperatures. Journal of materials science. 1981;16:523-30.

[169] Lee W-S, Liu C-Y. The effects of temperature and strain rate on the dynamic flow behaviour of different steels. Materials Science and Engineering: A. 2006;426:101-13.

[170] Hasegawa M, Fukutomi H. Microstructural study on dynamic recrystallization and texture formation in pure nickel. Materials Transactions. 2002;43:1183-90.

[171] Marquez AM, Braithwaite CH, Weihs TP, Krywopusk NM, Gibbins DJ, Vecchio KS, et al. Fragmentation and constitutive response of tailored mesostructured aluminum compacts. Journal of applied physics. 2016;119:145903.

[172] Sizek H, Gray G. Deformation of polycrystalline Ni3Al at high strain rates and elevated temperatures. Acta metallurgica et materialia. 1993;41:1855-60.

[173] Meyers MA, Pak H-R. Mechanical and thermal response of shock-consolidated Mar-M 200 rapidly-solidified powder. Journal of materials science. 1985;20:2133-40.

[174] Poggiali FSJ, Silva CLP, Pereira PHR, Figueiredo RB, Cetlin PR. Determination of mechanical anisotropy of magnesium processed by ECAP. Journal of Materials Research and Technology. 2014;3:331-7.

[175] Choi S-H, Shin E, Seong B. Simulation of deformation twins and deformation texture in an AZ31 Mg alloy under uniaxial compression. Acta Materialia. 2007;55:4181-92.

[176] Vecchio K, Thakur A. Effects of shock loading on cobalt-based solid-solution strengthened superalloys. Le Journal de Physique IV. 1994;4:C8-367-C8-72.

[177] Liu Y, Wang J, Fang Q, Liu B, Wu Y, Chen S. Preparation of superfine-grained high entropy

alloy by spark plasma sintering gas atomized powder. Intermetallics. 2016;68:16-22.

[178] Li Z, Zhao S, Alotaibi SM, Liu Y, Wang B, Meyers MA. Adiabatic shear localization in the CrMnFeCoNi high-entropy alloy. Acta Materialia. 2018;151:424-31.

[179] Laplanche G, Gadaud P, Horst O, Otto F, Eggeler G, George E. Temperature dependencies of the elastic moduli and thermal expansion coefficient of an equiatomic, single-phase CoCrFeMnNi high-entropy alloy. Journal of Alloys and Compounds. 2015;623:348-53.

[180] Tsai K-Y, Tsai M-H, Yeh J-W. Sluggish diffusion in Co–Cr–Fe–Mn–Ni high-entropy alloys. Acta Materialia. 2013;61:4887-97.

[181] Oh H, Ma D, Leyson G, Grabowski B, Park E, Körmann F, et al. Lattice distortions in the FeCoNiCrMn high entropy alloy studied by theory and experiment. Entropy. 2016;18:321.

[182] Rohatgi A, Vecchio KS, Gray GT. The influence of stacking fault energy on the mechanical behavior of Cu and Cu-Al alloys: deformation twinning, work hardening, and dynamic recovery. Metallurgical and Materials Transactions A. 2001;32:135-45.

[183] Li Z, Zhao S, Ritchie RO, Meyers MA. Mechanical properties of high-entropy alloys with emphasis on face-centered cubic alloys. Progress in Materials Science. 2018.

[184] Ding Q, Fu X, Chen D, Bei H, Gludovatz B, Li J, et al. Real-time nanoscale observation of deformation mechanisms in CrCoNi-based medium-to high-entropy alloys at cryogenic temperatures. Materials Today. 2019.

[185] Cai S, Li Z, Xia Y, Evolution equations of deformation twins in metals—Evolution of deformation twins in pure titanium, Physica B: Condensed Matter. 2008;403:1660-1665.

[186] Longère P. Respective/combined roles of thermal softening and dynamic recrystallization in adiabatic shear banding initiation. Mechanics of Materials. 2018;117:81-90.

[187] Meyers MA, Li Z, Zhao S, Wang B, Liu Y, Liaw PK. Shear localization of fcc high-entropy alloys. EPJ Web of Conferences: EDP Sciences. 2018:03028.

[188] Miracle D. High entropy alloys as a bold step forward in alloy development. Nature communications. 2019;10:1805.